



國立臺灣大學工學院機械工程學研究所

碩士論文

Department of Mechanical Engineering

College of Engineering

National Taiwan University

Master Thesis

機器人動態學習與人機互動

Robot Dynamics Learning and Human-Robot Interaction

鄭敬安

Ching-An Cheng

指導教授：黃漢邦 博士

Advisor: Han-Pang Huang, Ph.D.

中華民國 102 年 7 月

July 2013



國立臺灣大學碩士學位論文
口試委員會審定書

機器人動態學習與人機互動

Robot Dynamics Learning and Human-Robot Interaction

本論文係鄭敬安君（R00522817）在國立臺灣大學機械工程學系
完成之碩士學位論文，於民國 102 年 7 月 29 日承下列考試委員審查
通過及口試及格，特此證明

口試委員：

黃漢邦 黃漢邦 (簽名)

陳明新 陳明新 (指導教授)

羅仁權 羅仁權

林智仁 林智仁

系主任

楊耀州 楊耀州 (簽名)



Department of Mechanical Engineering
National Taiwan University
Taipei, TAIWAN, R.O.C.

Date: July 29, 2013

We have carefully read the thesis entitled

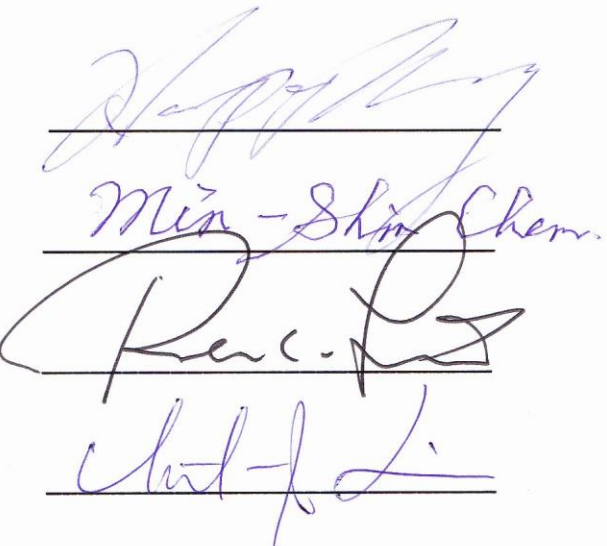
“*Robot Dynamics Learning and Human-Robot Interaction*”
submitted by Ching-An Cheng in partial fulfillment of the requirement of the degree
of **MASTER OF SCIENCE** and recommend its acceptance.

Han-Pang Huang

Min-Shin Chen

Ren C. Luo

Chih-Jen Lin



Advisor:

Chairperson of

Department of Mechanical Engineering:







致謝

如果在兩年前，我絕對沒辦法想像能夠完成如此豐腴的一本論文。

首先感謝指導教授，給予我空間和自由去冒險、研究各種可能古怪的想法，並能適時指引方向，避免迷失在一片廣闊誘人的知識海裡。另外感謝口試委員陳明新教授廣泛深入的發問，羅仁權教授嚴謹的態度，以及林智仁教授實用的觀點，帶來一場刺激精彩的口試。

在這兩年的研究中，能力的進度的速度是指數的，這最感謝子豪學長以及聖彥學長。自從大學專題生開始，這四年中，感謝子豪學長不論在實驗的技術或是理論的討論上的幫助，沒有這些詭異的辯論和美食，是不可能完成這本論文的；感謝聖彥學長不斷地瘋狂的想法和刺激，及在程式語言和實作上的幫助，使得虛無、睡覺想到的理論能夠得以實現；感謝曼寧及毓文耐心聽我自說自話和演奏音樂，祝你們幸福！感謝振虔、小叮噹、士益、書偉，常帶來歡笑和鼓勵；感謝環萍學姊、志豪學長、威志學長在腦波組一起鬼打牆；感謝煥坤學長、明寶學長、小威志、至峻、婉儒、哲軒和實驗室的所有的人的種種幫助。感謝實驗室的助理們瑩儒、鍾菁帶來滿滿的食物。感謝小木屋鬆餅，每天幸福的早餐和下午茶！感謝馬勒和巴哈提供論文的靈感和動力，另外還要特別感謝實驗室的老鼠們，不眠不休和我們一起在實驗室度過夜晚。

特別感謝我的家人和嘉珊，在我最需要幫助的時候，提供我最溫暖的慰藉。

最後感謝看完的讀者，希望這篇致謝能成為你們看完這篇論文的動力：)

2013/08/16

和大家在台大機器人實驗室





摘要

近幾年來，工業機器人以及服務機器人的需求正大幅增加，尤其人機互動的設計尤其受到重視，如機器人和人的偕同工作、用於導覽與居家看護的服務型機器人，或是能夠增強人類力量或是輔助病人復健的外骨骼機器人。而在人機互動的設計中，最重要的在於建模和控制，因為好的動態模型代表機器人能夠感測更多資訊並且能夠執行更精準的動作，而控制則關於安全、穩健的人機互動。為了下個世代機器人的發展和控制，本論文致力機器人動態學習以及人機互動的控制，並應用於以下三個主題：使用結構化再生核希爾伯特學習空間機器人動態、虛擬阻抗控制以及其在安全人機互動的應用、貝氏外骨骼系統。

為了能夠更準確以及更快速識別系統，結構核空間是一使用機器學習的技巧進行系統識別的架構。雖然適當的模型可以增加控制的效果，但傳統上，推導參數模型往往過於複雜，而廣義的機器學習方法則會引進偏差或是變異。因此，我們希望能夠設計一個方法綜合兩種方法的優點。所提出的核函數隱含了解析解並且能夠以黑盒子的方式學習，因此可以在不需推導系統的動態之下自動地識別系統，且所建構出的模型可以收斂至解析解。另外為了在非結構化空間中安全的人機互動，我們使用虛擬阻抗控制機器人，使得機器人在不論面對何種障礙物都以達到穩健、圓滑及一致的方式迴避障礙物，因此機器人可以在避免各種的碰撞下安全地進行它原本的任務。最後主題則是關於貝氏外骨骼系統的設計，運用適應性的輔助控制讓機器人可以最佳的回應操作者的意念。因此，外骨骼系統能夠同時兼顧安全以及有效的輔助控制。

關鍵字：人機互動、系統識別、再生核希爾伯特空間、外骨骼系統、意念估測、阻抗控制





Abstract

The need of robots in industries or as the service robots grows significantly in recent decades. Recently, many researches are devoted in the human-robot interactions. For examples, the collaborative working, the service robots for touring or attentive home care, or the exoskeletons for augmenting human powers or assisting the patient for normal functionalities are of interests. In the human-robot interaction, the modeling and the control of the dynamics are essential. With better modeling of the dynamical system, the robot can sensor more and provide accurate and precise responses, whereas the control scheme ensures the safety robustly and let the robot react in a human-friendly way. For better development and the control of the robot in the next generation, this thesis is devoted to the robot dynamics learning and the control of the human-robot interaction with applications in the three topics: the learning of the robot dynamics with the structured kernels, the virtual impedance control for safe human-robot interaction, and the Bayesian exoskeleton.

To model the robot dynamics automatically and accurately, the structured kernel concerns the system identification with the machine learning techniques. It is well-known that the proper model of the robot can boost the performance of the control. The tradition parametric models based on the analytic formulation are often too complex for general systems, while the other methods such as the autoregressive-moving-average (ARMA) model or the general machine learning models introduce either bias or variance in learning. The interest here is how to design a general system identification scheme that enjoys the benefits of both. The proposed kernels are designed so that not only the structures of the analytic model is implicitly



modeled but the system can be identified as the blackbox as in the machine learning approaches. In short, the proposed method is a system identification framework that learns the system automatically without any derivation of the system dynamics and yet converges to analytic model pointwisely as the number observations goes to infinity. For the control of the human-robot interaction, the virtual impedance control and the Bayesian exoskeleton system are proposed. For the robots with individual functionalities, the virtual impedance control is designed for the robust, smooth, and consistent collision avoidance that the robot can avoid all the possible collisions robustly while trying to accomplish the original task. Therefore, the robots can response the human nearby safely and compliantly. As for the robots on the human body, the Bayesian exoskeleton system assists human operators with the robust hybrid control. In the Bayesian exoskeleton system, the Bayesian estimator inferences the human intention adaptively, and the inner assistive torque control can ensure the robustness of the system by considering the ability of the operator. Therefore, the resultant exoskeleton system can ensure both the safety and the effective assistance.

Keywords: Human-Robot Interaction, System Identification, Reproducing Kernel Hilbert Space, Exoskeleton, Human Intention Estimation, Impedance Control



Contents

致謝	i
摘要	iii
Abstract	v
List of Tables	x
List of Figures	xi
Nomenclature	xiv
Chapter 1	Introduction.....	1
1.1	Human-Robot Interaction	1
1.2	Thesis Statement and Contributions	5
1.3	The Framework of the Thesis	5
Chapter 2	Reproducing Kernel Hilbert Space	9
2.1	Introduction.....	9
2.2	Reproducing Kernel Hilbert Space of Scalar Functions	10
2.3	Green's Function and the Dual Formulation.....	19
2.4	Reproducing Kernel Hilbert Space of Vector-Valued Functions	26
Chapter 3	Learning the Robot Dynamics with Structured Kernels	33
3.1	A Structured Kernel for Learning Robot Inverse Dynamics.....	35
3.1.1	Introduction.....	35
3.1.2	Reproducing Kernel Hilbert Space Revisited	39
3.1.3	Reproducing Kernel Hilbert Space of Rigid Body Dynamics	41
3.1.4	Learning the Inverse Dynamics in Multiple-Kernel Formulation	49
3.1.5	Simulations	50
3.1.6	Discussions	61
3.2	Learning the Dynamics of General Systems with the Vector-Valued Kernel.....	63
3.2.1	Introduction.....	64
3.2.2	Vector-Valued Reproducing Kernel Hilbert Space Revisited	66
3.2.3	Learning the Lagrangian and the Dynamics in the Vector-Valued Reproducing Kernel Hilbert Space	71
3.2.4	A Multiple-Kernel Framework for General Dynamics	82
3.2.5	Simulations	87
3.2.6	Discussions	91
3.3	Summary	96
Chapter 4	Virtual Impedance Control for Safe Human-Robot Interaction.....	97



4.1	Introduction.....	98
4.2	System Description	102
4.3	Virtual Impedance Control in the Risk Space.....	104
4.3.1	The Risk Space	106
4.3.2	Consistency of the Collision Dynamics	110
4.3.3	Control of the Dynamics in the Risk Space	112
4.3.4	Stability	115
4.3.5	Some Practical Issues.....	117
4.3.6	The Design of the Boundary Layer.....	118
4.3.7	The Selection of the Parameters	119
4.4	Experiments	120
4.5	Summary	132
Chapter 5	Bayesian Exoskeleton System	135
5.1	Introduction.....	136
5.2	A Robust Hybrid Control for Assistive Control with Knee Orthosis.	140
5.2.1	Introduction.....	141
5.2.2	Design of Backdrivable Torsion Spring Actuator	145
5.2.3	Robust Hybrid Control.....	149
5.2.4	Simulations	160
5.2.5	Experiments	163
5.2.6	Discussions	169
5.3	A Simple Self-Learning Scheme.....	169
5.3.1	Introduction.....	169
5.3.2	Knee Orthosis System and Modeling	171
5.3.3	Self-learning Scheme and Sliding Mode Admittance Control.....	174
5.3.4	Experimental Results	179
5.3.5	Discussions	184
5.4	Bayesian Exoskeleton System	185
5.4.1	Introduction.....	185
5.4.2	Bayesian Network and Gaussian Process Revisited	187
5.4.3	A Graphical Model for Exoskeleton System	190
5.4.4	Human Intention Estimation by Bayesian Reasoning	195
5.4.5	Control and Learning with Graphical Model	199
5.4.6	Experiments	204
5.4.7	Discussions	222
5.5	Summary	222

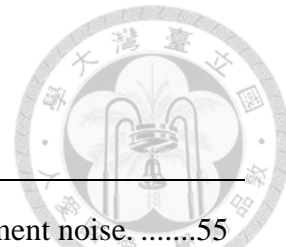
Chapter 6	Conclusions.....	227
References		233





List of Tables

Table 5-I	Comparison of rehabilitation and assistive exercise	143
Table 5-II	Specification of the designed torsion spring	147
Table 5-III	Specification of the BTSA	148



List of Figures

Fig. 3-1.	Prediction error of the ideal model without measurement noise.	55
Fig. 3-2.	Prediction error of the ideal model with measurement noise.	56
Fig. 3-3.	Prediction error of the ideal model with SMALL friction.	57
Fig. 3-4.	Prediction error of the ideal model with SMALL friction and measurement noise.	58
Fig. 3-5.	Prediction error of the ideal model with LARGE friction.	59
Fig. 3-6.	Prediction error of the ideal model with LARGE friction and measurement noise.	60
Fig. 3-7.	Computational time of evaluating 5000 testing samples given a model spanned by 5000 training samples.	61
Fig. 3-8.	The pseudo code of the MKL algorithm.	86
Fig. 3-9.	Simulation result of the ideal dynamics.	93
Fig. 3-10.	Simulation result of the ideal dynamics with frictions and measuring noises.	94
Fig. 3-11.	Asymptotical analysis.	95
Fig. 4-1.	The geometry model of the robotic manipulator	104
Fig. 4-2.	6-DOF NTU Robot Arm.	121
Fig. 4-3	The initial condition in Experiment 1.	124
Fig. 4-4.	The consistent risk space dynamics with the boundary layers of differnet sizes.	125
Fig. 4-5.	The asymptotical analysis of the boundary layer.	126
Fig. 4-6.	Obstacle avoidance of a sphere with virtual impedance control.....	127
Fig. 4-7.	The risk dynamics in Experiment 2.	128
Fig. 4-8.	The risk dynamics of the collision avoidance that do not compensate the dynamics in the risk space.....	128
Fig. 4-9.	The trajectory of the collision avoidance.	129
Fig. 4-10.	The modeling of the human and the robot in the virtual impedance control.	129
Fig. 4-11.	The safe human-robot interaction experiment part 1.....	130
Fig. 4-12.	The safe human-robot interaction experiment part 2.....	131
Fig. 5-1.	Exploded view of the proposed backdrivable torsion spring actuator.....	148
Fig. 5-2.	The knee orthosis and the backdrivable torsion spring actuator.....	148
Fig. 5-3.	Human-robot interaction model.	150



Fig. 5-4.	Block diagram of zero impedance control	151
Fig. 5-5.	Block diagram of intention feedback control.....	151
Fig. 5-6.	Block diagram of hybrid control.....	152
Fig. 5-7.	The mapping from $\hat{\tau}_H$ to τ_{ref}	154
Fig. 5-8.	The human-exoskeleton model with the hybrid control	154
Fig. 5-9.	The closed-loop system of the human-exoskeleton system.....	158
Fig. 5-10	The simulation result of the zero-impedance control	162
Fig. 5-11.	The simulation result of the intention feedback control	162
Fig. 5-12.	The simulation result of the hybrid control.....	162
Fig. 5-13.	Experimental results of the zero-impedance control	166
Fig. 5-14.	Experimental results of the intention feedback control	167
Fig. 5-15.	Experimental results of the hybrid control.....	168
Fig. 5-16.	Offline dynamics and EMG model identification.....	173
Fig. 5-17.	The self-learning control scheme of the exoskeleton system	174
Fig. 5-18.	(a) The EMG signal of the extensor. (b) The EMG signal of the flexor.	181
Fig. 5-19.	(a) The self-learning estimator, the dynamics model, and the EMG model. (b) The actual angle and the desired angle generated from admittance interface. (c) The torque command of the sliding mode controller and exoskeleton torque.....	182
Fig. 5-20.	Graphical model of the human-exoskeleton system	193
Fig. 5-21.	Control block diagram for human assistive exercises.....	200
Fig. 5-22.	Data collection procedure and the coordinates of joint angle and knee angle	201
Fig. 5-23.	Overview of the proposed backdrivable torsion spring actuator and the knee orthosis exoskeleton.....	205
Fig. 5-24.	The measured and estimated dynamics torque in dynamics data	213
Fig. 5-25.	The measured and estimated human torque in EMG model.....	213
Fig. 5-26.	The measured and estimated disturbance torque in the exogenous disturbance mode	213
Fig. 5-27.	The experimental results of swing motion without the assistive control	214
Fig. 5-28.	The experimental results of swing motion with the assistive control	216
Fig. 5-29.	The experimental results of climbing stair up and down without	



the assistive control.....	218
Fig. 5-30. The experimental results of climbing stair with the assistive control	220



Nomenclature

Notations

N	The degrees of freedom of a robot
ℓ	The number of training data
\mathbb{R}	The field of real numbers
\mathbb{R}_+	The field of positive real numbers
\mathbb{R}_{++}	The field of strictly positive real numbers
\mathbb{N}	The field of natural numbers
\mathbb{N}_+	The field of strictly positive natural numbers
\mathbb{N}_M	$\{1, \dots, M\}$, where $M \in \mathbb{N}_+$
\oplus	Direct sum
\otimes	Tensor product and Kronecker product
\circ	Hadamard product
\times	Cartesian product
$\dim(\cdot)$	Dimension of a vector space
$\ \cdot\ _p$	ℓ_p norm
$\ \cdot\ _{\mathcal{X}}$	Norm in Banach space \mathcal{X}
$\mathcal{L}^p(\mathcal{X}, \mu_x; \mathcal{Y})$	Banach spaces of functions $f : \mathcal{X} \rightarrow \mathcal{Y}$ such that $(\int_{\mathcal{X}} \ f\ _{\mathcal{Y}}^p d\mu_x)^{1/p} < \infty$, where \mathcal{Y} is often omitted to write $\mathcal{L}^p(\mathcal{X}, \mu_x)$ instead
$\ell^p(\mathcal{X})$	Banach spaces of vectors $x \in \mathcal{X}$ such that $\ x\ _p < \infty$
$C(\mathcal{X}; \mathcal{Y})$	Banach space of continuous function from \mathcal{X} to \mathcal{Y}
$L(\mathcal{X}; \mathcal{Y})$	Bounded linear operator form space from \mathcal{X} to \mathcal{Y}
$L(\mathcal{X})$	Bounded linear operator form space from \mathcal{X} to \mathcal{X}
$p(x)$	Probability density function of random variable x
$P(X)$	Probability of the occurring of the set X
$(x_i)_{i \in \mathbb{N}_N}$	$x = [x_1 \dots x_N]^T \in \mathbb{R}^N$
$(M_{ij})_{i \in \mathbb{N}_N, j \in \mathbb{N}_M}$	$M \in \mathbb{R}^{N \times M}$ with (i, j) entry M_{ij}
\mathcal{X}	Input space
\mathcal{Y}	Output space
\mathcal{Z}	$\mathcal{X} \times \mathcal{Y}$
\mathcal{F}	Feature space
X	$\{x_i x_i \in \mathcal{X}, i \in \mathbb{N}_{\ell}\}$ or a compact subset in \mathcal{X}
Y	$\{y_i x_i \in \mathcal{Y}, i \in \mathbb{N}_{\ell}\}$
Z	$X \times Y$



$\mathcal{N}(\mu, \sigma^2)$	Multivariate Gaussian probability distribution with mean μ and σ^2
$E_x\{\cdot\}$	Expectation with respect to the random variable x
$Var_x\{\cdot\}$	Expectation with respect to the random variable x
$q \in \mathbb{R}^N$	Generalized coordinates
$\tau \in \mathbb{R}^N$	Generalized forces
$T(q, \dot{q})$	Kinematic Energy
$U(q)$	Potential Energy
\mathcal{L}	Lagrangian
t	time
$M(q) \in \mathbb{R}^{N \times N}$	Generalized inertia matrix
$C(q, \dot{q}) \in \mathbb{R}^{N \times N}$	Coriolis/centrifugal matrix
$G(q) \in \mathbb{R}^N$	Gravitational term
τ_E	Exoskeleton assisting torque
τ_H	Human applying torque
τ_D	Exogenous disturbance torque

Acronyms

DOF	Degrees of freedom
RKHS	Reproducing kernel Hilbert space
BTSA	Backdrivable Torsion Spring Actuator
SEA	Serial elastic actuator
GPR	Gaussian process regression
SVM	Support vector machine
SVR	Support vector regression
i.i.d.	Independent and identically distributed





Chapter 1 Introduction

1.1 Human-Robot Interaction

Due to the rising needs of robots in the industries since past decades or as the service robots more recently, the control of the robots becomes more and more important and challenging. Among all the issues, the human-robot interaction receives most focuses nowadays. The key components to control the robot to interact with human includes: the modeling of the dynamical system, and the reactive control schemes ensuring the safety robustly.

The model of the robot, especially the dynamics model, can improve the control accuracy greatly, e.g. the computed torque control, and be used as the observers to detect the exogenous inputs, e.g. the impedance control, since the robot knows itself better; the model of the environments describes the environments mathematically, so robots can know how to react. In the tradition scenarios, the environment, in which the robot operates, is often well defined and controlled. However, the environment becomes unstructured and cannot be obtained beforehand in the human-robot interaction, such as the service robots, the human-robot collaboration, and the exoskeleton systems. In the first two cases, the major concerns are how to interact with human safely in terms of collisions while accomplishing some predefined tasks. As for the exoskeleton, the unmodeled term is operator's intention, which is important for the comfort and the controllability of the operator.

For operating in such uncertainties, the control schemes are, therefore, extremely critical. The control scheme makes decisions and plans the actions of the robot given the sensory information. In the unstructured environments, the sensory information

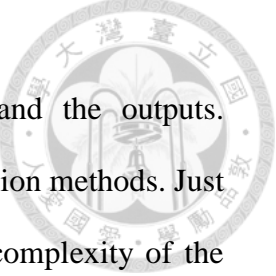


comes with uncertainties due to modeling error and noises, so the system may behave unpredictably or even be unstable, which is strictly forbidden especially in the interactions with human, if the controller is designed improperly. Therefore, efforts should be devoted into design the control schemes that can simultaneously tolerate the modeling errors and achieve performance indexes in the human-robot interaction, such as the safety, and performing human-friendly motions.

Modeling of the System Dynamics

Considering the modeling, the learning of the robot dynamics is essential to advanced control schemes for proper models can increase the performance significantly. Traditionally, the system dynamics of the robots is based on the rigid body assumption, in which each link of the robot is modeled as the rigid body and the governing equations of the system are derived from the Euler-Lagrange formulation or the iterative Newton-Euler method. We refer these to the *analytic methods* herein, in contrast to the *learning methods* based on machine learning. For the analytic method, the dynamics model can be arranged as a linear regression form, so the system identification problem can be solved by the ordinary linear regression on nonlinear basis functions. However, this ideal dynamics model does not include any frictions, motor dynamics, and elastic joint dynamics etc. To model the *unmodeled dynamics*, some analytical models are modified ad hoc. Besides, another issue is that the number of the nonlinear bases often grows in the worst case exponentially with the degrees of freedom of the system leading to necessary model simplification in practice.

On the contrary, the learning methods, which include the neural networks, support vector machines, Gaussian process regression, etc, treat the whole system as a



blackbox and learn directly the mapping between the inputs and the outputs. Concerning the system identification, we are interested in the regression methods. Just as the analytic method, the learning methods need to control the complexity of the model. In the *hypothesis space*, in which all possible models lie, the *regularization* penalizes the size or the *complexity* of the hypothesis space to prevent the overfitting due to limited observations.

On this viewpoint, the only difference between the analytic method and the learning methods are that whether the structure of the classical mechanics is considered. For example, the dynamics model based on the analytic method is structured in the sense that it is derived based on the Euler-Lagrange equation. In terms of regression, it is only the difference between the choices of bases. Therefore, a learning method can behave like the analytic method if similar bases are chosen. Thus, it may be possible to design a model that can contain the structure of analytic model implicitly and yet treat the system as the blackbox as in the learning model. Once the model of the robot is identified or learned, the controller can benefit from it. As a consequence, the performance of the whole system can be better. For example, the impedance controller and the computed torque control are closely related to the inverse dynamics model. On the other hand, a properly designed controller can adapt to unstructured scenarios, which may be also learned by the machine learning techniques.

Control of the Safe Human-Robot Interaction

The most critical factor of the control of the human-robot interaction is safety. The robot should ensure the safety first and then achieve other performance indexes under this constraint. Otherwise, the human will not be interacted with but hurt.

CHAPTER 1 INTRODUCTION

Therefore, the robustness of the safety and therefore the stability should always be guaranteed when designing the controller.



Under the safety constraint, reactive controller can be designed so that the robot can know how to response to the sensory information properly. By the reactive control, we mean a general control scheme that controls the response of the robot to the exogenous stimulus, which can be either physical or virtual like in the vision sensing. Therefore, the reactive control is like the model-reference control. Apart from the stability and the safety, another design factor is the human-friendly motion. In the interaction of human, the robot should behave as human anticipates and desires. The user-experience is decisive for the human-robot interaction. A behavior of a good reactive controller should be able to be learned intuitively by human, and be compliant rather menacing. Therefore, the robot needs to act with sufficient smoothness and elegancy. For examples in the collision avoidance, an abruptly stopping of the robot when facing the obstacles may terrorize and intimidate the human nearby, whereas a robot that circumvents the obstacles naturally is considered as friendlier. Another example is the control of the exoskeleton worn on the human directly. Because the exoskeleton is linked to the human body directly to assist motions or to amplify forces, both the safety and the tactile perception are important. The safety means both stability and the limits of the assisting force or the workspace, which is a more well-defined problem in the control system, whereas the tactile perception is intricate. An (in fact, many) exoskeleton system can be claimed to be both safe and stable, but cannot be guaranteed to make the human operator feel assisted. Just as in the collision avoidance, the human-friendly motion is the key to achieve decent assisting experience, so the exoskeleton should be compliant,



band-limited, and be guaranteed to provide the assistance robustly.

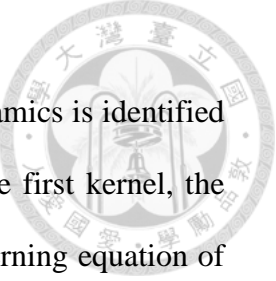
1.2 Thesis Statement and Contributions

For the development of sophisticated and intelligent robot systems for the human-robot interaction, this thesis is aimed to gain benefits from the theorems and the techniques developed for the dynamics, the machine learning, and the control system.

To unify the analytic method and the learning method in the system identification, we propose two schemes: a structured kernel specially tailored for the robot dynamics and a vector-valued kernel that learns the Lagrangian of the system for general systems; For the safe human-robot interaction, we designs the virtual impedance control by the control Lyapunov function, so that the robot can operates safely in the unstructured environment; considering the interaction between human and wearable robots, we propose the Bayesian exoskeleton system, in which the Bayesian exoskeleton system estimates the human intention optimally and adaptively in the Bayesian sense and controls the exoskeleton robustly by considering balancing ability of the operator and the dynamics of the robot.

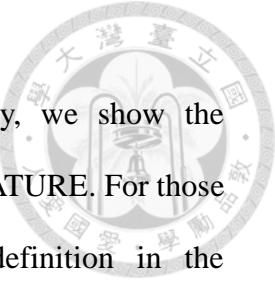
1.3 The Framework of the Thesis

This thesis is organized as follows. In Chapter 2, the theorems of reproducing kernel Hilbert space (RKHS) are reviewed, which consists most of the theoretical parts of the thesis. Especially, the relationship between the Green's function of the linear differential operator and the reproducing kernel Hilbert space is summarized. In Chapter 3, the system identification methods based on the machine learning are presented. We propose two kernels to incorporate the analytic method implicitly. In



the first scalar structured kernel, the function space of the robot dynamics is identified and modeled as the structured RKHS. Inspired by the results of the first kernel, the second kernel generalizes the idea. In contrast to modeling the governing equation of the dynamics, the second kernel directly models the Lagrangian of the system, and then induces the governing equation implicitly by the vector-valued RKHS. The result is the universal kernel that can replace any analytic method based on the Lagrangian, since the model converges to the model based on the analytic method pointwisely as the sample size goes to infinity. Chapter 4 shows the virtual impedance control framework for safe human-robot interaction. In this framework, the robot tries to achieve the original goal while avoiding possible collisions robustly and smoothly. To eliminate the chattering, a boundary layer on the spectrum of the Jacobian matrix is designed. Combined with the visual sensing, the robot successfully accomplishes the assigned task while maintaining the safety. In Chapter 5, the Bayesian exoskeleton system is proposed. We begin with the underlying robust assistive control loop, which is used throughout the chapter, and continue to demonstrate how the estimations of different sensors can be combined. Apart from the Bayesian framework, we also show another self-learning scheme. Finally, the complete Bayesian exoskeleton system based on the graphical model, the Gaussian process regression and the aforementioned robust controller is shown.

Finally, in Chapter 6, we summarize and discuss the contributions of this thesis, and give the possible future works to extend the current discoveries. We note that the proposed dissertational works are all original and novel in certain aspects compared to the literatures, and therefore we will compare them the literatures in the corresponding chapters. Also, we will bring up a short reminder of the theorems of RKHS if needed



in each section for the integrity and the continuity. For clarity, we show the nomenclature that will be used throughout the thesis in NOMENCLATURE. For those only used in the specific applications, please refer to the definition in the corresponding sections. For the conventions, the lower case denotes all the scalar, vector, matrices, and functions; the upper case denotes sets; the calligraphy denotes vector spaces, especially Hilbert space; the bold cases denote the variable related to empirical observations, or is used to distinguish the matrix from scalar especially in Chapter 3; the subscript denotes the entry of a vector or a matrix, or an instance in a set.





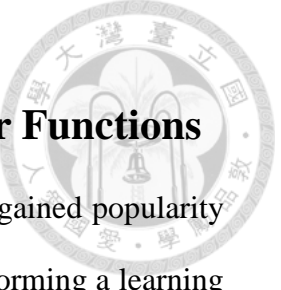
Chapter 2 Reproducing Kernel Hilbert Space

2.1 Introduction

This section serves as the surveying purpose, and summarizes the important properties of the reproducing kernel Hilbert space (RKHS) in terms of the functional analysis. We try to organize the literatures so that theorems of RKHS can be integral, but we only remark the properties and theorems that may concern the learning in RKHS for the compactness. For interested readers, we recommend [3, 86] and refer therein. On the other hand, the readers can omit this chapter without loss of continuity if the reader is familiar with RKHS.

First the RKHS of scalar functions is defined by the reproducing property and the representation theorem in the Hilbert space in Section 2.2. In Section 2.3, the connection between the quadratic penalty and the scalar RKHS in the dual problem is highlighted via the Green's function. In Section 2.4, a more general theory of RKHS of vector-valued functions is introduced. Since the vector-valued RKHS is the generalization of scalar RKHS, some theorems are only stated in Section 2.4, such as the composition of kernels. The vector-valued RKHS generalizes the theorems of the scalar RKHS and can model the vector-valued functions directly instead of multiple independent problems in scalar RKHS. In particular, the vector-valued RKHS will be used in Section 3.2 to learn the dynamics of a multi-joint robot by intrinsically considering the coupling dynamics of different joints.

In this thesis, we consider the RKHSs over real field \mathbb{R} only both for the simplicity and the sufficiency of learning the dynamics in Chapter 5 and Chapter 3.



2.2 Reproducing Kernel Hilbert Space of Scalar Functions

The RKHS formulation of the machine learning problems has gained popularity over the other methods due the elegancy and the generality of transforming a learning problem into a projection problem in the Hilbert space, and the inference problem becomes simply regressing the unknown vector given the projection of the vector in some random finite dimensional subspace. This section is partly based on [3, 10, 82, 86] and reviews the definition and the important properties of the RKHS of scalar functions as the reference for the following chapters, especially in Chapter 5 and Chapter 3.

To begin with, we review the definition of the measure space.

Definition 2.1

Let X be a set. X is said to be a measure space if there exists a σ -ring \mathfrak{R} of subsets of X and a nonnegative countably additive set function measure μ defined on \mathfrak{R} . In addition, if $X \in \mathfrak{R}$, the X is said to be a measurable space. Let $f : X \rightarrow \mathbb{R}$. The function f is said to be measurable if the set $\{x | f(x) > a\}$ is measurable for every real a .

In this thesis, we consider the reproducing kernel defined in $\mathcal{L}^2(\mathcal{X}, \mu_x)$ for a locally compact Hausdorff space \mathcal{X} with measure μ_x in general. In particular, μ_x is the probability measure, i.e. $0 \leq \mu_x \leq 1$ and $\mu_x(\mathcal{X}) = 1$. However, in some cases such as the Mercer's theorem, the RKHS is only property defined on the compact subset $X \subseteq \mathcal{X}$, in which we use the symbol X to highlight the requirement of compactness. Otherwise, \mathcal{X} is used in general.

Definition 2.2



Given a set \mathcal{X} , a compact kernel $k : \mathcal{X} \times \mathcal{X} \rightarrow \mathbb{R}$ is called of positive type if

$$\sum_{i,j}^{\ell} c_i c_j k(x_i, x_j) \geq 0$$

for any $\ell \in \mathbb{N}$, $x_1, \dots, x_\ell \in \mathcal{X}$ and $c_1, \dots, c_\ell \in \mathbb{R}$.

The kernel is also called positive (definite) kernel or Aronszajn kernel. To be clear, we call a kernel is *positive definite* if it is of positive type and a matrix *positive definite* if the spectrum is strictly positive. A positive kernel in (2.1) can also written as $c^T K c$, where $c \in \mathbb{R}^\ell$ and $K \in \mathbb{R}^{\ell \times \ell}$ is the kernel matrix. If the set $\{x_i \mid x_i \in \mathcal{X}, i \in \mathbb{N}_\ell\}$ is collected from the empirical observation, it is called the *empirical kernel matrix* denoted by \mathbf{K} herein. By Definition 2.2, the kernel matrix K is a Grammian matrix, and therefore it represents the inner product of a set of vectors in some inner product space [43]. In particular, there is Hilbert space fulfilling this property called the *reproducing kernel Hilbert space*.

Definition 2.3

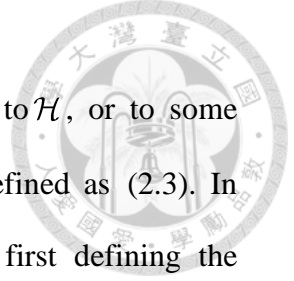
A Hilbert space \mathcal{H} of functions $f : \mathcal{X} \rightarrow \mathbb{R}$ endowed with the inner product $\langle \cdot, \cdot \rangle_{\mathcal{H}}$ is called a reproducing kernel Hilbert space on nonempty set \mathcal{X} , if $\forall x \in \mathcal{X}$ there exists a function $k_x \in \mathcal{H}$ satisfying

$$f(x) = \langle f, k_x \rangle_{\mathcal{H}}, \quad \forall f \in \mathcal{H}; \quad (2.2)$$

in particular, the reproducing kernel is defined as

$$k(x, u) = \langle k_u, k_x \rangle_{\mathcal{H}} = k_u(x) \quad x, u \in \mathcal{X}. \quad (2.3)$$

We remark the notation that the right argument of $k(x, u)$ is used as index and the left argument is used as the evaluation point of the functional. The requirement of the nonempty set X is loose. To be more specific, it only requires \mathcal{X} to be a subset in a locally compact Hausdorff space, not necessarily a Hilbert space. We mention



that k_x can be also treated also a possible nonlinear map from \mathcal{X} to \mathcal{H} , or to some isometric *feature space* \mathcal{F} , in which the inner product can be defined as (2.3). In addition to Definition 2.3, one can also define the RKHS by first defining the reproducing kernel as follows.

Definition 2.4 [3]

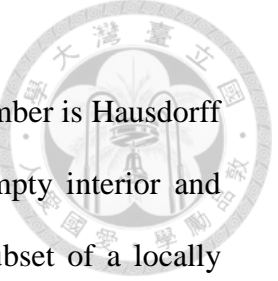
Let \mathcal{H} be a Hilbert space. The function $k(x, u)$ of $x, u \in \mathcal{X}$ is called a reproducing kernel if for every $u \in \mathcal{X}$, $k_u(x) = k(x, u)$ is a function of x and belongs to \mathcal{H} and the reproducing property that

$$f(x) = \langle f, k_x \rangle_{\mathcal{H}} \quad (2.4)$$

holds for all $f \in \mathcal{H}$ and $x \in \mathcal{X}$, then \mathcal{H} is called the reproducing kernel Hilbert space with reproducing kernel k .

Before proceeding, we recall some facts of Hausdorff space and compactness. A space is called a *Hausdorff* space if any two distinct points in it can be separated by neighborhoods, and therefore the Hausdorff space is also called *separable* space. \mathcal{X} is a Hausdroff space *iff* the limits in \mathcal{X} are unique. For example, the real line is a Hausdroff space. More generally, all metric spaces are Hausdroff, which is used in the functional analysis. Therefore, the requirement of being Hausdorff is loose.

To give the definition of compactness, we follow that: a topological space is called *compact* if each of its open covers has a finite subcover. Roughly speaking, a subsequence of an infinite series in the space accumulates at some particular points, which is a generalization of finite interval. A space is *locally-compact*, if every point in it has a compact neighborhood. For example, the Euclidean space is locally compact but not compact. Further if the space is locally compact and Hausdorff, every point in it has a closed compact neighborhood. We note that Hausdorff and local



compactness are not the same. For example, the space of rational number is Hausdorff but not locally compact, since all its compact subsets all have empty interior and therefore are not neighborhood. The example also shows that a subset of a locally compact space needs not to be locally compact. Also it can be shown that a Hausdorff space is locally compact if and only if it is finite-dimensional (as in the case of Euclidean space and Hilbert space). Also we recall that by Alexandroff one-point-compactification theorem, any locally compact Hausdorff space can be turned into a compact space by adding a single point into it.

The requirement of \mathcal{X} being Hausdorff is that evaluation functional (2.2) can be unique and identified, and the locally compactness is needed for the convergence.

Proposition 2.5 [10]

Let \mathcal{X} be locally compact Hausdorff space and \mathcal{H} be a reproducing kernel Hilbert space with kernel $k(x, u)$, $x, u \in \mathcal{X}$. The followings are equivalent:

1. *the map $k_x : \mathcal{X} \rightarrow \mathcal{H}$ is weakly continuous;*
2. *the function $k(x, u)$ is locally bounded and separately continuous.*

If one of the above condition holds, the inclusion operator $\iota : \mathcal{H} \rightarrow C^0(X, \mathbb{R})$ is continuous.

This proposition is important, because it describes the RKHS that can be included in $C^0(\mathcal{X}; \mathbb{R})$, the Banach space of continuous function. If a RKHS is the subspace of $C^0(\mathcal{X}; \mathbb{R})$, more can be said be define the corresponding integral operator in the famous Mercer's theorem.

Theorem 2.6 (Mercer's theorem of continuous kernel) [86]

Let (X, μ_x) be a finite measure space, and X is a compact subspace of \mathbb{R}^N .

Suppose $k \in \mathcal{L}^\infty(X, \mu_x) \cap C^0(X; \mathbb{R})$ is a symmetric real-valued function such that the



integral operator

$$\mathcal{T} : \mathcal{L}^2(X, \mu) \rightarrow \mathcal{L}^2(X, \mu)$$

$$(\mathcal{T}f)(u) := \int_X k(x, u) f(x) d\mu_x \quad (2.5)$$

is positive definite; that is $\forall f \in \mathcal{L}^2(X, \mu_x)$

$$\langle f, \mathcal{T}f \rangle_{\mathcal{L}^2} = \int_{X \times X} k(x, u) f(x) f(u) d\mu_x d\mu_u \geq 0. \quad (2.6)$$

Let $\phi_i \in \mathcal{L}^2(X)$ be the normalized orthogonal eigenfunctions of \mathcal{T} associated with the eigenvalues $\lambda_i > 0$, sorted in non-increasing order. Then

$$1. \quad \{\lambda_i\}_{i \in \mathbb{N}} \in \ell^1$$

$$2. \quad k(x, u) = \sum_i \lambda_i \phi_i(x) \phi_i(u) \text{ holds for almost all } x, y \in X,$$

Recall that the integral operator on a compact space has discrete eigenvalues, so the compactness assumption is necessary. For the continuous and bounded kernel defined on a compact subset X , the Mercer's theorem characterizes the norm in the RKHS by introducing the spectrum of the integral operator \mathcal{T} . Also, the boundedness and the continuity follow from each other on the assumption of the compact set. Since the spectrum is discrete, there is an isomorphism in ℓ^2 , i.e.

$$k_x : X \rightarrow \ell^2$$

$$x \rightarrow (\lambda_i \phi_i(x))_i, \quad i \in \mathbb{N}. \quad (2.7)$$

This ℓ^2 space is also called the *feature space* \mathcal{F} as mentioned earlier. On the other hand, the continuous RKHS is actually a subspace in $\mathcal{L}^2(X, \mu_x)$ as in the next corollary.

Corollary 2.7

The reproducing kernel Hilbert space \mathcal{H} in Theorem 2.6 with eigenvectors and



eigenvalues $\{\phi_i, \lambda_i\}_{i \in \mathbb{N}}$ is the set,

$$\mathcal{H} = \{f \mid f \in \mathcal{L}^2 \cap C^0, \|f\|_{\mathcal{H}}^2 < \infty\}, \quad (2.8)$$

where

$$\|f\|_{\mathcal{H}}^2 = \sum_j \frac{1}{\lambda_j} |\langle f, \phi_j \rangle_{\mathcal{L}^2}|^2 \quad (2.9)$$

In particular,

$$\langle f, g \rangle_{\mathcal{H}} = \sum_j \lambda_j \langle f, \phi_j \rangle_{\mathcal{H}} \langle g, \phi_j \rangle_{\mathcal{H}} = \sum_j \frac{1}{\lambda_j} \langle f, \phi_j \rangle_{\mathcal{L}^2} \langle g, \phi_j \rangle_{\mathcal{L}^2}. \quad (2.10)$$

Proof:

Since $\mathcal{H} = \overline{\text{span}}\{k_x \mid x \in X\}$, every $f \in \mathcal{H}$ has the following representation

$$f(x) = \sum_i \alpha_i k(x, x_i) = \sum_i \alpha_i \sum_j \lambda_j \phi_j(x) \phi_j(x_i), \quad (2.11)$$

for some $\alpha_i \in \mathbb{R}$. Define $\langle \phi_i, \phi_j \rangle_{\mathcal{H}} := \delta_{ij} / \lambda_j$. We then have

$$\langle f, k_x \rangle_{\mathcal{H}} = \sum_i \alpha_i \sum_{j,k} \lambda_j \phi_j(x_i) \langle \phi_j, \phi_k \rangle_{\mathcal{H}} \lambda_k \phi_k(x) = \sum_i \alpha_i \sum_j \lambda_j \phi_j(x) \phi_j(x_i) = f(x)$$

On the other hand,

$$f(x) = \sum_j \lambda_j \langle f, \phi_j \rangle_{\mathcal{H}} \phi_j(x) \quad (2.12)$$

Therefore, the inner product with the eigenvectors in \mathcal{L}^2 and \mathcal{H} satisfy the following equation

$$\lambda_j \langle f, \phi_j \rangle_{\mathcal{H}} = \langle f, \phi_j \rangle_{\mathcal{L}^2}, \quad (2.13)$$

since (2.11) and

$$\langle f, \phi_j \rangle_{\mathcal{H}} = \sum_i \alpha_i \phi_j(x_i). \quad (2.14)$$

The norm of $f \in \mathcal{H}$ is

$$\|f\|_{\mathcal{H}}^2 = \sum_{i,j} \alpha_i \alpha_j k(x_j, x_i) = \sum_j \lambda_j |\langle f, \phi_j \rangle_{\mathcal{H}}|^2 = \sum_j \frac{1}{\lambda_j} |\langle f, \phi_j \rangle_{\mathcal{L}^2}|^2, \quad (2.15)$$



and the inner product is

$$\langle f, g \rangle_{\mathcal{H}} = \sum_j \lambda_j \langle f, \phi_j \rangle_{\mathcal{H}} \langle g, \phi_j \rangle_{\mathcal{H}} = \sum_j \frac{1}{\lambda_j} \langle f, \phi_j \rangle_{\mathcal{L}^2} \langle g, \phi_j \rangle_{\mathcal{L}^2} \quad (2.16)$$

by using (2.12) and (2.13), which also proves

$$\{\lambda_i\}_{i \in \mathbb{N}} \in \ell^1$$

in Theorem 2.6.

Q.E.D.

This corollary also suggests the inner product in \mathcal{H} can be computed by defining another integral kernel

$$Q(x, u) = \sum_j \frac{1}{\lambda_j} \phi_j(x) \phi_j(u) \quad (2.17)$$

and the operator

$$(Qf)(x) := \langle f, Q(u, x) \rangle_{\mathcal{L}^2} = \sum_j \frac{1}{\lambda_j} \langle f, \phi_j \rangle_{\mathcal{L}^2} \phi_j(x), \quad (2.18)$$

So the inner product in \mathcal{H} in terms of $G(x, u)$ is

$$\langle f, g \rangle_{\mathcal{H}} = \langle f, Qg \rangle_{\mathcal{L}^2} \quad (2.19)$$

from (2.16).

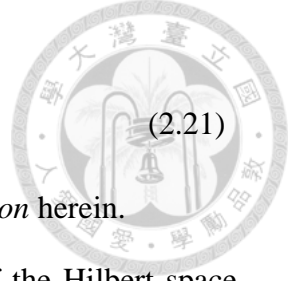
In summary, the inner product and the induced norm of \mathcal{H} can be defined in both in $\mathcal{L}^2(X, \mu_x)$ and \mathcal{H} or some other isometric Hilbert space. Recall the Mercer's theorem on the compact subset allows the eigen-decomposition of the reproducing kernel

$$k(x, u) = \sum_i \lambda_i \phi_i(x) \phi_i(u)$$

and therefore the norm of in have two representations

$$\|f\|_{\mathcal{H}}^2 = \sum_{i,j} \alpha_i \alpha_j k(x_j, x_i), \quad (2.20)$$

and



$$\|f\|_{\mathcal{H}}^2 = \langle f, Qf \rangle_{\mathcal{L}^2}, \quad (2.21)$$

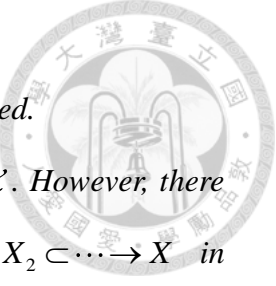
which are called the *dual representation* and the *primal representation* herein.

The dual representation is based on the representation theorem of the Hilbert space and the weak topology on \mathcal{H} ; the primal representation is formulated as the normed space in $\mathcal{L}^2(X, \mu_x)$ with the quadratic norm (2.21). The two representations are both useful to be considered in learning. Especially, the induced norm corresponds to the penalty or the prior probability of the underlying function, whereas the dual representation shows the clear connection to Representer theorem. The connection between (2.20)and (2.21) will be more focused in the next section by introducing the Green's function.

Before ending this section, we remark some informative properties of the scalar RKHS regarding the convergence, the boundedness, and the uniqueness.

Remark 2.8 [3]

1. If a reproducing kernel exists it is unique.
2. A reproducing kernel exists iff $\forall x \in \mathcal{X}$, $f(x)$ is a continuous functional of f running through the Hilbert space \mathcal{H} .
3. $k(x, u)$ is of positive type.
4. To every positive definite matrix $k(x, u)$, there corresponds one and only one class of functions with a uniquely determined quadratic form in it, forming a Hilbert space and admitting $k(x, u)$ as a reproducing kernel.
5. If the Hilbert space \mathcal{H} possess a reproducing kernel $k(x, u)$, every sequence function $\{f_n\}$, which converges strongly to a function $f \in \mathcal{H}$, converges also pointwisely in ordinary sense, i.e. $\lim f_n(x) = f(x)$. In particular, this convergence

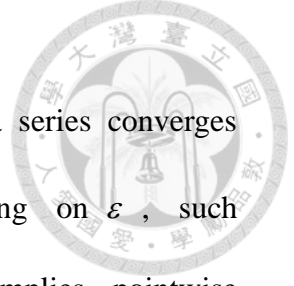


is uniform in every subset of \mathcal{X} in which $k(x, x)$ is uniformly bounded.

6. If $\{f_n\}$ converges to $f \in \mathcal{H}$ weakly, then $f_n(x) \rightarrow f(x)$ for every $x \in \mathcal{X}$. However, there is in general no increasing sequence of sets $X_1 \subset X_2 \subset \dots \rightarrow X$ in which $\{f_n\}$ converges uniformly to f .

For (X, μ_x) , by Remark 2.8, the reproducing kernel exists iff $f(x)$ is a continuous functional of f running through the Hilbert space \mathcal{H} iff $k(x, u)$ is continuous and locally bounded (which is the same as in [37]). In Mercer's theorem, $k(x, u)$ is assumed to be uniformly bounded; the RKHS defined in Mercer's theorem is a subspace in $\mathcal{L}_2(X)$ (also $C^0(X)$ from definition), where X is compact.

Finally, we give a short note on the convergence just for reminder. We first contrast the definition of weak convergence to strong convergence. Let X be topological vector space over a topological field, which is assumed to be the field of real numbers in throughout this context, and let X^* be the dual space of X , which is full of linear functions from X to the base field. The *weak topology* of X is the initial topology with respect to X^* , which is the coarsest topology such that each elements of X^* is a continuous function, whereas X is called the strong topology. The *strong convergence*, also known as *convergence in norm*, is defined with respect to the strong topology, that is $\{x_n\} \rightarrow x$ strongly then $\|x_n - x\| \rightarrow 0$. On the other hand, if $\{x_n\} \rightarrow x$ weakly means that $\phi(x_n) \rightarrow \phi(x)$ for all linear functions $\phi \in X^*$. Some famous examples are given in Hilbert space, e.g. $\sin(2nx)$ converges weakly to 0 but not strongly; the orthonormal bases in an infinite dimensional space converges weakly to 0. The other types of convergence are the *uniform convergence* and the *pointwise convergence*. A series converges uniformly if there exists $N > 0$, such



that $\|x_n - x\| < \varepsilon$ for all $n \geq N$ for any $\varepsilon > 0$; on the other hand, a series converges pointwisely if given any $\varepsilon > 0$ there exists $N > 0$ depending on ε , such that $\|x_n - x\| < \varepsilon$ for all $n \geq N$. The uniform convergence implies pointwise convergence and the converse is not true. The uniform convergence can be proved to be preserving many properties of the limit, such continuity, differentiability, etc. [82].

2.3 Green's Function and the Dual Formulation

In this section, we first introduce the Green's function of the linear differential operator and connect the Green's function to the RKHS. The Green's function of a linear differential operator can be used to induce a quadratic norm in $\mathcal{L}^2(X, \mu_x)$ which effectively creates a RKHS via (2.19). Note that X is used here for simplicity; otherwise, the spectrum may be continuous defined by the resolvent sets.

We first give the definition of the Green's function.

Definition 2.9 [30]

For a linear differential operator L defined on a set $X \in \mathbb{R}^N$,

$$Lg = f, \quad x \in X \tag{2.22}$$

with Neumann or Dirichlet boundary condition on the boundary ∂X , the Green's function $G(x, u)$ of L satisfies

$$\begin{cases} L^*G(x, u) = \delta_u(x), & x \in X \\ \text{adjoint boundary conditions, } x \in \partial X \end{cases} \tag{2.23}$$

Based on the bilinear identity, we can obtain the representation formula

For $Lg(x) = f(x)$,

$$g(u) = \langle g, \delta_u \rangle = \langle g, L^*G_u \rangle = \langle f, G_u \rangle = \int G(x, u) f(x) dx \tag{2.24}$$



That is, the linear integral operator \mathcal{G} , defined as

$$(\mathcal{G}f)(u) := \int G(x, u)f(x)dx, \quad (2.25)$$

or

$$\mathcal{G}_u f := \int G(x, u)f(x)dx, \quad (2.26)$$

is the left inverse of L , satisfying

$$\mathcal{G}Lg = g. \quad (2.27)$$

In particular, if $L: V \rightarrow V$ for some vector space V , then

$$f(y) = \langle f, \delta_y \rangle = \langle Lf, G_y \rangle = \int Lf(x)G(x, y)dx = Lg(y) = L \int G(x, y)f(x)dx.$$

For a linear differential equation with forcing term, the solution can be obtained by identifying the Green's function of the operator. We also remark that this property is similar to the reproducing property in RKHS. Before proceeding to connect the Green's function and the RKHS, we summarize some important properties of Green's function as follows.

Remarks 2.10

1. If the kernel of L is non-trivial, the Green's function is not unique.
2. Near the boundary, the Green's function often behaves badly [30].
3. If the operator is translation invariant, then $G(x, u) = G(x - u)$.
5. (**Reciprocity theorem**) If the operator L is self-adjoint the Green's function satisfies $G(x, u) = G(u, x)$ [30].
6. If ϕ and λ solves the eigenvalue problem $L\phi = \lambda\phi$, then $\mathcal{G}\phi = \frac{1}{\lambda}\phi$ as long as $\lambda \neq 0$.
7. If L is compact and self-adjoint, then \mathcal{G} is self-adjoint and $\{\phi_i\}$ is complete, since the eigenvectors of a compact, self-adjoint operator form a complete set. Then



$$G(x, y) = \sum_i \frac{1}{\lambda_i} \phi_i^*(x) \phi_i(y); \quad (2.28)$$

in particular

$$\delta_y(x) = \sum_i \phi_i^*(x) \phi_i(y). \quad (2.29)$$

After fully introducing the Green's function, we are now in the position two connect the RKHS and the Green's function. The key observation is that the inner product of two functions in RKHS can be stated as the inner product of the images of the two functions via a linear operator, as in the following theorem

Theorem 2.11 [86]

For every RKHS \mathcal{H} with reproducing kernel k , there exists a linear operator $\mathcal{S}: \mathcal{H} \rightarrow \mathcal{D}$ and a Hilbert space \mathcal{D} , such that $\forall f \in \mathcal{H}$

$$\langle \mathcal{S}f, \mathcal{S}k_x \rangle_{\mathcal{D}} = f(x)$$

In particular

$$\langle \mathcal{S}k_u, \mathcal{S}k_x \rangle_{\mathcal{D}} = k(x, u)$$

Likewise, for every positive definite linear self-adjoint operator $\tilde{\mathcal{S}}: \tilde{\mathcal{D}} \rightarrow \tilde{\mathcal{D}}$ for which a Green's function exists, there exists a corresponding RKHS \mathcal{H} with reproducing kernel k , an inner product space \mathcal{D} , and an operator $\mathcal{S}: \mathcal{H} \rightarrow \mathcal{D}$ such that the above holds.

The theorem above shows the existence of the linear operator or the RKHS are given from each other. Following the theorem above, given a linear differential operator L for which the Green's function exists, we can define a RKHS \mathcal{H} with reproducing kernel k by defining the inner product as

$$\langle f, g \rangle_{\mathcal{H}} := \langle Lf, Lg \rangle_{L^2} = \int Lf(x) Lg(x) dx \quad (2.30)$$



which is equal to

$$\langle f, L^* L g \rangle_{\mathcal{L}^2} = \langle f, Q g \rangle_{\mathcal{L}^2} \quad (2.31)$$

where $\mathcal{Q} := L^* L$ is self-adjoint and positive definite. That is, the linear operator L can be used to induce a inner product space with inner product $\langle \cdot, \mathcal{Q} \cdot \rangle_{\mathcal{L}^2}$ in $\mathcal{L}^2(X, \mu_x)$. We recall in (2.19) the integral operator \mathcal{T} also induce a inner product space in $\mathcal{L}^2(X, \mu_x)$.

In fact, \mathcal{T} and L are connected to each other through this formulation, so are the reproducing kernel $k(x, u)$ and the Green's function $G(x, u)$. We summarize this connection in the following theorem, which serves the alternative of Theorem 2.11.

Theorem 2.12

Let (X, μ_x) be a compact measurable space with finite measure, and let $k(x, u)$ be a Mercer's kernel with the integral operator

$$(\mathcal{I}f)(u) := \int_X k(x, u) f(x) d\mu_x$$

i.e.

$$k(x, u) = \sum_i \lambda_i \phi_i(x) \phi_i(u),$$

where $\phi_i, \lambda_i > 0$ for all $i \in \mathbb{N}$ is the normalized eigenvectors and the eigenvalues of \mathcal{T} in $\mathcal{L}^2(X, \mu_x)$. Let $G(x, u)$ be the Green's function of the linear differential operator L , and define the integral operator

$$(\mathcal{G}f)(u) := \int G(x, u) f(x) d\mu_x,$$

and assume L admits a set of complete eigenvectors φ_i with eigenvalues ω_i , i.e.

$$G(x, u) = \sum_i \frac{1}{\omega_i} \varphi_i(x) \varphi_i(u),$$

in which φ_i are normalized in $\mathcal{L}^2(X, \mu_x)$. Both $k(x, u)$ and $G(x, u)$ define the same



RKHS, i.e.

$$\langle f, g \rangle_{\mathcal{H}} = \langle Lf, Lg \rangle_{\mathcal{L}^2} = \sum_j \frac{1}{\lambda_j} \langle f, \phi_j \rangle_{\mathcal{L}^2} \langle g, \phi_j \rangle_{\mathcal{L}^2}, \quad (2.32)$$

If and only if the following holds:

1. $\varphi_i = \phi_i \lambda_i = \omega_i^{-2} > 0$, for all i
2. Let the integral kernel $Q(x, u) = \sum_j \frac{1}{\lambda_j} \phi_j(x) \phi_j(u)$ and the corresponding integral operator $\mathcal{Q} := \langle f, Q(\cdot, u) \rangle_{\mathcal{L}^2}$. Then

$$\langle f, g \rangle_{\mathcal{H}} = \langle f, \mathcal{Q}g \rangle_{\mathcal{L}^2} = \langle Lf, Lg \rangle_{\mathcal{L}^2}; \quad (2.33)$$

in particular,

$$k(x, u) = \langle k_u, k_x \rangle_{\mathcal{H}} = \langle G_u, G_x \rangle_{\mathcal{L}^2} \quad (2.34)$$

and

$$G(x, u) = Lk(x, u). \quad (2.35)$$

Proof:

—————

From (2.32), we have

$$\langle f, g \rangle_{\mathcal{H}} = \langle f, \tilde{\mathcal{Q}}g \rangle_{\mathcal{L}^2} = \langle Lf, Lg \rangle_{\mathcal{L}^2},$$

where $\tilde{\mathcal{Q}} = L^* L$. On the other hand,

$$k(x, u) = \langle k_u, k_x \rangle_{\mathcal{H}} = \langle Lk_u, Lk_x \rangle_{\mathcal{L}^2} = \langle k_y, \delta_x \rangle_{\mathcal{L}^2} = \langle Lk_y, G_x \rangle_{\mathcal{L}^2}, \quad (2.36)$$

so

$$G(x, u) = Lk(x, u),$$

In particular,

$$k(x, u) = \int G(s, x) G(s, u) ds = \langle G_u, G_x \rangle_{\mathcal{L}^2} \quad (2.37)$$



by applying \mathcal{G} on both sides of (2.35).

Rewriting (2.32) as

$$\langle f, g \rangle_{\mathcal{H}} = \sum_j \omega_j^2 \langle f, \varphi_j \rangle_{L^2} \langle g, \varphi_j \rangle_{L^2} = \sum_j \frac{1}{\lambda_j} \langle f, \phi_j \rangle_{L^2} \langle g, \phi_j \rangle_{L^2}$$

and substitute $f = \varphi_j, g = \phi_i$, we have for all i, j .

$$\omega_j^2 \langle \phi_i, \varphi_j \rangle_{L^2} = \frac{1}{\lambda_i} \langle \varphi_j, \phi_i \rangle_{L^2}. \quad (2.38)$$

Let $i = j$ in (2.38), we have $\lambda_i = \omega_i^{-2} > 0$, and

$$\langle \phi_i, \varphi_j \rangle_{L^2} = \frac{\lambda_j}{\lambda_i} \langle \varphi_j, \phi_i \rangle_{L^2}.$$

For general λ_i , we have $\langle \varphi_j, \phi_i \rangle_{L^2} = \delta_{ij}$ and therefore $\varphi_i = \phi_i$. Thus, $\mathcal{Q} = L^* L$.

←

If $\varphi_i = \phi_i$, $\lambda_i = \omega_i^{-2} > 0$, for all i , then

$$\langle f, g \rangle_{\mathcal{H}} = \sum_j \omega_j^2 \langle f, \varphi_j \rangle_{L^2} \langle g, \varphi_j \rangle_{L^2} = \sum_j \frac{1}{\lambda_j} \langle f, \phi_j \rangle_{L^2} \langle g, \phi_j \rangle_{L^2}.$$

Q.E.D.

From Theorem 2.12, it is clear the norm that Green's function induced with the eigenvalues of the differential linear operator is the inverse of that of the integral operator. Therefore, if we treat (2.31) as the regularization term in a learning algorithm, e.g. penalizing the terms of higher derivatives, the reproducing kernel will be dominated by the eigenfunction with less penalties.

Corollary 2.13

Let $\mathcal{R} : \mathcal{E} \rightarrow \mathbb{R}_+$ be a regularization on a function space \mathcal{E} defined on a compact set X ,

i.e. for all $f \in \mathcal{E}$

$$\mathcal{R}(f) = \langle f, \mathcal{Q}f \rangle_{L^2},$$



where \mathcal{Q} is the integral operator with the kernel

$$\mathcal{Q}(x, u) = \sum_j \frac{1}{\lambda_j} \phi_j(x) \phi_j(u)$$

where $\lambda_j > 0$. Then \mathcal{Q} defines a RKHS \mathcal{H} with the inner product $\langle \cdot, \cdot \rangle_{\mathcal{H}} = \langle \cdot, \mathcal{Q} \cdot \rangle_{\mathcal{L}^2}$, and

the reproducing kernel

$$k_u = k(x, u) = \sum_j \lambda_j \phi_j(x) \phi_j(u)$$

such that $\mathcal{H} = \overline{\text{span}}\{k_x \mid x \in X\}$. In particular, if $f(x) = \sum_i \alpha_i k(x, x_i)$ for some α_i ,

$$\text{then } \|f\|_{\mathcal{H}}^2 = \sum_{i,j} \alpha_i \alpha_j k(x_i, x_j) = \langle f, \mathcal{Q}f \rangle_{\mathcal{L}^2}.$$

Theorem 2.12 and Corollary 2.13 shows that a quadratic norm defined in $\mathcal{L}^2(X, \mu_x)$ defines an effective RKHS, which is very useful to analyzing a learning algorithm, since most of the algorithms use quadratic norm to regularize the complexity of the hypothesis space. Finally, we give an example of Laplacian regularization to end this section.

Example 2.14

Let \mathcal{M} be a compact manifold with or without boundary and

$$\mathcal{E} = \{f \mid f \in \mathcal{L}^2(\mathcal{M}) \cap C^0(\mathcal{M}), f \perp \mathbf{1}(\mathcal{M})\},$$

where $\mathbf{1}(\mathcal{M})$ denotes the space of constant function on the manifold.

Let $\Delta := -\sum_i \frac{\partial^2}{\partial x_i^2}$ be the Laplace-Beltrami operator on \mathcal{M} . Then Δ and \mathcal{E} defines a

RKHS \mathcal{H} such that for $f(x) = \sum_i \alpha_i k(x, x_i)$,

$$\|f\|_{\mathcal{H}}^2 = \langle f, \Delta f \rangle_{\mathcal{L}^2(\mathcal{M})} = \alpha^T K \alpha$$

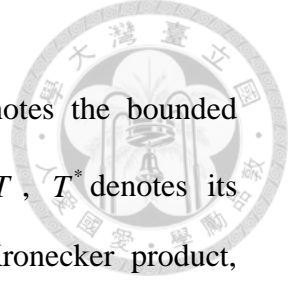
where α is the vector of α_i , K is the kernel matrix. In particular, K can be computed as the pseudoinverse of Δ .



2.4 Reproducing Kernel Hilbert Space of Vector-Valued Functions

In this section, we introduce the RKHS of vector-valued functions, denoted by *vector-valued RKHS* herein. The vector-valued RKHS generalize the theorem of the scalar RKHS so that it contains the vector-valued function intrinsically. Recently, the formal studies of RKHS generalizing the Mercer's theorem and the feature space [8, 11, 12, 31], and theory of convergence of learning in RKHS are established [9]. In this section, we shall follow these studies, especially [8], to give the definition and the properties of the vector-valued RKHS.

We try to parallel the scalar RKHS in this section so that the intricate differences can be contrasted, but we first begin with some notations for clarity. Let \mathcal{X} be a locally compact Hausdorff topological space, and \mathcal{Y} be a separable Hilbert space endowed with the inner product $\langle \cdot, \cdot \rangle_{\mathcal{Y}}$. We restrict our attention to the case when \mathcal{Y} is of finite dimensionality and defined over the real field \mathbb{R} hereafter, both for the need of the application and the simplicity. $\mathcal{Y}^{\mathcal{X}}$ denotes the space of functions that maps from \mathcal{X} to \mathcal{Y} , and $C(\mathcal{X}; \mathcal{Y})$ the Banach space of continuous functions from \mathcal{X} to \mathcal{Y} endowed with the infinity norm. Let $\mathcal{B}(\mathcal{X})$ be the Borel σ -algebra of \mathcal{X} and $\mu: \mathcal{B}(\mathcal{X}) \rightarrow [0, +\infty]$ be a Borel measure on \mathcal{X} , which is σ -additive and finite on compact sets. For $1 \leq p < \infty$, $\mathcal{L}^p(\mathcal{X}, \mu; \mathcal{Y})$ denotes the Banach space of measurable functions $f \in \mathcal{Y}^{\mathcal{X}}$ such that $|f|^p$ is μ -integrable, with norm $\|f\|_p = \left(\int_{\mathcal{X}} |f(x)|^p d\mu(x) \right)^{1/p}$. Also, given two nonempty sets A and B , we denote by $L(A; B)$ the Banach space of bounded linear operators from A to B , in which $L(A)$



is subspace of bounded linear operators from A to A . $L_+(A)$ denotes the bounded positive semidefinite operator. Finally, for a linear operator T , T^* denotes its adjoint; \otimes denotes both the tensor product of spaces and the Kronecker product, between which the discrimination will not be made if there is no ambiguity; \oplus denotes the direction sum of vector spaces.

Definition 2.15

Given a locally compact Hausdorff space \mathcal{X} and a Hilbert space \mathcal{Y} as defined previously, a kernel $K : \mathcal{X} \times \mathcal{X} \rightarrow L(\mathcal{Y})$ is said to be of positive-type, if K is positive semidefinite, i.e.

$$\sum_{i,j}^l c_i c_j \langle y_i, K(x_i, x_j) y_j \rangle_{\mathcal{Y}} \geq 0,$$

for any $l \in \mathbb{N}$, $\{x_j \mid j \in \mathbb{N}_l\} \subseteq \mathcal{X}$, $\{y_j \mid j \in \mathbb{N}_l\} \subseteq \mathcal{Y}$, and $c_1, \dots, c_l \in \mathbb{R}$.

This definition generalizes the notation of positive-type in the scalar RKHS where $\mathcal{Y} = \mathbb{R}$ in Definition 2.1. Also, one can think that a vector-valued RKHS is actually a scalar RKHS defined on the space $\mathcal{X} \times \mathcal{Y}$, by treating both the input space \mathcal{X} and the output space \mathcal{Y} as the indexes, i.e. $k_y(x_i, x_j) = \langle y_i, K(x_i, x_j) y_j \rangle_{\mathcal{Y}}$, where \times denotes the Cartesian product.

Definition 2.16

A Hilbert space \mathcal{H} of functions $f \in \mathcal{Y}^{\mathcal{X}}$ endowed with the inner product $\langle \cdot, \cdot \rangle_K$ and norm $\|\cdot\|_K$ is called a reproducing kernel Hilbert space on \mathcal{X} , if $\forall x \in \mathcal{X}$ there exists a map $K_x : \mathcal{Y} \rightarrow \mathcal{H}$ satisfying

$$\langle f(x), y \rangle_{\mathcal{Y}} = \langle f, K_x y \rangle_K, \quad \forall f \in \mathcal{H}.$$

In particular, the reproducing kernel $K : \mathcal{X} \times \mathcal{X} \rightarrow L(\mathcal{Y})$ is defined as



$$K(x, u) = K_x^* K_u, \quad \forall x, u \in \mathcal{X},$$

and

$$f(x) = K_x^* f, \quad \forall f \in \mathcal{H}_k$$

where $K_x^* : \mathcal{H} \rightarrow \mathcal{Y}$ is the adjoint of K_x .

In contrast to the scalar RKHS, the reproducing kernel of the vector-valued RKHS is a bounded linear operator $L(\mathcal{Y})$, or can be viewed as the mapping from \mathcal{Y} to \mathcal{H}_k and K_x^* is a linear operator from \mathcal{H} back to $\sum_{i,j}^l c_i \bar{c}_j \langle y_i, K(x_i, x_j) y_j \rangle_Y = \sum_{i,j}^l c_i \bar{c}_j \langle K_{x_i} y_i, K_{x_j} y_j \rangle_{\mathcal{H}} \geq 0$. In the second viewpoint vector space \mathcal{H} can be more easily understood. If we treat $K_x y$ as a function of both x, y , i.e. $K_x y : X \times Y \rightarrow \mathcal{H}$, the vector-valued RKHS is a then vector space defined by

$$\mathcal{H} = \overline{\text{span}}\{K_x y \mid x \in \mathcal{X}, y \in \mathcal{Y}\}.$$

In other words, if $\dim(\mathcal{H})$ is finite, \mathcal{H} is an isomorphism of $\mathbb{R}^{\dim(\mathcal{H})}$ and $K_x \in \mathbb{R}^{\dim(\mathcal{H}) \times \dim(\mathcal{Y})}$. Therefore, $K_x y$ is a vector in \mathcal{H} in the column space of K_x and combined by y . On the other hand, $K_x^* \in \mathbb{R}^{\dim(\mathcal{Y}) \times \dim(\mathcal{H})}$ as the evaluation matrix to map a vector in \mathcal{H} to multiple values in \mathcal{Y} . In short, a vector-valued function f is a vector in \mathcal{H} , the value of the function is the image of linear map K_x^* .

See [11, 31] for an alternative argument, but they define \mathcal{H} by first defining multiple scalar RKHSs so that \mathcal{H} should be at least large enough to contain all the scalar RKHSs. However, we define directly the vector-valued RKHS, and therefore the vector-valued RKHS may be smaller than that required in [31] as long as



proper K_x can be identified.

The following theorem is the replica of that of the scalar RKHS.

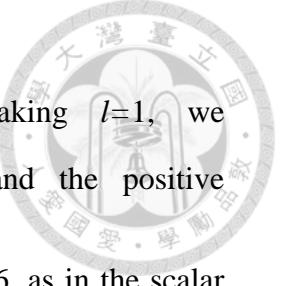
Remark 2.17

1. A reproducing kernel is unique up to isometries.
2. A bounded reproducing kernel exists if and only if $\forall x \in \mathcal{X}$, $f(x)$ is a continuous linear map of f running through the Hilbert space \mathcal{H} .
3. $K(x, u)$ is of positive type $\forall x, u \in \mathcal{X}$.
4. $\mathcal{H} \subseteq C(\mathcal{X}; \mathcal{Y})$ if and only if $K(x, u)$ is locally bounded and $\forall x \in X$, K_x is strongly continuous.
5. The uniform (weak) convergence of the series $\{f_i\} \in \mathcal{H}$ implies the uniform (locally) boundedness of the kernel K as in the scalar case. In particular, $\{f_i\}$ converges pointwisely to f . [3]
6. The set $\{K_x y \mid x \in X, y \in Y\}$ is total in \mathcal{H} , that is, $(\bigcup_{x \in X} \text{Im } K_x)^\perp = \{0\}$. [11]

In Remark 2.172, $|f(x)| = |K_x^* f| \leq \|K_x^*\|_{\mathcal{H}} \|f\|_{\mathcal{H}}$ from the definition. On the other hand, if $f(x)$ is continuous, then by the general theory of Hilbert space there exist a linear operator G_x such that $f(x) = G_x f$. In addition, since G_x is linear and continuous, G_x is bounded. In Remark 2.173, it is equivalent to

$$\sum_{i,j}^l c_i c_j \langle y_i, K(x_i, x_j) y_j \rangle_Y = \sum_{i,j}^l c_i c_j \langle K_{x_i} y_i, K_{x_j} y_j \rangle_{\mathcal{H}} \geq 0,$$

where $c_j \in \mathbb{R}$. If we treat $K(x, u)y = (K_u y)(x)$, we can have a similar argument in $L^2(\mathcal{X} \times \mathcal{Y}; \mu_x \times \mu_y)$. Moreover, $K(x, x)$ is positive definite for all $x \in X$ iff \mathcal{H} is normal. We recall that a space is *normal* if given two disjoint sets, there are open neighborhoods that are also disjoint and that all metric space are normal Hausdorff.



Indeed, this is a direct result of positive type. By taking $l=1$, we have $\sum_{i,j \in \mathbb{N}_{\dim(Y)}} y_i y_j K_{ij}(x,x) \geq 0$, which implies $K(x,x) \in L_+(Y)$, and the positive definiteness follows from the definition of normal. In Remark 2.176, as in the scalar case, we can define another Hilbert space alternatively that is partially isometry to \mathcal{H} [11] (p. 6), which is sometimes called the *feature space*. Also, for $f \in \mathcal{L}^2(X;Y) \cap C^0(X;Y)$, see chapter 6 in [11] for the Mercer's theorem of the vector-valued functions generalized to non-convex space X .

Note that we emphasize $K(x,u)y = (K_u y)(x)$, where the second argument is used as the index. Also, it can be shown that $K(x,u) = K(u,x)^T$ and $K(x,x) \in L_+(\mathcal{Y})$, i.e. $\|K(x,x)\|_{\mathcal{Y}}$ is a semi-norm of \mathcal{H}_k . In particular,

$$\|K_x\|_{\mathcal{H}} = \|K(x,x)\|_{\mathcal{Y}}^{1/2}$$

$$\langle v, K(u,x)y \rangle = \langle K_u v, K_x y \rangle, \quad \forall x, u \in \mathcal{X}, y, v \in \mathcal{Y}$$

The next proposition is parallel to Proposition 2.5.

Proposition 2.18 [11]

Let \mathcal{X} be locally compact space, \mathcal{Y} be a Hilbert space, and \mathcal{H} be a reproducing kernel Hilbert space with kernel $K(x,y)$. The followings are equivalent:

1. the elements of \mathcal{H} are continuous functions;
2. the kernel $K(x,y)$ is locally bounded and, for all $x \in X$, the map K_x is strongly continuous.

If one of the above condition holds, the inclusion operator $\iota: \mathcal{H} \rightarrow C(X;Y)$ is continuous.

In this thesis, we consider the case $\mathcal{H} \subseteq C(\mathcal{X};\mathcal{Y})$. To end this section, we



summarize some useful admissible constructions of a vector-valued RKHS, and the generalized representer theorem for vector-valued RKHS.

Proposition 2.19

Let G, K be two reproducing kernels of vector-valued RKHS as defined previously.

1. *The sum $K+G$ is a reproducing kernel and the corresponding RKHS is the direct sum of the two RKHSs.*
2. *Hadamard (Schur) product, $K \circ G$, is a reproducing kernel and the corresponding RKHS is the tensor product of the two RKHSs.*
3. *Let \mathcal{X}_0 be a compact Hausdorff space, $\mathcal{Y} \in \mathbb{R}^N$, $\Gamma_p : \mathcal{X} \rightarrow \mathcal{X}_0$ for all $p \in \mathbb{N}_N$. Given a scalar kernel $G : \mathcal{X}_0 \times \mathcal{X}_0 \rightarrow \mathbb{R}$, then*

$$K(x, u) = \left(G(\Gamma_p x, \Gamma_q u) \right)_{p, q \in \mathbb{N}_N}$$

is a vector-valued reproducing kernel.

These constructions are mostly commonly used to construct a new kernel. Please see [5] and therein for a complete survey of admissible constructions. Finally, we show the representer theorem for the vector-valued RKHS generalized from [85] for scalar RKHS, which can also apply to scalar RKHS.

Theorem 2.20 (Representer Theorem)

Given a locally compact Hausdorff space \mathcal{X} and a Hilbert space \mathcal{Y} , a reproducing kernel $K : \mathcal{X} \times \mathcal{X} \rightarrow L(\mathcal{Y})$ of the vector-valued RKHS \mathcal{H}_K , a strictly monotonically increasing real-valued function g on $[0, \infty)$, and an arbitrary cost function $c : (\mathcal{X} \times \mathbb{R}^2)^l \rightarrow \mathbb{R} \cup \{\infty\}$, a set of samples $\{(x_i, y_i) | x_i \in \mathcal{X}, y_i \in \mathcal{Y}\}_{i \in \mathbb{N}_l}$, the minimizer of

$$\min_{f \in \mathcal{H}_K} c((x_1, y_1, f(x_1), \dots, (x_l, y_l, f(x_l))) + g(\|f\|_K)$$

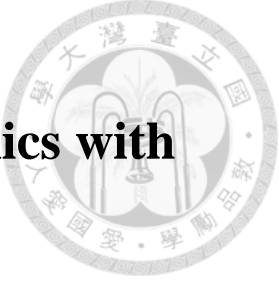
CHAPTER 2 REPRODUCING KERNEL HILBERT SPACE

admits a representation of the form

$$f = \sum_{i \in \mathbb{N}_l} K_{x_i} \alpha_i .$$

for some $\alpha_i \in \mathbb{R}^{\dim(\mathcal{Y})}$.

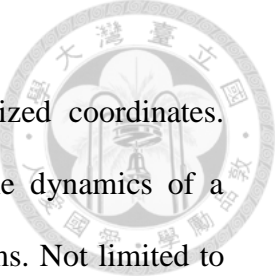




Chapter 3 Learning the Robot Dynamics with Structured Kernels

A precise model often means accurate control and more. For a multi-joint robot, the general model, however, is not trivial. In this chapter, we discuss the learning of general robot dynamics in reproducing kernel Hilbert space (RKHS). The RKHS in Chapter 2 is a nonparametric framework of machine learning in the dual space, in which the learning problem becomes the inference problem given the projection in certain random subspace. Despite the generality, the choice of RKHS is often an open and critical question, and may depend of the prior knowledge of the specific problem. Most importantly, the structure of the RKHS determines the generalization of the learning. For example, a quadratic kernel can capture quickly the quadratic characteristics, or a cosine kernel learns a sinusoidal function almost trivially if the frequency is known. Therefore, a structured kernel has good generalization on the dissimilar data, compared to the general kernels such as radial basis kernel, or the spline kernel.

In this chapter, we propose two different approaches to model the robot dynamics. In Section 3.1, a structured scalar RKHS is designed to capture the specific function space of the robot inverse dynamics. Although the kernel is derived under the assumption that all the joints are rotary, the kernel can be generalized to those with prismatic joints trivially. In addition, the universal radial basis kernel is introduced to model the friction and the unmodeled nonlinear terms. By the direct sum of the two spaces, the model can learn the inverse dynamics of the general robot more efficiently. In Section 3.2, the learning framework based on the vector-valued RKHS in proposed



to simultaneously model the coupling between different generalized coordinates. Compared to the previous approach, this framework considers the dynamics of a N -DOF robot as a single problem instead of N independent problems. Not limited to the robot dynamics, this framework is aimed to model general dynamical systems, and is believed to be even able to be generalized to those in the field, e.g. electro-magnetic dynamics, or fluid system, as long as the generalized coordinates and the generalized force can be measured. As previously, the universal scalar radial basis is introduced to model the unmodeled terms in the probably approximately correct learning framework, and the weighting of the kernels can be automatically tuned for the optimal combination.

For the ideal systems, we note that the proposed kernel based on vector-valued RKHS is at best as good as the models based on the energy criterion, especially the Euler-Lagrange equation, or the Hamilton principles. The difference is that no analytic derivation of the Lagrangian or the Hamiltonian is needed, since the proposed kernel implicitly models the coupling of the different coordinates in the vector-valued RKHS. This can be very helpful, especially in the complex system as long as the generalized force and the generalized coordinates can be properly measured. In addition, the proposed kernel can model any types of Lagrangian. That is, the unmodeled terms in the traditional analytic approach can also be considered as long as they are related to the measurements.

This chapter is partly based on the contributed works in conferences or journals [15] and [13].

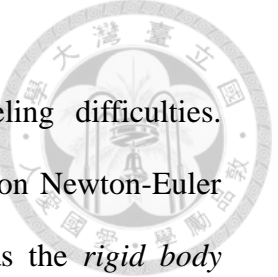


3.1 A Structured Kernel for Learning Robot Inverse Dynamics

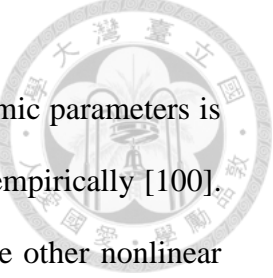
The inverse dynamics model of robots is often the key for accurate control. Especially in the computed torque control, the nonlinearity and the friction can be compensated leading better tracking or force control. The inverse models, however, is not trivial. The traditional Euler-Lagrange model based on the rigid body assumption often underfits in the presence of friction and requires tedious derivation for each new robot; the learning-based model needs larger training data set, since the structure of the dynamics is not considered. To overcome the aforementioned issues, we propose a structured kernel to replace the rigid body model and combine it with the universal radial basis kernel by direct sum. The proposed structured kernel asymptotically has the same convergence rate as the traditional model, and is general regardless of the configuration of the robot. Therefore, no analytic derivation is needed. Together with the universal radial basis kernel, the proposed approach enjoys the advantages of both the conventional and the learning-based models. To verify the proposed method, both simulations and experiments are conducted to investigate the performance in terms of the prediction errors and the tracking errors with the feedforward compensation.

3.1.1 Introduction

It is well known that a control loop that includes the inverse dynamics as the feed-forward compensation achieves better performance in tracking and force control [18]. In particular, the impedance control of robotics requires the inverse dynamics model to perform the desired dynamics [73], or the prediction of human intention in the exoskeleton control [44]. Despite the appealing success of the inverse dynamics



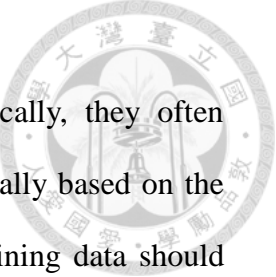
model, the application is limited in general due to the modeling difficulties. Traditionally, the dynamics model of the robotics is derived based on Newton-Euler method or Euler-Lagrange formulation [96], and we refer them as the *rigid body model* hereafter. Assuming that each link of the robot is a rigid body and the friction can be neglected, the unknowns in the dynamics model consists of the *kinematic parameters* and the *dynamics parameters*, in which the kinematic parameters are referred to those specifying the traditional Denavit-Hartenberg model, whereas the dynamics parameters consists of the inertia matrix, and the position and the mass of the center of mass for each link. Traditionally, the calibration of the dynamics model can be categorized into two approaches according to the formulation. In the Newton-Euler method, the kinematic parameters is first calibrated using laser [70] or camera [102], and the dynamics parameters are identified joint by joint iteratively [92]. This approach restricts the calibration to be carried only in offline, and the most importantly, the uncertainty of the former links passes to the following links. An alternative solution is based on the Euler-Lagrange formulation [92]. This approach explores all the unknown terms in the dynamics model in terms of the nonlinear bases, and therefore the identification problem becomes an ordinary linear regression problem, which is then solved by least-squares. While the Euler-Lagrange based approach is popular especially in the adaptive control community [79], the number of expanded terms of the dynamics model grows, however, in the worst case exponentially with the degrees of freedom of the robot. As a result, the computational burden may become intractable, which limits the usage for complex systems, e.g. robotics manipulators with arbitrary Denavit-Hartenberg parameters. Also, although the model converges to the underlying parameters in the L_2 sense, the factorization of



the learned parameters into physically plausible kinematic and dynamic parameters is not guaranteed, so additional constraints on the unknowns are used empirically [100]. Finally, none of the models above consider directly frictions and the other nonlinear coupling effects such as the joint flexibility of the robot.

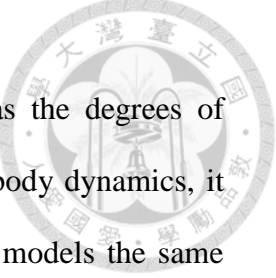
Considering the structured uncertainties due to frictions, damping, joint flexibility, and manufacturing errors, the machine learning based inverse dynamics models have been proposed [19, 24, 26, 27, 36, 56, 67, 107]. See [25, 93] for the recent surveys of the dynamics learning. The learning of the dynamics can be long dated back to the neural networks, and the following machines based on the reproducing kernel Hilbert space (RKHS), e.g. support vector machine and Gaussian process regression, etc. Despite the universality of these methods, the curse of dimensionality and the ability of generalization to the unseen data remain as the major issues. First, since the complexity of the underlying problem grows exponentially with the degrees of freedom of the robot, how to choose a proper kernel space and the regularization is the key to prevent the overfitting. Second, along with the curse of the dimensionality, the definition of sufficient rich data for a machine learning model in this learning the dynamics may vary and depend on the application. In the iterative learning control, the desired reference trajectory may be fixed from time to time, so there is no danger of overfitting; in the impedance control, the reference trajectory, however, is calculated in real time and cannot be known beforehand, or in the high speed position tracking, the training data of the high speed trajectory too cannot be acquired without the compensating feedforward term that is to be learned.

The popular radial basis kernel and those kernels that decay as the distance metric between the seen and the unseen data increases often fails to generalize well to



the unseen data in learning the inverse dynamics. More specifically, they often underestimate the predicted torque. Since these kernels are essentially based on the interpolation of the acquired training data, the sufficiently rich training data should cover all the frequencies and the magnitudes, or should be at least sufficiently rich in the space of possible reference trajectories so that the identically independently distributed (i.i.d.) sampling assumption holds. On the other hand, the rigid body model can generalize well, if the effect of the unmodeled dynamics is limited and negligible. Since it captures the polynomial tendency of the generalized force with respect to the accelerations and the velocities, the sufficiently rich data do not require the trajectories of all frequencies and magnitudes. That is, the model can predict for the high-speed trajectory with large magnitude well even with limited training data. Compared to the models with the radial basis kernel, the properly identified rigid body model is therefore more suited in the impedance control and the high-speed position control as long as the flexibility and the friction of the robot can be ignored.

Recently, Duy et al.[26] showed that the prediction and the control is more accurate by incorporating both the rigid body model and the radial basis kernel compared to the model used only either of them alone, in which the rigid body model is derived based on the Euler-Lagrange method. Along with this trend, we too propose to use the fusion the two models here. Compared to [26], no explicit derivation of the rigid body model is needed here. By formulating the proper RKHS, we can directly model the rigid body dynamics without referring to the Euler-Lagrange method, which is often tedious even with the symbolic mathematics toolbox, by giving the explicit form of the inner product in the RKHS. Also, we introduce an additional parameter to control the complexity of the overall model, so the model can regularize



the learning in the presence of the curse of the dimensionality as the degrees of freedom increase. Since the proposed RKHS is radically the rigid body dynamics, it too captures the polynomial characteristics of the dynamics, i.e. it models the same space of that of the Euler-Lagrange method.

In summary, we introduce the new structured reproducing kernel as the main contribution of this work, and further, in a multiple kernel fashion, incorporate it with the universal radial basis kernel, which is used to model the nonlinear dynamics and the frictions. To verify the proposed kernel, we test the ability both in the simulations and the experiments.

For the rest of this section, it is organized as follows. In Section 3.1.2, we give the definition and some properties of RKHS for the further derivation of the proposed space. Section 3.1.3 shows the main result of this work, the explicit formulation of the kernel space, and Section 3.1.4 shows how the multiple kernels is formulated to learn the inverse dynamics model with the standard kernel methods, such as support vector regression and kernel ridge regression. In Section 3.1.5 the simulation results are presented. Finally, we shall discuss the result and give a short conclusion in Section 3.1.6.

3.1.2 Reproducing Kernel Hilbert Space Revisited

In this section, we give the formal definition of RKHS and some important properties that will be used in the next section. For the application of identifying the inverse dynamics, we concern here only the RKHS in the field of real numbers. In the following, we assume X be a nonempty set in a locally compact Hausdorff space, and $Y \subseteq \mathbb{R}$. Most of the works here follow [3, 10].

Definition 3.1.



Given a nonempty set X , a compact kernel $k : X \times X \rightarrow \mathbb{R}$ is called of positive type, if

$$\sum_{i,j}^l c_i c_j k(x_i, x_j) \geq 0$$

for any $l \in \mathbb{N}$, $x_1, \dots, x_l \in X$ and $c_1, \dots, c_l \in \mathbb{R}$.

Such kernel is also called positive kernel or Aronszajn kernel. To be clear, we call a kernel positive definite if it is of positive type and a matrix positive definite if the spectrum is strictly positive.

Definition 3.2.

A Hilbert space \mathcal{H} of functions $f : X \rightarrow \mathbb{R}$ endowed with the inner product $\langle \cdot, \cdot \rangle_{\mathcal{H}}$ is called a reproducing kernel Hilbert space on a nonempty set X , if $\forall x \in X$ there exists a function $k_x \in \mathcal{H}$ satisfying

$$f(x) = \langle f, k_x \rangle_{\mathcal{H}}, \quad \forall f \in \mathcal{H};$$

in particular, the reproducing kernel is defined as

$$k(y, x) = \langle k_x, k_y \rangle_{\mathcal{H}} = k_x(y) \quad x, y \in \mathcal{X}.$$

Here we follow the convention that the first argument of $k(y, x)$ is the evaluation point of the functional and the second argument is used as index of the function. Also, one can also treat k_x as a possibly nonlinear map from X to ℓ^2 , which also called the *feature space*, since all the Hilbert spaces of same dimensionality are isometric isomorphism. We note here the requirement of X in a locally compact Hausdorff space is satisfied in the learning of inverse dynamics.

The next proposition shows that \mathcal{H} can be included continuously into the space of continuous functions $C^0(X, \mathbb{R})$.

Proposition 3.3.



The following arguments are equivalent:

1. the map k_x is weakly continuous.
2. the function $k(y, x)$ is locally bounded and separately continuous.

Proposition 3.4..

A reproducing kernel $k(y, x)$ exists if and only if $f(x)$ is a continuous linear functional of $f \in \mathcal{H}$ running through \mathcal{H} .

These are all derivable from Definition 3.2, and \mathcal{H} is unique up to isometric isomorphism. Finally we summarize some operations combining multiple RKHSs.

Proposition 3.5.

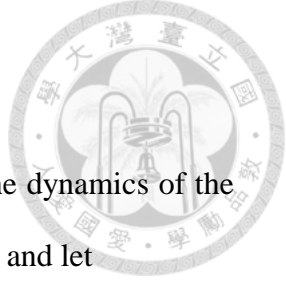
Let \mathcal{H}_1 and \mathcal{H}_2 be two RKHS. Then the following compositions show to be a proper RKHS

1. $\mathcal{H} = \mathcal{H}_1 \oplus \mathcal{H}_2$,
2. $\mathcal{H} = \mathcal{H}_1 \otimes \mathcal{H}_2$,

where \oplus and \otimes denote the direct sum and the tensor product of two vector spaces, respectively.

3.1.3 Reproducing Kernel Hilbert Space of Rigid Body Dynamics

This section presents the main work of Section 3.1. The derivation follows from the Euler-Lagrange formulation of the rigid body dynamics. By identifying the structure of the function space, we can derive the corresponding RKHS. The objective is to identify the smallest RKHS in the sense of dimensionality that can include the function space of the inverse dynamics. We assume the robot is holonomic and serial with all rotary joints. This framework can be easily extended to the cases with prismatic joints accordingly. We omitted here for the compactness. Also, we mention that the models of all the joints are learned independently.



A. The Euler-Lagrange Method

We begin with analyzing the Euler-Lagrange formulation of the dynamics of the robot. For a N -DOF robot, let $q \in \mathbb{R}^N$ be the generalized coordinates, and let

$$T(q, \dot{q}) = \frac{1}{2} \dot{q}^T M(q) \dot{q} \quad (3.1)$$

$$\begin{aligned} &= \frac{1}{2} \dot{q}^T \sum_{i=1}^N \left[m_i J_{v_i}(q)^T J_{v_i}(q) + J_{\omega_i}(q)^T R_i(q) \Omega_i R_i(q)^T J_{\omega_i}(q) \right] \dot{q} \\ U(q) &= \sum_{i=1}^N -m_i g^T r_{ci}(q) \end{aligned} \quad (3.2)$$

be the kinematic energy and the potential energy, where m_i is the mass, r_{ci} is the position of the center of the mass, Ω_i is the inertia tensor matrix, J_{v_i} is the Jacobian matrix of linear velocity, J_{ω_i} is the Jacobian matrix of angular velocity, R_i is the rotational matrix between the inertial frame to joint frame of link i , and g is the gravitational acceleration vector, and $M(q) \in \mathbb{R}^{N \times N}$ is the generalized inertia matrix of the whole robot defined as in (3.1). With the kinematic energy and the potential energy, we define the Lagrangian as

$$L := T - U. \quad (3.3)$$

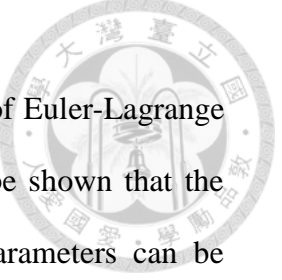
The Euler-Lagrange equation shows the generalized force is actually the image of the Lagrangian under a linear map, i.e.

$$\left(\frac{d}{dt} \frac{\partial}{\partial \dot{q}_n} - \frac{\partial}{\partial q_n} \right) L = \tau_n, \quad (3.4)$$

where q_n is the n th generalized coordinate, and τ_n is the n th generalized force. Or we can write it more compactly in matrix form

$$M(q) \ddot{q} + C(q, \dot{q}) \dot{q} + G(q) = \tau, \quad (3.5)$$

where $C(q, \dot{q}) \in \mathbb{R}^{N \times N}$ is the Coriolis/centrifugal matrix, $G(q) \in \mathbb{R}^N$ is the gravitational term, $\tau \in \mathbb{R}^N$ is the vector of generalized forces.



In the context of robotics, (3.5) are referred to the dynamics of Euler-Lagrange method, in contrast to the iterative Newton-Euler method. It can be shown that the unknowns in (3.5) including both the kinematic and dynamic parameters can be arranged in a linear regressor form, so they can be identified by the ordinary linear regression offline, or by the canonical adaptive law online. However, the number of the unknowns in the worst case grows exponentially with N , if there is no cancellation due to the zero terms in the kinematic parameters, i.e. the Denavit-Hartenberg (DH) parameters. Also, the derivation of the exact formulation of (3.5) is actually intricate and tedious, and in most of the cases, can only be solved by the symbolic mathematics toolbox under some model simplifications.

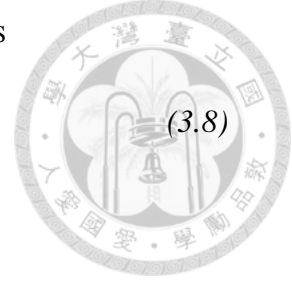
B. Reproducing Kernel Hilbert Space of Rigid Body Dynamics

Let \mathcal{X} be the set of all possible states (q, \dot{q}, \ddot{q}) of the robot, and with the abuse of notation we may write, for example, $q \in \mathcal{X}$ for simplicity. Since \mathcal{X} is a bounded and closed subset in the Euclidean space, and (3.4) is a bounded and continuous functional on \mathcal{X} , there exists at least one RKHS containing (3.4) according to Proposition 3.4.

The objective is to find a particular RKHS that is large enough to contain (3.4) and yet small enough to prevent overfitting given finite observations. Also the RKHS should be endowed with computationally efficient reproducing kernel. We denote \mathcal{H}_L the RKHS that contains (3.4) with such characteristics. Now we shall derive the analytic form of the reproducing kernel of \mathcal{H}_L . First, we define the following RKHSs,

$$\mathcal{H}_{\ddot{q}} = \overline{\text{span}}\left\{\frac{1}{\sqrt{N}} \ddot{q} \mid \ddot{q} \in \mathcal{X}\right\} \quad (3.6)$$

$$\mathcal{H}_{\dot{q} \otimes \dot{q}} = \overline{\text{span}}\left\{\frac{1}{\sqrt{N}} \dot{q} \otimes \frac{1}{\sqrt{N}} \dot{q} \mid \dot{q} \in \mathcal{X}\right\} \quad (3.7)$$



$$\mathcal{H}_\chi = \overline{\text{span}}\{\chi(q) \mid q \in \mathcal{X}\}, \quad (3.8)$$

where the nonlinear map

$$\begin{aligned} \chi : \mathcal{X} &\rightarrow \mathbb{R}^{3^N} \\ x = (q, \dot{q}, \ddot{q}) &\rightarrow \bigotimes_{n \in \mathbb{N}_N} (\cos q_n, \sin q_n, 1) \end{aligned}$$

the bar denotes the completion of a metric space, and \sqrt{N} is introduced as a normalization factor. Namely, $\mathcal{H}_{\ddot{q}}$ contains the linear functions of $\ddot{q} \in \mathcal{X}$, and $\mathcal{H}_{\dot{q} \otimes \dot{q}}$ contains the quadratic functions of $\dot{q} \in \mathcal{X}$, and so on.

Proposition 3.6.

The kinematic energy and the potential energy of the rigid body dynamics lie in the following RKHS,

$$T \in \mathcal{H}_{\dot{q} \otimes \dot{q}} \otimes \mathcal{H}_\chi \otimes \mathcal{H}_\chi =: \mathcal{H}_T,$$

$$U \in \mathcal{H}_\chi =: \mathcal{H}_U;$$

Proof:

Since the Jacobian matrices can be shown to be

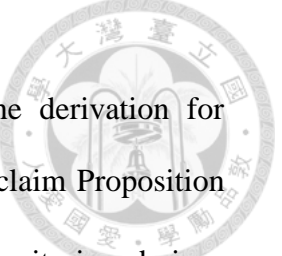
$$J_{v_i} = \left[\frac{\partial r_{ci}}{\partial q_1} \dots \frac{\partial r_{ci}}{\partial q_N} \right],$$

$$J_{\omega_i} = [\rho_1 z_0 \dots \rho_N z_{N-1}],$$

where

$$\rho_n = \begin{cases} 0, & \text{if joint } n \text{ prismatic} \\ 1, & \text{if joint } n \text{ rotary} \end{cases}$$

z_{n-1} is the axis of the n th generalized coordinate, and $n \in \mathbb{N}_N$. We note that the order of the subscript follows the traditional Denavit-Hartenberg convention, in which the frame $i-1$ is defined with respect to link i , and the two endpoints of link i are joint i



and joint $i+1$. Although we assume all the joints are rotary, the derivation for prismatic joints is simpler and can be done in the same fashion. To claim Proposition 3.6, it is sufficient to show $J_{v_i}, R_i(q)^T J_{\omega_i}(q) \in \mathcal{H}_\chi$, where it is obvious that $J_{v_i} \in \mathcal{H}_\chi$ since $r_{ci} \in \mathcal{H}_\chi$ and the linear operator $\partial/\partial q_n$ maps all the elements in \mathcal{H}_χ to the subspace in \mathcal{H}_χ . For the angular velocity, we have

$$R_i(q)^T \rho_n z_{n-1} = \rho_n R_{i-1}^0(q)^T R_n^0(q) e_3 = \rho_n R_n^{i-1}(q) e_3,$$

where $e_3 \in \mathbb{R}^3$ is the standard basis, and therefore it is in \mathcal{H}_χ . As for the potential energy, the derivation is similar.

Q.E.D.

After identifying the RKHSs of the kinematic energy and the potential energy, the RKHS \mathcal{H}_L should contains the image of $\mathcal{H}_T \oplus \mathcal{H}_U$ under the linear map (3.4).

Theorem 3.7.

Let $\text{Im}(\mathcal{H}_T \oplus \mathcal{H}_U)_n$ be the image of $\mathcal{H}_T \oplus \mathcal{H}_U$ under the linear map,

$$T_n := \left(\frac{d}{dt} \frac{\partial}{\partial \dot{q}_n} - \frac{\partial}{\partial q_n} \right), \quad n \in \mathbb{N}_N.$$

Then $\text{Im}(\mathcal{H}_T \oplus \mathcal{H}_U)_n$ can be included in the following RKHS

$$\mathcal{H}_L := (\mathcal{H}_{\dot{q}} \oplus \mathcal{H}_{\dot{q} \otimes \dot{q}}) \otimes (\mathcal{H}_\chi \otimes \mathcal{H}_\chi) \oplus \mathcal{H}_\chi \setminus \mathcal{H}_1,$$

for all $n \in \mathbb{N}_N$, where \mathcal{H}_1 is the space of constant function.

Proof:

Let $L = L_1 \otimes L_2 \oplus L_3 \in \mathcal{H}_{\dot{q} \otimes \dot{q}} \otimes (\mathcal{H}_\chi \otimes \mathcal{H}_\chi) \oplus \mathcal{H}_\chi$. Define

$$\chi_2(q) := (\chi \otimes \chi)(q)$$

and $\chi(q_n)$ such that $\chi(q) = \bigotimes_{n \in \mathbb{N}_N} \chi(q_n)$. Since \mathcal{H}_T and \mathcal{H}_U are the composition of some

simple RKHSs (3.6), (3.7), and (3.8), in which the reproducing kernels can be explicitly written. For joint n , we can calculate the image of the linear operator T_n by using the reproducing property, i.e.

$$\begin{aligned}\tau_n &= \left(\frac{d}{dt} \frac{\partial}{\partial \dot{q}_n} - \frac{\partial}{\partial q_n} \right) L(q, \dot{q}) = T_n \langle L, k_x(q, \dot{q}) \rangle_{\mathcal{H}_r \oplus \mathcal{H}_u} \\ &= T_n [\langle L_1, \dot{q} \otimes \dot{q} \rangle \langle L_2, \chi_2 \rangle + \langle L_3, \chi \rangle]\end{aligned}$$

Here we also use \otimes as the Kronecker product when considering vectors in finite dimensional space, and we do not particularly distinguish it with the tensor product unless the clearness is lost.

We first see that

$$\begin{aligned}\frac{d}{dt} \frac{\partial L}{\partial \dot{q}_n} &= \frac{d}{dt} \frac{\partial}{\partial \dot{q}_n} [\langle L_1, \dot{q} \otimes \dot{q} \rangle \langle L_2, \chi_2 \rangle + \langle L_3, \chi \rangle] \\ &= \underbrace{\left\langle L_1, \frac{d}{dt} \frac{\partial}{\partial \dot{q}_n} \dot{q} \otimes \dot{q} \right\rangle}_{(a)} \langle L_2, \chi_2 \rangle + \underbrace{\left\langle L_1, \frac{\partial}{\partial \dot{q}_n} \dot{q} \otimes \dot{q} \right\rangle}_{(b)} \left\langle L_2, \frac{d}{dt} \chi_2 \right\rangle\end{aligned}$$

Since

$$\frac{d}{dt} \frac{\partial}{\partial \dot{q}_n} \dot{q} \otimes \dot{q} = (\ddot{q} \otimes e_n) + (e_n \otimes \ddot{q})$$

and

$$\frac{d}{dt} \chi_2 = \sum_{i \in \mathbb{N}_N} \chi_2(q_i) \otimes \dots \otimes \dot{q}_i [D \otimes I_3 + I_3 \otimes D] \chi_2(q_i) \otimes \dots \otimes \chi_2(q_N)$$

we have

$$\begin{aligned}(a) &= \left\langle L_1, (e_n \otimes I_N + I_N \otimes e_n) \ddot{q} \right\rangle \langle L_2, \chi_2 \rangle \\ (b) &= \sum_{i \in \mathbb{N}_N} \left\langle L_1, [e_i^T \otimes (e_n \otimes I_n + I_n \otimes e_n)] \dot{q} \otimes \dot{q} \right\rangle \\ &\quad \left\langle L_2, \chi_2(q_i) \otimes \dots \otimes [D \otimes I_3 + I_3 \otimes D] \chi_2(q_i) \otimes \dots \otimes \chi_2(q_N) \right\rangle\end{aligned}$$

where





$$D := \begin{bmatrix} 0 & -1 & 0 \\ 1 & 0 & 0 \\ 0 & 0 & 0 \end{bmatrix} \in \mathbb{R}^{3 \times 3}.$$

On the other hand,

$$\frac{\partial L}{\partial q_n} = \underbrace{\left\langle L_1, \dot{q} \otimes \dot{q} \right\rangle}_{(c)} \underbrace{\left\langle L_2, \frac{\partial}{\partial q_n} \chi_2 \right\rangle}_{(d)} + \underbrace{\left\langle L_3, \frac{\partial}{\partial q_n} \chi \right\rangle}_{(d)}.$$

Following the similar arguments, we have

$$(c) = \left\langle L_1, \dot{q} \otimes \dot{q} \right\rangle \\ \left\langle L_2, \chi_2(q_1) \otimes \dots \otimes [D \otimes I_3 + I_3 \otimes D] \chi_2(q_n) \otimes \dots \otimes \chi_2(q_N) \right\rangle$$

$$(d) = \left\langle L_3, \chi(q_1) \otimes \dots \otimes D \chi(q_n) \otimes \dots \otimes \chi(q_N) \right\rangle$$

Combining (a), (b), (c), and (d), it is clear that for all $n \in \mathbb{N}_N$

$$\tau_n = (\langle \tau_{n1}, \ddot{q} \rangle + \langle \tau_{n2}, \dot{q} \otimes \dot{q} \rangle) \langle \tau_{n3}, \chi_2 \rangle + \langle \tau_{n4}, \chi \rangle$$

for some vectors $\tau_{n1}, \tau_{n2}, \tau_{n3}$, and τ_{n4} , which can be defined using the adjoint of the operators in (a), (b), (c), and (d). That is τ_n is in

$$(\mathcal{H}_{\dot{q}} \oplus \mathcal{H}_{\dot{q} \otimes \dot{q}}) \otimes (\mathcal{H}_{\chi} \otimes \mathcal{H}_{\chi}) \oplus \mathcal{H}_{\chi}$$

with the reproducing kernel

$$k_x(q, \dot{q}, \ddot{q}) = (\ddot{q} \oplus \dot{q} \otimes \dot{q}) \otimes \chi_2 \oplus \chi.$$

In addition, since the differentiation operator projects out the space of constant function, $\tau_n \in \mathcal{H}$ for all $n \in \mathbb{N}_N$.

Q.E.D.

The RKHS \mathcal{H}_L is indeed computationally efficient and can model the inverse dynamics. In fact, it is only slightly larger than the smallest RKHS possible by observing that the smallest RKHS to contain τ_n for all $n \in \mathbb{N}_N$ is of size N times



larger than $\text{Im}(\mathcal{H}_T \oplus \mathcal{H}_U)_n$. However, such a RKHS may loss the easily manipulated reproducing kernel function, whereas in \mathcal{H}_L the reproducing kernel has a simple closed form

$$\begin{aligned}\hat{k}_{\mathcal{H}_L}(x, y) = & (\langle \ddot{q}_y, \ddot{q}_x \rangle + \langle \dot{q}_y, \dot{q}_x \rangle^2) \prod_{i \in \mathbb{N}_N} (\cos(q_{x,i} - q_{y,i}) + 1)^2 \\ & + \prod_{i \in \mathbb{N}_N} (\cos(q_{x,i} - q_{y,i}) + 1) - 1\end{aligned}, \quad (3.9)$$

in which we use the trigonometric identity.

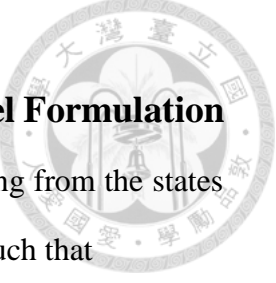
To this end, if (3.9) is used unreservedly, the curse of dimensionality may occur. We can observe that $\dim(\mathcal{H}_L) = \mathcal{O}(6^N N^2)$, and therefore the limited size of training data can never catch up the size of the hypothesis space. This obstruction can be circumvented by introducing an additional regularization parameter σ , and by scaling \mathcal{H}_L , we can obtain a new reproducing kernel

$$k_{\mathcal{H}_L}(x, y) = (\langle \ddot{q}_y, \ddot{q}_x \rangle + \langle \dot{q}_y, \dot{q}_x \rangle^2) k_\chi(q_x, q_y)^2 + k_\chi(q_x, q_y) - 1 \quad (3.10)$$

where

$$k_\chi(q_x, q_y) := \prod_{i \in \mathbb{N}_N} \frac{(\cos(q_{x,i} - q_{y,i}) + \sigma)}{1 + \sigma} - \left(\frac{\sigma}{1 + \sigma}\right)^N + 1.$$

In this scaled \mathcal{H}_L , the contributions of high-order terms are penalized, though the overall dimensionality is the same. The additional parameter σ , selected by validation, can guide the machine to bias to the correct parameterization. One can observe that the high-order terms in (3.4) are those without the cancellation due to the DH parameters, which shows the parameterization in (3.10) is a good prior knowledge to learn the inverse dynamics. Finally, we remark that \mathcal{H}_L is essentially the same as the rigid body dynamics, but no derivation of nonlinear bases in (3.5) is needed anymore.



3.1.4 Learning the Inverse Dynamics in Multiple-Kernel Formulation

By learning the inverse dynamics, we mean learning the mapping from the states of the dynamics and the actuation force τ_a , that is $\Gamma : (q, \dot{q}, \ddot{q}) \rightarrow \tau_a$ such that

$$\left(\frac{d}{dt} \frac{\partial}{\partial \dot{q}_n} - \frac{\partial}{\partial q_n} \right) L = \tau_n = \tau_{a,n} + \tau_{f,n}$$

holds for all $n \in \mathbb{N}_N$, where τ_f is the force due to frictions and other unmodeled dynamics, and the subscript denotes the n th component. In the presence of τ_f , the inverse map Γ is not in general well defined, whereas the inverse map between (q, \dot{q}, \ddot{q}) and τ_n always exists. Let μ_x be the probability measure on \mathcal{X} , the learning of inverse dynamics is aimed to find the actuation force $\hat{\tau}_a$ such that,

$$\hat{\tau}_{a,n} = \arg \min_{\tilde{\tau}_{a,n} \in \mathcal{H}} \left\| \tilde{\tau}_{a,n} + \tau_{f,n} - \tau_n \right\|_{\mathcal{L}^2(\mathcal{X}, \mu_x)}^2 \quad (3.11)$$

for all $n \in \mathbb{N}_N$, where \mathcal{H} is the hypothesis space.

As mentioned earlier and evidenced in [26], the combination of the rigid body dynamics and the radial basis kernel can model the dynamics better, since the rigid body dynamics captures quickly the structured component while the radial basis kernel can approximate universally any function. Therefore, to model the inverse dynamics we combine the proposed kernel (3.10) with a general radial basis kernel

$$k_{rbfs}(x, y) = \exp\left(-\frac{\|\cos(q_x) - \cos(q_y)\|^2 + \|\sin(q_x) - \sin(q_y)\|^2 + \|\dot{q}_x - \dot{q}_y\|^2 + \|\ddot{q}_x - \ddot{q}_y\|^2}{2\sigma}\right) \quad (3.12)$$

where the trigonometric mappings are introduced to better model the effect of the rotary joints, in contrast to the traditionally used radial basis kernel

$$k_{rbf}(x, y) = \exp\left(-\frac{\|q_x - q_y\|^2 + \|\dot{q}_x - \dot{q}_y\|^2 + \|\ddot{q}_x - \ddot{q}_y\|^2}{2\sigma}\right). \quad (3.13)$$

In terms of (3.11), it is equivalent to

$$\mathcal{H} = \mathcal{H}_L \oplus \mathcal{H}_{rbfs}, \quad (3.14)$$

where \mathcal{H}_{rbfs} is the RKHS with reproducing kernel (3.12). Since $\tau_n \in \mathcal{H}_L$ and \mathcal{H}_{rbfs} is universal, we can have

$$\begin{aligned} & \min_{\tilde{\tau}_{a,n} \in \mathcal{H}} \left\| \tilde{\tau}_{a,n} + \tau_{f,n} - \tau_n \right\|_{\mathcal{L}^2(\mathcal{X}, \mu_x)}^2 \\ &= \min_{\tilde{\tau}_{f,n} \in \mathcal{H}_{rbfs}} \left\| \tilde{\tau}_{f,n} - \tau_{f,n} \right\|_{\mathcal{L}^2(\mathcal{X}, \mu_x)}^2 = Var_x \{ \tau_{f,n} \} \end{aligned}$$

That is, the modeling error is due to the variance of τ_f with respect to the probability measure μ_x as the number of observations goes to infinity.

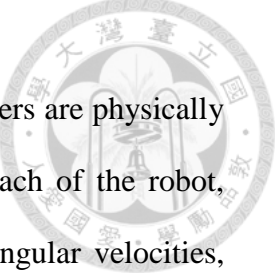
In implementation, the inverse dynamics is learned by the combination of kernels (3.10) and (3.12),

$$k_{mkl} = \delta k_{\mathcal{H}_L} + (1-\delta) k_{rbfs}, \quad (3.15)$$

where $\delta \in [0, 1]$ and $k_{\mathcal{H}_L}$ and k_{rbfs} are normalized so that the traces of the empirical kernel matrices are the same, and solved by the kernel ridge regression or the support vector regression.

3.1.5 Simulations

In this section, the simulation results are presented. We want to compare the generalization of the proposed kernels (3.10) and (3.15), and the traditional learning-based approaches (3.12) and (3.13). In each of the following simulations, we show the testing error with respect to the complexity of the underlying model, i.e. the degrees of freedom of the robot, in different scenarios: perfect rigid-body dynamics, the presence of measurement noise, and nonlinear frictions. In the following, for each of degree of freedoms, five different robots with random kinematic and dynamic parameters are used as the plant to be learned. We remark that the parameters are



sampled from a bounded uniform distribution so that all the parameters are physically feasible, e.g. the inertia matrix are always positive definite. For each of the robot, 5000 training data and 5000 testing data with angular positions, angular velocities, and angular accelerations generated from the uniform distribution are used for validation. Given the uniformly random states, the kinematic and the dynamic parameters, the generalized forces are computed using Newton-Euler method iteratively. Therefore, the data of the ideal robot dynamics can be obtained. As for the unmodeled dynamics, the adopted noise is the zero-mean Gaussian noise, the viscous friction is modeled by the force linear to the generalized velocity, and the Coulomb friction is modeled as the sign function of the generalized velocity. To learn the unknown model, we use the least-square regularized learning, i.e. the kernel ridge regression, and the kernel parameters and the parameter that controls the tradeoff between the complexity of the space and the fitting error all chosen by the 3-fold cross-validation, in which a small set of training data are used to find the optimal parameter. The optimal parameters is chosen to be the combination of parameters that minimize the empirically expected prediction error, and the whole training data set is used to retrain the final model with the optimal parameter.

Finally, to verify the result, the performances are shown in terms of prediction errors overall all the generalized coordinates both in root mean square (RMS) and the peak error (PE). Also, we note that all the generalized force in the simulation are normalized within [-1,1] for comparison. In the following, the proposed kernel (3.10) is denoted by pol , (3.13) is denoted by rbf , (3.12) is denoted by $rbfs$, and (3.15) is denoted by mkl .



A. Simulation Results with Ideal Robot Dynamics

This section shows the simulation results of the robot dynamics without any friction. The results compose of two parts according to the presence of the measurement noise. Fig. 3-1 (a) and (b) shows the prediction error of the normalized generalized force in terms of RMS and PE with respect to the complexity of the model. We remark here that the dimensionality of the proposed kernel is actually analytic

$$\dim(\mathcal{H}_L) = \left(N + \frac{1}{2}N(N+1)\right)6^N + 3^N - 1, \quad (3.16)$$

which is the upper bound of possible terms in a general Euler-Lagrange model. Since 5000 training data is sufficient to cover the whole space in terms of the dimensionality for a robot with $N \leq 3$, we can see a clear boundary on $N = 3$ in *pol*. On the other hand, 5000 training data no longer covers the whole hypothesis space for robot with $N > 3$. In this situation, the performance of the kernel depends on the quality of the regularized parameters, i.e. σ in each kernel function. As mentioned (3.16), the size of the training data may never catch up the dimensionality of the underlying model, so the performance of different models become close especially when $\ell \ll N^2 6^N$. Also, we can observe *rbfs* outperforms the traditional *rbf*, since the characteristics of the rotary joints are better captured. Comparing all the models, the proposed *pol* consistently shows better performance, which is expected since it is radically the Euler-Lagrange model.

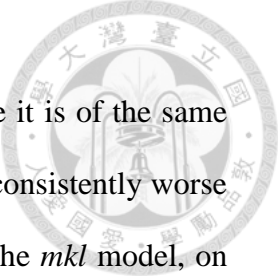
Fig. 3-2 (a) and (b) shows the prediction error of the normalized generalized force in terms of RMS and PE with respect to the complexity of the model. The standard deviation of the zero-mean noise model is chosen to be 0.05 so that 95 % of the noise is bounded by 0.1, which is the upper bound of the prediction error of the perfect model as shown in Fig. 3-1. The prediction results is similar to that without



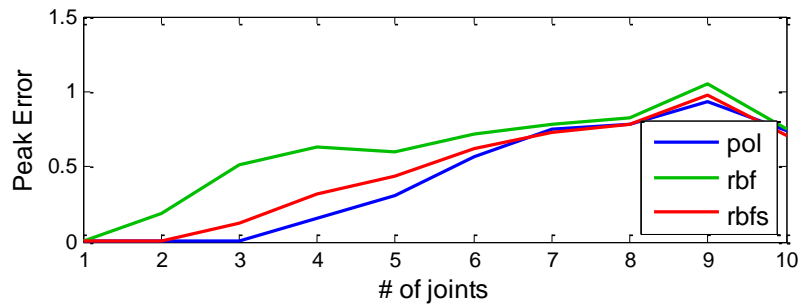
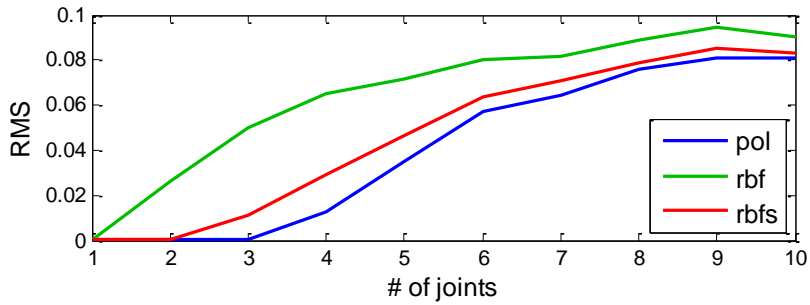
noise, since the least-square regularized is aimed for the Gaussian noise model.

B. Simulation Results with Ideal Robot Model and Frictions

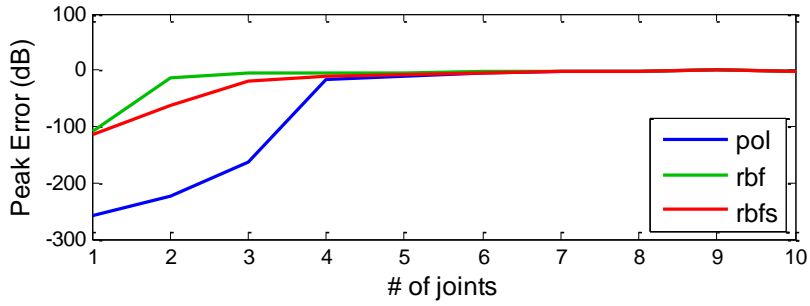
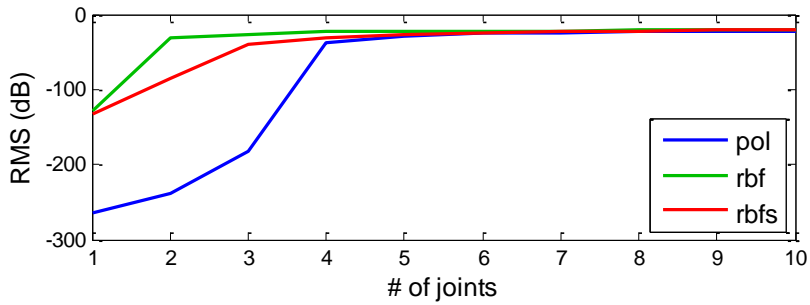
Similar to the setting in the previous section, the performances with and without measurement noises are compared. The Coulomb frictions and the viscous frictions are modeled as mentioned previously with the magnitude chosen randomly, and the noise is the zero-mean Gaussian noise with standard deviation 0.05. To show how the size of the friction affects the learning, we chose two different uniform probability distributions to generate the friction, denoted as SMALL and LARGE. In SMALL, the size of the friction is bounded one over five times the order of the generalized force due to the perfect model, whereas in LARGE the size of the friction is in the same order of the ideal generalized forces. For mkl , the weighting parameter δ in (3.15) is chosen by the cross-validation as the other parameters. Fig. 3-3 and Fig. 3-4 show the result of the ideal dynamics model with SMALL friction. In the presence of the friction, the pure pol learns badly, since it does not include the model of the friction. On the other hand, rbf , $rbfs$ and mkl can model arbitrary friction, so the results are similar to that without friction. In particular, mkl captures partly the structure of the dynamics, and therefore the performance is consistently better than rbf and $rbfs$. Another feature is that all the models seem to learn similarly as N increases. This is because the effect of the friction is neglectable when the training data is too scarce compared to the size of the space. In particular, pol learns as without friction and is better than both rbf and $rbfs$. In Fig. 3-4, the measurement noise makes the performance of pol worse, but pol becomes better as N increase due to the previous argument. Fig. 3-5 and Fig. 3-6 shows the simulation results with LARGE friction model. Compared to Fig. 3-3 and Fig. 3-4 with SMALL model, the LARGE friction



still contributed to the generalized force even when N is large, since it is of the same order the generalized force in the ideal dynamics. Therefore, *pol* is consistently worse than the other three models regardless of the measurement noise. The *mkl* model, on the contrary, performs better than the others regardless of the condition of frictions and noises. Still, one can observe that the discrepancy between *mkl* and *rbfs* becomes less obvious in LARGE noise, since the contribution of the frictions increases. Finally, we show the computational time of evaluating 5000 testing samples given the model spanned by 5000 training samples in Fig. 3-7 implemented in a standard PC with CPU i5-750 and ram 8GB. To predict a single instance, the computational time is bounded below 5ms, and therefore a real-time computation is possible.



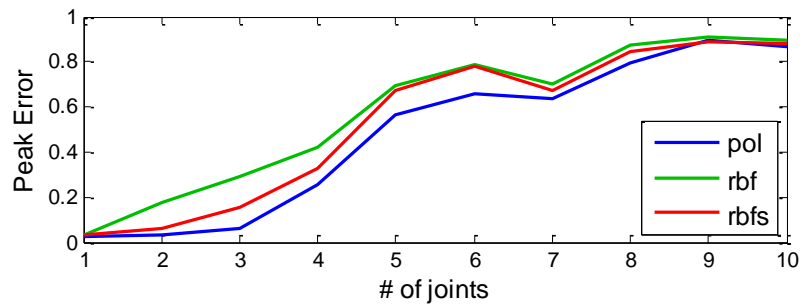
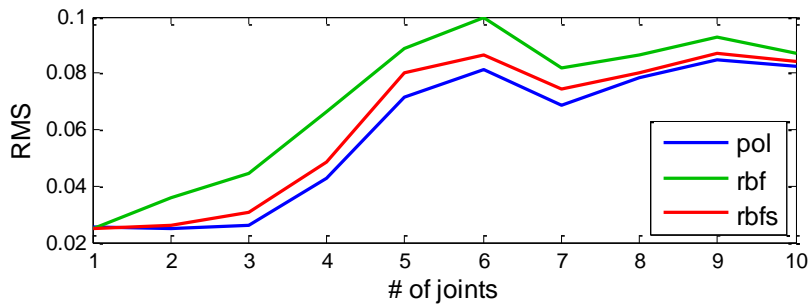
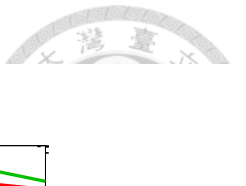
(a)



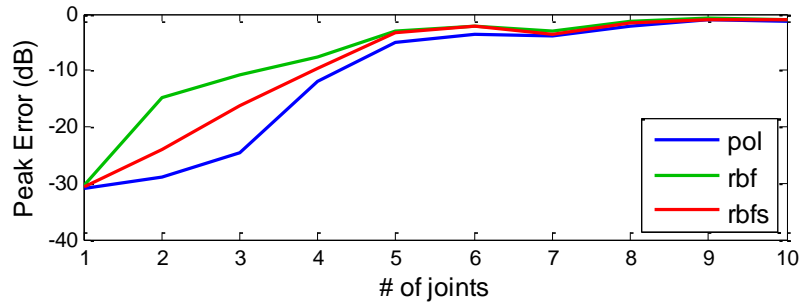
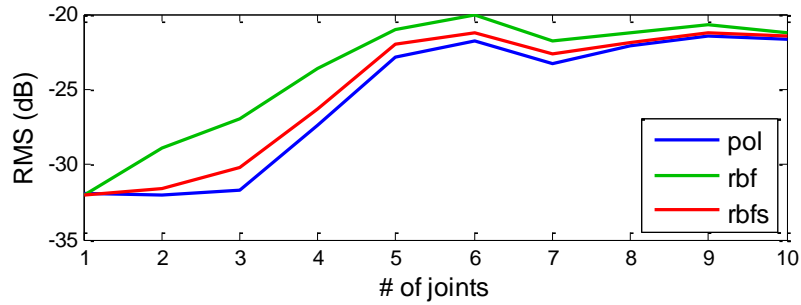
(b)

Fig. 3-1. Prediction error of the ideal model without measurement noise.

(a) prediction error (b) prediction error shown in dB



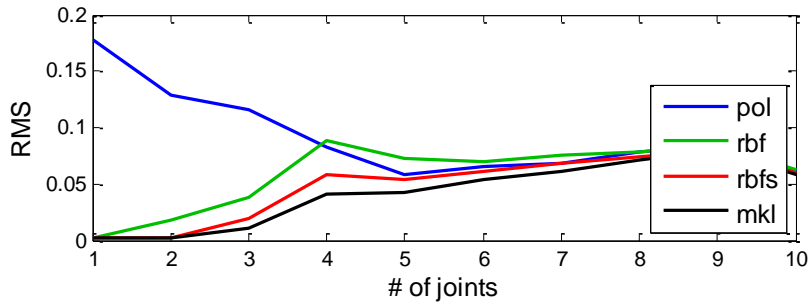
(a)



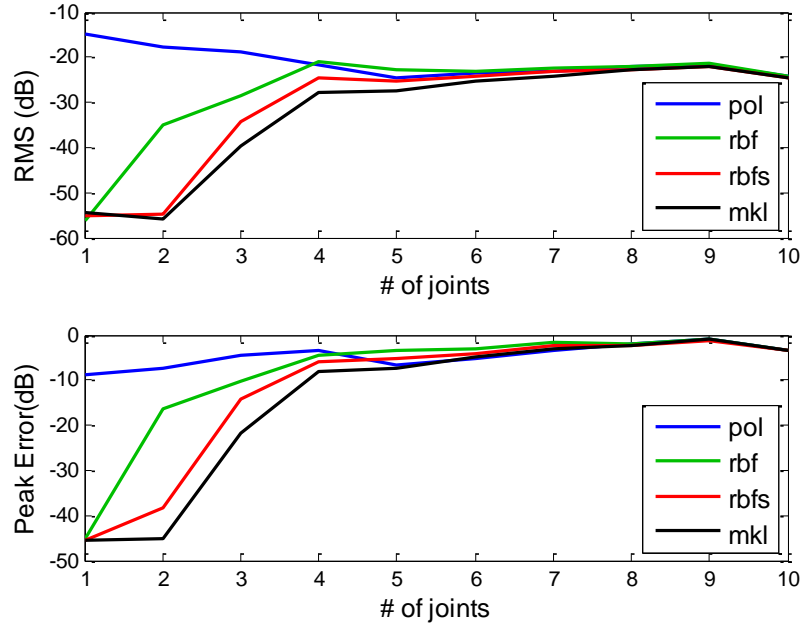
(b)

Fig. 3-2. Prediction error of the ideal model with measurement noise.

(a) prediction error (b) prediction error shown in dB



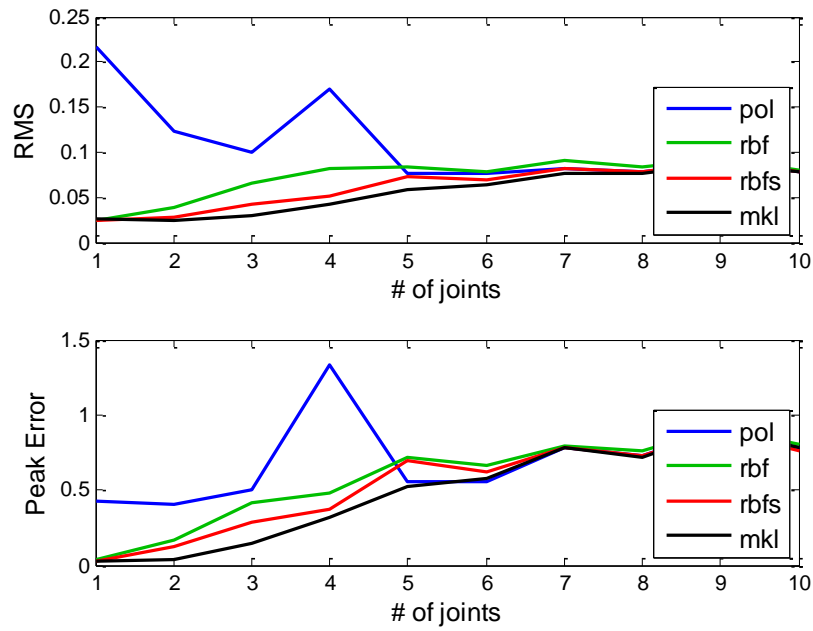
(a)



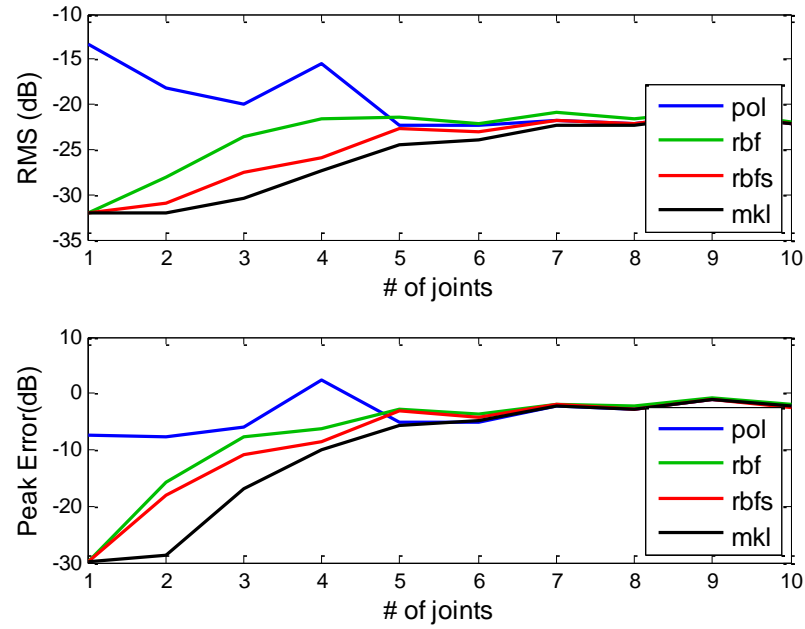
(b)

Fig. 3-3. Prediction error of the ideal model with SMALL friction.

(a) prediction error (b) prediction error shown in dB



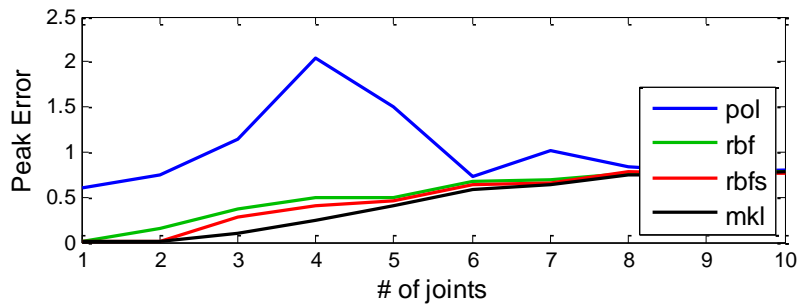
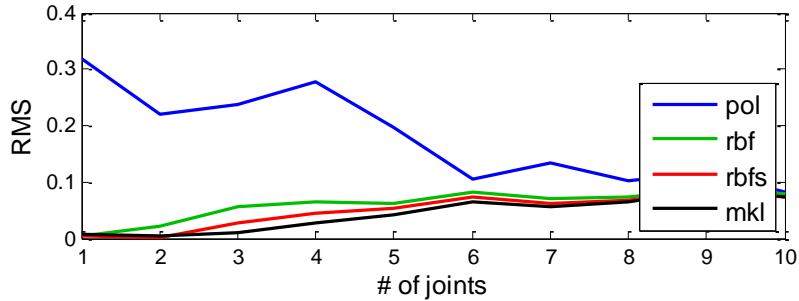
(a)



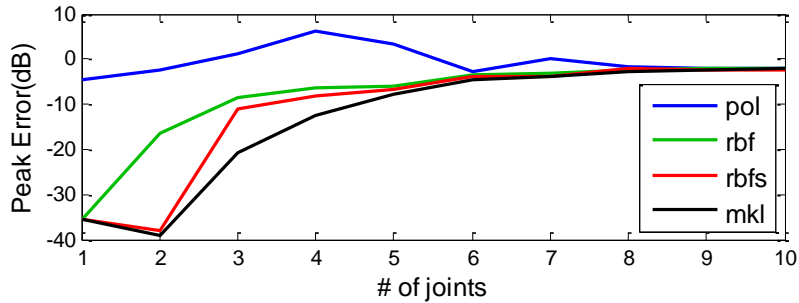
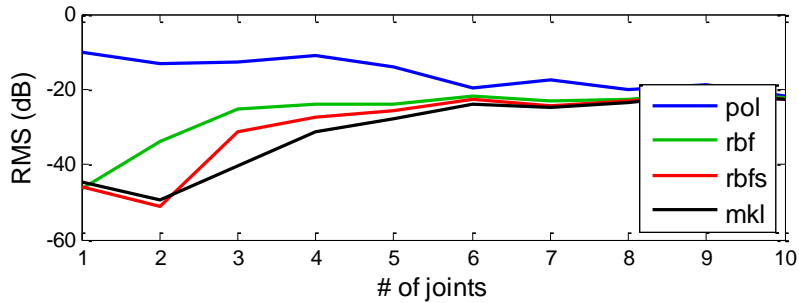
(b)

Fig. 3-4. Prediction error of the ideal model with SMALL friction and measurement noise.

(a) prediction error (b) prediction error shown in dB



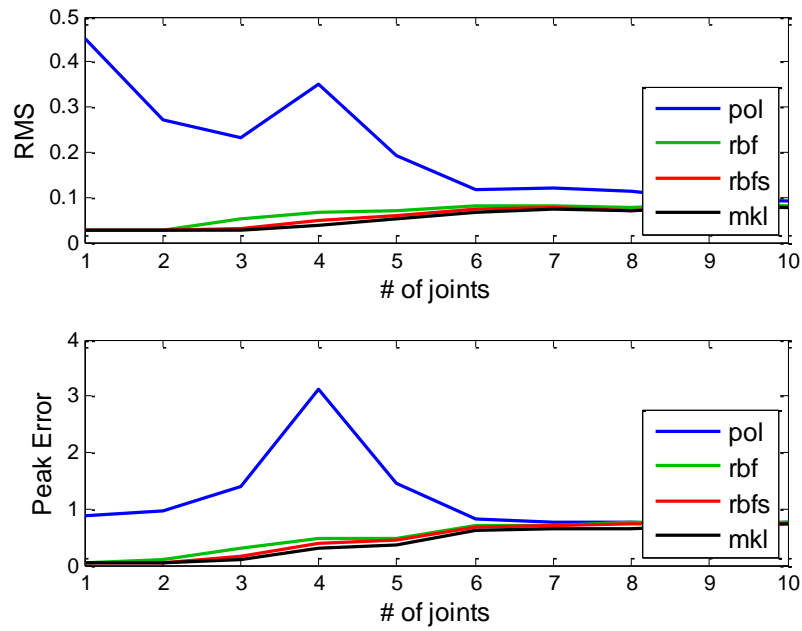
(a)



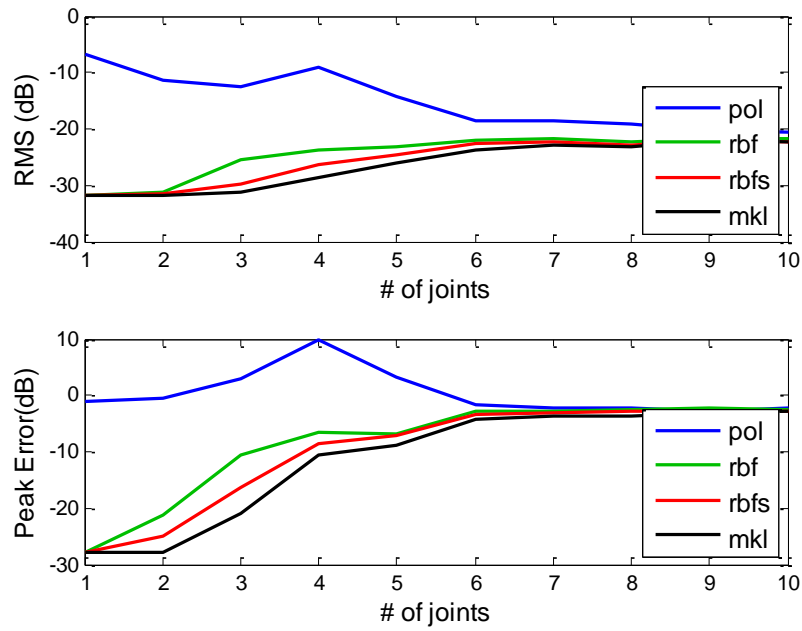
(b)

Fig. 3-5. Prediction error of the ideal model with LARGE friction.

(a) prediction error (b) prediction error shown in dB



(a)



(b)

Fig. 3-6. Prediction error of the ideal model with LARGE friction and measurement noise.

(a) prediction error (b) prediction error shown in dB

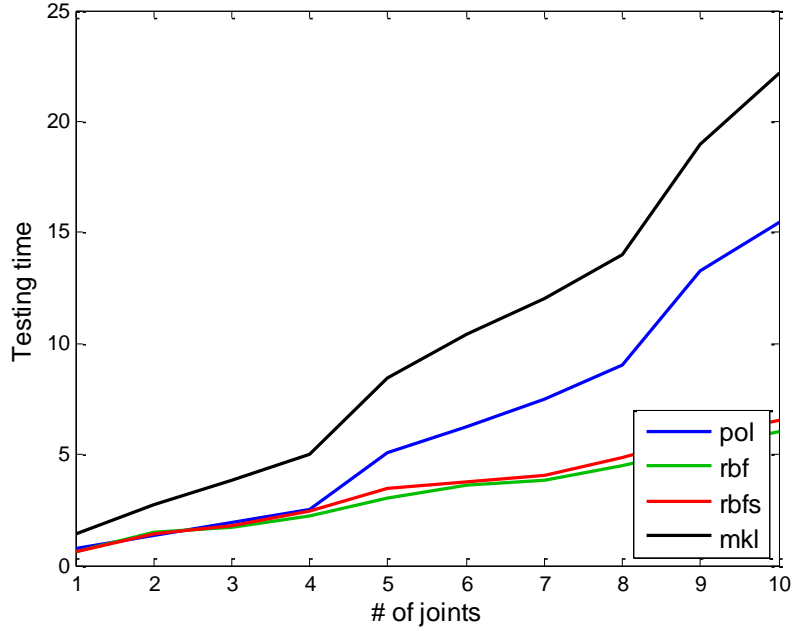
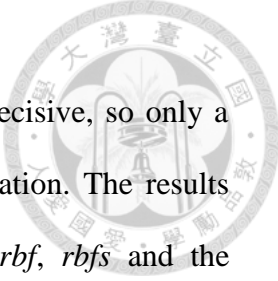


Fig. 3-7. Computational time of evaluating 5000 testing samples given a model spanned by 5000 training samples.

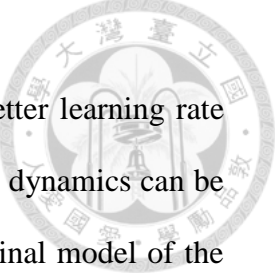
3.1.6 Discussions

In the simulation of ideal robot dynamics, the proposed *pol* kernel shows better generalization compared to the general learning kernel, since it captures the structure of the dynamics of the robot as the Euler-Lagrange model. However, *pol* may give unsatisfactory results when the friction cannot be neglected. To learn the unmodeled dynamics as well, we propose *mkl* to combine *pol* with *rbfs* by direct sum, where the weighting between two kernels δ is chosen by validation instead of using the general multiple-kernel learning that automatically tunes the weighting for the following two reasons. First, the multiple-kernel learning sometimes tends to overfit when quality of the training data is poor or the size of the training data is small, since the multiple-learning is actually an expectation maximization routine. Second, the precise



value of unknown parameter in our experiments tends not to be decisive, so only a small set of parameters are needed to be tested in the cross-validation. The results show that *mkl* predicts better compared to the general kernels *rbf*, *rbfs* and the structured kernel *pol* used alone. In comparison with [26], the proposed *mkl* is expected to give a similar result, since regularized-least square is essentially the Gaussian regression without the predicting variance. However, one may expect that *mkl* may be worse than the fusion kernel in [26], since they use the explicit Euler-Lagrange model compared to the proposed *pol*. This is the necessary tradeoff between the size of the hypothesis space and the generality. Since *pol* is general to all the rigid body dynamics, *pol* uses larger hypothesis space than the Euler-Lagrange model given specific kinematic parameters. On the contrary, *pol* does not need any derivation, and can calibrate the kinematic parameters as well. Thus, we regard *mkl* as an efficient alternative, since they shared the same asymptotical learning rate.

In Section 3.1, we demonstrate how to design a reproducing kernel that naturally models the function space of the robot dynamics. The experimental results show that the learning can indeed benefit from the structure of the unknown functions, which is evidenced both in *pol* and *rbfs*. In designing *pol*, we analyze the function space of the robot dynamics and then use the Euler-Lagrange method to derive the reproducing kernel of the inverse dynamics. This formulation actually shows an interesting yet well-known fact – the dynamics model is based on the Lagrangian of the system. Therefore, if we can model the Lagrangian, we know the dynamics. Inspired by this finding, we propose a dynamics learning scheme with the vector-valued RKHS in next section. In addition to modeling the structure of dynamics of a particular generalized coordinate as in *pol*, the learning scheme in Section 3.2 models the



correlation between different generalized coordinates as well, so better learning rate can be expected. Finally, we note that the nominal plant of the robot dynamics can be included trivially in this framework. In many applications, the nominal model of the robot dynamics can be obtained in the design of the mechanism, e.g. the dynamics parameters computed in the SolidWorksTM. In this case, we can compute the nominal torque by iterative Newton-Euler method and use it as the bias term in our framework. That is, the nonparametric kernel only learns the error dynamics. If the norm of the error dynamics is smaller than that of the unknown dynamics in the RKHS, better generalization can be foreseen, since the kernel method favors the small norm solution.

3.2 Learning the Dynamics of General Systems with the Vector-Valued Kernel

The identification of dynamical system is critical both in modeling and control. Despite the success of the machine learning for the universality, most of the machine learning algorithms, however, fail to model the coupling of the outputs for a multi-output system, and therefore the curse of dimensionality occurs. To address this issue, we first propose a learning scheme with the vector-valued reproducing kernel that exploits the structure of the dynamics of the holonomic and monogenic system. By modeling the Euler-Lagrange equation implicitly, the proposed method effectively learns the Lagrangian of the system. Therefore, for a system with N outputs, the convergence rate can be increased by N -times observations compared to the traditional approach. To model general system, a multiple kernel framework is posed in the probably approximately correct learning. To demonstrate and verify the effects

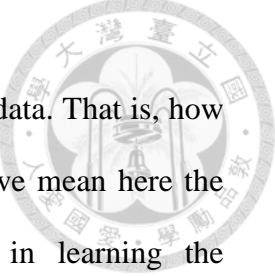


of the proposed scheme, the dynamics of a N -DOF serial robot is investigated both in simulation and experiments.

3.2.1 Introduction

The machine learning techniques have played a successful role in system identifications through the past decades. Notable for the ability to model any nonlinear function, the machine learning can treat the whole system as a black-box function and model the dynamics by learning the mapping between the inputs and the outputs. In this paper, we put our focus particularly on the machine learning algorithms based on the reproducing kernel Hilbert space (RKHS) and refer them as *kernel methods* hereafter. Among the modern learning algorithm, the kernel methods, such as support vector machine and Gaussian process regression, have become ubiquitous, because the learning can be simply treated as a sampling problem in RKHS. Compared to other parametric machine learning methods such as neural networks, the kernel methods can be proved to converge to the underlying function pointwisely if the universal kernels are used, and the optimization in training the model is convex, so the best model given finite observations can be easily computed. By defining a RKHS as the hypothesis space, the kernel method infers the best hypothesis in the RKHS given the projection of the target function in a subspace of finite dimensionality. For simplicity, assume the target function to be learned or approximated is in $\mathcal{L}^p(X)$, where X is a nonempty set in a locally compact Hausdorff space so that the RKHS on X is well defined. If the chosen RKHS space on X is dense in $\mathcal{L}^p(X)$, a good approximation can be expected as the sample size goes to infinity. In particular, the radial basis kernel is one of such universal kernels [12].

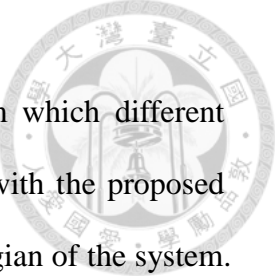
Despite such simplicity in modeling, the only question lies on the necessary



number of observations and the generalization ability to the unseen data. That is, how efficiently a machine learning algorithm can learn. By efficiency, we mean here the ability to generalize with limited observations. Especially in learning the multi-output dynamics system, the curse of dimensionality occurs, since the traditional approach does not consider the correlation between the outputs but model them independently instead. Let N be the number of the outputs. The expected learning error is multiplied N times if all the outputs are modeled disjointly. Therefore, for better generalization, efforts have been put into the regularization on the hypothesis following Occam's razor, e.g. searching the simplest yet complex enough hypothesis space by cross-validation. These methods are effective but rather restrictive.

The learning can be more efficient if the correlations between the outputs are considered. Instead of using the RKHSs of scalar value, the vector-valued RKHS can gain more insights into the coupling of the system. In the vector-valued RKHS, the learning becomes approximate not N but one target function, or the number of observation is multiplied by N . Therefore, given the same number of observations, the learning of the multi-output system becomes more efficient than that of the system with single output, which is on the converse when traditional independent approach is adopted.

In this section, we propose a novel learning scheme with the vector-valued RKHS \mathcal{H}_k for learning the dynamical system. In particular, we consider the dynamical system with exogenous force inputs, and we are interested in the relationship between the generalized coordinates and the generalized force. For a holonomic and monogenic system with exogenous force inputs, the relation is completely



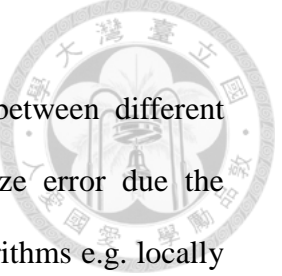
characterized by the Euler-Lagrange equation of the system, from which different generalized coordinates are coupled. By exploiting such structure with the proposed kernel, the dynamics is identified by effectively learning the Lagrangian of the system. Therefore, the learning can be more efficiency. In addition, since not all the systems satisfy the requirement of being holonomic and monogenic, we propose a multiple-kernel framework for learning the dynamics of general systems in probably approximately correct learning.

The section is organized as follows. Section 3.2.2 reviews the essentials of the vector-valued RKHS. For more, readers can refer to Chapter 2. In Section 3.2.3, the main contribution of this section is presented. Inspired by the finding in Section 3.1, the proposed scheme models the Euler-Lagrange method implicitly in the vector-valued RKHS. As the demonstration, the dynamics of serial robots is investigated in simulation in Section 3.2.5. Finally, we close this section by giving the discussion and a short conclusion in Section 3.2.6.

3.2.2 Vector-Valued Reproducing Kernel Hilbert Space Revisited

As the space of vector-valued functions, the vector-valued RKHS is the generalization of the scalar RKHS, in which the elements are scalar function. In contrast to the well-studied scalar RKHS, the vector-valued RKHS has drawn few attentions until the last decade, although the mathematical studies can be dated back to [7, 76]. Due to the increasing needs in the multi-task learning and the transfer learning, the vector-valued RKHS is aimed to generalize the algorithms based on the scalar RKHS and the representer theorem [85] for the learning of vector-valued functions

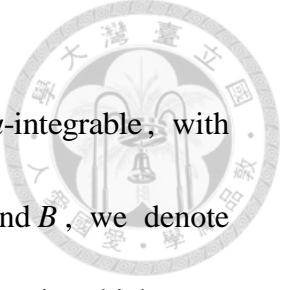
Traditionally, the learning of the vector-valued functions is done by the multiple



independent scalar learners. To further consider the correlations between different outputs, most of the algorithms are modified in order to penalize error due the difference between outputs [83, 103, 105, 111], although some algorithms e.g. locally weighted projection regression [106] can intrinsically be extended to vector-valued problems. Nevertheless, these methods rather induce biases or are *ad hoc*. On the contrary, the theory of vector-valued RKHS is general and the correlations between different outputs are considered intrinsically. Therefore, the learning [31, 78] can gained from modeling the dependencies in the vector-valued RKHS directly.

Recently, the formal studies of RKHS generalizing the Mercer's theorem and the feature space [8, 11, 12, 31], and theory of convergence of learning in RKHS are established [9]. In this section, we shall follow these studies, especially [8], to give the definition and the properties of the vector-valued RKHS, which will be used to model the relationship between the generalized coordinates and the generalized forces in the next section. For more information and the reference, please refer to Chapter 2, [8, 11] and therein.

We first begin with some notations. Let \mathcal{X} be a locally compact Hausdorff topological space, and \mathcal{Y} be a separable Hilbert space endowed with the inner product $\langle \cdot, \cdot \rangle_{\mathcal{Y}}$. We restrict our attention to the case when \mathcal{Y} is of finite dimensionality and defined over the real field hereafter, both for the need of the application and the simplicity. $\mathcal{Y}^{\mathcal{X}}$ denotes the space of functions that maps from \mathcal{X} to \mathcal{Y} , and $C(\mathcal{X}; \mathcal{Y})$ the Banach space of continuous functions from \mathcal{X} to \mathcal{Y} endowed with the infinity norm. Let $\mathcal{B}(\mathcal{X})$ be the Borel σ -algebra of \mathcal{X} and $\mu: \mathcal{B}(\mathcal{X}) \rightarrow [0, +\infty]$ be a Borel measure on \mathcal{X} , which is σ -additive and finite on compact sets. For $1 \leq p < \infty$, $\mathcal{L}^p(\mathcal{X}, \mu; \mathcal{Y})$ denotes the



Banach space of measurable functions $f \in \mathcal{Y}^{\mathcal{X}}$ such that $|f|^p$ is μ -integrable, with norm $\|f\|_p = \int_{\mathcal{X}} |f(x)|^p d\mu(x)$. Also, given two nonempty sets A and B , we denote by $L(A; B)$ the Banach space of bounded linear operators from A to B , in which $L(A)$ is subspace of bounded linear operators from A to A . $L_+(A)$ denotes the bounded positive semidefinite operator. Finally, for a linear operator T , T^* denotes its adjoint; \otimes denotes both the tensor product of spaces and the Kronecker product, between which the discrimination will not be made if there is no ambiguity; \oplus denotes the direct sum of vector spaces; For simplicity, the convention $\mathbb{N}_M = \{1, \dots, M\}$ is used, where $M \in \mathbb{N}_+$.

Definition 3.8.

Given a locally compact Hausdorff space \mathcal{X} and a Hilbert space \mathcal{Y} as defined previously, a kernel $K : \mathcal{X} \times \mathcal{X} \rightarrow L(\mathcal{Y})$ is said to be of positive-type, if K is positive semidefinite, i.e.

$$\sum_{i,j}^l c_i c_j \langle y_i, K(x_i, x_j) y_j \rangle_{\mathcal{Y}} \geq 0,$$

for any $l \in \mathbb{N}$, $\{x_j \mid j \in \mathbb{N}_l\} \subseteq \mathcal{X}$, $\{y_j \mid j \in \mathbb{N}_l\} \subseteq \mathcal{Y}$, and $c_1, \dots, c_l \in \mathbb{R}$.

This definition generalizes the notation of positive-type in the scalar RKHS where $\mathcal{Y} = \mathbb{R}$. Also, one can think that a vector-value RKHS is actually a scalar RKHS defined on the space $\mathcal{X} \times \mathcal{Y}$.

Definition 3.9.

A Hilbert space \mathcal{H}_K of functions $f \in \mathcal{Y}^{\mathcal{X}}$ endowed with the inner product $\langle \cdot, \cdot \rangle_K$ and norm

$\|\cdot\|_K$ *is called a reproducing kernel Hilbert space on \mathcal{X} , if $\forall x \in \mathcal{X}$ there exists a map $K_x : \mathcal{Y} \rightarrow \mathcal{H}_K$ satisfying*



$$\langle f(x), y \rangle_{\mathcal{Y}} = \langle f, K_x y \rangle_K, \quad \forall f \in \mathcal{H}_K.$$

In particular, the reproducing kernel $K : \mathcal{X} \times \mathcal{X} \rightarrow L(\mathcal{Y})$ is defined as

$$K(x, u) = K_x^* K_u, \quad \forall x, u \in \mathcal{X},$$

and

$$f(x) = K_x^* f, \quad \forall f \in \mathcal{H}_k$$

where $K_x^* : \mathcal{H}_k \rightarrow \mathcal{Y}$ is the adjoint of K_x .

As a consequence, we have that

$$\mathcal{H}_K = \overline{\text{span}}\{K_x y \mid x \in \mathcal{X}, y \in \mathcal{Y}\}.$$

Proposition 3.10.

1. A reproducing kernel is unique up to isometries.
2. A bounded reproducing kernel exists if and only if $\forall x \in \mathcal{X}$, $f(x)$ is a continuous linear map of f running through the Hilbert space \mathcal{H}_K .
3. $K(x, u)$ is of positive type $\forall x, u \in \mathcal{X}$.
4. $\mathcal{H}_k \subseteq C(\mathcal{X}; \mathcal{Y})$ if and only if $K(x, u)$ is locally bounded and $\forall x \in X$, K_x is strongly continuous.

In particular, we emphasize $K(x, u)y = (K_u y)(x)$, where the second argument is used as the index. Also, it can be shown that $K(x, u) = K(u, x)^*$ and $K(x, x) \in L_+(\mathcal{Y})$, i.e. $\|K(x, x)\|_{\mathcal{Y}}$ is a semi-norm of \mathcal{H}_k . In particular,

$$\|K_x\|_{\mathcal{H}} = \|K(x, x)\|_{\mathcal{Y}}^{1/2}$$

$$\langle v, K(u, x)y \rangle = \langle K_u v, K_x y \rangle, \quad \forall x, u \in \mathcal{X}, y, v \in \mathcal{Y}$$

In the following, we consider the case $\mathcal{H}_k \subseteq C(\mathcal{X}; \mathcal{Y})$ when learning the Lagrangian.



To end this section, we summarize some useful admissible constructions of a vector-valued RKHS, and the generalized representer theorem for vector-valued RKHS..

Proposition 3.11.

Let G, K be two reproducing kernels of vector-valued RKHS as defined previously.

1. The sum $K+G$ is a reproducing kernel and the corresponding RKHS is the direct sum of the two RKHSs.

2. Hadamard (Schur) product, $K \circ G$, is a reproducing kernel and the corresponding RKHS is the tensor product of the two RKHSs.

3. Let \mathcal{X}_0 be a compact Hausdorff space, $\mathcal{Y} \in \mathbb{R}^N$, $\Gamma_p : \mathcal{X} \rightarrow \mathcal{X}_0$ for all $p \in \mathbb{N}_N$. Given a scalar kernel $G : \mathcal{X}_0 \times \mathcal{X}_0 \rightarrow \mathbb{R}$, then

$$K(x, u) = \left(G(\Gamma_p x, \Gamma_q u) \right)_{p, q \in \mathbb{N}_N}$$

is a vector-valued reproducing kernel.

Theorem 3.12. (Representer Theorem)

Given a locally compact Hausdorff space \mathcal{X} and a Hilbert space \mathcal{Y} , a reproducing kernel $K : \mathcal{X} \times \mathcal{X} \rightarrow L(\mathcal{Y})$ of the vector-valued RKHS \mathcal{H}_K , a strictly monotonically increasing real-valued function g on $[0, \infty)$, and an arbitrary cost function $c : (\mathcal{X} \times \mathbb{R}^2)^l \rightarrow \mathbb{R} \cup \{\infty\}$, a set of samples $\{(x_i, y_i) \mid x_i \in \mathcal{X}, y_i \in \mathcal{Y}\}_{i \in \mathbb{N}_l}$, the minimizer of

$$\min_{f \in \mathcal{H}_K} c((x_1, y_1, f(x_1)), \dots, (x_l, y_l, f(x_l))) + g(\|f\|_K)$$

admits a representation of the form

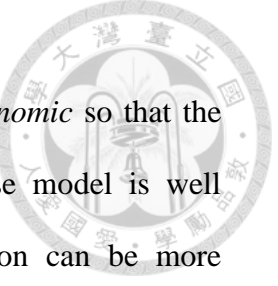
$$f = \sum_{i \in \mathbb{N}_l} K_{x_i} \alpha_i.$$



3.2.3 Learning the Lagrangian and the Dynamics in the Vector-Valued Reproducing Kernel Hilbert Space

With the vector-valued RKHS introduced in the previous section, we now present the main work of this paper: modeling the system dynamics by learning the Lagrangian in the vector-valued RKHS. As mentioned before, the choice of the kernel is a fundamental and open question, which depends on prior knowledge of the application. Without general guidance, most of the algorithms can only try to penalize the differences between different outputs so that the hypothesis space in learning can be smaller.

For the learning of the system dynamics, we propose to use the vector-valued RKHS derived from the Lagrangian of the system. By learning the system dynamics, we mean both the forward model, where the generalize accelerations are the output of the system given the generalized forces, and the inverse model, where the generalized forces are the output and states of systems are the input. Therefore, for the system with multiple degree-of-freedoms, the learning problem is a multi-input-multi-output problem, i.e. a system with vector-valued output and high dimensional input. More specifically, we are interested in forward model that models the response of the system with exogenous force inputs, and the inverse model for the required exogenous force so that the system can achieve the desired states. Such models are useful in various applications, especially in the control system. Forward model can be used to predict and simulate the system's behavior at least for a short period ahead, whereas the inverse model is widely used in sophisticated control schemes [26, 73]. Also, some algorithms combine both the forward and the inverse model for better results [24].



In the following, we shall first assume that the system is *holonomic* so that the Euler-Lagrange equation holds and *monogenic* so that the inverse model is well defined. Under these restrictions, the modeling and the derivation can be more transparent. Then these constraints will be relaxed into a probabilistic framework, and the system dynamics is modeled within the multiple kernel framework [65] studied in Section 3.2.4. In a holonomic system of classical mechanics, the Lagrangian can be treated as an invariant and often regular function, from which the relationships between the generalized coordinates and the generalized forces can be derived according to the Euler-Lagrange equation. That is, the dynamics of different generalized coordinates in a holonomic dynamic system are coupled via the Lagrangian. Therefore, the vector-valued RKHS based on the Lagrangian will be the natural kernel to model the system dynamics.

In the following, we shall review some essences of classical mechanics for the completeness of the paper in *part A*. The formulation of the vector-valued RKHS for dynamics learning is presented in *part B*, and finally we use the robot dynamics as an example to show how the proposed vector-valued RKHS can be tailored for a specific system in *part C*.

A. Classical Mechanics Revisited

In this section, the definitions of some terminologies in the classical mechanics [35] are given for the formulation of the learning problem. Although our interests are in the Lagrangian mechanics, we believe this framework can be generalized to other systems such as Hamiltonian mechanics. We leave it for the further works.

Definition 3.13.

Let r_1, r_2, \dots be the coordinates of the system. A constraint is said to be holonomic if it



can be expressed in terms of the coordinates and possibly time, i.e.

$$f(r_1, r_2, \dots, t) = 0.$$

Otherwise, it is nonholonomic. A system is called holonomic if all the constraints specifying the dynamics of the system are holonomic.

In a holonomic system, it is possible to find a set of independent generalized coordinates (possibly varying with time) that governs the whole system. For a holonomic system, let $q \in \mathbb{R}^N$ be the generalized coordinates and $\tau \in \mathbb{R}^N$ be the generalized forces, where N is the degree-of-freedoms of the system. For $n \in \mathbb{N}_N$, the Euler-Lagrange equation is as follows:

$$\left(\frac{d}{dt} \frac{\partial}{\partial \dot{q}_n} - \frac{\partial}{\partial q_n} \right) \mathcal{L}(q, \dot{q}, t) = \tau_n, \quad (3.17)$$

where the Lagrangian is defined as

$$\mathcal{L} = E_T - E_U, \quad (3.18)$$

$E_T(q, \dot{q}, t)$ is the kinematic energy, and $E_U(q, \dot{q}, t)$ is the generalized potential. We note that there is no unique choice of the Lagrangian. For a Lagrangian \mathcal{L} and a differentiable function $F(q, t)$,

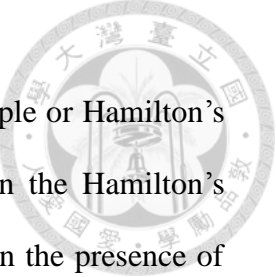
$$\mathcal{L}'(q, \dot{q}, t) = \mathcal{L}(q, \dot{q}, t) + \frac{dF}{dt}$$

is also a valid Lagrangian satisfying (3.17).

Definition 3.14.

A system is called monogenic if all forces except the forces of the constraints are derivable from a generalized scalar potential that may be a function of (q, \dot{q}, t) the coordinates, velocities, and time.

For monogenic systems, the Hamilton's principle holds, where the motion of the system is the stationary solution of the action integral. Although the Euler-Lagrange



equation (3.17) can be either derived from the D'Alembert's principle or Hamilton's principle, the effects of nonholonomic constraints is more clear in the Hamilton's formulation by the introduction of Lagrange multiplier. Therefore, in the presence of nonholonomic constraints so that the generalized coordinates q are no longer independent, (3.17) can be rewritten as

$$\left(\frac{d}{dt} \frac{\partial}{\partial \dot{q}_n} - \frac{\partial}{\partial q_n} \right) \mathcal{L}(q, \dot{q}, t) = \tau'_n, \quad (3.19)$$

where τ'_n is the forces due to Lagrangian multipliers and the exogenous forces. In contrast to τ_n , we note that τ'_n may not be a proper function of (q, \dot{q}, t) due to the Lagrange multipliers, and therefore, traditionally, the nonholonomic systems are simplified as the holonomic system for analysis and modeling.

B. Modeling the System Dynamics by Learning the Lagrangian

Assume that the system is holonomic and monogenic with measurable exogenous force inputs τ_a , i.e. $\tau_n = \tau_{a,n}$ in (3.17). We denote by $\{q, \dot{q}\}$ the set of all possible generalized coordinates and the generalized velocities of the system and so on. Let $\mathcal{X} = \{(q, \dot{q})\}$ and $\dot{\mathcal{X}} = \{(\dot{q}, \ddot{q})\}$; let \mathcal{Y} be the Hilbert spaces of generalized forces. With the abuse of notations, we may write $q \in \mathcal{X}$ or $(q, \dot{q}) \in \mathcal{X}$ for convenience. For the consistency of learning, we assume the Lagrangian is analytic, $\mathcal{L} \in \mathcal{L}^2(\mathcal{X}, \mu_x; \mathbb{R})$ and it is not explicit in time, i.e. $\mathcal{L} = \mathcal{L}(q, \dot{q})$.

Since \mathcal{L} is analytic and therefore continuous, we assume there exists a scalar RKHS \mathcal{H}_L contains \mathcal{L} endowed with the inner product $\langle \cdot, \cdot \rangle_L$. The whole idea of learning the Lagrangian is based on the observation that fixed time t and given $(q(t), \dot{q}(t), \ddot{q}(t))$, (3.17) can be written as

$$\tau_n = T_n \mathcal{L}, \quad (3.20)$$



where

$$T_n := \left(\frac{d}{dt} \frac{\partial}{\partial \dot{q}_n} - \frac{\partial}{\partial q_n} \right)$$

is a linear operator $T_n : \mathcal{H}_{\mathcal{L}} \rightarrow \mathcal{H}_{\mathcal{L}}$. We note that T_n can be regarded as a function of time t and $\ddot{q}(t)$. Since we do not know the exact formulation of $\mathcal{H}_{\mathcal{L}}$ in general, we can, for instance, choose $\mathcal{H}_{\mathcal{L}}$ to be scalar RKHS with reproducing kernel,

$$k_L(u, x) = k_{L,x}(u) = \exp\left(-\frac{\|u-x\|^2}{2\sigma}\right), \quad x, u \in \mathcal{X}, \quad (3.22)$$

which is the standard radial basis kernel, where $0 < \sigma < \infty$. Since $\mathcal{H}_{\mathcal{L}}$ is dense in $C(\mathcal{X}; \mathbb{R})$, it is dense in $\mathcal{L}^2(\mathcal{X}, \mu_x; \mathbb{R})$ and therefore the approximation converges to \mathcal{L} consistently as the sample size goes to infinity.

In terms of the inner product in RKHS, we can write (3.20) as

$$\tau_n(q, \dot{q}, \ddot{q}) = \langle \mathcal{L}, T_n k_{L,x} \rangle_L = \langle T_n^* \mathcal{L}, k_{L,x} \rangle_L, \quad (3.23)$$

where $x \in \mathcal{X}$, $z \in \mathcal{X} \cup \dot{\mathcal{X}}$. We recall that the linear map T_n is actually time-dependent, so $T_n^* \mathcal{L}$ cannot be learned directly. On the contrary, we can observe in (3.23) that τ_n is the projection of Lagrangian on the image of the reproducing kernel $k_{L,x}$ via a time-dependent linear map T_n . By the representer theorem, the Lagrangian admits the following representation

$$\mathcal{L} = \sum_{m \in \mathbb{N}_N} \int_0^\infty \int_{\mathcal{X}} \alpha(t, u) T_m k_{L,u} du dt. \quad (3.24)$$

Empirically, given ℓ training data set,

$$X = \{(q_i, \dot{q}_i) \in \mathcal{X} | i \in \mathbb{N}_\ell\}, \quad (3.25)$$

the empirical approximation of the Lagrangian admits the representation,

$$\hat{\mathcal{L}} = \sum_{i \in \mathbb{N}_\ell} \sum_{m \in \mathbb{N}_N} \alpha_{i,m} T_m k_{L,x_i}, \quad (3.26)$$



or

$$\hat{\mathcal{L}}(q, \dot{q}) = \sum_{i \in \mathbb{N}_\ell} \sum_{m \in \mathbb{N}_N} \alpha_{i,m} \langle T_m k_{L,x_i}, k_{L,x} \rangle_L, \quad (3.27)$$

in which the unknown coefficients $\alpha_{i,m}$ can be learned by standard kernel methods [86].

To cut the clutter, we omit the explicit representation of \ddot{q}_m in $T_n k_{L,x_m}$ hereafter, although care should be taken in that T_n is time-dependent, and therefore $\langle T_n k_{L,x_m}, k_{L,x} \rangle_L$ actually includes the information of \ddot{q}_m . Similarly, the generalized torque can be represented as

$$\tau_n(q, \dot{q}, \ddot{q}) = \sum_{m \in \mathbb{N}_N} \int_0^\infty \int_{\mathcal{X}} \alpha(t, u) \langle T_m k_{L,u}, T_n k_{L,x} \rangle_L dudt \quad (3.28)$$

or empirically

$$\hat{\tau}_n(q, \dot{q}, \ddot{q}) = \sum_{i \in \mathbb{N}_\ell} \sum_{m \in \mathbb{N}_N} \alpha_{i,m} \langle T_m k_{L,x_i}, T_n k_{L,x} \rangle_L. \quad (3.29)$$

We recall from Theorem 5 that (3.29) is actually the result of representer theorem in a vector-valued RKHS. We summarize it in the next theorem.

Theorem 3.15.

Let $q \in \mathbb{R}^N$ and $\tau \in \mathbb{R}^N$ be the generalized coordinates and the generalized forces of a N -DOF holonomic and monogenic system such that τ consists of only the exogenous force inputs, and define $\mathcal{X} = \{(q, \dot{q})\}$ and $\dot{\mathcal{X}} = \{(\dot{q}, \ddot{q})\}$. Assume there exists a scalar RKHS \mathcal{H}_L with reproducing kernel k_L such that the Lagrangian $\mathcal{L} \in \mathcal{H}_L$, i.e.

$$\mathcal{L}(x) = \langle \mathcal{L}, k_{L,x} \rangle_L \quad (3.30)$$

$\forall x \in \mathcal{X}$. Let $T_n : \mathcal{H}_L \rightarrow \mathcal{H}_L$ be the linear map such that

$$\tau_n = T_n \mathcal{L}. \quad (3.31)$$

Then there exists a vector-valued RKHS \mathcal{H}_K with the reproducing



kernel $K : (\mathcal{X} \cup \dot{\mathcal{X}})^2 \rightarrow L(\mathbb{R}^N)$

$$K(x, u) = \left(\langle T_m k_{L,u}, T_n k_{L,x} \rangle_L \right)_{n,m \in \mathbb{N}_N}$$

such that $\tau \in \mathcal{H}_K$. In particular, the (n, m) entry of $K(x, u)$ is defined as

$$\begin{aligned} K_{nm}(x, u) &:= \langle T_m k_{L,u}, T_n k_{L,x} \rangle_L = \\ &(\frac{\partial x}{\partial q_n})^T \frac{\partial}{\partial x} \frac{\partial k_L}{\partial u} (\frac{\partial u}{\partial q}) - (\frac{\partial x}{\partial \dot{q}_n})^T \frac{d}{dt} \frac{\partial}{\partial x} (\frac{\partial k_L}{\partial u}) (\frac{\partial u}{\partial q_m}) \\ &- (\frac{\partial x}{\partial q_n})^T \frac{\partial}{\partial x} (\frac{d}{dt} \frac{\partial}{\partial u} k_L) \frac{\partial u}{\partial \dot{q}_m} + (\frac{\partial x}{\partial \dot{q}_n})^T \frac{d}{dt} \frac{\partial}{\partial x} (\frac{d}{dt} \frac{\partial}{\partial u} k_L) \frac{\partial u}{\partial \dot{q}_m} \end{aligned} \quad (3.33)$$

where $x, u \in \mathcal{X}$ and $\dot{x}, \dot{u} \in \dot{\mathcal{X}}$.

Proof:

The first part of proof follows from the derivations from (3.20) to (3.29), and with Proposition 4, (3.32) can be shown to be a valid reproducing kernel for the vector-valued RKHS \mathcal{H}_K . To prove (3.33), we first discriminate the linear differentiation operators $T_{x,n}$ and $T_{u,m}$ that act on different arguments. In

$$T_{x,n} k_L(x, u) = \langle k_{L,u}, T_n k_{L,x} \rangle_L, \quad (3.34)$$

the time derivative is taken with u fixed, whereas

$$T_{u,m} k_L(x, u) = \langle T_m k_{L,u}, k_{L,x} \rangle_L \quad (3.35)$$

is taken with respect to u . Therefore, we have

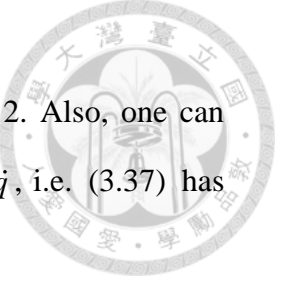
$$K_{nm}(x, u) := \langle T_m \phi_u, T_n \phi_x \rangle_{\mathcal{H}} = T_{x,n} T_{u,m} k_L(x, u) = T_{u,m} T_{x,n} k_L(x, u) \quad (3.36)$$

in which the two operators commute, and (3.33) follows from (3.21).

Q.E.D.

By substituting (3.32) into (3.29), (3.29) can be rewritten as

$$\hat{\tau}(q, \dot{q}, \ddot{q}) = \sum_{i \in \mathbb{N}_l} K(x_i, x) \alpha_i, \quad (3.37)$$



which is the just result of the representer theorem in Theorem 3.12. Also, one can observe that the reproducing kernel K is actually linear in terms of \ddot{q} , i.e. (3.37) has the form

$$\hat{\tau}(q, \dot{q}, \ddot{q}) = M\ddot{q} + B(q, \dot{q}) , \quad (3.38)$$

for some matrices $M, B \in \mathbb{R}^{N \times N}$.

Therefore, not only (3.37) can be used as an inverse model, it can be used as a forward model as well. Compared with the traditional independent approach and those vector-valued RKHS with primitive kernels, \mathcal{H}_k is the vector-valued RKHS that models the Euler-Lagrange equation (3.17) implicitly. Therefore, it models the linear dependency on \ddot{q} intrinsically, and can be used as both the forward and the inverse model serving as the natural vector-valued RKHS for the holonomic and monogenic system with exogenous force inputs.

For the general systems in the assumption, we can use the kernel space (3.22) to be \mathcal{H}_L , and we show the corresponding vector-valued RKHS \mathcal{H}_k in the next proposition.

Proposition 3.16.

Let \mathcal{H}_L be the scalar RKHS with reproducing kernel

$$k_L(x, u) = k_{L,u}(x) = \exp\left(-\frac{\|x - u\|^2}{2\sigma}\right), \quad x, u \in \mathcal{X}. \quad (3.39)$$

The corresponding vector-valued RKHS \mathcal{H}_k that contains the generalized force τ as a function $\{q, \dot{q}, \ddot{q}\} \rightarrow \mathbb{R}^N$ is endowed with the reproducing kernel $K: (\mathcal{X} \cup \dot{\mathcal{X}})^2 \rightarrow L(\mathbb{R}^N)$ defined as

$$K = k_L(x, u)(K_1 + K_2 + K_3 + K_4), \quad (3.40)$$

where



$$\begin{aligned}
K_1 &= \frac{-1}{\sigma} \left(\frac{1}{\sigma} (q_x - q_u)(q_x - q_u)^T - I \right) \\
K_2 &= -\frac{(x-u)^T \dot{u}}{\sigma^2} \frac{1}{\sigma} (\dot{q}_x - \dot{q}_u)(q_x - q_u)^T \\
&\quad + \frac{1}{\sigma^2} (\ddot{q}_x (q_x - q_u)^T + (\dot{q}_x - \dot{q}_u) \dot{q}_x^T) \\
K_3 &= \frac{(x-u)^T \dot{u}}{\sigma^2} \frac{1}{\sigma} (q_x - q_u)(\dot{q}_x - \dot{q}_u)^T \\
&\quad - \frac{1}{\sigma^2} (\dot{q}_u (\dot{q}_x - \dot{q}_u)^T + (q_x - q_u) \ddot{q}_u^T) \\
K_4 &= \frac{\sigma^{-1} (x-u)^T \dot{x} (x-u)^T \dot{u} - \dot{x}^T \dot{u}}{\sigma^2} \left(\frac{1}{\sigma} (\dot{q}_x - \dot{q}_u)(\dot{q}_x - \dot{q}_u)^T - I \right) \\
&\quad - \frac{(x-u)^T \dot{x}}{\sigma^3} (\ddot{q}_u (\dot{q}_x - \dot{q}_u)^T + (\dot{q}_x - \dot{q}_u) \ddot{q}_u^T) \\
&\quad - \frac{(x-u)^T \dot{u}}{\sigma^3} (\ddot{q}_x (\dot{q}_x - \dot{q}_u)^T + (\dot{q}_x - \dot{q}_u) \ddot{q}_x^T) \} \\
&\quad + \frac{1}{\sigma^2} (\ddot{q}_u \ddot{q}_x^T + \ddot{q}_x \ddot{q}_u^T)
\end{aligned}$$

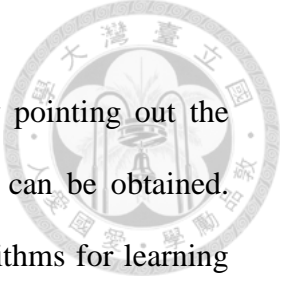
$x, u \in \mathcal{X}$, $\dot{x}, \dot{u} \in \dot{\mathcal{X}}$ and $I \in \mathbb{R}^{N \times N}$ is the identity matrix.

Proof:

This proposition can be proved by substituting (3.39) into Theorem 3.15.

Q.E.D.

In Proposition 3.16, the linear dependency of \ddot{q} is explicit, and the matrix M can be identified by writing (3.37) in terms of Kronecker product. However, the matrix M in (3.38) cannot be guaranteed to positive definite in general during the learning. To enforce M to be positive definite, an additional matrix inequality constraint should be used in solving the program, which may make most of the existing machine learning algorithms semidefinite programming problems. Since our focus and most of the applications are on the inverse model, we leave the exact



formulation of learning the forward model in the future work by pointing out the matrix M can be identified and at least a pseudo-inverse solution can be obtained. However, more efforts still need to be done to customize the algorithms for learning the forward model.

Now we want to compare the proposed approach to the traditional independent models. Assume the traditional model uses the universal scalar RKHS \mathcal{H}_0 with the reproducing kernel

$$k_0(u, x) = \exp\left(-\frac{\|u - x\|^2}{2\sigma}\right), \quad x, u \in \mathcal{X} \cup \dot{\mathcal{X}}, \quad (3.41)$$

and the models of different generalized coordinates in (3.17) are learned separately and independently. In other words, the traditional approach uses the vector-valued RKHS \mathcal{H}_σ with the reproducing kernel,

$$K_\sigma(u, x) = \exp\left(-\frac{\|u - x\|^2}{2\sigma}\right)I, \quad x, u \in \mathcal{X} \cup \dot{\mathcal{X}}. \quad (3.42)$$

Compared to the independent approach, the convergence rate in learning with the proposed vector-valued RKHS \mathcal{H}_κ is faster. It can be explained in two folds. First, we can regard that the learning takes place in \mathcal{H}_κ to learn the Lagrangian in (3.27), from which the models of different generalized coordinates are then derived. From this viewpoint, both the traditional approach and the proposed approach are in scalar RKHSs, but the sample size in (3.27) is N times more than that when models of different generalized coordinates are considered separately. Also, the hypothesis space is smaller. Since \mathcal{H}_κ is the image of \mathcal{X} only, \mathcal{H}_0 is the image of $\mathcal{X} \cup \dot{\mathcal{X}}$. Second, we can treat the learning in \mathcal{H}_κ as (3.37). In this way, although the sample sizes of the two approaches are the same, only one model is needed to learn the whole dynamics compared to the independent approach, where N models are learned separately.



Therefore, the expected error can decreases N times.

C. Example: Robot Dynamics

In this part, we demonstrate the robot dynamics as an example for the proposed method to show how the RKHS can be tailored for the particular system with structure. Let the robot be holonomic and serial, and all the joints be rotary. Therefore, the generalized coordinates are the angular position of each joint and the generalized forces are the joint torques. Assuming the friction can be neglected and the robot is rigid body, the dynamics pacifies the requirement in this section. Since all the joints are rotary, a feature map can be used for better generalization, that is

$$q \rightarrow (\cos q, \sin q). \quad (3.43)$$

With the feature map, the sets \mathcal{X} and $\dot{\mathcal{X}}$ are defined as

$$\mathcal{X} = \{(\chi_q, \dot{q})\} \quad (3.44)$$

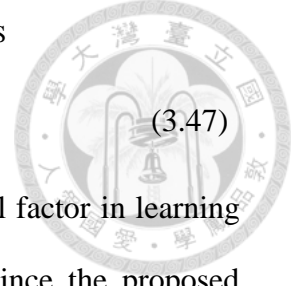
and

$$\dot{\mathcal{X}} = \{(\dot{\chi}_q, \ddot{q})\}, \quad (3.45)$$

where $\chi_q := (\cos q, \sin q)$, $\dot{\chi}_q := (-\dot{q} \circ \sin q, \dot{q} \circ \cos q)$ and \circ denotes the Hadamard product. The vector-valued RKHS similar to that of the Proposition 3.16 can be derived based on Theorem 3.15, where \mathcal{X} and $\dot{\mathcal{X}}$ are replaced by (3.44) and (3.45), respectively. Other modifications similar to (3.44) and (3.45) can also be derived. For example, let $c > 0$ be the constant for normalizing the feature due to the generalized velocity \dot{q} . Then the corresponding sets \mathcal{X} and $\dot{\mathcal{X}}$ can be defined as

$$\mathcal{X} = \{(\chi_q, c\dot{q})\} \quad (3.46)$$

and



$$\dot{\mathcal{X}} = \{(\dot{q}_a, c\ddot{q})\}. \quad (3.47)$$

The normalization of the feature space is a well-known and critical factor in learning with the rbf kernel, and can largely affect the generalization. Since the proposed vector-valued kernel essentially models the Lagrangian function, in which the feature is the set \mathcal{X} , the normalization is can be performed as learning a scalar function with the scalar rbf kernel such as (3.46). Finally, we note that the common term σ^{-1} in (3.40) can be removed in implementation for better numerical stability.

3.2.4 A Multiple-Kernel Framework for General Dynamics

In the section, the restriction on holonomic and monogenic system is relaxed in a multiple-kernel framework. Let \mathcal{H}_K be given as in Proposition 3.16, and consider (3.19), where we may write

$$\tau' = \tau_a + \tilde{\tau} \quad (3.48)$$

and $\tilde{\tau}$ is the force due to nonholonomic constraints and other forces that are not derived from the generalized potential such as frictions. For simplicity, we consider $\mathcal{X} = \{(q, \dot{q})\}$ and $\dot{\mathcal{X}} = \{(\dot{q}, \ddot{q})\}$, and let μ be the joint probability of (q, \dot{q}, \ddot{q}) . Recall that we are interested in the mapping between τ_a and (q, \dot{q}, \ddot{q}) , and that τ' is not in general a well-defined function of (q, \dot{q}, \ddot{q}) . Despite these issues, the learning can be well-defined by introducing the regression function $\tau_{\mu,a}$ defined as

$$\tau_{\mu,a} := \arg \min_{\tilde{\tau}_a \in \mathcal{H}} \|\tilde{\tau}_a + \tilde{\tau} - \tau'\|_{\mathcal{L}^2(X \cup \dot{\mathcal{X}}, \mu)}^2, \quad (3.49)$$

where \mathcal{H} is the hypothesis space to be defined. Assuming the training data set are independently and identically distributed samples according to μ , the learning algorithm can learn the regression function $\tau_{\mu,a}$ as the sample size goes to infinity.

As for the hypothesis space \mathcal{H} , we choose the vector-valued RKHS constructed



by the direct sum of RKHSs, i.e.

$$\mathcal{H} = \mathcal{H}_{MKL} := \mathcal{H}_K \oplus \mathcal{H}_\sigma,$$

with the reproducing kernel

and

$$K_{MKL} = d_K K + d_\sigma K_\sigma, \quad (3.51)$$

where d_K, d_σ are the weightings to be defined so that

$$\mathcal{H}_K = \{f \mid f \in \mathcal{H}_K, \frac{\|f\|_{K'}^2}{d_K} < \infty\} \quad (3.52)$$

with the inner product

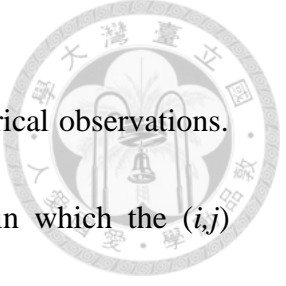
$$\langle f, g \rangle_{K'} = \frac{1}{d_K} \langle f, g \rangle_K \quad (3.53)$$

and \mathcal{H}_σ is defined similarly. Since \mathcal{H}_σ is universal, we can expect in \mathcal{H}_{MKL}

$$\tau_{\mu,a} = \arg \min_{\tilde{\tau}_a \in C(X \cup \dot{\mathcal{X}}; \mathcal{Y})} \|\tilde{\tau}_a + \tilde{\tau} - \tau\|_{\mathcal{L}^2(X \cup \dot{\mathcal{X}}, \mu)}^2. \quad (3.54)$$

By introducing the \mathcal{H}_K , we hope the learner can fast adapt to the structure of the dynamics, as long as the term τ_a dominates $\tilde{\tau}$. Otherwise, the learning can gain little by exploiting the structure of the Lagrangian.

To solve the learning problem, we adopt ε -support vector regression (ε -SVR) [94] with multiple-kernel learning inspired by SimplMKL [77]. SVR is a robust nonlinear multivariate regression for scalar output*, and SimpleMKL is a wrapper algorithm based on the primal problem of multiple-kernel learning solved by reduced gradient descent. As mention in Section II, the vector-valued RKHS is actually a scalar RKHS on the space $\mathcal{X} \times \mathcal{Y}$, so it can be solved by substituting the correct kernel matrix in SVR.



Let $X = \{x_i \mid x_i \in \mathcal{X} \cup \dot{\mathcal{X}}\}_{i \in \mathbb{N}_\ell}$ and $Y = \{y_i \mid y_i \in \mathcal{Y}\}_{i \in \mathbb{N}_\ell}$ be the empirical observations.

The empirical kernel matrix $\mathbf{K}_{MKL} \in \mathbb{R}^{N\ell \times N\ell}$ is the block matrix, in which the (i,j) block is defined as

$$\mathbf{K}_{MKL,ij} = K_{MKL}(x_i, x_j). \quad (3.55)$$

Also we define $\mathbf{K} \in \mathbb{R}^{N\ell \times N\ell}$, $\mathbf{K}_\sigma \in \mathbb{R}^{N\ell \times N\ell}$ associated with the RKHS \mathcal{H}_K and \mathcal{H}_σ .

We note the spaces \mathcal{H}_K and \mathcal{H}_σ are scaled empirically before constructing \mathcal{H}_{MKL} so that the empirical kernel matrices $\mathbf{K}, \mathbf{K}_\sigma$ have the same trace.

Using the Karush-Kuhn-Tuker condition, the multiple-kernel SVR can be expressed as

$$\begin{aligned} & \min_{d_K, d_\sigma} J(d_K, d_\sigma) \\ & \text{s.t.} \\ & \quad d_K^2 + d_\sigma^2 \leq 1 \\ & \quad d_K, d_\sigma \geq 0 \end{aligned} \quad (3.56)$$

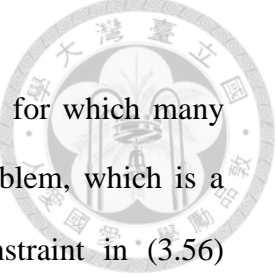
where

$$\begin{aligned} & J(d_K, d_\sigma) \\ &= \max_{\mathbf{a}_0, \mathbf{a}_0^* \in \mathcal{C}} \frac{-1}{2} (\mathbf{a}_0 - \mathbf{a}_0^*)^T (d_K \mathbf{K} + d_\sigma \mathbf{K}_\sigma) (\mathbf{a}_0 - \mathbf{a}_0^*), \\ & \quad -\varepsilon \mathbf{1}^T (\mathbf{a}_0 + \mathbf{a}_0^*) + \mathbf{y}^T (\mathbf{a}_0 - \mathbf{a}_0^*) \end{aligned} \quad (3.57)$$

and

$$\mathcal{C} = \{\mathbf{a}_0, \mathbf{a}_0^* \mid \mathbf{1}^T (\mathbf{a}_0 - \mathbf{a}_0^*) = 0, \mathbf{0} \leq \mathbf{a}_0, \mathbf{a}_0^* \leq C/N\ell \mathbf{1}\},$$

$\mathbf{a}_0, \mathbf{a}_0^* \in \mathbb{R}^{N\ell}$ are the slack variables, ε is the size of the ε insensitive cost and the parameter C trades off the penalty between the fitting error and the complexity of the hypothesis space. After computing the optimal $\mathbf{a}_0, \mathbf{a}_0^*, d_K$ and d_σ , the coefficients in (3.37) can be obtained by factorizing the block structure. See [94] for more details.



In this formulation, (3.57) is the single kernel SVR problem, for which many efficient solvers are available; (3.56) is the ℓ_2 -multiple-kernel problem, which is a convex nonlinear programming problem. We choose the ℓ_2 constraint in (3.56) instead of ℓ_1 , so the contributions of the two kernels can be balanced. Otherwise, MKL will select only one kernel empirically in the ℓ_1 formulation. It is shown that the objective function in (3.56) is differentiable and the gradient can be computed at ease [77] as

$$\begin{aligned}\frac{\partial J}{\partial d_K} &= \frac{-1}{2}(\mathbf{a}_0 - \mathbf{a}_0^*)^\top \mathbf{K}(\mathbf{a}_0 - \mathbf{a}_0^*) \\ \frac{\partial J}{\partial d_\sigma} &= \frac{-1}{2}(\mathbf{a}_0 - \mathbf{a}_0^*)^\top \mathbf{K}_\sigma(\mathbf{a}_0 - \mathbf{a}_0^*)\end{aligned}\quad (3.58)$$

and therefore, we can use a wrapper algorithm to solve the problem as SimpleMKL.

The algorithm based on reduced gradient method is shown in pseudo-code in Fig. 3-8, which is based on an off-the-shelf second-order cone programming (SOCP) solver and the conventional SVR solver. The algorithm is similar to SimpleMKL, but the ℓ_2 constraint is used and Step 2 is solved by SOCP solver to compute the update direction. Therefore, the convergence and the computational complexity are the same as SimpleMKL, since the SOCP problem only has two variables, which can be solved efficiently, and that the SVR solver can benefit from the *warm start* of the previously computed $\mathbf{a}_0, \mathbf{a}_0^*$ so the updating and the line search is fast. In particular, we choose the stopping criterion as the stepsize to accelerate the algorithm, since we do not concern the accurate value of d_K and d_σ . Thus the computational complexity of the whole algorithm is determined by the complexity of the SVR solver.

**Algorithm (ℓ_2 Multiple-Kernel SVR)**

Given $\delta = 1e-4$

Initialize $d_K^{(0)}, d_\sigma^{(0)} = 1/\sqrt{2}$

$i = 0$

While (1)

1. *Update* $\mathbf{a}_0, \mathbf{a}_0^*$ by solving the SVR problem (3.57) with $d_K^{(0)}, d_\sigma^{(0)}$.

2. *Solve*

$$\min_{\Delta d_K, \Delta d_\sigma} \nabla J^{(i)T}(\Delta d_K, \Delta d_\sigma)$$

s.t.

$$(d_K^{(i)} + \Delta d_K)^2 + (d_\sigma^{(i)} + \Delta d_\sigma)^2 \leq 1$$

$$d_K^{(i)} + \Delta d_K, d_\sigma^{(i)} + \Delta d_\sigma \geq 0$$

3. *Compute the stepsize* $\gamma \in [0,1]$ by line search such that the objective function decreases strictly.

4. **If** $\gamma < \delta$

Break

Else Update

$$d_K^{(i+1)} = d_K^{(i)} + \gamma \Delta d_K$$

$$d_\sigma^{(i+1)} = d_\sigma^{(i)} + \gamma \Delta d_\sigma$$

5. $i = i + 1$

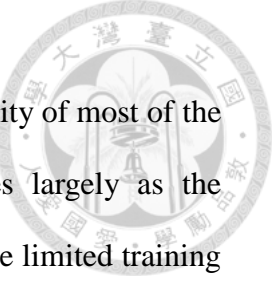
End of While

Fig. 3-8. The pseudo code of the MKL algorithm.



3.2.5 Simulations

In this section, the simulation results of learning the inverse dynamics of the robot system are presented. We want to compare the generalization of the proposed vector-valued kernel and the scalar rbf kernel, which is used commonly in the learning for its universality. We test our scheme with the simulated dynamics data of the serial robot. Therefore, we adopt the modification in Section 3.2.3.C as the vector-valued kernel. In each of the following simulations, we show the testing error with respect to the complexity of the underlying model, i.e. the degrees of freedom of the robot, in different scenarios: perfect rigid-body dynamics, the presence of measurement noise, and nonlinear frictions. In the following, for each of degree of freedoms, ten different robots with random kinematic and dynamic parameters are used as the plant to be learned. We remark that the parameters are sampled from a bounded uniform distribution so that all the parameters are physically feasible, e.g. the inertia matrix are always positive definite. For each of the robot, 500 training data and 3000 testing data with angular positions, angular velocities, and angular accelerations generated from the uniform distribution are used for validation. Given the uniformly random states, the kinematic and the dynamic parameters, the generalized forces are computed using Newton-Euler method iteratively. Therefore, the data of the ideal robot dynamics can be obtained. As for the unmodeled dynamics, the adopted noise is the zero-mean Gaussian noise, the viscous friction is modeled by the force linear to the generalized velocity, and the Coulomb friction is modeled as the sign function of the generalized velocity. We remark that we limit ourselves to only 500 training data for the computational complexity. Since the vector-valued kernel matrix is of



size $(N\ell)^2$ given ℓ samples of N -DOF, and the computational complexity of most of the kernel method is polynomial, the computational burden increases largely as the number of the training instances and the DOF. Therefore, we only use limited training data to show the behavior of our scheme, since our focus is on the design of the kernel not the efficiency of the algorithm.

In the simulation of the ideal dynamics without frictions and measuring noises, we use the least-square regularized learning, i.e. the kernel ridge regression, and the kernel parameters and the parameter that controls the tradeoff between the complexity of the space and the fitting error all chosen by 3-fold cross-validation. The optimal parameters is chosen to be the combination of parameters that minimize the empirically expected prediction error, and the whole training data set is used to retrain the final model with the optimal parameter.

On the other hand, we use the MKL algorithm in Section 3.2.4, for the cases where frictions and measuring noises are present. Since the MKL algorithm determines automatically the weighting, the left parameters of the two kernels and the weighting C in SVR are chosen by the cross-validation mentioned above. For the SVR implementation, we adopt LIBSVM and integrate it with the pre-computed kernel in Matlab and warm start.

Finally, to verify the result, the performances are shown in terms of prediction errors overall all the generalized coordinates both in root mean square (RMS) and the peak error (PE). Also, we note that all the generalized force in the simulation are normalized within [-1,1] for comparison. In the following, the proposed kernel is denoted by $vrbfs$, the rbf kernel (3.43) is denoted by $rbfs$, and the MKL kernel is denoted by mkl which combines the kernel in Section 3.2.3 and another rbf kernel



with the joint velocity as the input.

D. Simulation Results with Ideal Robot Dynamics

This section shows the simulation results of the robot dynamics without any friction and measuring noises in Fig. 3-9. The kernel method here is SVR with the insensitive of size 0.03, which denotes 97% accuracy, and we set the parameter C to some large constant. Since there is no friction presented, we only use the kernel in Section 3.2.3 without the MKL in Section 3.2.4. The x-axis is the DOF of the underlying system, and the y-axis is the prediction error of the normalized torque. The result shows that the proposed vector-valued kernel indeed performs better compared to the traditional *rbfs* kernel by taking into account the correlation between different generalized coordinates.

E. Simulation Results with Ideal Robot Model and Frictions

Similar to the setting in the previous section, the performances with the Coulomb frictions, the viscous frictions, and the measuring noise are compared. The Coulomb frictions and the viscous frictions are modeled as mentioned previously with the magnitude chosen randomly, and the noise is the zero-mean Gaussian noise with standard deviation 0.05. The results are shown in Fig. 3-10. Compared to Fig. 3-9, the vector-valued kernel performs as in the ideal case. However, the prediction error of *rbfs* increases almost twice. Because the dynamics of the system becomes more complex with the presence of the friction, the pure *rbfs* kernel introduces larger variance in the learning. On the contrary, the vector-valued MKL kernel *vrbfs* uses the vector-valued part models the correlation between the generalized coordinates and the *rbfs* part to model the friction forces. As a consequence, the vector-valued part introduces a natural bias to learn the system dynamics owing to implicit

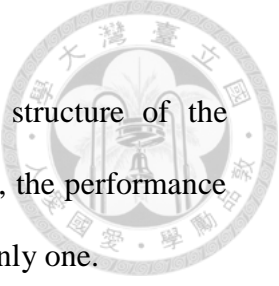
Euler-Lagrange method, making the generalization of *vrbfs* better than that of *rbfs* just as in the ideal case.

Finally, before showing the experimental results, we discuss some discoveries in the simulation. First, we find that the precise value of the weighting in the MKL formulation seems not so important. In most of models learned in the simulation, the weights of the two models are equal. This suggests that the performance of the learning can be simply increased by considering both the kernels. Also, we find that the warm start does not save times as expected in the current LIBSVM implementation, because of the overhead of converting the data from dense format to sparse format. Since our kernel is a large dense kernel, the current data structure in LIBSVM seems not suitable for our application. We believe rewrite it in a dense format may increase the speed in MKL learning. Thus, for simplicity, we may take the weighting of the two kernel equal without sacrificing much performance while saving lots of times in the MKL learning.

F. Asymptotical Analysis

In this simulation, we want to analyze the asymptotical behavior of the kernel as the number of the observations increases. The prediction errors in terms of the number of the observations are shown in Fig. 3-11, in which the trainings are performed in the same fashion as in Part D, and the number of the testing data is 8000. To compare the performance, we use the same testing data for all settings. From the figures, we can observe that the vector-valued kernel converges faster, and has lower prediction errors, compared to the traditional approach. Because the correlations are considered, the scheme with the vector-valued kernel, the effective number of the observations is increased by N times. Also, we note that the prediction of the 1-DOF robot is also





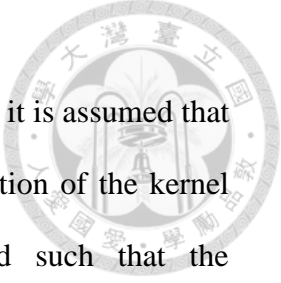
better. By observing (3.40), the vector-valued models also the structure of the dynamics, which is linear in the generalized acceleration. Therefore, the performance is still better compared to *rbfs* kernel, even the DOF of the robot is only one.

3.2.6 Discussions

In this section, the generalized vector-valued kernel for learning the dynamical system is proposed. By modeling both of the structure of the dynamics and the correlations between different generalized coordinates, the proposed scheme shows better prediction error and the convergence rates in the simulations, compared to the rbf kernel used in most of the literatures. The proposed kernel can adapt universally to arbitrary dynamics system as long as the Lagrangian of the system can be defined. In the future, we want to design another vector-valued kernel by exploiting the Hamiltonian of the system so that the kernel can model a larger class of dynamical systems. Evidenced by the findings here, we are confident and excited that good results can be expected with the Hamiltonian approach.

Although we focus on the identification of the inverse dynamics, we note that the kernel can be used to model the forward dynamics by isolating the inertia matrix in (3.40). Since (3.40) is linear in the generalized acceleration, the inertia matrix is properly defined. Although this matrix cannot be guaranteed to be positive definite in our current approach, the constraint can be added to the learning problem, which is still a convex problem. We believe by doing so, both of the forward dynamics and the inverse dynamics can be learned faster, since an additional and important prior is considered. We leave this in the future works.

For the future works, the vector-valued kernel will be tested with experimental data. Compared to the simulation, the major differences would be sensory noises in



the state estimations and the calibrations of the torque sensors. Since it is assumed that the output of the regression is the generalized torque in the derivation of the kernel (3.17), it is important that the torque sensors are calibrated such that the measurements are expressed in the same units. If the calibrations are not performed correctly, the vector-valued kernel may introduce a bad bias instead of an informative prior. Otherwise, if the calibration errors are small and can be tolerated by the insensitive tube of SVR, the vector-valued kernel should improve the generalization just as in the simulations.

In summary, the Lagrangian or the possibly Hamiltonian design of the reproducing kernels discovers an interesting link between the dynamics and the machine learning. To the best of our knowledge, such an elegant relationship is novel. We believe the findings here imply the next generation of the system identification and control theory.

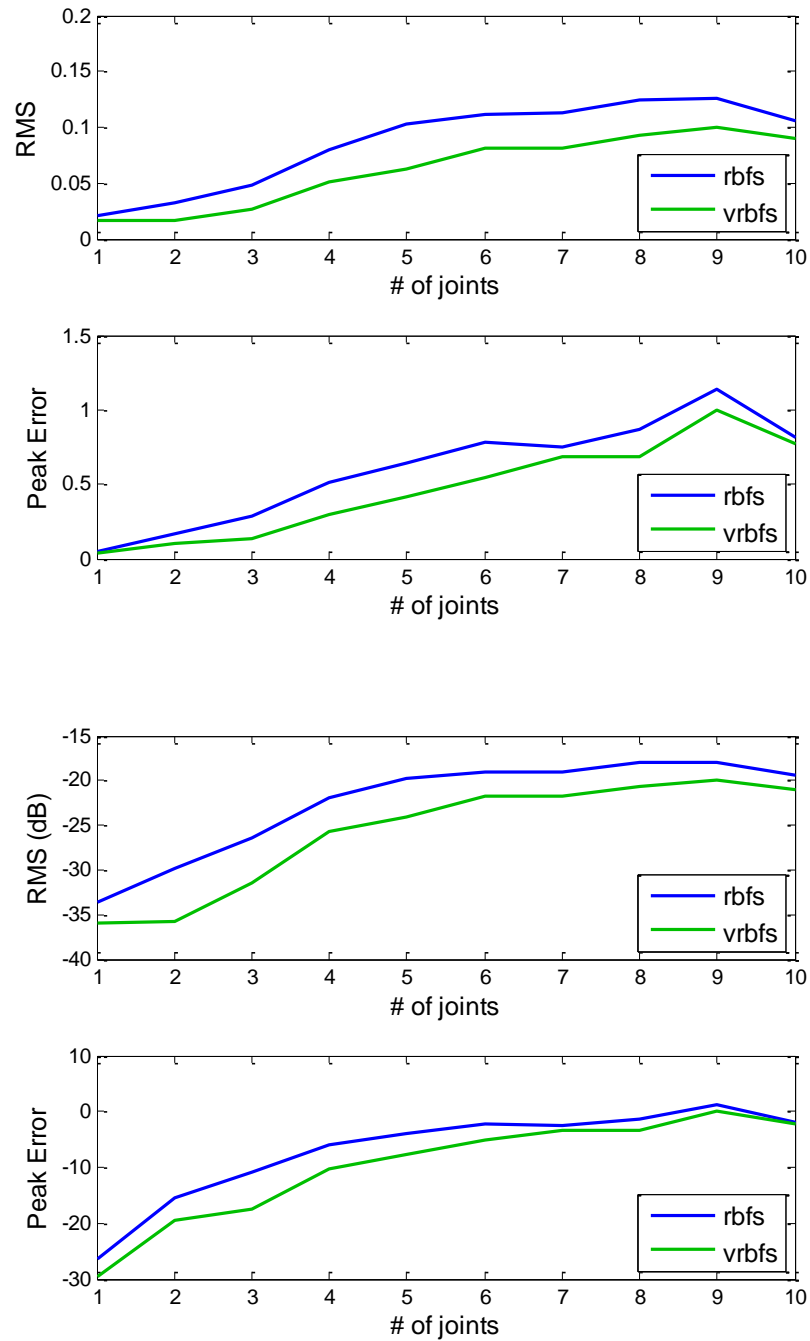
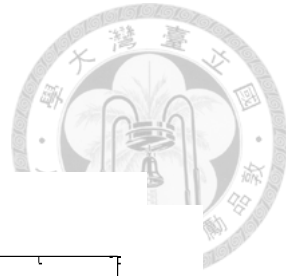


Fig. 3-9. Simulation result of the ideal dynamics.

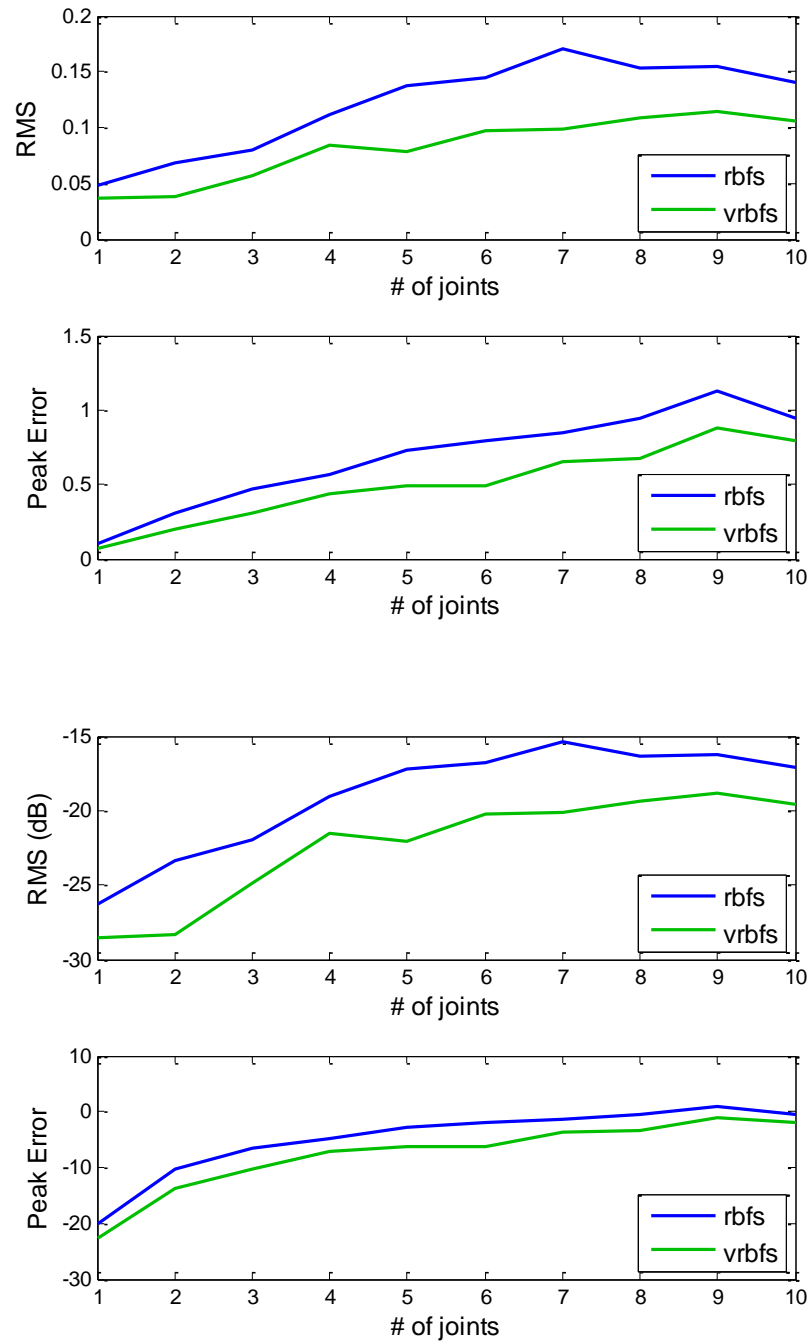


Fig. 3-10. Simulation result of the ideal dynamics with frictions and

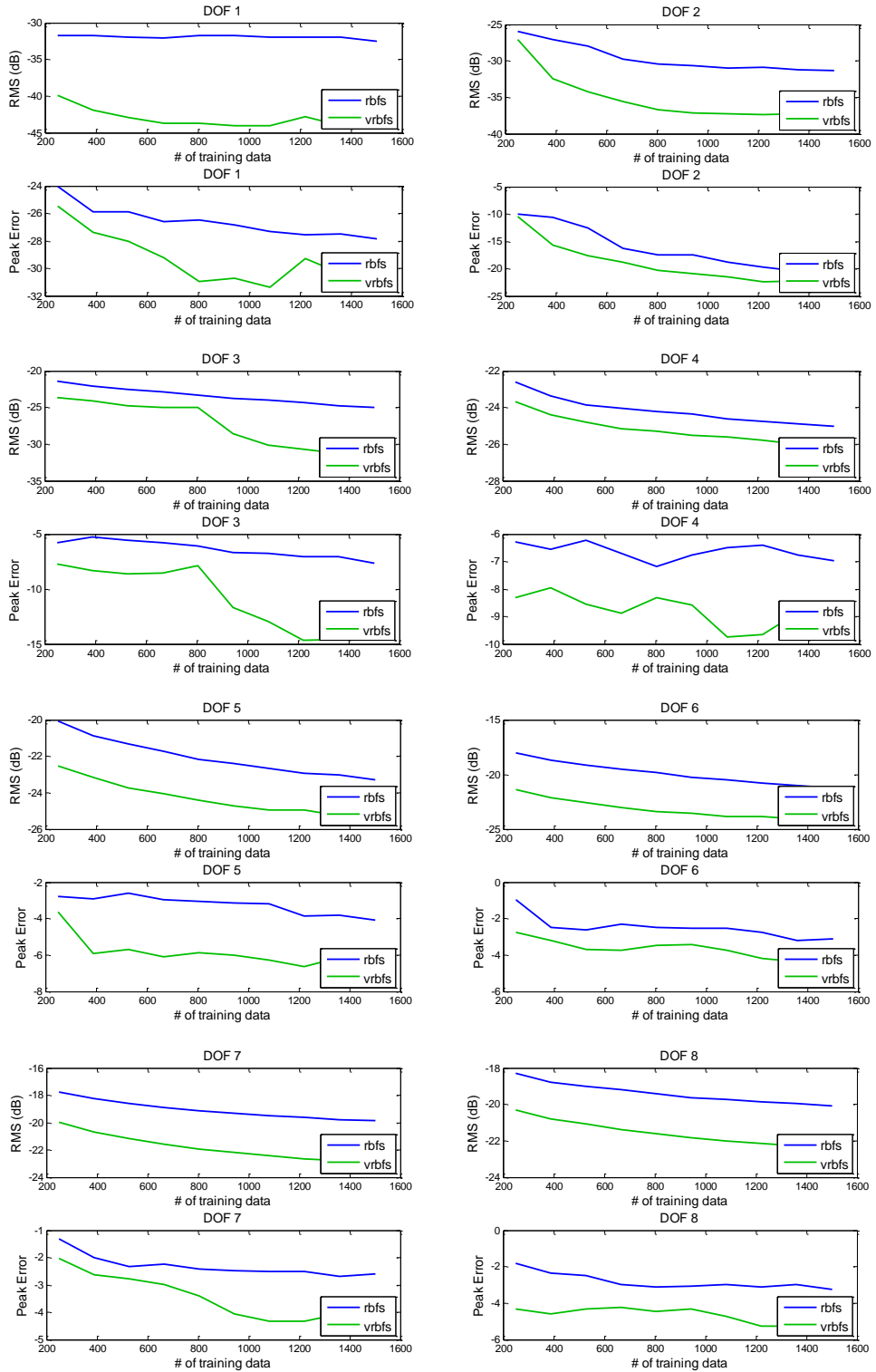


Fig. 3-11. Asymptotical analysis.



3.3 Summary

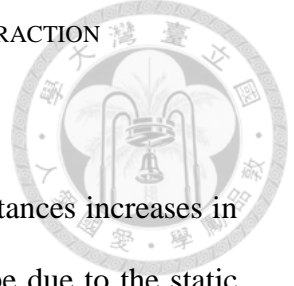
In this chapter, the main contribution is the reproducing kernels that incorporates the Euler-Lagrange method implicitly to models the dynamical system. To encode the Euler-Lagrange method, the *structure* of the function space and the *correlations* between different generalized coordinates should be considered. In Section 3.1, the first scalar kernel is designed by identifying the functional space of the governing equation of the robot dynamics, which is derived based on the structured Lagrangian. Therefore, this kernel not only encodes the structure due to the Lagrange-Euler method such as the linear tendency in the joint acceleration but also the structure of the tensor product of the serial robot. In Section 3.2, we generalize the previous idea and relax the constraint of knowing the form of the Lagrangian. The result is an universal vector-valued kernel that considers both of the structure and the correlations by learning the Lagrangian of the system implicitly. Compared to the scalar kernel in the previous section, the correlation is considered here, which largely increases the performance in term of the prediction error both theoretically and experimentally. In the simulations, the proposed schemes are indeed more competitive compared to the traditional kernels used in the machine learning. We believe this finding is inspiring and exciting, which builds a link between the machine learning and the parametric system identification used in the control community. In the near future, the experiments will be performed to verify these kernels.



Chapter 4 Virtual Impedance Control for Safe Human-Robot Interaction

The collision avoidance problem is essential for safe manipulation. Especially with human around, the robot should work only when the safety can be robustly guaranteed. Unlike the traditional path planning offline, the collision avoidance problem based on the reactive control incorporates the dynamic objects into the path planning and the response should be real-time yet smooth. Although this problem is not new, it is not completely solved. The dilemma between the robust and the consistent reaction and the response of multiple collision points is still an issue. In this chapter, we propose a generalized framework for the reactive control based on the virtual impedance control. The virtual impedance control shapes the dynamics in some abstract vector space so that it follows the spring-damper system. Along with the other impedance control schemes, the virtual impedance control benefits from that the characteristics of the system can be easily designed by tuning the damping ratio and the bandwidth. To robustly, smoothly, and consistently avoid the obstacles while minimizing the interference on the original task of the robot, the virtual impedance control is designed in the risk space, which governs the dynamics of all the possible collision. In implementation, we integrate the system with Microsoft KinectTM for the real-time collision detection and avoidance. Finally, we demonstrate the safe human-robot interaction in the experiments.

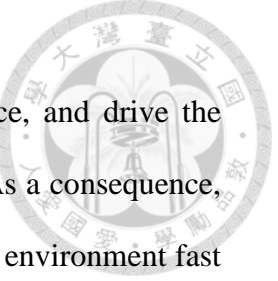
This chapter is partly based on the contributed works in conferences or journals [17].



4.1 Introduction

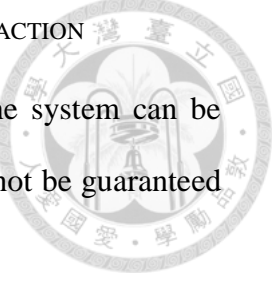
The need of robots operating in partially unstructured circumstances increases in recent years. In these tasks, the environmental uncertainties may be due to the static objects that are unknown or expensive to be modeled beforehand, or due to the dynamics objects such as the human working in cooperation with the robot, or the sudden change of the environment, and the objective of the robot is to achieve some predefined control schemes, such as the position tracking or the impedance control, while guaranteeing the safety of the operation. However, due to such uncertainties, the pre-planned paths or the controller of the robot may not be able to guarantee both the performance and the safety of the robot. In this case, the safety requirement should be put into the highest priority, and the robot should try to accomplish the predefined task within this constraint. The safety issue is especially stressed when it comes to the human-robot interaction.

To achieve the safety requirement, the robot should detect and avoid the collision before the physical contact. Since the classical path planning and obstacle avoiding schemes such as the rapidly-exploring random tree (RRT) needs global information of the surroundings, they may be too slow, or even incapable of reacting to such tasks. For real-time control in the uncertain environment, the reactive control [2] is introduced to cope with such difficulties. In contrast to the global path planning schemes, the reactive control uses only the local information from the proximity sensors or the computational vision to control the movement of the robot to responses simultaneously. The most popular approaches are those based on the potential fields [54], which guides the robot through the environment by defining the attractive potentials and the repulsive potentials. The forces, defined as the negative gradient of



the potential fields, form the vector field in the configuration space, and drive the robot to achieve the task while preventing the collision avoidance. As a consequence, the reactive controls based on the potential fields can response to the environment fast and smoothly, and have been applied successfully [6, 21, 22, 32, 37, 89, 90].

Nonetheless, the potential field scheme is not perfect. As mentioned, the safety of the operation should come first. Therefore, this is potentially the multi-priority problem. To ensure the robustness of the collision avoidance, the original potential field scheme [6, 54] compensates the dynamics of the point at risk, so the chosen point can avoid the obstacle regardless of the predefined trajectory or the control scheme. Therefore, the original control scheme only operates in the null space of the Jacobian of the chosen point. However, the consistent behavior of the collision avoidance cannot be guaranteed when facing multiple collisions, since the degrees of freedom (DOF) of the robot is finite. To address this dilemma, we categorize the literatures according to use of the projection matrix in the collision avoiding. Without the use of the projection matrix, the repulsive forces from different obstacles are transmitted and summed to exert on the robot dynamics. In [91], they transmit the repulsive forces on the defined the points at risks to the some predefined control points to handle the multiple collision problem; to unify both the virtual and physical forces, all the repulsive forces are transmitted by the corresponding Jacobian matrices and transmitted torques are summed in the joint space in [21, 22, 37-39]; similarly in [87], the contributions of different potentials of the collision avoidances, the joint limit avoidances, and the manipulation are summed and the dynamics of the robot follows the effective torque from all the potentials. This approach that summing up all the forces seems intuitive and simple, yet some underlying problems exist. The most



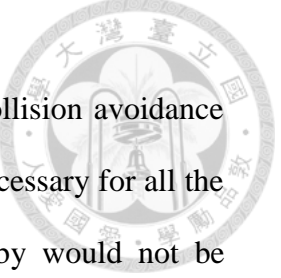
serious question is that what the equilibrium point is. Although the system can be stabilized by introducing proper damping, the equilibrium point cannot be guaranteed to be collision-free.

On the contrary, the projection matrix is used to isolate the dynamics of the original task and the collision. Brock et al. [6] put the original task in the first priority and the collision avoidance only operates in the null-space of the original task, which is appealing for the highly redundant robot. Sugiura et al. [98] design the collision avoidance scheme for ASIMO by preventing the collision of the point that is closest to obstacle in the null space of the original task. However, it is not sure whether the null space of the original task is large enough to prevent the collision. To robustly enforce the priority of the collision avoidance, [97] operates the original task only in the null space of the self-collision avoidance. Also, for multiple collision points, they define a vector-valued potential. However, due to the asymptotical nature of the design, the robot may be trapped in the potential fields.

In summary, a good reactive control scheme should possess the following qualities:

1. The collision should be robustly and consistently avoided regardless of the types of the collisions, and the original tasks.
2. The interference on the original task in the collision avoidance should be minimized.
3. The collision avoidance should be smooth and stable.

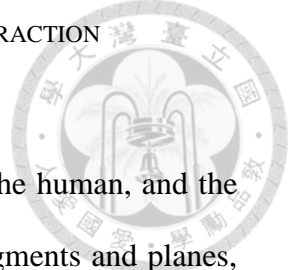
The first requires not only the collision avoidance to be put in the first priority, but also the equilibrium point to be collision free. Such requirement cannot be satisfied in the aforementioned works except in [97]. On the other hand, the second requirement



is satisfied by most of the schemes, especially those operate the collision avoidance only in the null space of the original tasks. Finally, the stability is necessary for all the systems and the smoothness is required so that the human nearby would not be intimidated and the robot would be damaged from the abrupt motion.

In this chapter, we propose the virtual impedance control in the risk space to fulfill the requirement of a good collision avoidance scheme. The risk space is a vector space of the risk functions defined as the normalized distance to the collision of the active collision points, and therefore we can control the dynamics in the risk space to prevent the collision avoidance. To robustly avoid the collisions, the original dynamics only operates in the null space of the Jacobian matrix of the risk functions; to limit the interference, the collision points is only activated if the distance to the obstacles is below some predefined threshold, and also the null space of the risk function is maximized such that it contains all the spaces that do increase the active risk functions; to ensure the smoothness and the stability, the virtual impedance control scheme controls the dynamics in the risk space as the second-order spring-damper system, so the desired dynamics can be easily tuned by setting the damping ratio and the bandwidth of the system.

Compared to [97], the proposed scheme generalizes naturally for multiple collision points regardless of the types, and solves the asymptotical and the switching problem by defining the boundary layer on the spectrum of the Jacobian matrix. In the boundary layer, the repulsive forces and the force of the original dynamics balance, so the robot will not be trapped in the potential fields, i.e. the active risk function; the chattering of the switching is also lessened. In addition, the velocity profile of the proposed scheme is continuous intrinsically, since the impedance control works in the



acceleration domain.

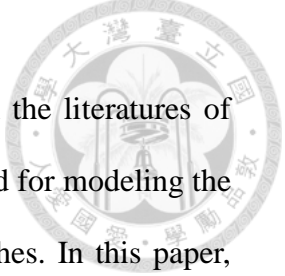
In the partially structured environment, we model the robot, the human, and the surroundings by the spherically extended convex bodies of line segments and planes, so the computational burden is lessened. Although the dynamic object such as the human cannot be known beforehand unlike the robot and the static part of the environment, the low-cost Microsoft KinectTM serves as a good option. In our implementation, we use Kinect to capture the exoskeleton and of the human nearby, so the collision avoidance between the robot and the human can be addressed as the self-collision.

In Section 4.2, we give the formal description of the system and the modeling. The main result of the proposed impedance control in the risk space is presented in Section 4.3. In particular, we highlight the benefits of maintaining the consistently smooth dynamics of the collision avoidance. In Section 4.4, we validate the proposed scheme in the experiments with the 6-DOF NTU robot arm. Finally, we give a short conclusion in Section V.

4.2 System Description

Since the collision problem is related not only to the kinematic description of the robot but also to the geometry, how to efficiently model the appearance of the general robot is important. In the following, we model the robotic manipulator based on the union of the convex sets and the traditional Denavit-Hartenberg notation.

In Fig. 4-1, link i is connected by joint i and joint $i+1$, and frame i is assigned to joint $i+1$, with the link length a_i , the link twist α_i , the link offset d_i , and the joint angle θ_i . The indexes of the joints from the base to the end effector are arranged in the ascending order. For the links with non-zero link length or link offset, it is necessary



to model the geometry of the links for the collision avoidance. In the literatures of robotics and computation vision, various models have been proposed for modeling the robot geometry, such as convex hulls, cylinders, or triangular meshes. In this paper, we consider the simplest convex geometry, namely the line segment. We use the union of the fully connected line segments to describe the skeleton of the robotic manipulator, which is the piecewise linear approximation of the geometry. Since one of the critical steps of collision problem involves in the online computation of the distance between the models of the links, we choose the line segment model to lower the computational burden. Efficient algorithms [84] for the distance computation between line segments are available, and it is much simpler than the computation of the distance between the general convex sets. $\mathcal{L}_{i,k}$

To model the geometry of link i , we use the union of the spherically extended convex hulls of line segment,

$$\mathcal{L}_i = \bigcup_{k=1}^{n_i} \mathcal{L}_{i,k}, \quad (4.1)$$

$$\begin{aligned} \mathcal{L}_{i,k} = & \{ \mathbf{x} \in \mathbb{R}^3 \mid \mathbf{x} = \mathbf{v}_{i,k,1} + (1-\lambda)(\mathbf{v}_{i,k,2} - \mathbf{v}_{i,k,1}) + \mathbf{u}, \\ & \mathbf{u} \in \mathbb{R}^3, \|\mathbf{u}\| \leq r_{i,k}, 0 \leq \lambda \leq 1 \} \end{aligned} \quad (4.2)$$

for $k = 1, \dots, n_i$, where $\mathbf{v}_{i,k,1} \in \mathbb{R}^3$ and $\mathbf{v}_{i,k,2} \in \mathbb{R}^3$ are the two vertices of the line segment, $r_{i,k} \geq 0$ is the radius of the sphere, and n_i is the size of the set. The indexes are arranged as $\mathbf{v}_{i,k,2} = \mathbf{v}_{i,k+1,1}$ and $\mathbf{v}_{i,n_i,2} = \mathbf{v}_{i+1,1,1}$ so that all the links are fully connected. For link i , the line segments are chosen giving the best piecewise linear approximation of the appearance while limiting the size of the set n_i , and the radius of the sphere is then designed such that the union of the convex sets covers link i completely as in Fig. 4-1.

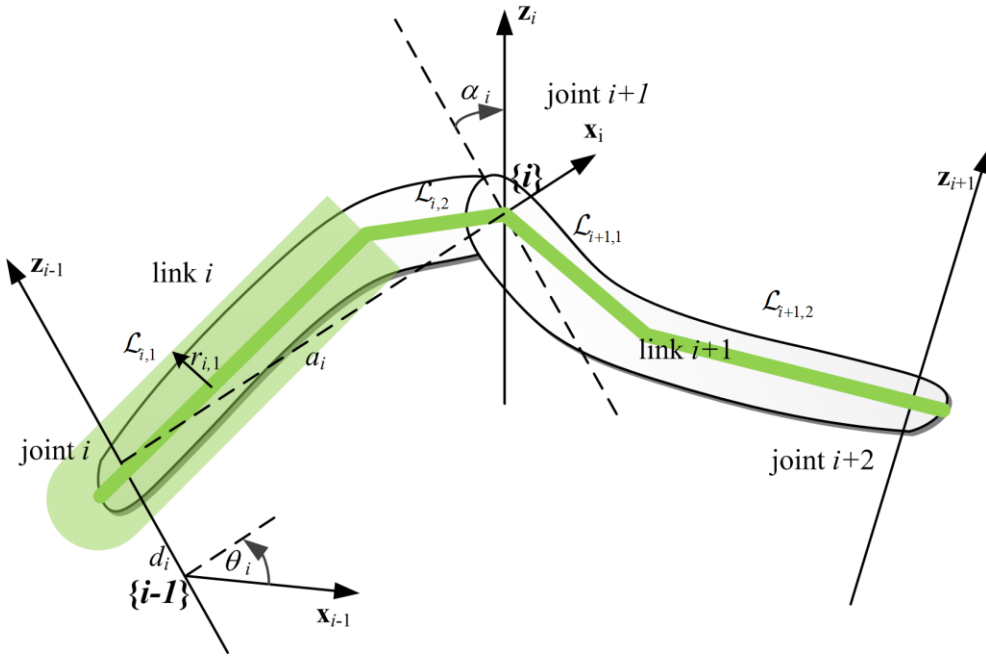


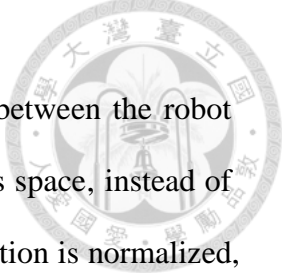
Fig. 4-1. The geometry model of the robotic manipulator

It can be easily shown that the shortest distance between two spherically extended convex hulls of the line segment is the same as the shortest distance between two line segments minus the radii of the sets, and therefore the efficient algorithm for line segments can be used.

As for the environments, the skeleton model of line segments can also be used, e.g. human skeleton model can be detected by KinectTM. Moreover, the spherically extended parallelograms are used to model the static platforms, such as desks and walls in the environment. Thus, the body-to-body collision can be efficiently prevented by the computing the shortest distance between two convex bodies.

4.3 Virtual Impedance Control in the Risk Space

In this section, we describe the proposed control scheme. To robustly ensure the success of the collision avoidance for all the possible collisions, we define the risk



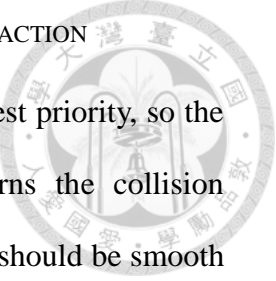
space, which describes the dynamics of the normalized distances between the robot and the obstacles, and control the dynamics of the robot in the risks space, instead of the Cartesian or the joint space used in common. Since the risk function is normalized, the consistent dynamics in the risk space guarantees the behavior of the robot regardless of the types of the upcoming collisions. Therefore, the collisions can be avoided robustly.

In the following, we assume that the robot is originally stabilized with some control laws such that the joint space dynamics admits the following form,

$$\mathbf{M}(\mathbf{q})\ddot{\mathbf{q}} + \mathbf{F}(\mathbf{q}, \dot{\mathbf{q}}, \ddot{\mathbf{q}}) = \mathbf{0} \quad (4.3)$$

where $\mathbf{M}(\mathbf{q}) \in \mathbb{R}^{N \times N}$ is the inertia matrix, $\mathbf{F}(\mathbf{q}, \dot{\mathbf{q}}, \ddot{\mathbf{q}}) \in \mathbb{R}^N$ is the result of the (nonlinear) control law. This form (4.3) is general. For example, it can be the independent PD-control with the gravity compensation, or the joint space or the Cartesian space impedance control, or the admittance interface for a position-controlled robot to imitate the impedance effects. The only requirement here is that closed loop system (4.3) is stable and $\mathbf{M}(\mathbf{q})$ is known and positive definite.

Before entering the subject, we briefly discuss the control scheme. The overall control scheme can be divided into two parts: collision detection and collision avoidance control. In the first stage, the risk functions are updated based on the closest distance between two convex bodies in the Cartesian space or the distance to the joint limit, which measure the degrees of possible collisions. If the risk function is nonzero, then the collision avoidance control starts. In order to prevent the collision regardless of the scenarios, the proposed control scheme first cancels part of the dynamics of (4.3) that is related to the upcoming collisions and then compensates the angular acceleration $\ddot{\mathbf{q}}$ such that the forthcoming collisions can be avoided smoothly.

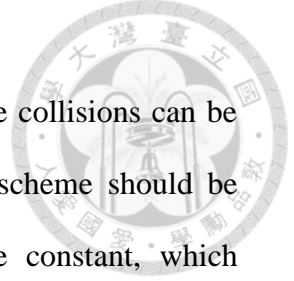


The control policy here is that the collision avoidance is in the highest priority, so the original control law has no effect on the subspace that concerns the collision whenever the risk function is nonzero, and that the avoiding motion should be smooth instead of stopping abruptly for better user interaction experience. Therefore, on the subspace related to the collisions, we control the dynamics behavior of the system in the risk space such that the dynamics of collision avoidance is independent of the configuration and the types of collisions, whereas (4.3) is maintained on the complement space to continue the original task. To control risk dynamics, we define the *control-Lyapunov function* so that the risks can be persistently minimized in a consistent manner. As for the stability, if (4.3) converges to a bounded set asymptotically and the environment is stationary, the overall control law is proved to be asymptotically stable. Since the control-Lyapunov function forces the system to converge to a positively invariant set in the joint space, the system converges to projection of the original equilibrium of (4.3) in that positively invariant set asymptotically.

This section is organized as follows. In Section 4.3.1, we define the risk function as the normalized measure of the closeness to the potential risks, and emphasizes why the consistent dynamics in the risk space is important in Section 4.3.2. Section 4.3.3 shows the proposed control law for the consistent collision prevention based on the control-Lyapunov function. Finally, we give the proof the stability of the system in Section 4.3.4, discuss some issues in implementation in Section 4.3.5 and Section 4.3.6.

4.3.1 The Risk Space

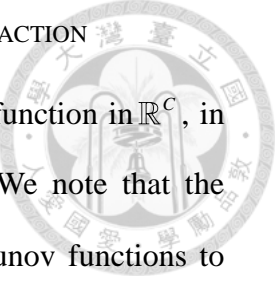
The concept of risk function is to define a normalized distance representing the



degrees of the forthcoming collisions, so that different types of the collisions can be unified. If the risk function is nonzero, the collision avoidance scheme should be activated so that the risk function is bounded above by some constant, which represents the physical collision of the robot and the obstacles. With the defined risk function, the risk space describes the dynamics of the risk function during the whole operation of the robot. Therefore, the success of the collision avoidance can be easily analyzed by just looking into the dynamics in the risk space, the *risk dynamics*.

In our scenario of the human-robot safety, the possible collisions can be categorized into: the self-collision of the robot, and the collision between the robot and the environment. By the environment, we mean both the static surroundings and the human nearby that may possibly move. The self-collision occurs due to the geometry interference of the robot and can be further classified by considering the topology of the collision pairs. If the two links are adjacent as described in the previous section, the collision can be avoided just by setting proper joint limits. On the other hand, the collision of the non-adjacent links and the collisions between the robot and the environment are the body-to-body collision problem in the Cartesian space, and therefore the distance between the collision pairs in the Cartesian space is used to detect the collision. Therefore, the risk function should serve as the normalized measure for both the Cartesian space and the joint space.

In the following we define the risk space and the risk function for the human-robot safety. If the links that defines the robot and the environment is finite, the possible collisions define a finite set $\mathcal{C} = \{\mathcal{P}(i, j) | i, j \in \mathbb{N}_L\} = \mathcal{C}_c \cup \mathcal{C}_J$, where \mathcal{C}_c is the set of collision pairs defined in the Cartesian space, \mathcal{C}_J is the set of joint limit collisions, and L is the number of all the links. Let $C = |\mathcal{C}| < \infty$. Given finite pairs of



collisions, the *risk space* is defined as the convex cone of the risk function in \mathbb{R}^C , in which the risk function is a diffeomorphism of the joint space. We note that the requirement of differentiability is necessary to define proper Lyapunov functions to govern the dynamics in the risk space. Since the risk inherits the switching nature, i.e. the collision avoidance starts only when the risk function is nonzero, additional smoothness must be applied on the risk function, so that the velocity and the acceleration of the risk function is well defined.

To fulfill the requirement, we propose to use the risk function

$$\mathbf{r}_+ = p_\beta(\mathbf{r}(\mathbf{q})), \quad (4.4)$$

where

$$p_\beta(x) = \begin{cases} (\beta x)^3, & x \geq 0 \\ 0, & \text{otherwise} \end{cases} \quad (4.5)$$

is defined for each entry of the vector $\mathbf{r}(\mathbf{q})$, $\beta > 0$ is the scaling factor to control the norm of the derivative of (4.5), and for the *i*th collision pair $\mathcal{P}_i, i \in C$, the *i*th entry $\mathbf{r}_i(\mathbf{q})$ of $\mathbf{r}(\mathbf{q}): \mathbb{R}^N \rightarrow \mathbb{R}^C$ is defined as,

$$\mathbf{r}_i(\mathbf{q}) = \begin{cases} \frac{\bar{d}_{C,i} + r_{i,1} + r_{j,2} - d_{C,i}(\mathbf{q})}{\bar{d}_{C,i}}, & \mathcal{P}_i \in \mathcal{C}_C \\ \frac{\bar{d}_{J,i} - d_{J,i}(\mathbf{q})}{\bar{d}_{J,i}}, & \mathcal{P}_i \in \mathcal{C}_J \end{cases} \quad (4.6)$$

$\bar{d}_{C,i}, \bar{d}_{J,i}$ is the size of the buffer zone, $r_{i,1}$ and $r_{j,2}$ are the thickness of the two convex bodies in \mathcal{P}_i for the Cartesian collision, $d_i(\mathbf{q})$ is the shortest distance between the pair in \mathcal{P}_i in the Cartesian space, $d_{J,i}(\mathbf{q})$ is the distance to the joint limit defined in the joint space. The constant $\bar{d}_{C,i}$ and $\bar{d}_{J,i}$ are chosen manually to ensure the robustness of the



collision while not limiting too much workspace manually. Also, we note that the joint limit may be two-sided. In this case, we duplicate the pair of links in \mathcal{C} so that $d_{J,i}(\mathbf{q})$ in (4.6) is well defined.

From the definition of (4.4), the vector function \mathbf{r}_+ is twice continuously differentiable with respect the angular position \mathbf{q} , and therefore the velocity $\dot{\mathbf{r}}_+$ and the acceleration $\ddot{\mathbf{r}}_+$ exist and can be computed as

$$\dot{\mathbf{r}}_+ = 3\beta^3 \mathbf{r} \circ \mathbf{r} \circ \dot{\mathbf{r}}, \quad (4.7)$$

and

$$\ddot{\mathbf{r}}_+ = 3\beta^3 (2\mathbf{r} \circ \dot{\mathbf{r}} \circ \dot{\mathbf{r}} + \mathbf{r} \circ \mathbf{r} \circ \ddot{\mathbf{r}}), \quad (4.8)$$

where

$$\dot{\mathbf{r}} = \mathbf{J}\dot{\mathbf{q}} \quad (4.9)$$

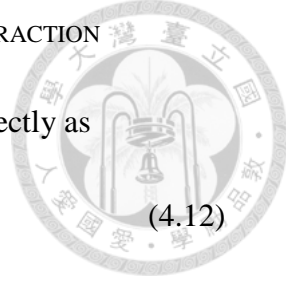
and

$$\ddot{\mathbf{r}} = \mathbf{J}\dot{\mathbf{q}} + \mathbf{J}\ddot{\mathbf{q}} \quad (4.10)$$

$\mathbf{J} = \frac{\partial}{\partial \mathbf{q}} \mathbf{r}(\mathbf{q}) \in \mathbb{R}^{C \times N}$ is the Jacobian matrix, and \circ denotes the Hadamard product. The Jacobian matrix defines the differentiation between the joint space and the task function and can be computed as follows. By the definition of (4.6), the i th row \mathbf{J}_i of the Jacobian matrix \mathbf{J} is

$$-\hat{\mathbf{d}}_i^T (\mathbf{j}_2 - \mathbf{j}_1) \quad (4.11)$$

if $\mathcal{P}_i \in \mathcal{C}_c$, where $\hat{\mathbf{d}}_i = \frac{\mathbf{x}_2 - \mathbf{x}_1}{\|\mathbf{x}_2 - \mathbf{x}_1\|}$, $\mathbf{x}_1, \mathbf{x}_2 \in \mathbb{R}^3$ are the two vertices of the line segment of the shortest distance in \mathcal{P}_i , $\mathbf{j}_1, \mathbf{j}_2 \in \mathbb{R}^{3 \times N}$ are Jacobian matrix of the linear velocity of



points \mathbf{x}_1 and \mathbf{x}_2 , respectively; else if $\mathcal{P}_i \in \mathcal{C}_J$, \mathbf{J}_i can be computed directly as

$$-\bar{d}_{J,i}^{-1} \frac{d}{d\mathbf{q}} d_{J,i}(\mathbf{q}), \quad (4.12)$$

which concerns only the sign of the definition of $d_{J,i}(\mathbf{q})$. As a consequence, the i th row of $\dot{\mathbf{J}}$ can be computed as

$$-\frac{((\mathbf{j}_2 - \mathbf{j}_1)\dot{\mathbf{q}})^T}{\|\mathbf{d}\|} (\mathbf{I} - \hat{\mathbf{d}}\hat{\mathbf{d}}^T)(\mathbf{j}_2 - \mathbf{j}_1) - \hat{\mathbf{d}}_i^T \frac{d}{dt}(\mathbf{j}_2 - \mathbf{j}_1) \quad (4.13)$$

if $\mathcal{P}_i \in \mathcal{C}_J$; otherwise, it is a zero vector.

In summary, the collision occurs when $\mathbf{r}_i(\mathbf{q}) = 1$, the potential collision is omitted when $\mathbf{r}_i(\mathbf{q}) < 0$, and the collision avoidance control is activated in between. Also, due to the chosen risk function (4.4), which is twice differentiable, the second-order dynamics in the risk space can be properly defined. Therefore, the virtual impedance control scheme proposed in Section 4.3.3 can prevent the collision smoothly by controlling the dynamics in the risk space.

4.3.2 Consistency of the Collision Dynamics

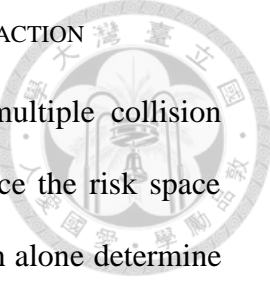
To robustly prevent the collision, it is important to ensure that the collision dynamics is independent of the configuration of the robot. In [54], the impedance of the end effector in the Cartesian space is controlled as a unit mass system, so that the end effector can consistently avoid the obstacles regardless of the configuration of the robot. However, it is well known that the impedance control in the Cartesian space of a robot can be in general only defined on a single point, due to the limited degrees of freedom. Therefore, the existence of the consistent dynamics when multiple collision points are present is a question.

To enforce the consistent impedance, one may choose to design a consistent



collision dynamics on a single point and an alternative scheme to transfer the repulsive forces of the other collision points to that point. For example, when multiple potential collision points are presented [54], the forces originally exerted on different points are transferred to the endeffector, whose dynamics is consistently a unit mass model, so that the collision dynamics is consistent at least in terms of the endeffector. This approach, however, cannot guarantee the success of the avoidance of the whole body but the endeffector. Another intuitive solution is continuously switching between the collision points. Since only one point is selected as a time, the collision dynamics can be consistent at least in the short interval of the current selection. Due to the switching, the chattering may occur, and also the system can be only proved to be bounded not asymptotically stable by considering the behavior when multiple collision points with similar risks are presented. If other uncertainties are present such as the discretization of the control and the detection, the stability of the switching scheme is in doubt.

On the other extremity, the consistency requirement may be dropped to avoid multiple obstacles stably. In [20], they do not consider the consistency of the collision dynamics and let the forces of the repulsive potentials exert on the robot via the Jacobian matrix. Since the original system is passive and the transmitted torques is the negative gradient of the potential, the overall system converges asymptotically to the point where all the transmitted torques balance the torque of the original system. However, this equilibrium point is not guaranteed to be collision-free. Also, the collision dynamics depends largely on the configuration of the robot, since there is no compensation of the original dynamics and the kinematics. Therefore, this scheme cannot robustly avoid the collision in general tasks.

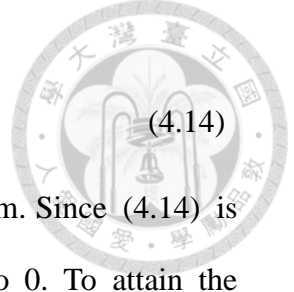


By defining the risk space, the contradiction between the multiple collision points and the consistent collision dynamics can be addressed. Since the risk space unifies all the possible collisions, the dynamics in the risk space can alone determine the success of the collision avoidance. Also, for the consistency, we maintain the dynamics in the risk space instead of either the Cartesian space or the joint space so that the dynamic behavior of the collision avoidance is consistent regardless of the number of the collision points. In summary, the introduction of the risk space solves the dilemma between the consistency and the number of the collision points. Because the risk function is twicely differentiable, the dynamics behavior in the risk space can be properly controlled just as the impedance control of a single point so that the overall system can be both consistent and stable.

4.3.3 Control of the Dynamics in the Risk Space

Continuously detecting the possible collisions, the collision avoidance control is turned on when the risk function is nonzero to maintain the risk function below certain upper bound in the risk space. For better human perception, we desire the motion of the collision avoidance to be smooth. Therefore, we propose the virtual impedance control in the risk space by designing the control-Lyapunov function. To ensure the collision can be avoided robustly regardless of the configuration of the robot, we put the collision avoidance control in the first priority. That is, the original dynamics (4.3) only operates on the subspace that is independent of the collision, when the collision avoidance control starts. Therefore, the robot can continue performing the original task, if the subspace related to the collision is small.

To control the dynamics of the risk space, we first consider the following control-Lyapunov function,



$$V_R(\mathbf{q}, \dot{\mathbf{q}}) = \frac{\sigma}{2} \mathbf{r}_+^T \mathbf{r}_+ + \frac{1}{2} \dot{\mathbf{r}}_+^T \dot{\mathbf{r}}_+, \quad (4.14)$$

where $\sigma > 0$ is the parameter controlling the bandwidth of the system. Since (4.14) is positive definite, all the risk reaches zero if (4.14) converges to 0. To attain the objective, we can design a control law to ensure the time derivative of (4.14) to be negative semidefinite. The time derivative \dot{V}_R of (4.14) can be shown as

$$\begin{aligned} \dot{V}_R &= \sigma \mathbf{r}_+^T \dot{\mathbf{r}}_+ + \dot{\mathbf{r}}_+^T \ddot{\mathbf{r}}_+ \\ &= \sigma \mathbf{r}_+^T \dot{\mathbf{r}}_+ + \dot{\mathbf{r}}_+^T 3\beta^3 (2\mathbf{r} \circ \dot{\mathbf{r}} \circ \dot{\mathbf{r}} + \mathbf{r} \circ \mathbf{r} \circ (\mathbf{J}\dot{\mathbf{q}} + \mathbf{J}\ddot{\mathbf{q}})) \\ &= \dot{\mathbf{r}}_+^T \mathbf{S}^T \mathbf{S} (\sigma \mathbf{r}_+ + \mathbf{a} + \mathbf{A}(\mathbf{J}\dot{\mathbf{q}} + \mathbf{J}\ddot{\mathbf{q}})) \end{aligned} \quad (4.15)$$

where $\mathbf{S} \in \mathbb{R}^{\bar{C} \times C}$ is the selection matrix of the active risks, i.e. $\mathbf{S}_{ij} = \delta_{ij}$, and δ_{ij} is the Kronecker delta function, $\bar{C} \leq C$ is the number of the active risks $\mathbf{r}_i(\mathbf{q}) > 0$, $\mathbf{A} = 3\beta^3 \text{diag}(\mathbf{r} \circ \mathbf{r})$, and $\mathbf{a} = 6\beta^3 (\mathbf{r} \circ \dot{\mathbf{r}} \circ \dot{\mathbf{r}})$. To make the time derivative negative semidefinite, we may choose $\ddot{\mathbf{q}}$ such that

$$\bar{\mathbf{J}}\ddot{\mathbf{q}} \rightarrow -\mathbf{S}(\sigma \mathbf{r}_+ + \mathbf{a} + \mathbf{A}\dot{\mathbf{J}}\dot{\mathbf{q}}) - \mu \bar{\mathbf{J}}\dot{\mathbf{q}}, \quad (4.16)$$

where $\bar{\mathbf{J}} = \mathbf{S} \mathbf{A} \mathbf{J} \in \mathbb{R}^{\bar{C} \times N}$ is the active Jacobian matrix and $\mu > 0$ is the damping. If (4.16) is achieved, $\dot{V}_L = -\mu \|\dot{\mathbf{r}}_+\|^2$, then $\|\dot{\mathbf{r}}_+\|$ can converge to zero asymptotically with the consistent dynamics, i.e.

$$\ddot{\mathbf{r}}_+ = -\mathbf{S}^T \mathbf{S} (\sigma \mathbf{r}_+ + \mu \dot{\mathbf{r}}_+), \quad (4.17)$$

which is independent of the configuration of the robot. However, (4.16) does not hold in general, so this intuitive approach may fail. As the problem of controlling the impedance of multiple points in the Cartesian space, (4.16) may fail due to the limited degrees of freedom. Especially, $\text{rank}(\bar{\mathbf{J}}) < \bar{C}$ may occur even if $\bar{C} < N$.

To approximate the solution, we may use the pseudo-inverse, so the control



scheme is to design a controller in (4.3) such that

$$\ddot{\mathbf{q}} = \mathbf{N}\ddot{\mathbf{q}}_0 + \mathbf{P}(\ddot{\mathbf{q}}_c - \mu\dot{\mathbf{q}}) \quad (4.18)$$

where $\ddot{\mathbf{q}}_0 = -\mathbf{M}^{-1}\mathbf{F}(\mathbf{q}, \dot{\mathbf{q}}, \ddot{\mathbf{q}})$ is the resultant joint acceleration of the original system

(4.3),

$$\ddot{\mathbf{q}}_c = -\mathbf{V}\Sigma^{-1}\mathbf{U}^T\mathbf{S}(\sigma\mathbf{r}_+ + \mathbf{a} + \mathbf{A}\dot{\mathbf{q}}), \quad (4.19)$$

is the joint acceleration used to compensate the dynamics of the risk space,

$\mathbf{P} := \mathbf{M}^{-1}\bar{\mathbf{J}}^T(\bar{\mathbf{J}}\mathbf{M}^{-1}\bar{\mathbf{J}}^T)^{-1}\bar{\mathbf{J}}$ and $\mathbf{N} := \mathbf{I} - \mathbf{P}$ are the projection matrices in the space with the

inner product defined by \mathbf{M}^{-1} , $\bar{\mathbf{J}} = \mathbf{U}\Sigma\mathbf{V}^T$ is the reduced SVD of the Jacobian matrix

with $\mathbf{U} \in \mathbb{R}^{\bar{C} \times \rho}$ and $\mathbf{V} \in \mathbb{R}^{N \times \rho}$ the basis of the non-zero singular values $\Sigma \in \mathbb{R}^{\rho \times \rho}$,

and ρ is the rank of $\bar{\mathbf{J}}$. Here we assume the joint acceleration is controllable in the

original dynamics system (4.3), so that (4.18) is realizable by designing proper control

input in (4.18). The first term in (4.18) $\mathbf{N}\ddot{\mathbf{q}}_0$ projects the original dynamics into the

null space of the active Jacobian matrix $\bar{\mathbf{J}}$, so the original dynamics have no effect on

the risk dynamics once the collision avoidance starts; the second

term $\mathbf{P}(\ddot{\mathbf{q}}_c - \mu\dot{\mathbf{q}})$ controls the risk dynamics so that it is consistent in controllable

subspace, which is the column space of the active Jacobian matrix $\bar{\mathbf{J}}$. That is, in the

column space of $\bar{\mathbf{J}}$, the risk acceleration (4.8) is consistently

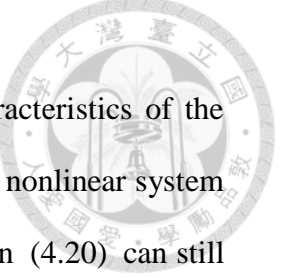
$$\mathbf{S}^T\mathbf{U}\mathbf{U}^T\mathbf{S}\ddot{\mathbf{r}}_+ = -\mathbf{S}^T\mathbf{U}\mathbf{U}^T\mathbf{S}(\sigma\mathbf{r}_+ + \mu\dot{\mathbf{r}}_+). \quad (4.20)$$

Therefore, in the controllable subspace in the risk space, the dynamics of the risk

function \mathbf{r}_+ actually follows a second-order spring-damping system regardless of the

number of the active collision \bar{C} , and the configuration of the robot, where the

stiffness σ and the damping μ can be designed to realize specific bandwidth and



damping ratio. Before analyzing the stability and the detailed characteristics of the closed loop system, we note that although (4.20) actually realizes a nonlinear system in terms of \mathbf{r} due to the nonlinear mapping (4.5), the damping ratio in (4.20) can still prevent the undesirable effects such as overshooting of \mathbf{r} .

4.3.4 Stability

In this section, we first show that the proposed control scheme (4.18) is asymptotically stable if the environment is static and the original dynamics (4.3) is asymptotically stable, and then discuss the properties of the closed-loop system. We neglect the discussion of the dynamic environment. Since the overall system is continuously differentiable, the system can be easily proved to be input-to-state stable provided with the stability with the static environment.

Assuming the environment is static and the original dynamics (4.3) is asymptotically stable converging to the set $\{\dot{\mathbf{q}} \mid \|\dot{\mathbf{q}}\| = 0\}$ and \mathbf{M} is known and positive definite, we first consider the behavior of the risk dynamics. Substituting (4.18) into the time derivative (4.15), we have

$$\dot{V}_R = -\mu \|\dot{\mathbf{r}}_+\|^2 \leq 0. \quad (4.21)$$

Since $\dot{\mathbf{r}}_+ = \mathbf{S}^T \bar{\mathbf{J}} \dot{\mathbf{q}}$, the system converges to the positively invariant set

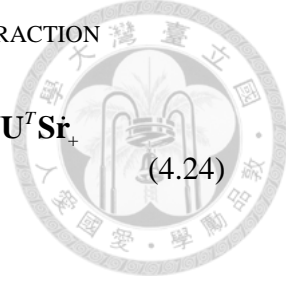
$$\mathcal{A} = \{(\mathbf{q}, \dot{\mathbf{q}}, \ddot{\mathbf{q}}) \mid \|\bar{\mathbf{J}} \dot{\mathbf{q}}\| = 0\}, \quad (4.22)$$

which implies either $\|\bar{\mathbf{J}}\| = 0$, i.e. $\|\mathbf{A}\| = 0$, leading to all the risks are successfully avoided, or $\|\mathbf{V}^T \dot{\mathbf{q}}\| = 0$. In addition, since $\|\bar{\mathbf{J}} \dot{\mathbf{q}}\| = 0$ in \mathcal{A} , the acceleration

$$\mathbf{S}^T \mathbf{U} \mathbf{U}^T \mathbf{S} \ddot{\mathbf{r}}_+ = \mathbf{S}^T \mathbf{U} \mathbf{U}^T \mathbf{S} (\sigma \mathbf{r}_+) = \mathbf{0} \quad (4.23)$$

from (4.20), which implies the control-Lyapunov function in \mathcal{A} is

$$\begin{aligned}
V_R &= \frac{\sigma}{2} \mathbf{r}_+^T \mathbf{S}^T (\mathbf{I} - \mathbf{U} \mathbf{U}^T) \mathbf{S} \mathbf{r}_+ + \frac{\sigma}{2} \mathbf{r}_+^T \mathbf{S}^T \mathbf{U} \mathbf{U}^T \mathbf{S} \mathbf{r}_+ + \frac{1}{2} \dot{\mathbf{r}}_+^T \mathbf{S}^T \mathbf{U} \mathbf{U}^T \mathbf{S} \dot{\mathbf{r}}_+ \\
&= \frac{\sigma}{2} \mathbf{r}_+^T \mathbf{S}^T (\mathbf{I} - \mathbf{U} \mathbf{U}^T) \mathbf{S} \mathbf{r}_+
\end{aligned} \tag{4.24}$$



i.e. the uncontrollable potential energy, which is constant since $\dot{V}_R = 0$ in \mathcal{A} . Thus, in

\mathcal{A} , $\|\bar{\mathbf{J}}\dot{\mathbf{q}}\| = 0 \rightarrow \|\mathbf{P}\dot{\mathbf{q}}\| = 0$. On the other hand, we consider the original dynamics in the null space \mathbf{N} starting from \mathcal{A} . Since the original dynamics is asymptotically stable, the null space joint velocity,

$$\lim_{t \rightarrow \infty} \|\mathbf{N}\dot{\mathbf{q}}\| \rightarrow 0. \tag{4.25}$$

From (4.22) and (4.25), we have both $\|\mathbf{P}\dot{\mathbf{q}}\| = 0$ and $\|\mathbf{N}\dot{\mathbf{q}}\| = 0$, and therefore $\|\dot{\mathbf{q}}\| = 0$ and therefore $\|\ddot{\mathbf{q}}\| = 0$ as time goes to infinity. Thus, the closed-loop system is asymptotically stable.

At the equilibrium point, the risk function is either zero, or the energy of the risks converges to a constant that cannot be further reduced due to the configuration of the collision. The irreducible risk in (4.24) is due to the configuration of the environment. For example, if the robot is in a fully cluttered environment, in which there is no configuration of the robot with zero risks, the irreducible risk exists. Otherwise, the proposed control scheme leads to the asymptotical equilibrium point, where all the risks, the joint velocity, and the joint acceleration are zero. We summarize the results as follows.

Theorem 4.1

The Virtual Impedance Control

$$\ddot{\mathbf{q}} = \mathbf{N}\ddot{\mathbf{q}}_0 + \mathbf{P}(\ddot{\mathbf{q}}_c - \mu\dot{\mathbf{q}}) \tag{4.26}$$

with $\mathbf{P} = \mathbf{M}^{-1} \bar{\mathbf{J}}^T (\bar{\mathbf{J}} \mathbf{M}^{-1} \bar{\mathbf{J}}^T)^{-1} \bar{\mathbf{J}}$ and $\mathbf{N} = \mathbf{I} - \mathbf{P}$ converges asymptotically to the set



$$\{(\mathbf{q}, \dot{\mathbf{q}}, \ddot{\mathbf{q}}) \mid \|\dot{\mathbf{q}}\| = 0, \|\mathbf{U}\mathbf{S}\mathbf{r}_+\| = 0\}, \quad (4.27)$$

if the original dynamics of the robot converges asymptotically to the set

$$\{(\mathbf{q}, \dot{\mathbf{q}}, \ddot{\mathbf{q}}) \mid \|\mathbf{N}\dot{\mathbf{q}}\| = 0\} \quad (4.28)$$

regardless of the projection matrix \mathbf{N} .

4.3.5 Some Practical Issues

We now consider some imperfection that may happen in practice, due to the discrete control and the finite computational power. Although the Jacobian matrix \mathbf{J} is defined as $\mathbf{J} = \frac{\partial}{\partial \mathbf{q}} \mathbf{r}(\mathbf{q})$ in (4.10), there is, however, actually another implicit parameter ρ that determines the possible collision point in the joint space. Therefore, the Jacobian matrix should ideally be defined as

$$\mathbf{J} = \frac{\partial}{\partial \mathbf{q}} \mathbf{r}(\mathbf{q}) + \frac{\partial}{\partial \rho} \mathbf{r}(\mathbf{q}) \frac{\partial \rho}{\partial \mathbf{q}}. \quad (4.29)$$

Because the variation $\frac{\partial \rho}{\partial \mathbf{q}}$ is hard or costly to be computed, we implement (4.10)

instead of (4.29). We note that the same assumption is made to compute $\dot{\mathbf{J}}$ in (4.13).

Since $\left\| \frac{\partial}{\partial \rho} \mathbf{r}(\mathbf{q}) \frac{\partial \rho}{\partial \mathbf{q}} \right\|$ is upper bounded by the factor due the geometry of the robot and

the sampling time, we can expect that the system can still be asymptotically stable by selecting μ large enough. Therefore, the bandwidth of the risk dynamics is limited.

As for the collision detection, the self-collision detection is much faster than the detection of the collision between the human and the robot by KinectTM, which is limited by the sampling rate of the visual sensing. Therefore, the human is assumed to be a static object between the updates of the visual sensing. Also, the second-order virtual impedance system in (4.20) actually filters the noise of the visual sensing since it acts as a lowpass filter in the risk space. Therefore, the overall system can be more



stable.

4.3.6 The Design of the Boundary Layer

Apart from the issues mentioned above, the chattering may occur, since the controller in (4.18) actually switches as the dimension of the projection matrix changes. For example, on the boundary where the risk function is activated, the magnitude of the chattering is large if the force of the original dynamics tends to push the system deeply into the region where the risk function is high. Although the risk function converges exponentially to the boundary once activated, the risk function will be largely increased once it reaches the boundary due to the control delay. To eliminate the chattering, we design a boundary layer on the spectrum of the weighted Jacobian matrix $\bar{\mathbf{J}}\mathbf{M}^{-1/2}$. Since the singular value and the right singular vector of $\bar{\mathbf{J}} = \mathbf{S}\mathbf{A}\mathbf{J}$ and $\mathbf{A}\mathbf{J}$, which is a continuously differentiable function, are the same, we can define the boundary layer by introducing the function

$$\phi(\tilde{\sigma}_i) = \begin{cases} 1, & \varepsilon \leq \tilde{\sigma}_i \\ g(\tilde{\sigma}_i), & 0 \leq \tilde{\sigma}_i < \varepsilon \end{cases} \quad (4.30)$$

on the spectrum of $\bar{\mathbf{J}}\mathbf{M}^{-1/2}$, where $\tilde{\sigma}_i$ is the i th singular value of $\bar{\mathbf{J}}\mathbf{M}^{-1/2}$, ε is the thickness of the boundary layer, and $g(\cdot)$ is the third-order polynomial satisfying the boundary conditions that $g(0) = 0$, $g(1) = 1$, $\dot{g}(0) = 0$, and $\dot{g}(1) = 0$. With (4.30), we can substitute it in (4.18) by changing the definition of the projection matrix, leading to

$$\mathbf{P} := \mathbf{M}^{-1/2} [\tilde{\mathbf{V}} \Phi \tilde{\mathbf{V}}^T] \mathbf{M}^{1/2} \quad (4.31)$$

where $\bar{\mathbf{J}}\mathbf{M}^{-1/2} = \tilde{\mathbf{U}}\tilde{\Sigma}\tilde{\mathbf{V}}^T$ is the reduced singular decomposition and Φ is the diagonal matrix formed by (4.30). In particular, if the inertia matrix in (4.3) is of the form $\mathbf{M} = m\mathbf{I}$, which is the case when the original control loop is the joint space



impedance control for instance, (4.31) can be simplified into

$$\mathbf{P} := \mathbf{V}\Phi\mathbf{V}^T. \quad (4.32)$$

In summary, the risk function converges exponentially into the boundary layer, and once into the boundary the repulsive force will balance the force due to the original dynamics. Therefore, the trapping phenomenon in [97] and the chattering due to the control delay will not occur by selecting ε large enough. As for the convergence in the boundary layer, we believe it can be proved that the norm of the states can be bounded by some constant relative to the thickness of the boundary layer ε . We leave it in the future works.

4.3.7 The Selection of the Parameters

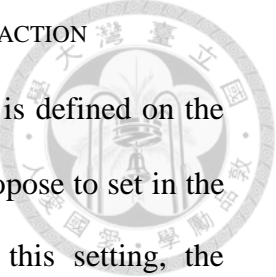
The tuning of the parameters is simple. Due to dynamics compensation in (4.19), the risk dynamics depends fully on the choice of the damping ratio ζ and the bandwidth ω_0 of (4.20), i.e.

$$\sigma = m\omega_0^2, \quad (4.33)$$

$$\mu = 2\zeta\sqrt{m\sigma}, \quad (4.34)$$

where m is mass of the virtual impedance system. The choice of these parameters can follow the behavior of the canonical second-order linear dynamics. For example, if the no overshooting is allowed when leaving the potential field, ζ can be critically damped; m can be used to tune the magnitude of the initial response.

In the implementation, we design the system with $m = 1$ and $\zeta = 1$, and choose the bandwidth empirically such that it is large enough to prevent the collision fast but small enough to stabilize the system due to the imperfections mentioned above. The other parameters are β to define the risk function and ε the thickness of the boundary



layer. The optimal choice of ε is actually a function of β , because ε is defined on the spectrum of $\bar{\mathbf{J}} = \mathbf{SAJ}$ and recall $\mathbf{A} = 3\beta^3 \text{diag}(\mathbf{r} \circ \mathbf{r})$. Therefore, we propose to set in the parametric form $\varepsilon = \bar{\varepsilon}\beta^3$, where $\bar{\varepsilon}$ is a constant to be tuned. In this setting, the normalized thickness $\bar{\varepsilon}$ is more easily tuned. As for the scaling parameter β , it should be as small as possible yet large enough for preventing numerical errors in computing β^3 and $\bar{\varepsilon}$. The reasons for choosing β to be small are as follows. The compensating term $\mathbf{a} = 6\beta^3(\mathbf{r} \circ \dot{\mathbf{r}} \circ \ddot{\mathbf{r}})$ involves the quadratic term of the normalized risk velocity, which may be large when the robot enter the boundary with high velocity. To limit the require joint acceleration to cancel the fictitious Coriolis acceleration \mathbf{a} due to the definition of the risk function, β should be chosen to be small. Also, the choice of β does not actually affect the dynamics of \mathbf{r} . From(4.17), we have

$$\ddot{\mathbf{r}} = -\mathbf{S}^T \mathbf{S} \left(\frac{\sigma}{3} \mathbf{r} + \mu \dot{\mathbf{r}} + \mathbf{A}^{-1} \mathbf{a} \right), \quad (4.35)$$

which is independent of the choice of β , since (4.5) is only used to define a proper dynamics system for the collision avoidance. Therefore, β can be arbitrarily small as long as it is numerically stable.

4.4 Experiments

In this section, we demonstrate three experiments to show the performance of the proposed control scheme with the 6-DOF NTU Robot Arm in Fig. 4-2. The 6-DOF NTU Robot Arm is a position-controlled manipulator, and we implement the original task of the robot in (4.3) as the position-based impedance controller.

In the first experiment, we test the consistency of the dynamics in the risk space regarding different configurations, and discuss the effect of the boundary layer. In the second experiment, we demonstrate the ability of the robot circumvents through the

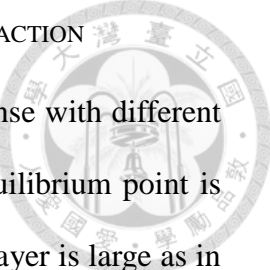


obstacle. Finally, the integrated system with the robot performing some predefined task and the KinectTM detecting the human nearby the robot is tested with the interaction with the human.

We first want to test the consistency of the obstacle avoidance. In Experiment 1, we initialize the robot in different poses with zero velocity and acceleration, such that the initial value of the risk functions are similar, 0.016432 and 0.016416 respectively, as shown in Fig. 4-3, and the original controller is the joint space impedance controller trying to stabilize the robot in the initial condition. Here we demonstrate the toy example in which only one risk function is activated in the Cartesian for better visualization to understand the characteristics of the proposed method. In this case, the proposed scheme is actually the Cartesian space impedance control in the one-dimensional space of the collision. First, we observe that the risk dynamics of the two cases are the same regardless of the pose of the robot in the region where $\phi(\tilde{\sigma})=1$, which is never the case, when the collision avoidance scheme transmitting the

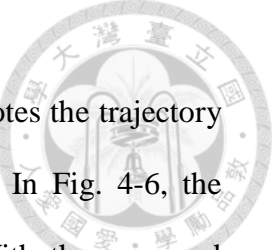


Fig. 4-2. 6-DOF NTU Robot Arm.



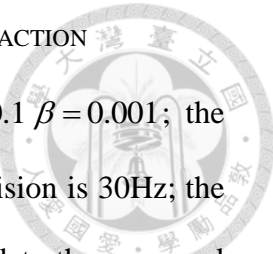
repulsive force by the Jacobian is used. Then we compare the response with different boundary layers. In Fig. 4-4, the size of the risk function at the equilibrium point is related to the size of the boundary. If the thickness of the boundary layer is large as in the first figure, the risk function converges to larger value. Also, we can observe that the dynamics of the risk space is consistent only outside the boundary, i.e. $\phi(\tilde{\sigma}_i) = 1$, so the overshoot may happen in the boundary layer despite the critically damped risk dynamics. In Fig. 4-5, we show the asymptotically behavior of the risk dynamics inside the boundary layer. If the boundary layer is large enough as the case $\varepsilon = 1e-2$ and $\varepsilon = 1e-4$, we observe that the chattering does not occur by the variation of $\phi(\tilde{\sigma})$. Also, the norm of $\dot{\mathbf{r}}_+$ is bounded by the constant related to the thickness of the boundary layer. As the boundary gets smaller, the variation of $\dot{\mathbf{r}}_+$ is smaller. However, the chattering occurs if the thickness is below some threshold as in the case of $\varepsilon = 1e-6$. The robot is oscillating on the boundary as it is pushed in and out by the force of the original dynamics and the repulsive force for the obstacle avoidance. In this case, the boundary layer is not large enough to overcome the imperfection due to the control delay.

In Experiment 2, we want verify that the propose scheme has small impact on the original dynamics in (4.3), since only the subspace related to the active risk function is projected into the null space. In Fig. 4-6, the obstacle avoidance of a ball in the Cartesian space with the proposed virtual impedance control is shown. The yellow ball is the obstacle and the transparent red ball is the potential field, where the risk function is active. We choose the size of the potential field to be larger than the needed one in practice for the demonstration purpose. The dark blue line denotes the trajectory of the endeffector if the original control scheme is applied; the light blue



line denotes direction related to the risk function; the green line denotes the trajectory of the endeffector when the virtual impedance control is applied. In Fig. 4-6, the original trajectory passes the obstacle, so the collision occurs. With the proposed control, the robot arm can smoothly pass by the obstacle by gliding along the surface of the potential field. As in the previous experiment, the virtual impedance control scheme becomes the Cartesian space impedance control operating in the subspace that relates to the increase of the risk function, since only single risk function is activated. In Fig. 4-7, we show the risk dynamics in Experiment 2. According to the figure, the collision avoidance control is activated two-times. As in Experiment 1, the dynamics outside the boundary layer is persistently controlled; in the boundary, the external force balances the repulsive force. Also, the impact on the original dynamics is minimized, since the virtual impedance controller only compensates the dynamics of the active risks. Finally, we implement the avoidance collision scheme that transmits the repulsive force by the Jacobian matrix as in [20] for comparison. The result is shown in Fig. 4-8. As expected, the configuration and the original dynamics of the robot affect the dynamics of the collision avoidance. Therefore, the risk cannot be bounded robustly, in contrast to our approach as shown in Fig. 4-9.

For multiple activated risks, we conduct the following experiment with the fully integrated system with KinectTM. In Fig. 4-10 the modeling of the human and the robot in the virtual impedance control is shown. With the SDK of KinectTM, the skeleton of the human can be identified in the depth image, which can be incorporated into our framework trivially. The light blue lines in the figures are the direction of the upcoming collisions, and the other sticks denote the robot and the human. With these directions, the Jacobian matrix $\bar{\mathbf{J}}$ can be computed as shown in Section 4.3. The



parameters of the risk dynamics is selected as. $\zeta = 1$ $\omega_0 = 15$ $\bar{\varepsilon} = 0.1$ $\beta = 0.001$; the control rate the collision avoidance is 1kHz; the sampling rate the vision is 30Hz; the transmission of the position trajectory via RS232 is 40Hz. To validate the proposed scheme, we perform the following experiment. The robot is operated with a joint space impedance control law performing some predefined movements repetitively, and the human nearby command the robot to behave well not the come closer. In Fig. 4-11 and Fig. 4-12 the snapshots of the experiment is shown. With the virtual impedance control, the follows the direction of the human, and does not come any closer to the safe zone indicated by the potential field. We can observe that the motion of the robot is smooth due to the controlled impedance. Therefore, the robot shows satisfactory and consistent performance regardless of the types of the collisions.

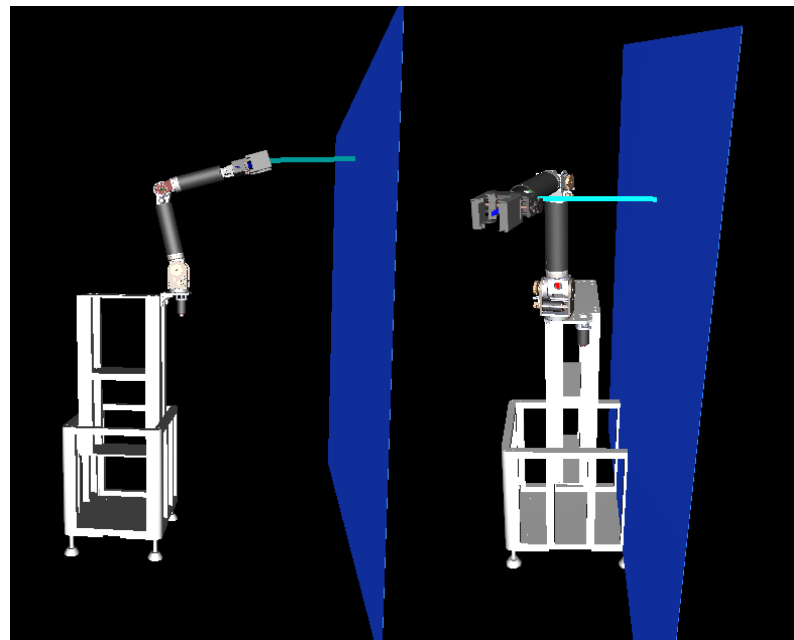


Fig. 4-3 The initial condition in Experiment 1.

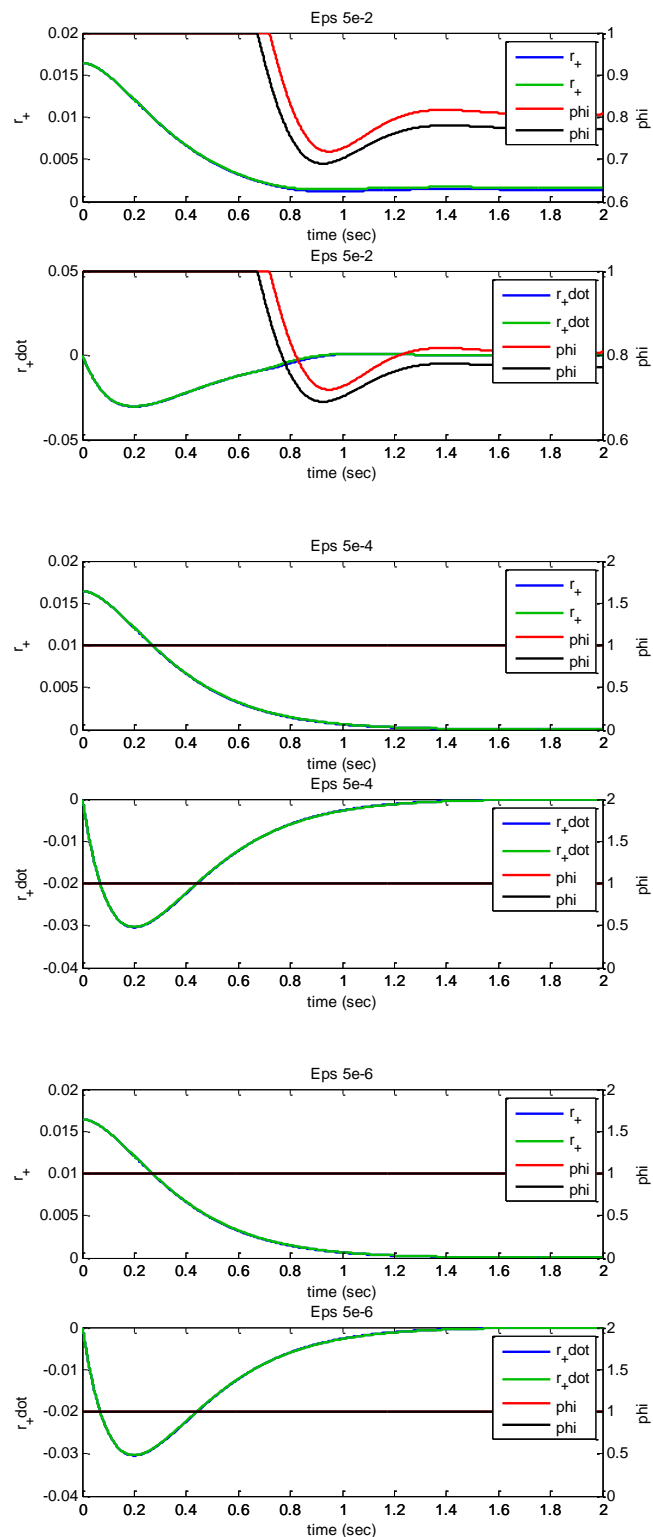


Fig. 4-4. The consistent risk space dynamics with the boundary layers of different sizes.

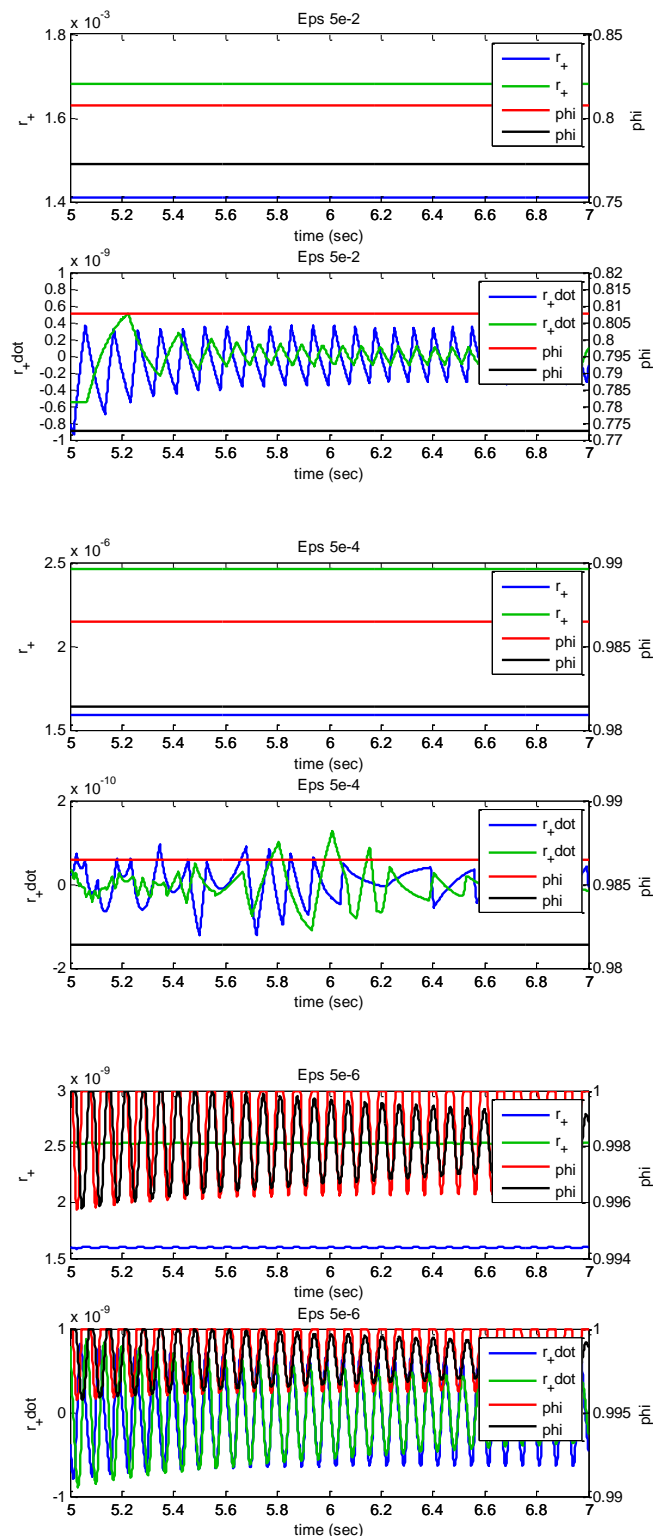
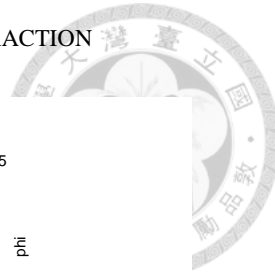


Fig. 4-5.The asymptotical analysis of the boundary layer.

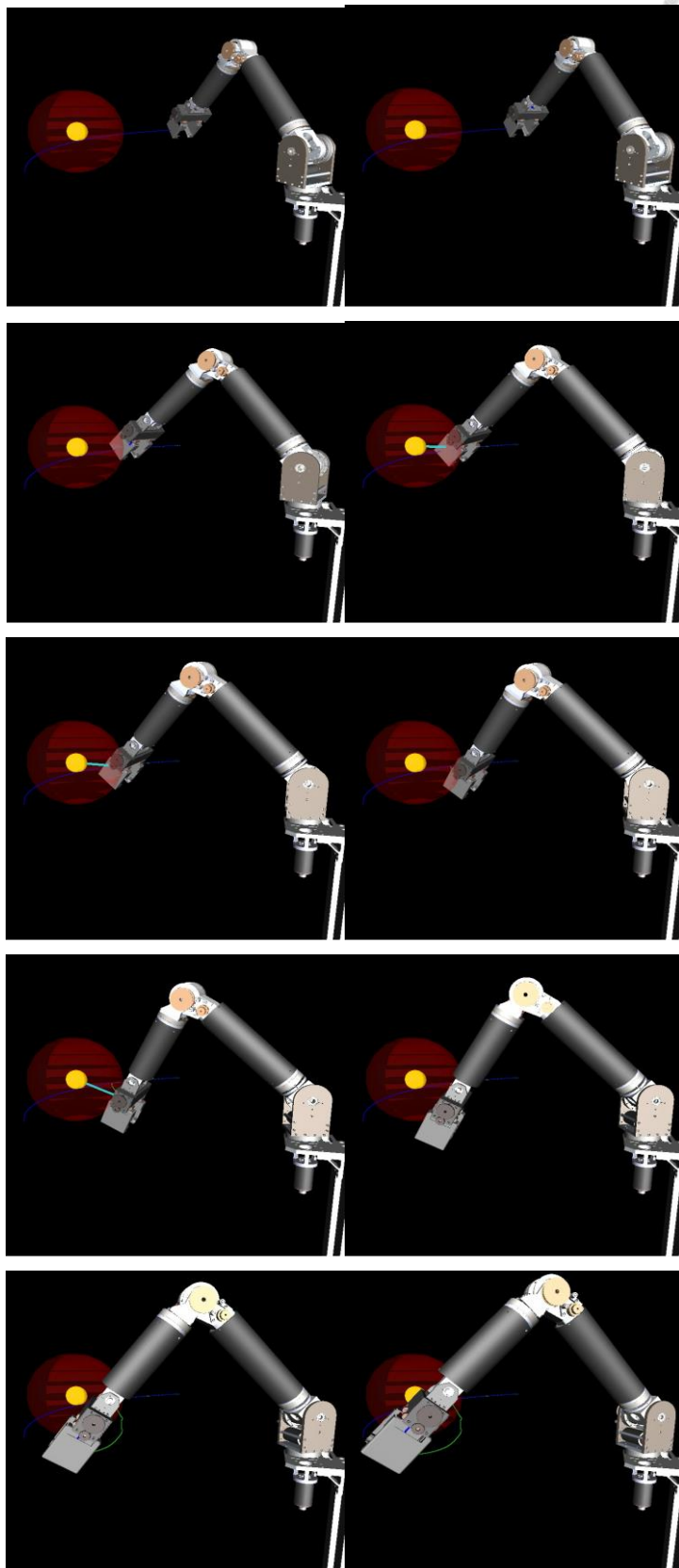


Fig. 4-6. Obstacle avoidance of a sphere with virtual impedance control.

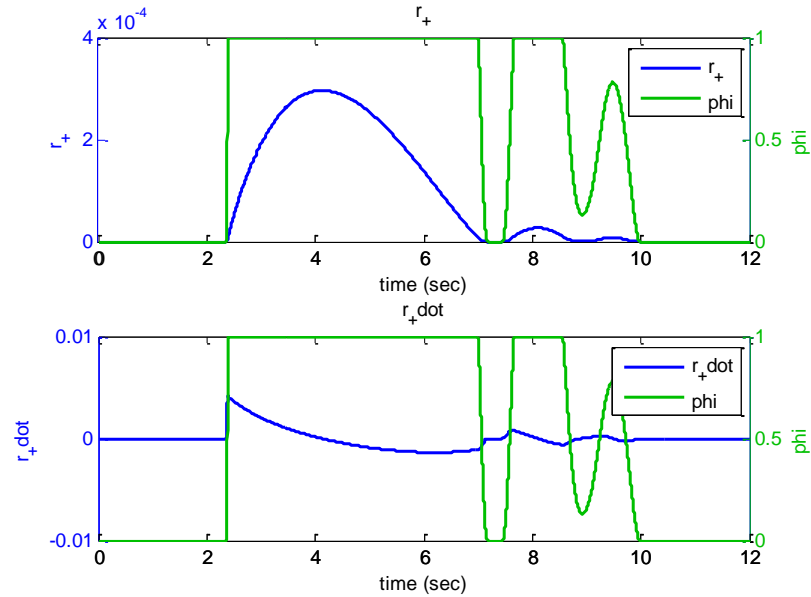


Fig. 4-7. The risk dynamics in Experiment 2.

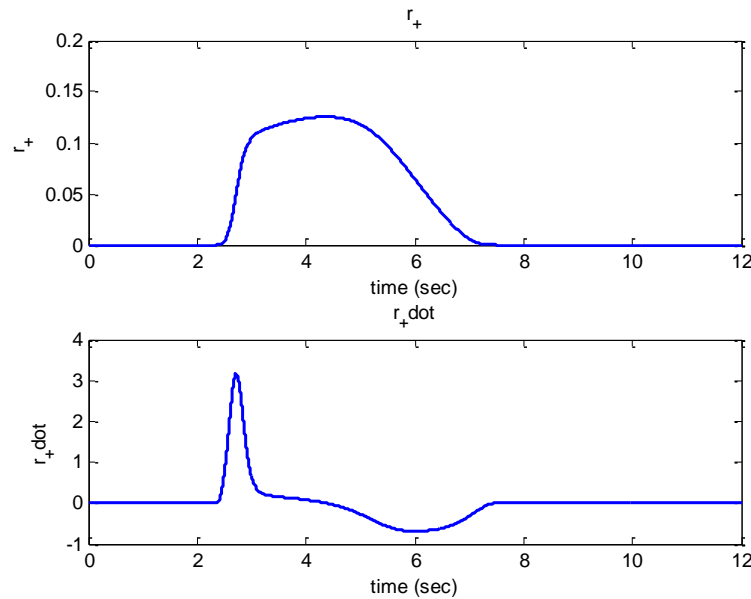
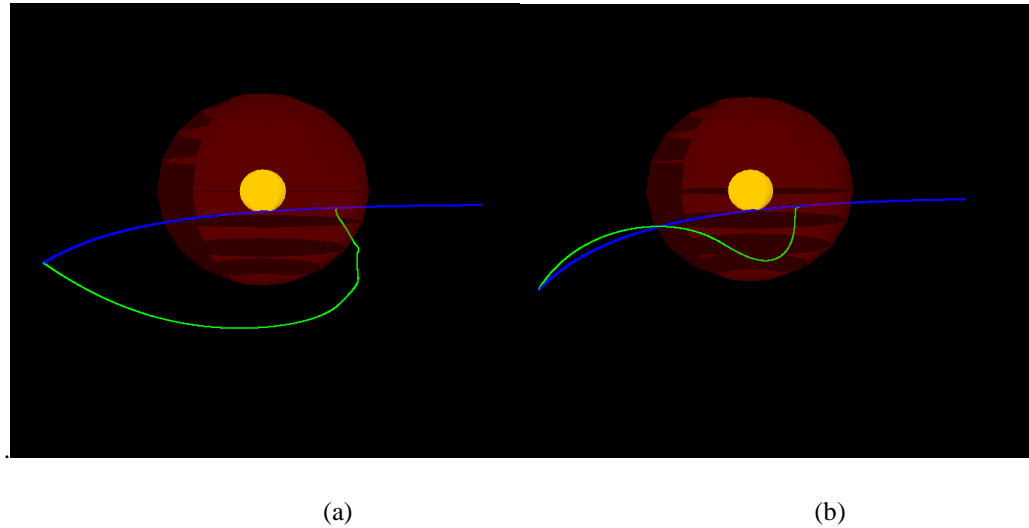


Fig. 4-8. The risk dynamics of the collision avoidance that do not compensate the dynamics in the risk space.



(a)

(b)

Fig. 4-9. The trajectory of the collision avoidance.

(a) the virtual impedance control (b) the force transmitted by the Jacobian matrix

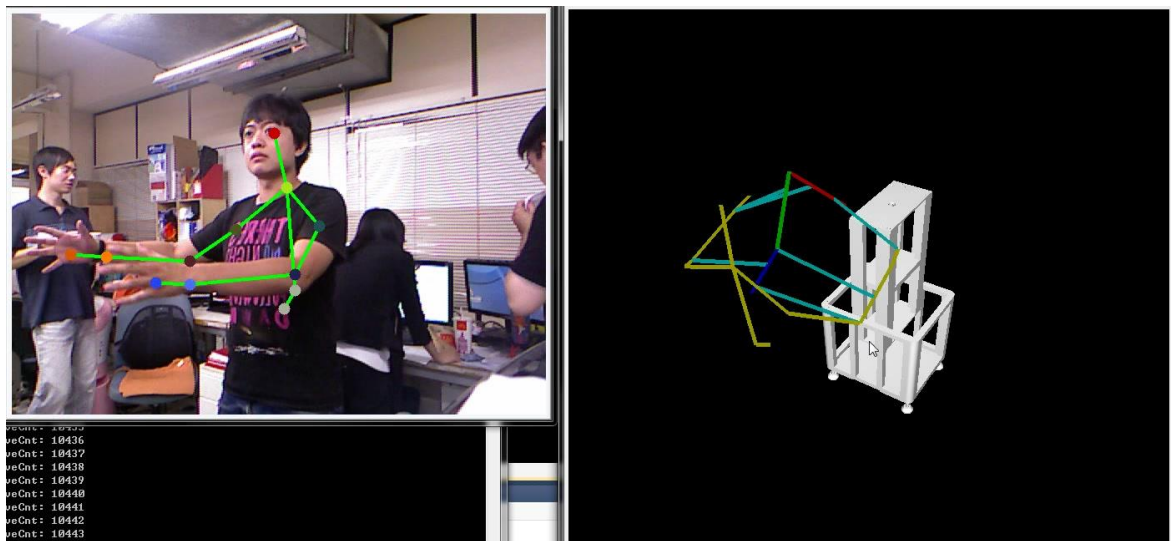


Fig. 4-10. The modeling of the human and the robot in the virtual impedance control.

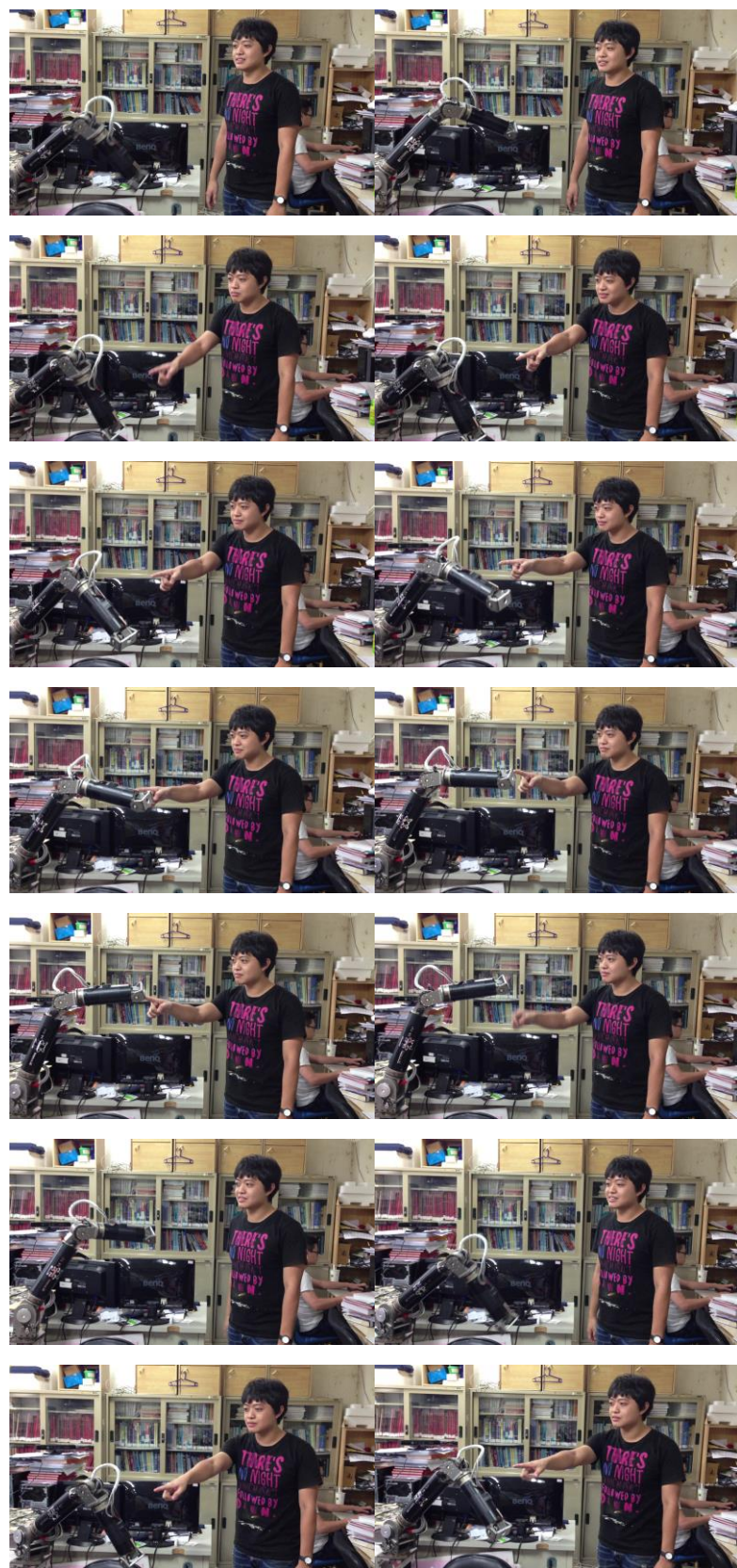
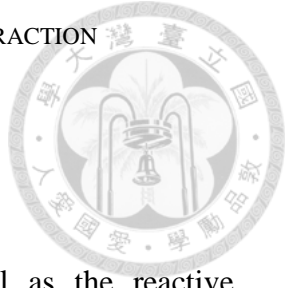


Fig. 4-11. The safe human-robot interaction experiment part 1.

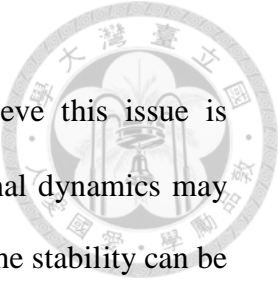


Fig. 4-12. The safe human-robot interaction experiment part 2.



4.5 Summary

In this chapter, we propose the virtual impedance control as the reactive controller for the safe human-robot interaction. The virtual impedance control is a model-reference control scheme defined in a abstract vector space so that the dynamics in that space can be controlled as the second-order linear system. To unify all the possible collisions, we define the risk space which is a normalized measure of the degree of the upcoming collisions and apply the virtual impedance controller. As the consequence, the dynamic response of the collision avoidance is smooth and consistent regardless of the types of the collision, and most importantly the collision can be robustly avoided. Compared with the other reactive controls for the collision avoidance, the proposed control is not only state-of the-art but also easily tuned, since the dynamic characteristics is completely determined by the damping ratio and the bandwidth of the second-order system. In the experiments, we integrate the 6-DOF NTU Robot arm with Kinect to detect the dynamic environment, and demonstrate our control scheme for the safe human-robot interaction. In the future works, we want to incorporate the physical forces into the risk space, since the dynamics now is only the initial response of the second-order system. By defining the proper map to transfer the physical contact force into the normalized risk space, the forcing term in the second-order linear system can be defined. This can improve the performance of the system by considering the physical interaction that may not be detectable by the machine vision, or is more suitable in some collaborative scenarios. Also, we mention another potential limitation of the current scheme. Since it is the dynamics of $\dot{\mathbf{r}}_+$ not \mathbf{r} is controlled, the velocity $\dot{\mathbf{r}}$ may be large when leaving the potential field even



if $\dot{\mathbf{r}}_+ \rightarrow 0$ due to the critically damped system. However, we believe this issue is addressed by the boundary layer, because the force from the original dynamics may balance the system. Therefore, if the two systems are both passive, the stability can be proved, which is the case in our experiments.

Also, we want to prove the stability and the convergence properties of the boundary layer.





Chapter 5 Bayesian Exoskeleton System

The essence of an exoskeleton system is the estimation of human intention. That is, the human applying torque. Once the intention of the operator is known or can be estimated, the exoskeleton can perform arbitrary tasks and movement freely. Although the dynamics model and the biosignal model are the most common approaches in the literatures, none of them is universal. The dynamics model suffers from the unobservable disturbance torques due to exogenous disturbances or the unmodeled nonlinear dynamics, such as flexible joints and frictions; the biosignal is very noisy, time-variant, and nonlinear. In most of the cases, the biosignal can only picture of the intention vaguely, instead of estimating the precise value of the human applying torque. In lieu of using only either of the models, the proposed Bayesian exoskeleton system provides an alternative by optimally combining the two models in the Bayesian sense, so that the estimation can be more accurate when either of the two models fails. By modeling the human-exoskeleton system as the graphical model, the Bayesian human torque estimator can online adaptively fuse the information from the two models. In addition, a robust torque control loop is design to achieve the assistive control. In the experiments, the performance and validity of the Bayesian scheme is examined. The experimental results show prominently that the Bayesian exoskeleton system performs nearly as good as theoretically guaranteed.

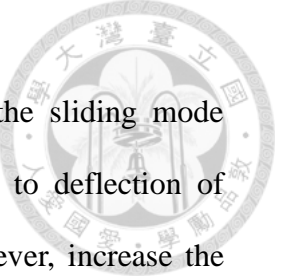
This chapter is partly based on the contributed works in conferences or journals [14, 16, 44-46].



5.1 Introduction

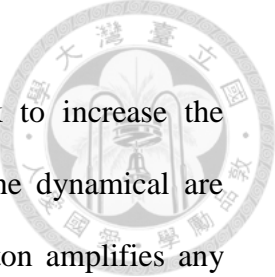
Exoskeleton system draws attention in recent years. The objective of the exoskeleton design is to augment the operator with assistive forces to support the movement or to amplify the force of the operator. The scheme is called *assistive control*. In contrast to the traditional tracking or regularization control, the reference trajectory in the assistive control is usually hard to be characterized. In the application of the exoskeleton system, the reference trajectory is the desired torque exerted by the operator on the human-exoskeleton system, which is called *human applying torque* herein. The human applying torque is often referred as the human intention in the context of the exoskeleton system, and is the essence of a exoskeleton system, since most of the exoskeleton systems can be regarded as the human torque amplifier. Once the human applying torque is known or can be estimated, the exoskeleton control problem can almost be regarded as solved. The exoskeleton system can augment the operator and then perform freely in any task if the correct human intention is known, since, in this case, the human-exoskeleton is identical to the operator himself.

Despite the merit of the human applying torque, the estimation is difficult in general. In the literatures, various assumptions and models have been proposed during last decades. We roughly classify them according to the existence of the force model. In the modeless design, the force sensor is implemented directly on the exoskeleton to measure the interaction forces between the operator and the exoskeleton system [108, 112]. The EXO-UL7 [112] uses three force sensors to estimate the interaction between human and robot, and the position trajectories of upper limber exoskeleton are generated by the admittance model. In [108], the similar admittance model is adopted



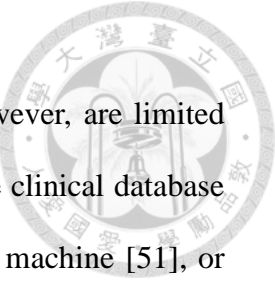
with the force sensors on the fingers. Moreover, they included the sliding mode control to overcome the mechanical parameters uncertainties due to deflection of Bowden cables and the disturbance. The extra force sensors, however, increase the costs and the weight, and decrease the compactness of the exoskeleton system, making the design impractical. Also, we need to emphasize that measured force of the force sensor cannot truly represent the human applying torque in general. More specifically, the operator can only exercise ultimately as if without the existence of the exoskeleton and the possible external loadings. For instance, in both designs, the objective is to minimize the interaction force between the user and the robot so that the robot follows the motion of the user. This design, however, does not directly minimize the loading of the operator. In fact, the control scheme only lowers the impedance between the exoskeleton and the user. Therefore, the exoskeleton cannot directly lessen the loading due to the inertia of the operator. In assistive applications, the exoskeleton, however, should provide additional power to support the user.

The model-based methods, on the other hand, are more suitable to be used in practices. According to the types of the feedback sensors, the model-based method can be further classified into the *dynamics model* [52, 57] and the *biosignal model* [40, 55]. In the literatures, most of the dynamics models are referred to the inverse dynamics model. The inverse dynamics model is based on the dynamics equation of the exoskeleton system, and can infer the human applying torque if all the states, the unknown parameters, and the torque contributed by the exogenous disturbance of the system are known. Although all the states, the unknown parameters can be calibrated or estimated by the canonical estimation method in the system theory, the exogenous disturbance is hard to be estimated empirically. In [52], they derived the dynamics



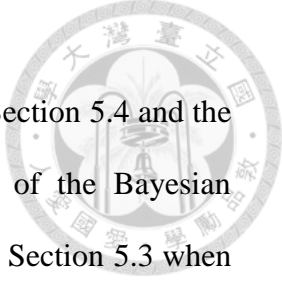
model of the exoskeleton system and use the positive feedback to increase the sensitivity to the disturbance of the system. The parameters of the dynamical are calibrated in the experiments [34]. The controller of the exoskeleton amplifies any disturbance that comes into the system – even the exogenous disturbances, e.g. the ground reaction forces. They claimed “*...which does not stabilize, will only make us stronger.*” The real question is whether the sensitivity design is stable for all the users regardless of the fitness. The stability issue of the sensitivity increasing design is addressed in [57]. They applied the band-pass filter to guarantee the robust stability of the overall system. Further, they proposed a sophisticated smart shoe [58] to estimate the ground reaction force. The dynamics model is standard in the community of the control system, but the main drawbacks are the need of the precise modeling, expensive sensors and actuators, not to mention the time delay due to the stability and the causality, since the disturbance comes into the system only when the operator has moved already. Therefore, the dynamics model fails when the exogenous disturbance cannot be measured accurately, for example using the footswitch as the exogenous force sensor, or when the structured unmodeled dynamics in the exoskeleton is large.

The biosignal model, on the other hand, alleviates the complexity of the dynamics model and uses only the biosignals, such as the electromyography (EMG) signal or the electroencephalography (EEG) signal, to estimate the human intention [40]. One of the characteristics of the biosignal is that it activates earlier before the actual movement of the operator and it is directly related to the human intention. As the result, a real-time system is possible ultimately. Many biosignal models have been proposed, including the linear model, the nonlinear physiology model, and the fuzzy-neural networks, etc [33, 55]. Due to the low signal-to-noise-ratio (SNR) nature



of the biosignals, the application of the pure biosignal models, however, are limited and can only perform simple or predefined movements. [50] use the clinical database to improve the estimation results and the others use the finite state machine [51], or hybrid control scheme [46]. The results are not satisfactory for the general tasks and the freedom of the movement is limited.

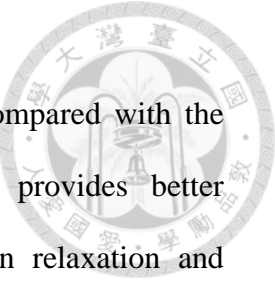
Aimed for better human intention estimation and assisting control, this chapter is devoted to the estimation schemes that combine both the dynamics model and the biosignal model, and the robust assistive control to strengthen the operator. The chapter is organized as follows. Section 5.2 introduces the knee exoskeleton and the inner torque control scheme that will be used throughout the whole chapter. The knee exoskeleton is based on the serial elastic actuator (SEA) mechanism, which can provide intrinsically safe assistance. The inner torque control scheme is implemented as the PD type position control due to the nature of the SEA system. The proposed scheme shows to be robust in presence of the unmodeled dynamics and the estimation error of the human intention. Section 5.3 demonstrates a simple adaptive scheme of combining both the biosignal model and the dynamics model based on switching control to compensate the defects of using either of the models alone. The self-learning scheme in Section 5.3 is designed to learn the non-stationary biosignal model online in a semi-supervised fashion, and the inner sliding mode control with admittance interface can provide robust and continuous assisting forces. Based on the simple heuristics of considering nature of the two models, Section 5.3 is introduced to be compared with the Bayesian framework in Section 5.4, whereas in Section 5.4, the main contribution of this chapter is given, the general *Bayesian exoskeleton system*. To ultimately combine the biosignal model and the dynamics model, the Bayesian



exoskeleton is based on the Bayesian human intention estimator in Section 5.4 and the robust assistive control in Section 5.2. Interestingly, the results of the Bayesian Exoskeleton System are similar to the heuristic switching scheme in Section 5.3 when a footswitch is used as the exogenous disturbance sensor. Finally, Section 5.5 summarizes the contributions in this chapter, and discusses the effects of different control schemes.

5.2 A Robust Hybrid Control for Assistive Control with Knee Orthosis

The assistive control is a general framework for the exoskeleton system to augment human by amplifying the human applying forces. Given the estimated human applying force, the assistive control provides an effective gain by injecting the amplified estimation into the system. However, the stability and the robustness of such scheme are unknown in general. Aimed at both safe and effectual robot-assisted walking, this paper proposed a hybrid control scheme for the robust assistive control. To provide robust assistance, the hybrid scheme switches between the intention feedback control and the zero-impedance control. In major movements, the intention feedback control amplifies the force of the operator, whereas in minor movements, the zero-impedance control provides compliance property for comfortable interaction between the operator and the robot. The switching effectively introduces an insensitive zone in the assistive control so that the exoskeleton can reject uncertainties and provide assistance consistently. Further, a new human-exoskeleton model is proposed to investigate the stability considering the motor feedback of human, and the hybrid scheme is proved to be robustly stable. In addition, a new backdrivable torsion



spring actuator (BTSA) is designed to achieve intrinsic safety. Compared with the state-of-the-art assistive methods, the robust hybrid controller provides better interaction experience in that the operator feels unconstrained in relaxation and boosted in motions. In the experiments, a knee exoskeleton is designed based on the BTSA to validate the performance. Both the simulations and the experimental results show the effectiveness of the hybrid scheme.

5.2.1 Introduction

In the field of physical human-robot interaction (pHRI), the fundamental tradeoff is how to maximize the performance and detect the human intention while maintaining the safety [29]. The general scenario is that the robot performs some specific tasks in the presence of human, and, meanwhile, tries to understand and response to the human intention. However, the interaction can be carried on, only when the safety is asserted.

As for the application of walking assistance, the goal is to enhance or to recover the locomotion ability of the users, especially for the patients with neurological dysfunctions that affect the activities of daily living permanently, such as cerebral vascular accidents (CVA), spinal cord injury (SCI), traumatic brain injury (TBI) [47]. Despite the neurological impairment, it is possible to improve the motor ability and the quality of life by rehabilitation. In particular, neuroplasticity can amend of motor ability even for patients with 6 to 12 months post-stroke [47]. If full recovery is not possible, rehabilitation can maintain the patient's present condition. Hence the development of the exoskeleton for walking assistance is important.

In this paper, a biofeedback knee orthosis with the backdrivable torsion spring actuator (BTSA) is designed for the subjects with normal or minor damaged neural



signals. With the new hybrid control scheme and the BTSA, the exoskeleton provides robust assistance in general walking scenarios, and offers both the intrinsic safety and the support. In following, we give the introduction to exoskeleton design and the comparison with the other biofeedback exoskeletons.

A. *Design of the Knee Orthosis with Intrinsic Safety*

Considering the knee motion assistance, the important features are the backdrivable property, the actuators that are compact and light-weighted yet have sufficient power for human locomotion, and most importantly, the intrinsically safe mechanism. Although the non-backdrivable mechanism with high reduction ratio, such as worm gears [1, 104], has larger output force, it is only suitable for those with severe motor disability in rehabilitation because of the self-lock and the isolation of external forces. For the healthy subjects or those with mild motor disability, the backdrivable actuator with low reduction ratio transmission, for example bevel gears, cable transmission, or direct drive [47], are more suitable because it is more sensitive to the external forces, the interaction force between human and the robot. That is, the overall system is more stable because it includes the operator's feedback, and the interaction remains smooth in the presence of minor control error. On the other hand, the non-backdrivable relies highly on accurate controllers and trajectory planning, and therefore even little control error may cause discomfort of the operator. In summary, the comparison between rehabilitation and assistive exercise is shown in Table 5-I.

For both safety and efficiency, various mechanisms have been devised for intrinsically safe robot actuation, such as serial elastic actuators (SEA) [28, 41, 59, 66, 72, 88], programmed impedance actuators [81, 101], variable stiffness actuators [4, 49, 69, 74, 75, 110], etc.. The programmed impedance actuator controls the force



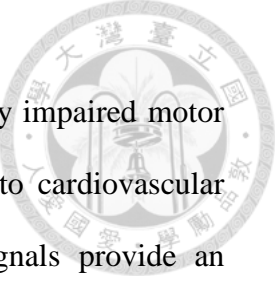
TABLE 5-I COMPARISON OF REHABILITATION AND ASSISTIVE EXERCISE

	Rehabilitation	Assistive Exercise
Frequency	Low	High
Load	High	Medium
User	Patient with Movement Impairment or Disability	Healthy Person, Elder, Patient with Impairment
Mechanical System	Non-Backdrivable System High-Gear Ratio	Backdrivable System Medium-Gear Ratio

profile to generate the piecewise linear impedance; the variable stiffness actuator is more flexible and can control the bandwidth, the payload capacity, and the safety level of the pHRI in versatile tasks [47]. However, both the programmed impedance actuator and variable stiffness mechanism are usually too complex, and the volume required is larger than that of the traditional SEAs. Therefore, SEA is more practical. To achieve the backdrivable property, various SEA designs with constant stiffness have been proposed. According to the spring, they can be roughly categorized into rotational [61, 62] and linear SEA [63]. In this paper, the rotational SEA is adopted for the compactness and the simplicity of fabrication.

B. Biofeedback Control

How are those assistance and rehabilitation devices controlled by the biofeedback signals? The biofeedback signals used to control or to estimate the subject's performance can be categorized into the electromyography signals (EMG) [62, 63], the electroencephalograph signals (EEG) [61, 95], and the sensing of the human motion and the external force [23, 99]. The most common biofeedback signals are the motion detection and the force sensing, because these signals are more stable than EMG signals, and, especially, the EEG signals. However, the motion detection



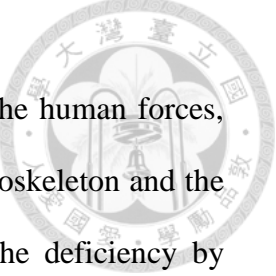
and the force sensing fail when the subjects have partially or totally impaired motor ability. For the patients with partially impaired motor ability due to cardiovascular accidents or the spinal cord injury, the EMG and the EEG signals provide an alternative. While the EEG signals are limited to certain simple motions, the EMG signals can detect abnormal situations, such as spasticity, and can estimate the human applying torque directly, providing directly the feedback signals for control.

To estimate the human intention, the EMG models are commonly based on the general learning techniques [109] or the bio-inspired models [47, 60]. With the estimation, the amplified estimated biological torque is used as the torque reference for the inner torque control loop. Therefore, this *intention feedback control* acts effectively as the human force amplifier, assisting the operator of the exoskeleton performing arbitrary motions.

C. Robust Hybrid Control and Knee Orthosis

It has not been proven whether users are comfortable when wearing the exoskeleton to perform the tasks. Some articles have argued that the assist-as-needed method is more suitable for human use [71]. However, the authors do not consider how the exoskeleton system influences the user's limb dynamics when the EMG feedback is turned off. Although the EMG biofeedback control can be used to assist humans to perform any task, the muscles become weaker under this control law, because muscles degenerate without being used. One solution is to give a specific task-oriented command trajectory, but this requires a great deal of data for various kinds of tasks.

In this paper, a robust hybrid control scheme switching between the intention feedback control and the zero-impedance control is proposed, in which the intention



feedback control uses the estimations by EMG signals to amplify the human forces, and the zero-impedance compensates the impedance between the exoskeleton and the operator. The hybrid scheme is inspired by [71], and improves the deficiency by compensating the mechanical impedance when the EMG estimation is off. The switching is necessary, because of the uncertainty of EMG signal when the measurement is low. Compared with [71], the zero-impedance control compensates the mechanical impedance, and therefore with the new hybrid control, the user can move as freely as possible in minor movements and be supported in major movements. In summary, the proposed hybrid control creates an insensitive zone such that the exoskeleton can provide assistance robustly regardless of the sensory uncertainties in the intention estimation. In addition, a new human-exoskeleton model is proposed to reveal more insights of the interaction, and the hybrid control is proved to be robustly stable considering the ability of the motor feedback of human.

Overcoming aforementioned problems, the proposed hybrid control that switches between the intention feedback control and the zero-impedance control with the knee orthosis composed of the BTSA provides a new paradigm of rehabilitation training and walking assistance. In Section 5.2.2, the design concept and the dynamic properties of the proposed system are addressed. The main contribution, the robust hybrid control scheme, is introduced and the stability is proved in Section 5.2.3. The simulations and experimental performance of the BTSA with the hybrid control are presented and discussed in Section 5.2.4 and Section 5.2.5, respectively. Finally, a short conclusion is drawn in Section 5.2.6.

5.2.2 Design of Backdrivable Torsion Spring Actuator

A new BTSA system is designed with a torsion spring, bevel gears, and a



DC-mircomotor. The soft stiffness of the BTSA provides mechanically intrinsic safety and can measure the interaction torque between the operator and the exoskeleton. The detailed working principle and design are addressed in this section.

To design the torsion spring, it is crucial to consider the torque range and the deformable range of the knee during walking. In order to avoid the plastic deformation of spring, the spring stress must be lower than the yield stress. Meanwhile, the deflection angle should be sufficient large to provide enough sensitivity so that the torsion spring can be used as a torque sensor. In order to design a compliant mechanism with large torque output and high sensitivity within a limited space, the torsion spring must be small in size yet can deflect largely. To fulfill such requirements, we list the specification as shown in Table 5-I: the desired maximum torque $\pm 50\text{Nm}$, the yield stress 15000 MPa , and the maximum deflection ± 21.89 degrees. The deflection, the stress, and the spring constant are calculated by formulas below.

$$\alpha = \frac{12 \cdot 180 \cdot M \cdot n \cdot D}{E \cdot b \cdot t^3} \quad (5.1)$$

$$\sigma = K_b \cdot \frac{6 \cdot M}{b \cdot t^2}, \quad K_b \approx \frac{3c - 1}{3c - 3}, \quad c = \frac{D}{t} \quad (5.2)$$

$$k = \frac{E \cdot b \cdot t^3}{12 \cdot 180 \cdot n \cdot D} \quad (5.3)$$

where α is the deflection [deg.], σ is the spring stress [MPa], M is the torque [$N \cdot m$] and E is the elastic modulus [MPa].

We fabricate the torsion spring with S45500 with the geometry parameters listed in Table II. Within the torque range (50Nm), the designed spring stress is strictly under the yield stress, and the deflection is large enough to provide enough sensitivity. Therefore, the designed spring satisfies the need of the BTSA. Fig. 5-1 shows the



exploded view of the BTSA, where the actuator, the bevel gears, the output bevel gear, and the torsion spring are in serial. Two potentiometers are installed. One potentiometer inside the spring measures the displacement of the torsion spring so that the interaction force can be estimated by the Hooke's law, and the other potentiometer measures the knee angle. Finally, the knee orthosis driven by the BTSA is shown in Fig. 5-2 and the specification is summarized in Table 5-III.

TABLE 5-II SPECIFICATION OF THE DESIGNED TORSION SPRING

Specification	Values
Desired maximum deflection	± 21.89 deg.
Desired maximum torque	± 50 Nm
Yield stress of the spring material	± 1500 MPa
Mean diameter of spring (D)	26.3 mm
Wire thickness (t)	8 mm
Wire width (b)	4 mm
Number of turns (n)	3
Desired spring constant (k)	2.284 Nm/deg.
Measured spring constant (k)	1.94 Nm/deg.

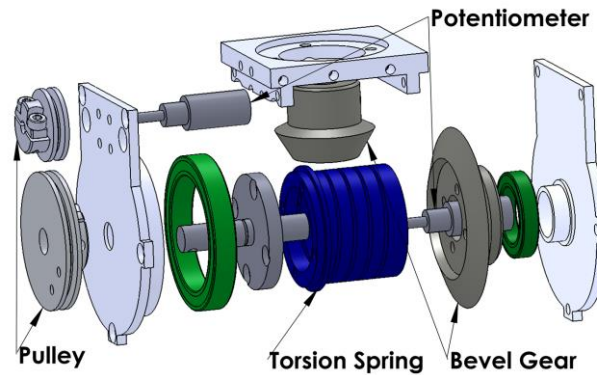


Fig. 5-1. Exploded view of the proposed backdrivable torsion spring actuator

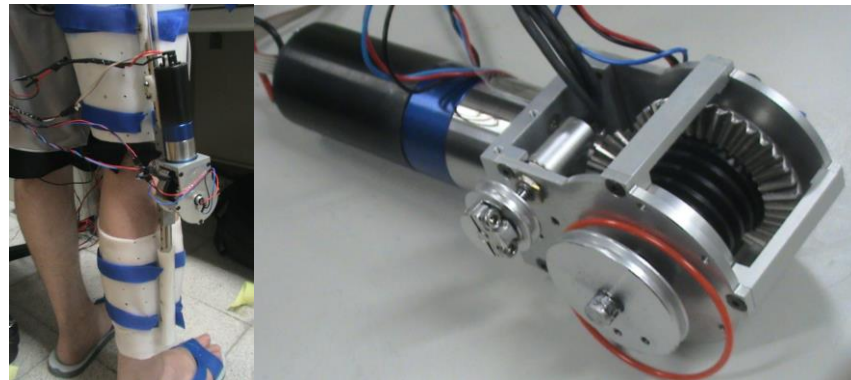


Fig. 5-2. The knee orthosis and the backdrivable torsion spring actuator

TABLE 5-III Specification OF THE BTSA

Weight (including the motor)	835 g
Length*Width*Height	62x50x187 mm ³
Reduction Ratio of Bevel Gear	2:1
Reduction Ratio of Motor Gear Head	43:1
Stall Torque	87.5 Nm
No-Load Speed	404 deg/sec

*The input motor used in this design is a Faulhaber DC-micromotor 3863H024CR with gear head 38/2 S (43:1).



5.2.3 Robust Hybrid Control

The BTSA approach is a general concept that cascades a torsion spring serial with the mechanical system. In our case, the system is the human-exoskeleton system, and we adopt the human-robot interaction model [47] to investigate system properties and the stability during human-robot interaction. This section is organized as follows. First, the nominal multi-input-multi-output linear model of the human-exoskeleton system is presented in Section A. In the following, Section B and Section C show the zero-impedance control and the EMG-control, respectively. By combining the human intention feedbacks and the compliant zero-impedance control, the hybrid scheme is proposed in Section D to provide robust assistance. Finally, we analyze and prove the robust stability of the human-exoskeleton system in Section E.

A. A Simple Human-Robot Interaction Model

The human-robot interaction model is shown in Fig. 5-3, and the governing equations of the system with gravity compensation is given as

$$\begin{cases} m_e \ddot{x}_e = k_e(x_o - x_e) + b_e(\dot{x}_o - \dot{x}_e) - B_e \dot{x}_e + \tau_e \\ m_h \ddot{x}_h = k_h(x_o - x_h) + b_h(\dot{x}_o - \dot{x}_h) - B_h \dot{x}_h + \tau_h \\ M \ddot{x}_3 = k_e(x_e - x_o) + k_h(x_h - x_o) + b_e(\dot{x}_e - \dot{x}_o) + b_h(\dot{x}_h - \dot{x}_o) + \tau_D \end{cases} \quad (5.4)$$

and the transfer functions are

$$\begin{bmatrix} \Delta x_e \\ \Delta x_h \\ x_o \end{bmatrix} = P\tau := \begin{bmatrix} P_{11} & P_{12} & P_{13} \\ P_{21} & P_{22} & P_{23} \\ P_{31} & P_{32} & P_{33} \end{bmatrix} \begin{bmatrix} \tau_e \\ \tau_h \\ \tau_D \end{bmatrix}, \quad (5.5)$$

where $\Delta x_e := x_o - x_e$, $\Delta x_h := x_o - x_h$, and P_{ij} , $i, j = 1, \dots, 3$, are the corresponding Hurwitz transfer functions in Fig. 3. In the model, the force is used as a generalized term and therefore the actuator can be either linear or rotary. By linearizing the Hill's

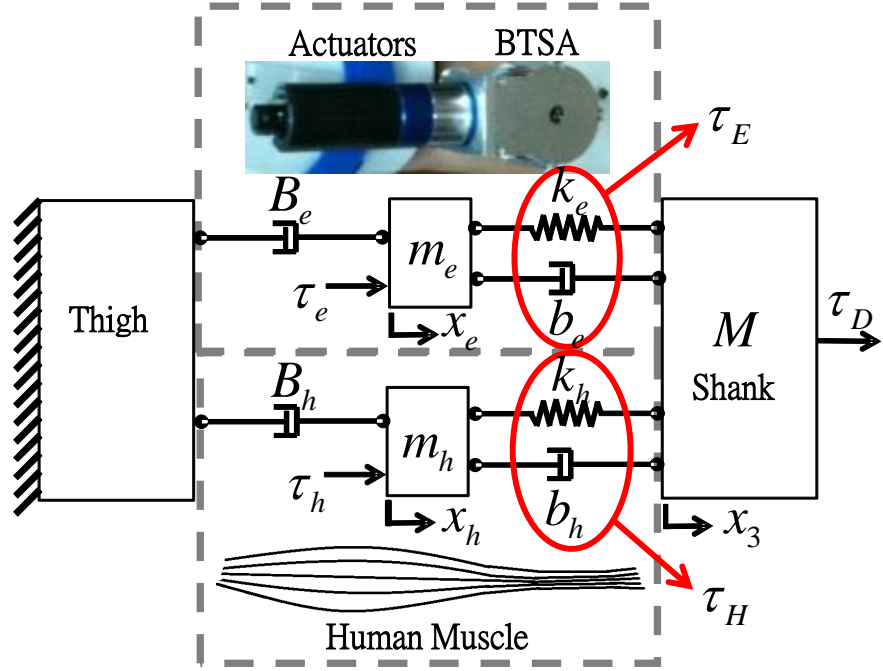


Fig. 5-3. Human-robot interaction model.

M the mass the shank with exoskeleton, m_e the mass of actuator, m_h the mass of muscle, B_e the damper of motor, b_e the damper of BTSA, k_e the spring of BTSA, B_h the effective serial damper of the muscles, b_h the effective parallel damper of the muscles, k_h the effective parallel spring of the muscles, τ_e the motor force, τ_h the muscle force, τ_H the external force, τ_E the force exerted on the leg from the BSTA, τ_H the force exerted on the leg from the muscles, x_e the displacement of the motor, x_h the displacement of the muscles, x_o the displacement of the shank

muscle model [42], the linear system in (5.4) can be derived. Therefore, we can model the dynamics with the nominal plant (5.5) and analyze the stability by introducing the set of uncertainties. More macroscopically, the human-exoskeleton system can be described by

$$x_o = P_{33}(\tau_E + \tau_H + \tau_D), \quad (5.6)$$

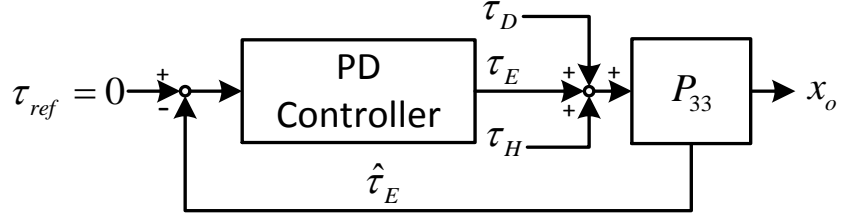


Fig. 5-4. Block diagram of zero impedance control

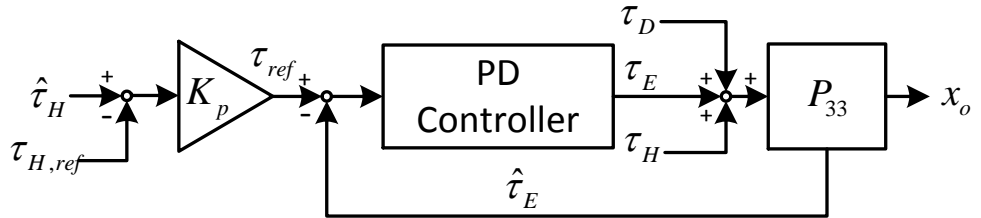


Fig. 5-5. Block diagram of intention feedback control

by neglecting the internal models, where τ_E is the assistive force from the exoskeleton and τ_H is the muscle force as in Fig. 5-3. In this setting, $\tilde{\tau}_H$ is the linearized nominal plant of the nonlinear robot dynamics. By assuming proper inner force control feedbacks of both the actuator and the human operator, the internal models are stable, and we shall assume them as the ideal lowpass filters with limited bandwidth in the following. Therefore, they can be neglected as long as the system operates in the bandwidth within the human capability.

B. Zero-Impedance Control

The zero-impedance control compensates the impedance of the BTSA such that

$$\tau_E \rightarrow 0. \quad (5.7)$$

Neglecting the damping b_e , τ_E can be estimated as $\hat{\tau}_E$ by measuring of the deflection of the rotary spring Δx_1 . Feeding back this estimation, the zero-impedance control can be achieved, resulting to the compliant mechanism as in Fig. 5-4. In this



control mode, the operator should feel no resistance due to the actuator but only the weights and the inertias of the exoskeleton.

C. Intention Feedback Control

To assist arbitrary motions, the intention feedback control is a force control scheme that feedbacks the human intention, i.e. the human applying torque τ_H into the system, so that the exoskeleton can control the inputs from the human operator to track some predefined references. Here, the human intention τ_H applied by the muscles on the shank and the exoskeleton is estimated by using the EMG signals. Assuming the human applying force τ_H is linear in terms of the instantaneous energy of the EMG signal, the model can be calibrated experimentally by the ordinary regression to provide the estimation $\hat{\tau}_H$. We choose the EMG feedback for the simplicity, since it is almost modeless. We note that other models also fit in our framework. For examples, a nonlinear muscle-model-based method [60] can be used. However, such model

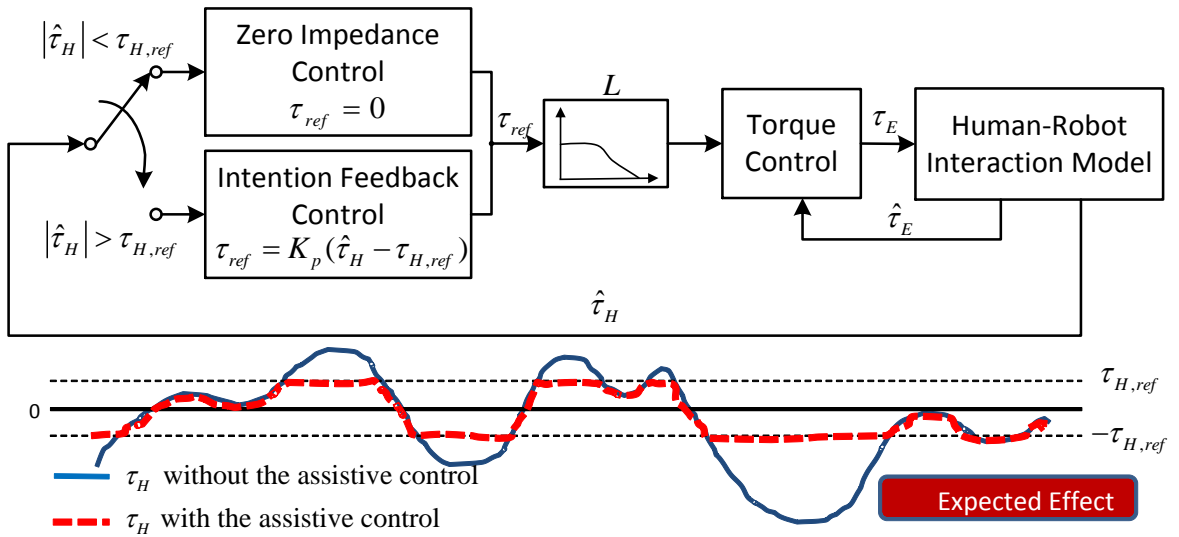
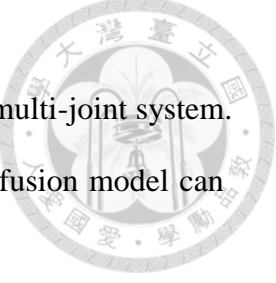


Fig. 5-6. Block diagram of hybrid control



sometimes leads to over-fitting and is too complicated to model the multi-joint system.

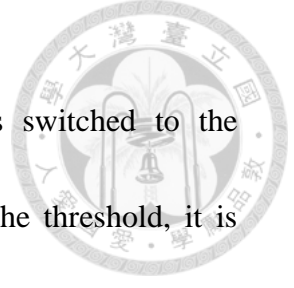
In addition to the biofeedback, the inverse dynamics model, or the fusion model can also be used to estimate the human intention τ_H [16].

The objective of the intention feedback control is to make τ_H track some predefined trajectories. Here, the trajectory is defined as a constant value $\tau_{H,ref}$. The block diagram is shown in Fig. 5-5, in which the seemingly positive feedback of the estimation $\hat{\tau}_H$ is actually a negative feedback, since there is actually a latent negative feedback of the human motor control as shown in Fig. 5-8 in the next section. Therefore, the EMG biofeedback control in Fig. 5-5 is effective a proportional force controller with the gain K_p . If $\tau_{H,ref}$ is set zero, which will be used in following experiments of pure intention feedback control, the intention feedback control provides a constant fictitious gain as in [64].

D. Hybrid Control with Robust Assistance

The main objective of the hybrid scheme is to provide robust assistances. Since estimation of human applying torque is contaminated with noises and estimation errors, the pure intention feedback control may deteriorate the system – the expected assistance may become the resistance. To robustly provide assistance during the operation, the hybrid scheme is proposed by introducing an insensitive zone. Based on the threshold $\tau_{thre} > 0$ of the estimated human applying torque, the hybrid scheme switches between the zero-impedance control and the intention feedback control, i.e.

$$\begin{cases} \text{intention feedback control, } & |\hat{\tau}_H| \geq \tau_{thre} \\ \text{zero-impedance control, } & \text{otherwise} \end{cases} \quad (5.8)$$



If $|\hat{\tau}_h|$ is greater than or equal to the threshold τ_{thre} , it is switched to the EMG-biofeedback control mode. Conversely, if $|\hat{\tau}_h|$ is less than the threshold, it is switched to the zero-impedance control mode. With this hybrid scheme, we can expect that $|\hat{\tau}_h| \leq \tau_{thre}$ in the ideal case, which is shown in Fig. 5-6. Also, we note that the switching law (5.8) is actually a continuous map from $\hat{\tau}_h$ to τ_{ref} if we set $\tau_{H,ref} = \pm\tau_{thre}$ in the intention feedback control, as shown in Fig. 5-7, which will be used in the following hybrid scheme.

The hybrid control scheme is motivated by the fact that the force τ_H intended by

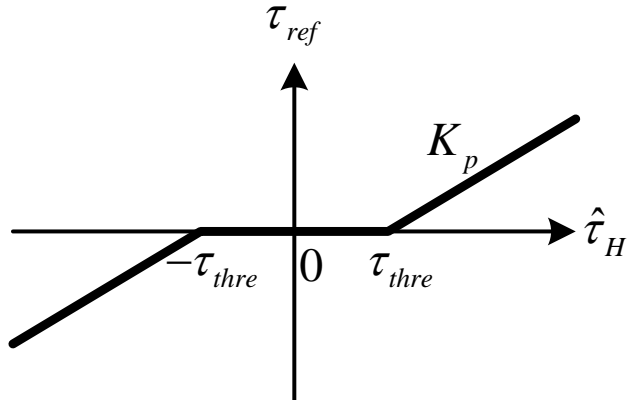


Fig. 5-7. The mapping from $\hat{\tau}_H$ to τ_{ref} .

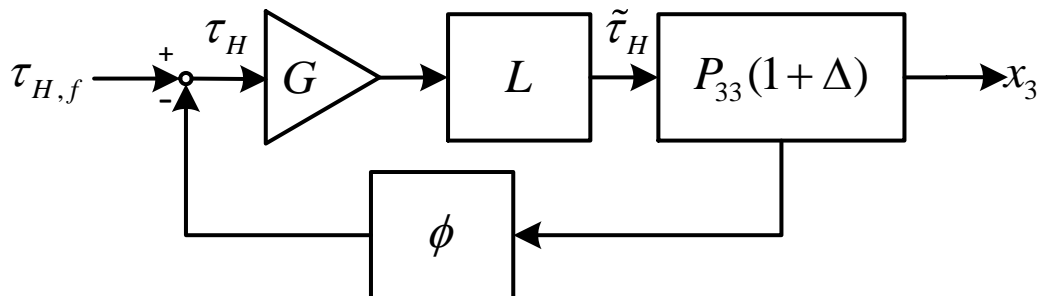


Fig. 5-8. The human-exoskeleton model with the hybrid control



the operator is difficult to be estimated by $\hat{\tau}_H$ especially when $\|\tau_H\|$ is small owing to the noises and the modeling errors. The hybrid control resolves this issue by the switching control scheme, so the exoskeleton can assist the operator robustly. To show this, we rearrange the block diagram of the system in Fig. 5-8. The human motor control is modeled as a feedforward force $\tau_{H,f}$, which is based on the experiences, and a (possibly) nonlinear and time-varying feedback ϕ , of which the input is the sensory neurons and the output is the muscle force of the feedback compensation. Together with the assistive torque τ_E , the muscle force τ_H is first amplified by the effective gain G and then the filtered by the stable lowpass linear time-invariant filter L . The resultant $\tilde{\tau}_H$ applies on the single-input-single-output linear system $P_{33}(1+\Delta)$, in which Δ is a relation containing the modeling uncertainties. We choose the linear nominal plant both for the simplicity of the analysis and, most importantly, for the fact that human tend to linearize the system in control. Therefore, P_{33} is actually the linearized plant apprehended by the human operator.

By neglecting the exogenous input τ_D and assuming perfect force tracking such that $\tau_E = \tau_{ref}$, the hybrid control can be treated as an effective gain amplifying the human applying force,

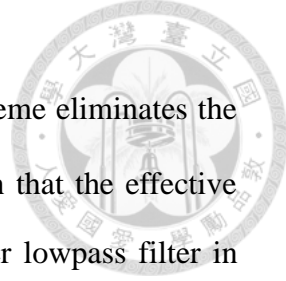
$$G(t) := 1 + \tau_{ref} / \tau_H. \quad (5.9)$$

Moreover, assuming $\|\hat{\tau}_h - \tau_h\|_\infty < \delta$ for some $0 < \delta < \infty$, we have

$$1 \leq G(t) < 1 + K_p \quad (5.10)$$

uniformly over $t \in [0, \infty)$ by choosing $\tau_{thre} > \delta$, since

$$\lim_{\tau_H \rightarrow \infty} G = \lim_{\tau_H \rightarrow \infty} 1 + K_p \frac{\hat{\tau}_H - \tau_{H,ref}}{\tau_H} = 1 + K_p. \quad (5.11)$$



Compared to [64], $G(t)$ is actually time varying and the hybrid scheme eliminates the noise and the uncertainties in the human intention estimation such that the effective gain can be guaranteed to $G(t) \geq 1$ robustly. Finally, we add another lowpass filter in Fig. 5-6, so that $G(t)$ and the disturbances due to the estimation errors can vary slowly for the comfort of the operator and for the stability, which is proved in the next section.

As a consequence, the operator can move as freely as possible when the applied force is small. This scenario occurs when the user adjusts his posture rather than actually intends to move, in which the pure intention feedback control may result in instability and vibrations, whereas the hybrid control scheme gains the overall smoothness and the stability by switching to the zero-impedance control. On the other hand, for the large motions and the loadings, the hybrid control behaves like the traditional assistive control with the fictitious gain.

E. Stability

The stability of the human-exoskeleton system is strictly required, because it relates to the safety of the operator. The exoskeleton system should magnify the human force and meanwhile maintain stability of the overall system. Although the analysis of the stability of the system involving human is difficult in general, we can at least qualitatively investigate the stability of the proposed hybrid control method.

Let Ω_H be the bandwidth of the human motion, and define the *sector* of memoryless function as follows.



Definition 5.1

A memoryless function $h:[0,\infty) \times \mathbb{R}^p \rightarrow \mathbb{R}^p$ is said to belong to the sector $[K_1, K_2]$ with $K = K_2 - K_1 = K^T > 0$, if

$$[h(t,u) - K_1 u]^T [h(t,u) - K_2 u] \leq 0. \quad (5.12)$$

We can show the stability of the hybrid control by making the following assumptions.

Assumption 5.2

1. If $\tilde{\tau}_H$ is within Ω_H , the feedback of human $\phi(t,u)$ is a (time-varying) memoryless nonlinear function belonging to the sector $[\alpha, \beta]$ such that $\beta > \alpha > 0$.
2. The estimated error is uniformly bounded, i.e. $\|\hat{\tau}_H - \tau_H\|_\infty < \delta$ for all $t \in [0, \infty)$, and $\delta < \tau_{thre}$.
3. The inner torque is robustly stable and tracks the reference perfectly within Ω_h .
4. The uncertainty model of the nominal plant P_{33} is a high-pass multiplicative uncertainty Δ with bandwidth over Ω_h .

The first assumption is critical for our modeling. It states that the feedback of the human motor control is input strictly passive as long as the system operates within the controllable bandwidth Ω_H that the human has learned and accustomed to. Outside Ω_H , we cannot expect strictly that $\phi(t,u)$ is passive. For examples, α may be negative if $\tilde{\tau}_H$ changes abruptly, since the response time of the sensory motor cortices is limited.

The second assumption is valid for many human intention estimation models, which is required to provide robust assistance; the third assumption is standard in the exoskeleton modeling. Finally, the last assumption states the expectation of the operator to system. Since human tend to learn and adapt to the system quickly especially for the low frequency profiles by the linearization, the uncertainty is

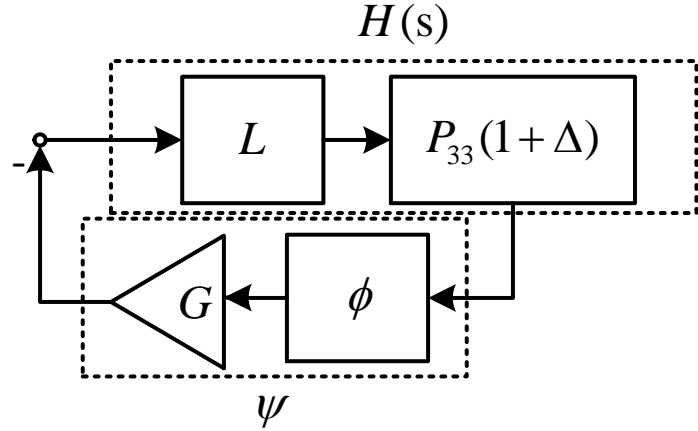


Fig. 5-9. The closed-loop system of the human-exoskeleton system

modeled as a family of high-pass uncertainties.

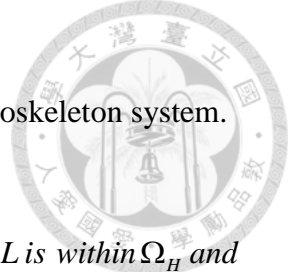
Under these assumptions, we can prove the stability of the closed loop system of the human-exoskeleton system by recalling the following lemma, known as the circle criterion.

Definition 5.3

Consider the system with linear plant with transfer function $H(s)$ and negative feedback ψ belonging to the sector $[a,b]$ with $b-a > 0$. The system is said to be absolutely stable if the origin is globally uniformly asymptotically stable for any nonlinearity in the given sector.

Lemma 5.4 [53]

Following the conditions of the system in Definition 5.3, the system is absolutely stable if $0 < a < b$ and the Nyquist plot of $H(s)$ does not enter the disk $D(a,b)$, whose diameter passes through the line segment joined by $-a^{-1} + j0$ and $-b^{-1} + j0$, and encircles it m times in the counterclockwise direction, where m is the number of poles of $H(s)$ with positive real parts.



Using this lemma, we can easily prove the stability of the human-exoskeleton system.

Theorem 5.5

The closed-loop system in Fig. 5-8 is robustly absolutely stable, if L is within Ω_H and the gain K_p is bounded by a constant determined by the human operator.

Proof:

Let the lowpass filter L in Fig. 5-8 with cutoff frequency Ω_H . Then we have $\tilde{\tau}_H$ is within Ω_H so that the Assumption 1 and 3 is valid. Therefore, the robust stability can be proved by showing the system is absolutely stable over all possible uncertainties with Lemma. To use Lemma, we first rearrange the block diagram in Fig. 5-8 into Fig. 5-9. The time varying gain $G(t)$ and the negative feedback can commute due to that $G(t) \in [a, b]$ with $b = 1 + K_p$ and $a = 1 > 0$ due to the insensitive zone introduced in (5.8). Combining $G(t)$ and $\phi(t, u)$, we define a new time-varying nonlinear memoryless function

$$\psi(t, u) := G(t)\phi(t, u), \quad (5.13)$$

where u is sensory feedback of the neurons, and it can be shown that

$$\psi(t, u) \in [\alpha, \beta(1 + K_p)] \quad (5.14)$$

uniformly, since $\alpha, \beta, (1 + K_p) > 0$. Define

$$H := L(P_{33} + \Delta). \quad (5.15)$$

The system is robustly absolute stable if the Nyquist plot of H does not pass the disk $D(\alpha, \beta(1 + K_p))$ defined in Lemma. A sufficient condition would be

$$\|L(P_{33} + \Delta)\|_\infty < \frac{1}{\beta(1 + K_p)}. \quad (5.16)$$

Therefore, the proportional gain K_p for the assistance should be bounded by

$$K_p < \frac{1}{\beta \|L(P_{33} + \Delta)\|_\infty} - 1. \quad (5.17)$$



Since we do not know α and β in general, Theorem qualitatively analyzes the stability criterion of the assistive control including the human feedback. The result is intuitive that there should be sufficient *gain margin* to provide the robust stability. Also, interesting results can be shown by (5.16). First, the lowpass filter L eliminates the uncertainties from Δ , so the operator actually perceives a similar system that he is already familiar with. Therefore, assuming there is sufficient gain margin without the assistant, i.e. $G = 1$, the bound (5.17) is not trivial, i.e. there exists $K_p > 0$ that does not unstabilize the system. Secondly, although we assume α and β to be constant in this analysis to prove the uniformity, one can model further that $\beta \in \mathcal{B}$, in which \mathcal{B} is a compact set, and β is piecewise constant, which varies much slower compared to Ω_H . Because the strong learning ability of human, the bound β may decrease once he observes and adapt to the system with the gain $G(t)$, just as human learns to limit the maximum force output if he is in a low gravity environment. Therefore, the bound (5.17) can be tighter by considering this ability. Finally, we note that the proof actually relies on that $G(t)$ is passive. Otherwise, the stability cannot be proved by limiting the assistance gain [53].

5.2.4 Simulations

The simulation environment is the GUI-based simulation interface, SimMechanics in MATLAB/Simulink. We use the simplified human-exoskeleton model in Fig. 5-3 to investigate the effect of the proposed control schemes. In the simulations, we assume the muscle is perfectly controlled such that the muscle



displacement x_h follows some predefined trajectories. To see the effects of the control schemes, the responses of Δx_e and Δx_h are investigated.

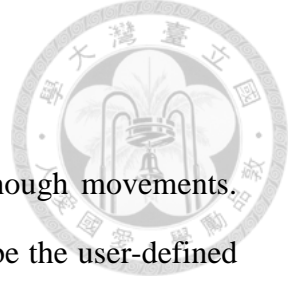
A. Simulation Results of Zero-Impedance Control

The result for the zero-impedance control is shown in Fig. 5-10. The input command, the muscle displacement x_h , is a sinusoidal trajectory. Because of the zero-impedance control, the displacement of the torsion spring Δx_e , the red solid line, in the simulation is approximately zero. This also indicates that the subject feels no resistance from the mechanism under the zero-impedance control.

B. Simulation Results of the Intention Feedback Control

The simulation results of the intention feedback control are shown in Fig. 5-11. Here, we set $\tau_{H,ref} = 0$, and the input command, the muscle displacement x_h , is a sinusoidal trajectory. With the intention feedback control, the displacement of the muscle spring Δx_h in simulation is approximated to zero. Therefore, the subject can move easily with little muscle effort. However, the results may be compromised in practice due to the noise of EMG signals. In this simulation model, the relationship between the EMG signal and the torque is modeled as a linear model, and, without loss of generality, the proportional gain K_p is set as unity for explaining the control concept, since we assume perfect control of the muscle in the simulations and $\hat{\tau}_H = \tau_H$.

In the experiments, the EMG signals are filtered and normalized, and the linear EMG model learned by the ordinary regression is used. It deviates from the simulation setting and therefore the error in the experiments of the pure intention feedback control is much larger.



C. Simulation Results of the Hybrid Control Scheme

The hybrid control provides assisting force only for large enough movements. That is, the objective is to control the human applying force τ_H to be the user-defined threshold $\tau_{H,ref}$ when it is over the threshold, and to control the exoskeleton force τ_E to

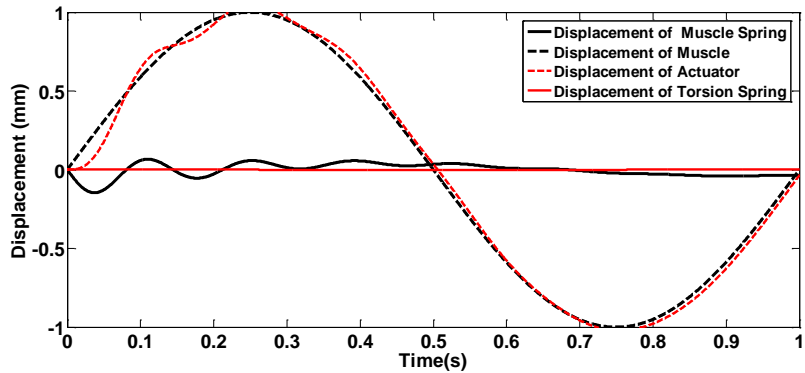


Fig. 5-10 The simulation result of the zero-impedance control

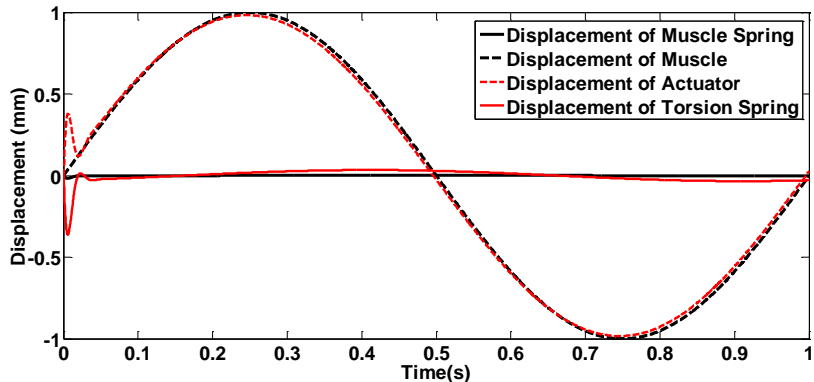


Fig. 5-11. The simulation result of the intention feedback control

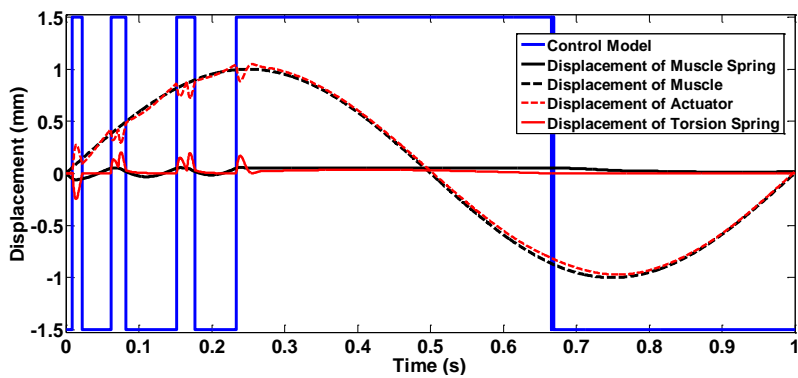
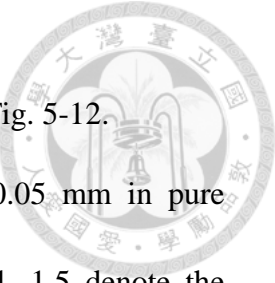


Fig. 5-12. The simulation result of the hybrid control



be zero otherwise. The simulation of the hybrid control is shown in Fig. 5-12.

In this simulation, $\tau_{H,ref}$ is set such that Δx_h should below 0.05 mm in pure intention feedback control. In the Fig. 5-12., the number 1.5 and -1.5 denote the intention feedback control and the zero-impedance control, respectively. It is clear that the displacement of the muscle spring Δx_h is under 0.15 mm and it is larger than the displacement in the intention feedback control yet smaller than that in the zero-impedance control.

5.2.5 Experiments

In the experiments, the subject is a healthy 23-year-old male. The subject sat on a chair in relaxation, and was asked to extend the knee joint and then return it to the original position. The knee angle is defined as zero degrees when the thigh and shank are perpendicular, and it is defined as 90 degrees as the knee fully extends.

In this work, a knee exoskeleton system was designed based on the proposed BTSA, as shown in Fig. 5-2. In order to satisfy the individual needs of the knee assistive exercise, a level arm with a shank holder was designed to move with the subject's shank, and another thigh holder was designed to fix the BTSA on user's leg. The results of the three control methods are discussed below.

The experimental results of the zero-impedance control are shown in Fig. 5-13. The first two figures are the extensor EMG signal and flexor EMG signal, respectively. In the preprocessing, the raw EMG signal is first rectified and then the filtered by the Kalman filter [4], which is used as a lowpass filter. The filter makes the feedback EMG signal smoother and the user may feel more comfortable in practice. The third figure is the estimated human intention $\hat{\tau}_H$. The calibration of the linear EMG model is carried through a slow motion experiment, in which the position of the output

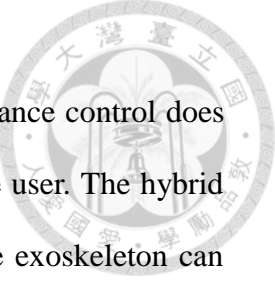


link x_o is fixed as the user extends and flexes the knee joint slowly, and the feedback information are the torsion spring torque τ_E and the filtered EMG signals. The bottom figure shows the knee joint angle x_o and the exoskeleton force τ_E . The exoskeleton force τ_E is nearly zero under the zero-impedance control as expected. The result is that the subject still needs to move the lower limb by himself, but the mechanism resistance is lowered. Therefore, the EMG signals of the extensor and the flexor are larger than that of the other two controls.

The results for the intention feedback control with $\tau_{H,ref} = 0$ are shown in Fig. 5-14. However, the estimated human intention $\hat{\tau}_H$ is not zero even with the assistance. The main reason is that the EMG noise is large and influences the performance greatly. Compared to the zero-impedance control in Fig. 5-10, the assistance is still valid.

Fig. 5-15 shows the results of the hybrid control, where the threshold $\tau_{thre} = \tau_{H,ref}$ is set as 1.3 in this experiment. Although the controller does not track perfectly, the hybrid control helps the user exercise with smaller torque than that in the zero-impedance control, and provides assistance forces stably and robustly. Comparing the exoskeleton torques τ_E in the intention feedback control and the hybrid control, it shows that the hybrid control assists the user as needed, but the intention feedback control assists whenever the muscle contracts. Compared with the zero-impedance control, τ_E is zero in the hybrid control only when muscle contraction is small. It is because when the estimated human torque is larger than the threshold, the EMG feedback control takes over.

Comparing all the three control approaches, it shows that the hybrid control outperforms other two control methods. The main reason is that for small EMG



signals, the simple linear model fits poorly, and that the zero-impedance control does not support only the weight of the exoskeleton, not the body of the user. The hybrid control, on the other hand, is more suitable for human, because the exoskeleton can provide the assistance robustly and overcomes the mechanical impedance due to the deadzone as in [71]. Because the noise level of the EMG signal is larger than other torque sensors, a wide dead zone is usually necessary for the stability. However, in the dead zone, the user wastes energies to overcome the resistance from the mechanism. In contrast, the zero-impedance control in the hybrid scheme can solve this problem easily, and therefore the interaction is more comfortable than using either of the controllers alone, leading to the effective gain $G(t) > 1$ consistently. However, the hybrid control may not be suitable for the severe patients with feeble muscle forces and abnormal muscle activations. In such situations, there should be another mechanism to detect of the spasticity and the co-contraction, where the controller stops the movement and fixes at the current position in order to protect the muscle from danger.

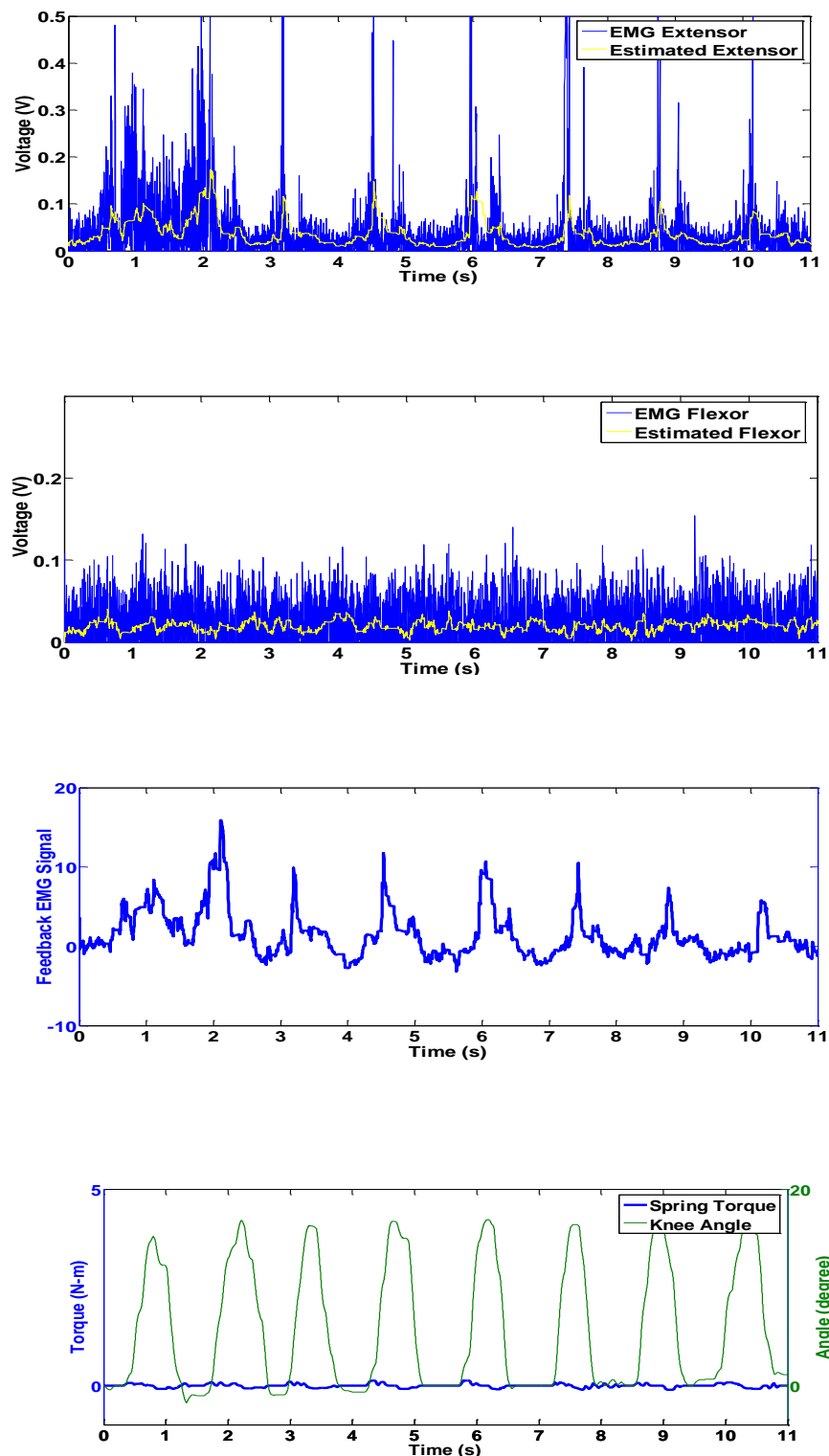


Fig. 5-13. Experimental results of the zero-impedance control

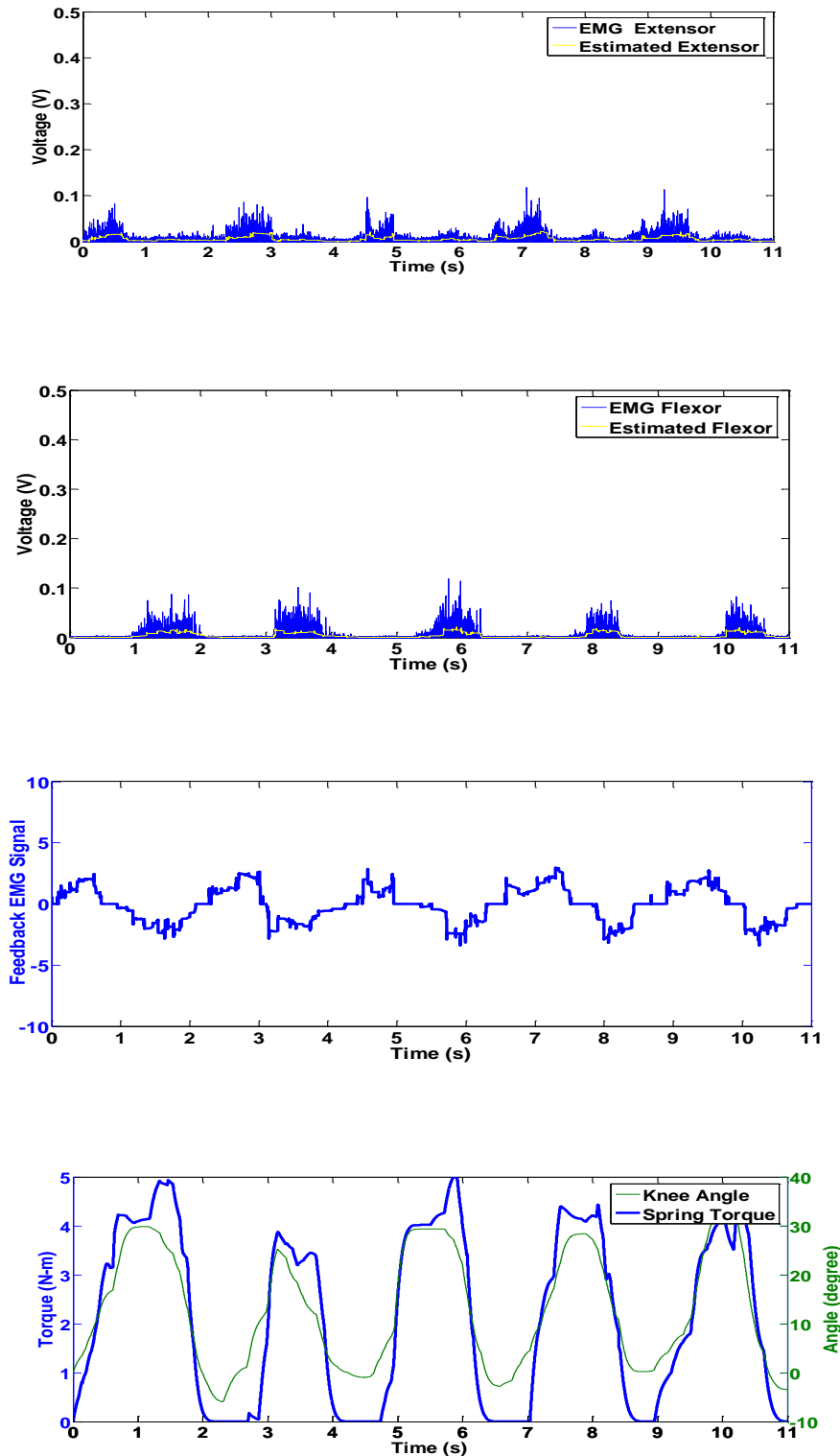


Fig. 5-14. Experimental results of the intention feedback control

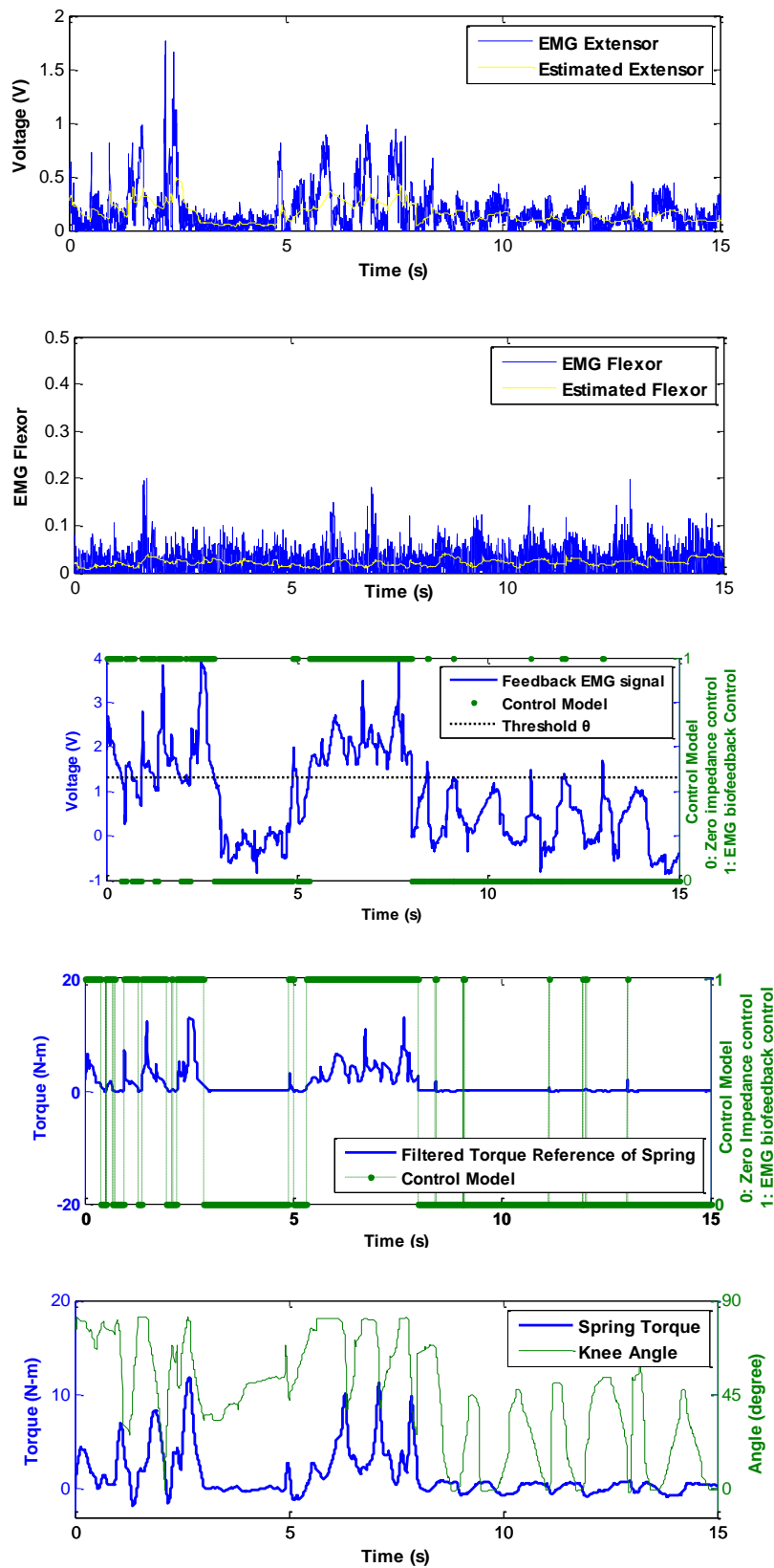


Fig. 5-15.Experimental results of the hybrid control



5.2.6 Discussions

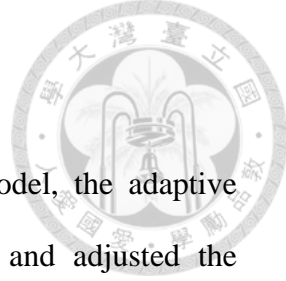
In Section 5.2, a robust hybrid control scheme with the new BTSA, was proposed as a new way to assist humans in walking and rehabilitation. By introducing an insensitive zone, the hybrid scheme is proved to provide robust system and be robustly stable.

Considering the mechanism of human muscles, the proposed control can deal with possible muscle degenerations while successfully assisting human motion. Namely, this mechanism not only considers the assistance method when performing large movements or carrying the loads, but also considers control methods when assistance is not needed. The proposed system combines intrinsic safety with performance, and provides flexibility for the users with different movement abilities by setting different thresholds. In the future, more experiments should be conducted. The optimization of BTSA stiffness is also an important issue for performance and safety tradeoff. In summary, the proposed BTSA approach with the hybrid control helps the patients with weak muscle ability, the elderly, and even those with normal abilities.

5.3 A Simple Self-Learning Scheme

5.3.1 Introduction

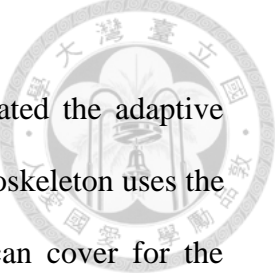
Human intention estimation is important for assistive lower limb exoskeleton, and the task is realized mostly by the dynamics model or the EMG model. Although the dynamics model offers better estimation, it fails when unmodeled disturbances come into the system, such as the ground reaction force. On the contrary, the EMG model is non-stationary, and therefore the offline calibrated EMG model is not



satisfactory for long-time operation.

Considering the unmodeled disturbance in the dynamics model, the adaptive control in Knee Orthosis [80] tracks the predefined trajectory and adjusted the dynamics parameters online. In [68], they identified the parameters of the model for the lower limb offline, and controlled the knee orthosis by the high-order sliding model controller to overcome the uncertainty of the online parameter estimation. Because the robots in [68, 80] are used in rehabilitation, the position trajectories are predefined by the doctor or the user. No online feedback of the operator's intention is presented, yet it is crucial to estimate the human intention and to control the robot accordingly for assistive exoskeletons.

Combing the benefits of both the dynamics model and the EMG model, we propose the self-learning scheme for human walking assistance with the sliding mode admittance control. During the swing phase, the inverse dynamics model estimates the human intended torque and teaches the EMG model with the estimation. The taught EMG model is then used in the consecutive stance phase to overcome the disturbance uncertainty in the dynamics model, such as the ground reaction force. The self-learning scheme updates the parameters of the EMG model so that it can adapt to the time variant nature. In summary, the estimator of the human intended torque switches between the dynamics model and the EMG model in the swing phase and in the stance phase, respectively, so the most accurate estimate of the two models can always be used for the assisting. With the estimation, we treat the human intention as the forced response of the estimated human intended torque exerting on a second-order linear system - the admittance interface. Finally, the sliding mode controller is used to overcome the uncertainties of modeling errors and disturbances.



To the best of our knowledge, no other papers have investigated the adaptive estimation of the EMG model via self-learning. Our self-learning exoskeleton uses the dynamics model to teach EMG model so that the EMG model can cover for the dynamics model when needed. The hybrid scheme overcomes the insufficiency of using only a single model alone. Compared to [44], the dynamics model, identified offline, serves as the supervisor and teaches the EMG model online in this paper, whereas Cheng et al. [44] use the Bayesian committee machines to combine the two models, which are both trained offline. Finally, the control scheme is justified by the knee orthosis with the backdrivable spring torsion actuator in Section 5.3.4, and the experimental results are prominent.

This section is organized as follows. Section 5.3.2 gives the knee orthosis system, and the modeling. In Section 5.3.3, we described the self-learning scheme and the sliding mode admittance control. In Section 5.3.4, we verify the performance of the proposed scheme in simulations and experiments, and the results are discussed. Finally, we give a short summary in Section 5.3.5.

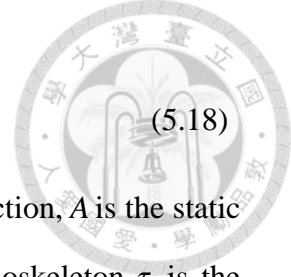
5.3.2 Knee Orthosis System and Modeling

A. Exoskeleton System

The exoskeleton system comprises the knee orthosis system and the footswitch as mentioned in Section 5.2.2. The knee orthosis system is driven by a backdrivable spring torsion actuator (BTSA) and, the soft stiffness of the BTSA provides mechanically intrinsic safety and measures the torque between the human and the actuator. For details, please refer to [46], Section 5.2 and therein.

B. The Dynamics Model and the Biosignal Model

The dynamics model of the human-knee orthosis system is given by:



$$M\ddot{q} + B\dot{q} + A\text{sign}(\dot{q}) + G\sin(q) = \tau_E + \tau_h + \tau_g , \quad (5.18)$$

where q is the angular position, M is the inertia, B is the viscous friction, A is the static friction, G is the gravity torque, τ_E is the external torque of the exoskeleton, τ_h is the external torque of the human muscle, and τ_g is the external torque of the ground reaction force, which is assumed to be zero during the swing phase. The parameters of the dynamics model are calibrated offline in the experiments.

As in Section 5.2.3.C we use the linear combination of the filtered EMG signals, the flexor E_f and the extensor E_e , as the EMG model. That is,

$$\hat{\tau}_h = a_e E_e + a_f E_f + a_{bias} , \quad (5.19)$$

where a_e , a_f , a_{bias} are the unknown parameters to be identified. Although more sophisticated EMG models are possible, in our experience, the linear model suffices to predict the human intended torque.

C. Offline System Identification

In this section, we describe how the unknown coefficients in (5.18) and (5.19) are identified offline. Unlike the EMG model, the dynamics model identified offline can predict with high accuracy as long as no unmodeled dynamics is neglectable, since it is time invariant. The EMG model, however, can only approximate locally due to the unmodeled uncertainties and the slow variation of the parameters over time. Therefore, the identification of the dynamics model is carried offline, whereas the EMG model learns online from the dynamics model in the swing phase with the initial parameters identified offline.

The task for the identification of the dynamics model is shown in Fig. 5-16 (a).

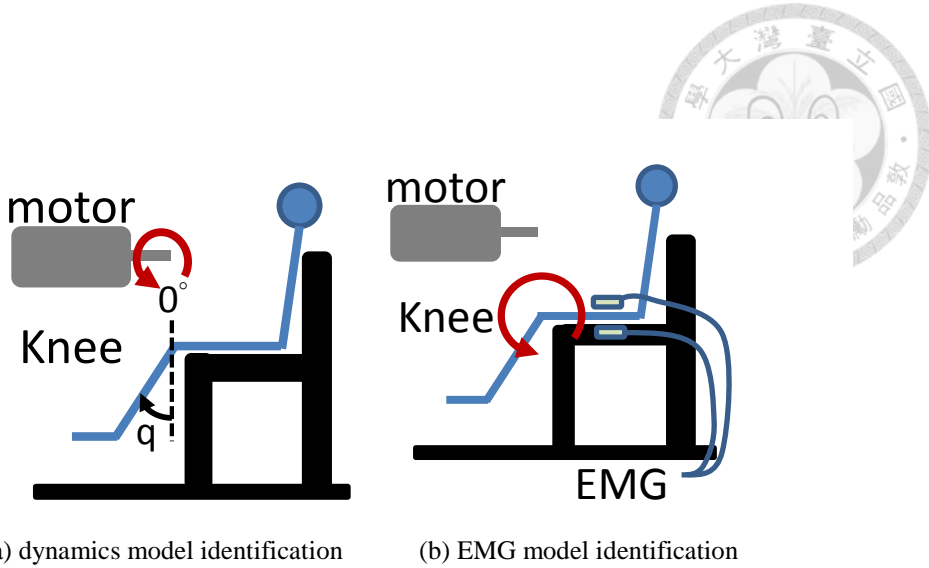


Fig. 5-16. Offline dynamics and EMG model identification

During this task, the user needs to relax totally such that τ_h can be approximated to be zero. The system model becomes

$$\tau_E = M\ddot{q} + B\dot{q} + A\text{sign}(\dot{q}) + G \sin(q) \quad (5.20)$$

The stimulus signals are the sinusoidal position trajectories of q with different frequencies. The filtered angular position q , the angular velocity \dot{q} , the angular acceleration \ddot{q} , and the torque τ_E are collected to identify the unknowns by the ordinary linear regression.

The task for the EMG model identification is shown in Fig. 5-17 (b). During this task, the user tries to exercise his leg, while the knee angle is fixed to be a constant position by the position controller. The system model becomes

$$-\tau_E = \tau_h = a_{e_0}E_e + a_{f_0}E_f + a_{bias_0}, \quad (5.21)$$

and the identified parameters $\Theta_0 := [a_{e_0}, a_{f_0}, a_{bias_0}]$ are used as the initial condition for the online learning.



5.3.3 Self-learning Scheme and Sliding Mode Admittance Control

The general idea of the exoskeleton control is to exert the force desired by the operator. We believe that human reduces the muscle force when feeling the positive feedback. Therefore, the exoskeleton can assist the operator and reduces the payloads by providing the desired force.

We classify the walking phases into the *swing phase* and the *stance phase*, and the controller switches in between according to the footswitch. In the swing phase, the dynamics model identified offline is used to estimate the human intended torque, and to teach the EMG model; in the stance phase, the EMG model becomes the estimator. In both phases, the admittance interface transfers the estimated torque of either the dynamics model or the EMG model to the position command, and effectively filters

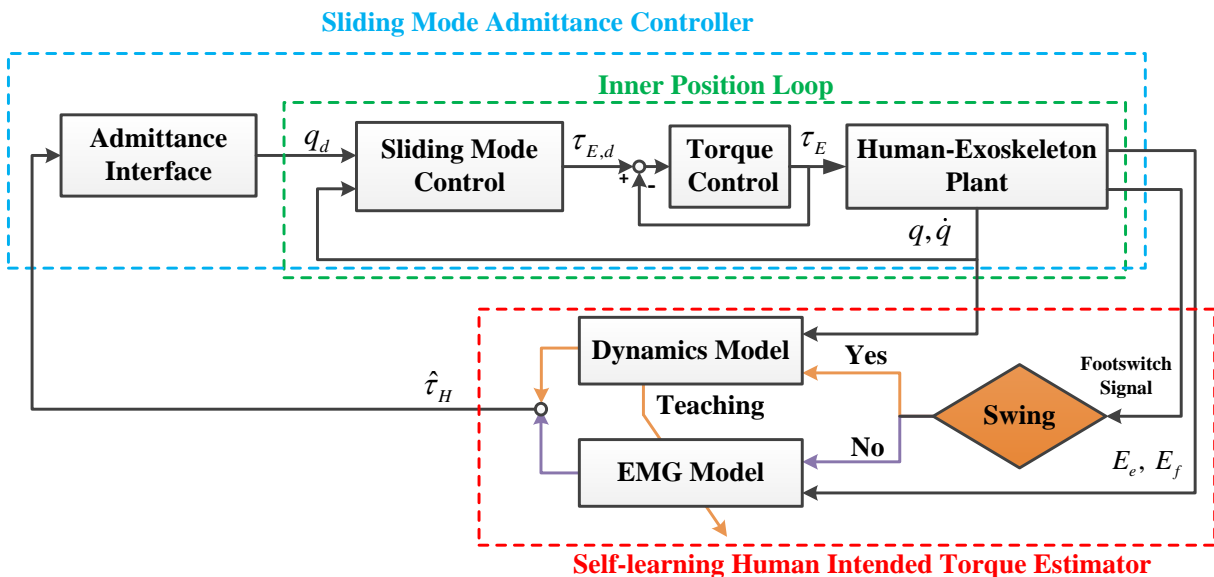


Fig. 5-17. The self-learning control scheme of the exoskeleton system



the discontinuities of the switching. Therefore, the reference position trajectory for the inner position controller is continuously differentiable, and is tracked by the sliding mode controller in the inner position control loop. In summary, the exoskeleton system consists of two control loops. The upper control loop estimates the human intention and learns online; the lower control loop tracks the reference trajectory robustly by the sliding mode controller, as shown in Fig. 5-17.

A. *Self-Learning Scheme*

Self-learning, also called self-training, is a technique for semi-supervised learning. Semi-supervised learning [113] is a methodology of machine learning and used in the scenario where accessing the labeled data is hard or expensive. The semi-supervised learning machine takes into account both the labeled and the unlabeled data to improve the performance. In the supervised step, the machine is first trained with the small amount of labeled data, and then it is used to predict the unlabeled data. During the unsupervised process, the machine labels parts of the confident unlabeled data and retrains. We found the mechanism very suitable for the exoskeleton. In our case, the exoskeleton learns offline with the data collected from the strictly controlled experiments, which is time consuming if large amount of data are in need. In the unsupervised step, the machine labels the unlabeled data by the dynamics model, and the newly labeled data are used to teach the EMG model. In this design, the exoskeleton system consists of a weak learner, the EMG model, and a strong learner, the dynamics model. In spite of the ability, the strong learner can only be used in the restricted domain, and therefore the strong learner has to teach the weak learner to compensate the deficits. That is, in the swing phase, the dynamics model teaches the EMG model, since it is accurate in absence of external disturbances. And



then the EMG model takes over when the dynamics model fails. We detail the process as follows.

In the swing phase, using (5.18) with the parameters identified offline and τ_E measured by the BTSA, the dynamics model can estimate the human intended torque. The estimation is used to teach the EMG model by the following adaptive law with the initial parameters identified offline in (5.21). From (5.18) and (5.19),

$$\begin{aligned} & M\ddot{q} + B\dot{q} + A\text{sign}(\dot{q}) + G\sin(q) - \tau_E \\ & \approx a_e E_e + a_f E_f + a_{bias} \end{aligned}, \quad (5.22)$$

so the human intended torque can be measured by the dynamics model with

$$z := \frac{[M\ddot{q} + B\dot{q} + A\text{sign}(\dot{q}) + G\sin(q) - \tau_E]}{\Lambda(s)} = \boldsymbol{\theta}^{*T} \boldsymbol{\Phi}, \quad (5.23)$$

where $\boldsymbol{\theta}^{*T} = [a_e^*, a_f^*, a_{bias}^*]^T$ is the optimal parameter with respect the \mathcal{L}^2 -norm error,

$$\boldsymbol{\Phi} = [\Lambda(s)^{-1} E_e, \Lambda(s)^{-1} E_f, \Lambda(s)^{-1}]^T$$

is the regressor vector, and with the abuse of notation, $\Lambda(s)$ denotes Hurwitz system, which is chosen as the Butterworth lowpass filter in the experiments, and s is the variable of Laplace transform. Let the empirical estimation be

$$\hat{z} = \tilde{\boldsymbol{\theta}}^T \boldsymbol{\Phi}, \quad (5.24)$$

where $\tilde{\boldsymbol{\theta}} = [\hat{a}_e, \hat{a}_f, \hat{a}_{bias}]^T$ is estimated parameters. The error between the measurement and estimation is given as

$$\varepsilon = \frac{z - \hat{z}}{m_s^2} = \frac{\tilde{\boldsymbol{\theta}}^T \boldsymbol{\Phi}}{m_s^2}, \quad (5.25)$$

where $\tilde{\boldsymbol{\theta}} = \boldsymbol{\theta} - \hat{\boldsymbol{\theta}}$, and m_s is the normalization factor such that $\boldsymbol{\Phi} / m_s^2 < \infty$. Considering the cost function $J(\boldsymbol{\theta})$,

$$J(\boldsymbol{\theta}) = \frac{\varepsilon^2 m_s^2}{2} = \frac{(\tilde{\boldsymbol{\theta}}^T \boldsymbol{\Phi})^2}{2m_s^2}, \quad (5.26)$$



the adaptive law is given by taking the negative gradient of $J(\boldsymbol{\theta})$, that is

$$\dot{\boldsymbol{\theta}} = -\gamma \nabla J(\boldsymbol{\theta}) = \gamma \varepsilon \boldsymbol{\Phi}, \quad \boldsymbol{\theta}(0) = \boldsymbol{\theta}_0, \quad (5.27)$$

$$\nabla J(\boldsymbol{\theta}) = -\frac{(z - \boldsymbol{\theta}^T \boldsymbol{\Phi})}{m_s^2} \boldsymbol{\Phi} = -\varepsilon \boldsymbol{\Phi}, \quad (5.28)$$

where $\gamma > 0$ is the learning rate. Let

$$V := \frac{1}{2\gamma} \|\tilde{\boldsymbol{\theta}}\|_{\ell^2}^2 \geq 0 \quad (5.29)$$

be the Lyapunov function. The adaptive law is stable since

$$\dot{V} = \frac{\tilde{\boldsymbol{\theta}}^T d\tilde{\boldsymbol{\theta}}}{\gamma dt} = -\frac{(\tilde{\boldsymbol{\theta}}^T \boldsymbol{\Phi})^2}{m_s^2} = -\varepsilon^2 m_s^2 \leq 0. \quad (5.30)$$

B. Sliding Mode Admittance Control

The sliding mode admittance control consists of the admittance interface, the sliding mode controller, and the PD torque controller. The main advantages of sliding mode admittance control are that the admittance interface in fact acts as a low pass filter, so the tracking position trajectory is smoother than the estimated human intended torque, and that the sliding mode controller can handle the uncertainty of the modeling errors and the disturbance robustly. Compared to the methods [68, 80, 108, 112] that compensates only impedance of the dynamics, the main difference here is that the human intended torque is also considered, and therefore the assistance is more direct and more precise.

The admittance is used to model the relationship between the human intended force and the relative angular position,

$$M_h(\ddot{q}_d - \ddot{q}) + B_h(\dot{q}_d - \dot{q}) + D_h(q_d - q) = \hat{\tau}_h \quad (5.31)$$

where M_h , B_h , and D_h are user-specific dynamics parameters, q_d is the desired trajectory of the output link, q is the current position, and $\hat{\tau}_h$ is the estimated human intended torque. The desired trajectory is forced response of the second-order system,



so it is continuously differentiable. Note that, (5.31) is the compliance control in the impedance control literatures, so exoskeleton follows smoothly regardless of the discontinuities in the estimated human intended torque.

With the desired trajectory from the admittance interface, the sliding mode controller uses the sliding surface to generate the torque command, which is tracked by the PD torque controller.

The nominal model of the human-exoskeleton system can be modeled as

$$\ddot{q} = \hat{f} + \hat{M}^{-1}\tau_E + \delta \quad (5.32)$$

$$\hat{f} = -\frac{1}{\hat{M}}[\hat{B}\dot{q} - \hat{G}\sin(q) + \hat{\tau}_h] \quad (5.33)$$

where $\hat{\tau}_h$ is the estimated human intended torque, \hat{M} , \hat{B} , \hat{G} are the estimated parameters, $\|\delta\|_\infty < D$ is contribution of all the modeling uncertainties and the disturbances and is bounded by some constant $D < \infty$. Notice that we include the static friction term $A\text{sign}(\dot{q})$ in δ so that the nominal plant (5.32) is bounded and continuous. In order to let the system track $q \approx q_d$, the sliding surface $S = 0$ is defined as (5.34)

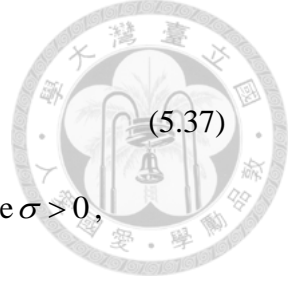
$$S = \dot{\tilde{q}} + \lambda\tilde{q} \quad (5.34)$$

$$\dot{S} = \ddot{q} - \ddot{q}_d + \lambda\dot{\tilde{q}} = f + \hat{M}^{-1}\tau_E + \delta - \ddot{q}_d + \lambda\dot{\tilde{q}}, \quad (5.35)$$

where $\tilde{q} = q - q_d$ and $\lambda > 0$. Assuming $\hat{M}(f + \delta - \ddot{q}_d + \lambda\dot{\tilde{q}}) < \infty$, to achieve $\dot{S} = 0$, we set

$$\bar{\tau}_E = \hat{M}(-f + \ddot{q}_d - \lambda\dot{\tilde{q}}). \quad (5.36)$$

To satisfy the sliding condition under the uncertainty d , the torque reference is designed as (27).



$$\tau_{E,d} = \bar{\tau}_E - \sigma \hat{M} \text{sat}(S / \beta), \quad (5.37)$$

which is the torque reference for the inner torque control loop, where $\sigma > 0$,

$$\text{sat}(x) = \begin{cases} x, & \text{if } |x| \leq 1 \\ \text{sgn}(x), & \text{if } |x| > 1 \end{cases}$$

$\text{sgn}(\cdot) = \{\pm 1, 0\}$ denotes the sign function, and $\beta > 0$ is the thickness of the boundary layer. Choose the Lyapunov function as

$$V_1 = \frac{1}{2} S^2 \geq 0 \quad (5.38)$$

Set $\eta > 0$, we can show that for $|S / \varepsilon| > 1$

$$\dot{V}_1 = \frac{1}{2} \dot{S} \cdot S = [\delta - \sigma \text{sgn}(S)]S < -\eta |S| < 0. \quad (5.39)$$

Therefore, $\{S \mid |S / \beta| \leq 1\}$ is positively invariant. Inside the boundary layer, take

$$V_2 = \frac{1}{2} \tilde{q}^2 \quad (5.40)$$

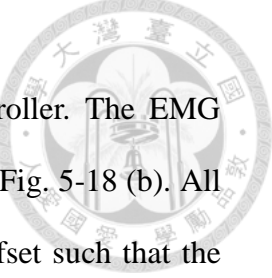
and we have

$$\dot{V}_2 = \tilde{q}(S - \lambda \tilde{q}) < -\lambda(1 - \theta)\tilde{q}^2 < 0 \quad (5.41)$$

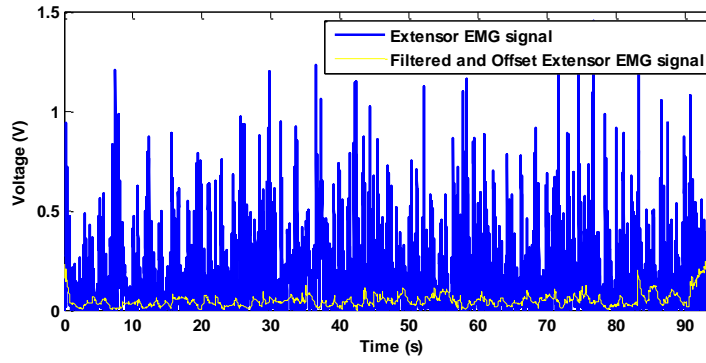
for $|\tilde{q}| \geq (\theta\lambda)^{-1}|S|$, where $0 < \theta < 1$. The error \tilde{q} is ultimately bounded in the ball $|\tilde{q}| < (\theta\lambda)^{-1}|S|$.

5.3.4 Experimental Results

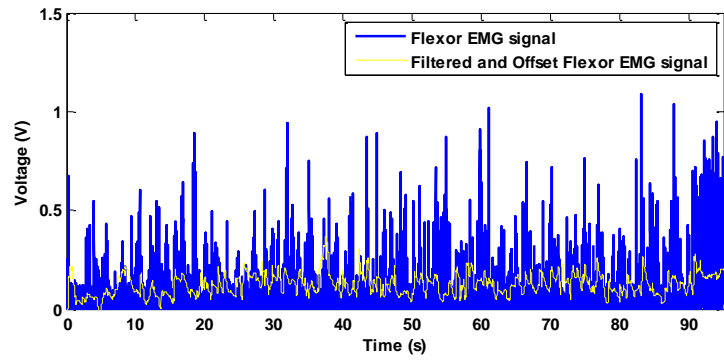
In the experiments, the subject is a healthy 32-year-old male, and he is asked to climb the stairs up and down with the BTSA knee orthosis. Before the task starts, the exoskeleton system is calibrated offline according to Section II. During the task, the self-learning exoskeleton estimates the human intended torque with the dynamics model and the EMG model in the swing phase and the stance phase, respectively. And



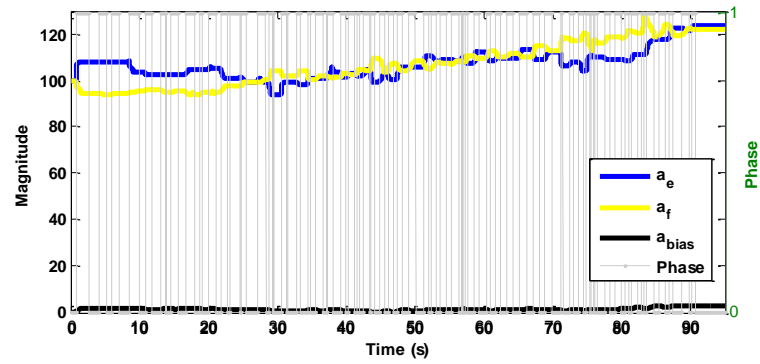
then the estimation is used for the sliding mode admittance controller. The EMG signals of the extensor and the flexor are shown in Fig. 5-18 (a) and Fig. 5-18 (b). All the EMG signals are rectified, filtered by the Kalman filter, and offset such that the EMG signal is zero when muscles are totally relaxed. Fig. 5-18 (c) shows how the EMG model learns during the task with the initial parameters identified offline. In each swing phase, the EMG model is updated to adapt to current condition, and the result shows the parameters of the EMG model fluctuate with time. The bias term remains almost constant while the parameters of the flexor and the extensor vary slowly. This is because, to approximate the nonlinear model, the linear model is only valid locally, and the electric resistance between the electrodes and the operator changes with time due to sweats and slipping. Therefore, it is necessary to learn the EMG model online.



(a)



(b)



(c)

Fig. 5-18. (a) The EMG signal of the extensor. (b) The EMG signal of the flexor.

(c) The parameters of the EMG model.

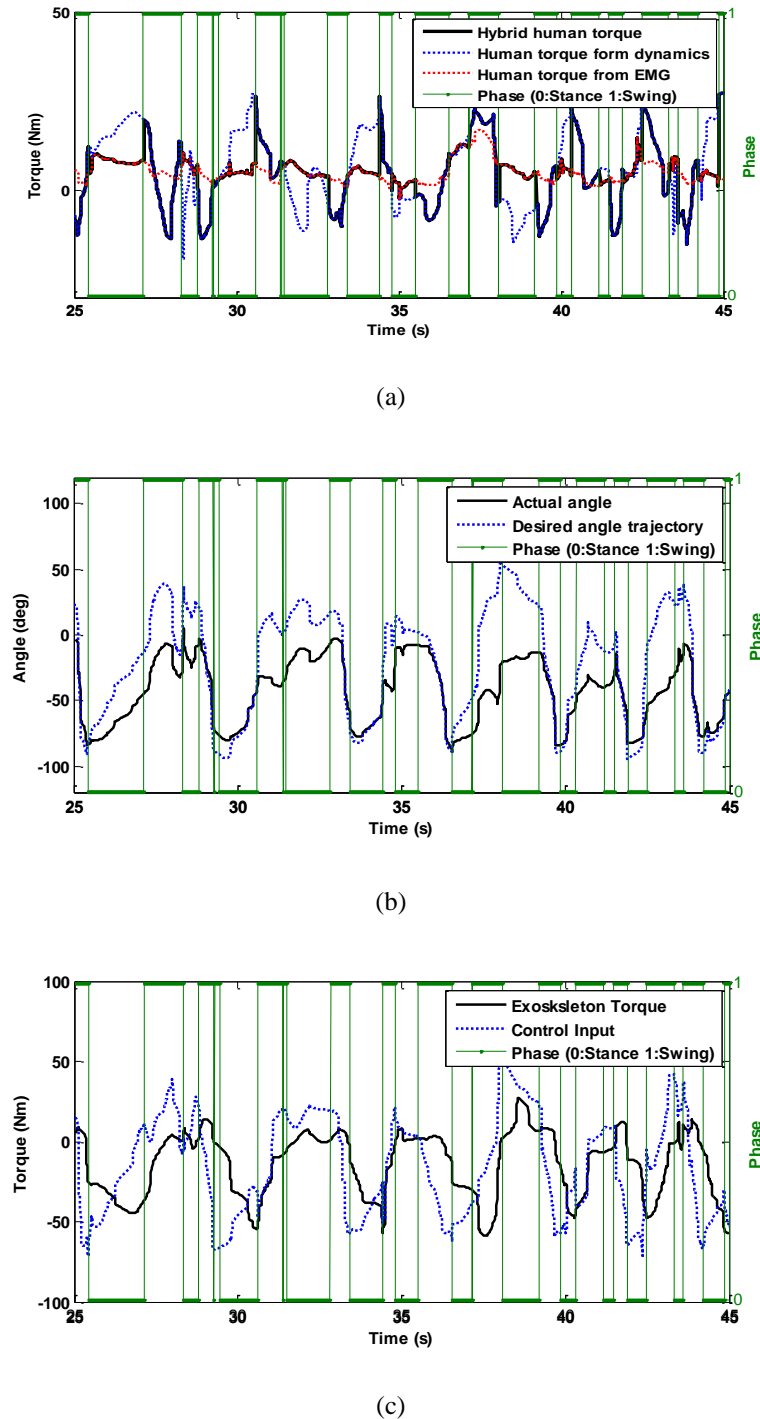
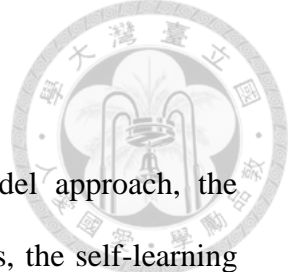
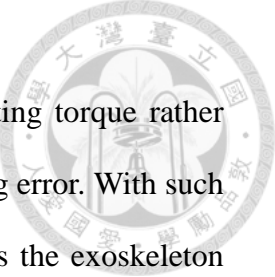


Fig. 5-19(a) The self-learning estimator, the dynamics model, and the EMG model. (b) The actual angle and the



To compare the self-learning estimator and the single model approach, the estimations are shown in Fig. 5-19 (a). Combining the two models, the self-learning estimator switches between the two models according to the gait phase. In the swing phase, the EMG model tries to learn from the dynamics model, so it can encounter the uncertainties in the stance phase. We observe that the dynamics model overestimate the human intended torque in the stance phase, because it includes the torques from the disturbance and the exoskeleton. Indeed, when climbing, the hamstrings and the quadriceps exert the most in the swing phase and relax in the stance phase. This accounts for the estimation of the EMG model. Therefore, if we use the dynamics model in all the phases, the operator might be easily injured by the large forces provided by the exoskeleton in the stance phase, since it not only amplifies the human intended torque but also the torque due to exogenous disturbance. In this case, the operator has to exert large forces to compensate the disturbance, which is the major defects of most of the exoskeleton with only the dynamics model. Fig. 5-19 (b) shows the reference position from the admittance interface. Despite the discontinuity of the torque estimation in Fig. 5-19 (a), the desired position trajectory is continuously differentiable owing to the second-order system. Finally, the torque command of the sliding mode controller is shown in Fig. 5-19 (c).

In the implementation, the sliding mode control plays an important figure. As discussed, the thickness of the boundary layer trades off the magnitude of the chattering and the tracking error. In contrast to the conventional sliding mode controller used in the tracking, we design our sliding mode controller with large boundary layer. Augmented on human, the success of an assistive controller relies



more on the smoothness, the phase, and the direction of the assisting torque rather than the actual value of the supporting force and the position tracking error. With such knowledge, the boundary layer should be large as long as it pushes the exoskeleton from large tracking errors; inside the boundary, the sliding mode control is actually a proportional feedback controller providing smooth assisting.

In the experiments, we observe that the optimal parameters of the admittance interface vary with the configurations and the tasks. It is interesting that human expect different impedance with various poses. We suggest identifying the task-dependent impedance and using the gain scheduling technique to control the impedance system in the future works. Also, the learning rate affects the performance of the EMG model much. With small learning rate, the EMG model cannot learn fast enough within the short swing phase, while the learning becomes more unstable when large learning rate is used. Therefore, the learning rate trades off the performance and the stability. We hope this can be addressed by incorporating the adaptive learning rate and the Hessian matrix. Finally, we are considering whether the robust control approach is suitable in the application of exoskeleton. Most of the robust control uses finite bounds for the disturbances and the uncertainty, and forces the tracking error to stay within some bounded domain. On the other hand, the interaction with human does not emphasize the absolute error. Indeed, only the bandwidth and smoothness matters. In our experience, human seems to be able to adapt to the errors easily as long as the bandwidth is limited.

5.3.5 Discussions

In this section, we propose the self-learning scheme with the sliding mode admittance controller for the assistive exoskeleton system. The self-learning scheme



combines both the dynamics model and the EMG model to achieve better performance. In the swing phase, the dynamics model teaches the EMG model, so that the estimated human intended torque can tolerate the disturbance uncertainties in the stance phase. With the estimated human intended torque, the sliding mode admittance controller assists the operator robustly. Despite the discontinuity of the switching, the desired position trajectory is smooth owing to the admittance interface. In the experiments, we justify the control scheme with the BTSA knee orthosis. The results are satisfactory, and show the deficiency of single dynamics model. In the future works, we want to address the issue of pose-dependent desired impedance and design a more sophisticated self-learning scheme.

5.4 Bayesian Exoskeleton System

5.4.1 Introduction

According to the previous sections, an exoskeleton system consists of two parts: intention estimation and assistive control. The estimation of the human intention provides the adaptivity of the system, so the operator can move freely wearing the exoskeleton; the assistive control should be robust against the estimation noise and the modeling uncertainties, so the safe interaction between human and robot can be guaranteed. This section proposes a novel Bayesian estimation human estimator for general exoskeleton. Together with the robust hybrid control scheme in Section 5.2, the Bayesian exoskeleton system can assist the operator freely and robustly. Taking the advantages of both the dynamics model and biosignal model, the proposed Bayesian human torque estimator based on the probabilistic graphical model. Combined with the assistive toque controller and the knee orthosis in [45], the resultant Bayesian exoskeleton system can adaptively perform the optimal sensory



fusion in the Bayesian sense to infer the human applying torque, which is used generate thereafter the reference trajectory in the robust assistive controller to provide assistance for the operator.

The major contribution of this section is the construction of the graphical model of the human-exoskeleton system. We treat all the measurements, the biosignals and the states of the dynamics model, as random variables, and use the graphical model to model the dependency of the variables. With the graphical model, the *a posteriori* probability of the human applying torque can be easily inferred by optimally combining the information of the biosignal model and the dynamics model. The major breakthrough in this model is the structure of the *Naïve Bayesian assumption*, so that the biosignal model and the dynamics model are independent once the true human intention is known, which corresponds to the common intuition. In the graphical model, three Gaussian process models are used to model the conditional probabilities: the biosignal model, the inverse dynamics model, and the exogenous disturbance model. Also, the experiments needed to learn the conditional probabilities are given in details. Remarkably, the proposed Bayesian framework is general in the sense it does not specify the particular form of the sensors. For example, the biosignal is not limited to the EMG signals; the exogenous disturbance can be as simple as the footswitch, which is the case in our experiments. The Bayesian human torque estimator can optimally use the sensory information to infer the human intention.

In the experiments, we show the calibration of the Gaussian process models, and verify the proposed Bayesian exoskeleton system by demonstrating two types of motions: the swing motion, as the toy example, and the stair climbing task to resemble the possible scenarios in the real applications. Despite the adoption of the simple



footswitch, the experimental results of the proposed Bayesian exoskeleton system are prominent, and the performance index in the experiments is close to the theoretical bound.

This section describes the modeling of the human-exoskeleton system in the Bayesian fashion, which is the major contribution of this chapter. By using the graphical model, the dependencies of each states of the system are clear as indicated by the factorization of the joint probability. The main purpose of the model is to infer the human intention. In this context, by human intention, we mean the intended applying torque of the operator on the human-exoskeleton system. The estimation of the intended applying torque is critical in the application of the exoskeleton system. Once the estimation is obtained, the assistive control is designed under the scheme of our previous work [45].

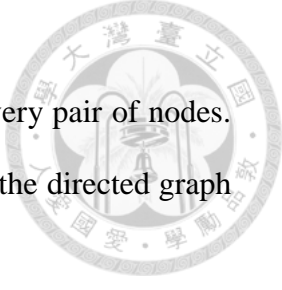
5.4.2 Bayesian Network and Gaussian Process Revisited

In this section, we review the essence of the graphical model and the Gaussian process regression that will be used in the following section. Please refer to [5] for the details.

A. Bayesian Network and Graphical Model

The Bayesian network is known as the directed graphical model in which the links has particular directionality indicated by the arrows. Each node in the graph represents a random variable; the directed link indicates the factorization of joint probability, and each directed link represents the conditional probability. If there is a link that goes from node a to node b , we say a is the parent of b , and b is the child of a . Also, the joint probability of a and b can be factorized into

$$p(a,b) = p(b | a)p(a).$$



We say a graph is fully-connected if there is a link between every pair of nodes. In particular, we consider here the directed acyclic graphs, which is the directed graph without cycle.

One of the features of the directed graphical model is that the conditional independence can be easily inferred from the structure of the graph. This call *d-separation*, shorted for directed separation, and the definition is given as follows.

Definition 5.6.

Let A , B , and C be arbitrary non-intersecting sets of nodes in a directed acyclic graph.

A path along the links from A to B is blocked if one of the following holds:

- (1) There exists a node in the set C that the arrows in the path pass either head-to-tail or tail-to-tail, or
- (2) the arrows in the path pass a node head-to-head, and neither the node itself, nor any of its descendants is in the set C .

If all paths from A to B are blocked when observing C , then we say A is d-separated from B by C , and the graph implies that A and B are conditionally independent given C , i.e. $P(A, B | C) = P(A | C)P(B | C)$.

In the graphical model, each arrow denotes the conditional probability and the structure of the graph indicates the factorization of the joint probability of all the random variables. Together with the d-separation property, the *a posteriori* probability of the node can be inferred by Bayes' theorem. The inference is called maximum *a posteriori* estimation (MAP) in machine learning. Given the prior probabilities, the algorithm can return the model that maximizes the *a posterior* probability of the latent variables after observing the outcomes.



B. Gaussian Process Regression

The Gaussian process regression (GPR) is one of the Bayesian machine learning methods, which can infer the probability distribution of the prediction directly by incorporating the prior knowledge. Let \mathcal{X} and \mathcal{Y} be the input space and the output space with probability measure. Without loss of generality, we assume \mathcal{X} is in a vector space ranging over the real field and $\mathcal{Y} \subseteq \mathbb{R}$. Assume there exists a linear map $f : \mathcal{X} \rightarrow \mathcal{Y}$, that is for all $y \in \mathcal{Y}$ there is $x \in \mathcal{X}$ and the zero-mean Gaussian random variable η with probability distribution $\mathcal{N}(\eta | 0, \beta^{-1})$ such that $y = f(x) + \eta$, where $\beta > 0$ is the precision. If \mathcal{X} is in a subset in Hilbert space \mathcal{H} , for all $f \in \mathcal{H}^*$, Riesz representation theorem shows that there exists one and only one $w \in \mathcal{H}$ such that $f(x) = \langle w, x \rangle_{\mathcal{H}}$, where \mathcal{H}^* is the dual space of \mathcal{H} . We note that the linear functional is not restrictive, since \mathcal{H} can be an arbitrary Hilbert space as long as the inner product can be computed efficiently, e.g. kernel trick [86].

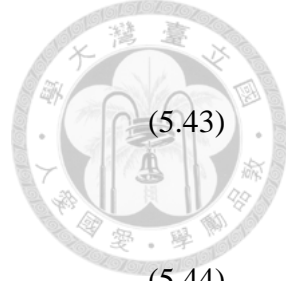
Given M observations, we denote $X = \{x_i \in \mathcal{X} | i \in \mathbb{N}_M\}$ and $Y = \{y_i \in \mathcal{Y} | i \in \mathbb{N}_M\}$. Assuming the observations are independent and identically distributed (i.i.d.) samples from the underlying distribution, the conditional probability can be written as

$$p(Y | X) = \mathcal{N}(\mathbf{y} | \mathbf{X}w, \beta^{-1}\mathbf{I}_N), \quad (5.42)$$

where $\mathbf{X} \in \mathbb{R}^{M \times d}$ is defined as $(x_i^T)_{i \in \mathbb{N}_M}$, $\mathbf{y} := (y_i)_{i \in \mathbb{N}_M}$, and $0 \leq d \leq +\infty$ is the dimension of the Hilbert space \mathcal{H} . Supposing the *a priori* distribution of the function w is a Gaussian distribution in \mathcal{H} , the learning of w , and the prediction of y given a new sample are identically equal to solving the conditional distribution in the joint Gaussian distribution of $P(X, Y)$, given in Appendix A.

Let the *a priori* probability distribution of w is given as

$$p(w) = \mathcal{N}(w | 0, \alpha^{-1} I_d). \quad (5.43)$$



where $\alpha > 0$, and define a new random variable

$$\mathbf{t} := \mathbf{X}w, \quad (5.44)$$

which is the mode of the estimation of the sampled data. The marginal probability of \mathbf{t} is then

$$p(\mathbf{t}) = \mathcal{N}(\mathbf{t} | \mathbf{0}, \mathbf{K}),$$

where $\mathbf{K} := \alpha^{-1} \mathbf{X} \mathbf{X}^T$ is the Grammian matrix with entries defined as $K_{ij}(x_i, x_j) := k(x_i, x_j) = \alpha^{-1} \langle x_j, x_i \rangle_H$, and therefore the marginal probability of Y is

$$p(\mathbf{y}) = \int p(\mathbf{y} | \mathbf{t}) p(\mathbf{t}) dt = \mathcal{N}(\mathbf{y} | \mathbf{0}, \mathbf{C}),$$

where

$$\mathbf{C} = \mathbf{K} + \beta^{-1} \mathbf{I}_M. \quad (5.45)$$

The objective of the Gaussian process distribution is to predict the output given a new query point x_{M+1} , that is the conditional probability

$$p(y_{M+1}(x_{N+1}) | Y, X) = \mathcal{N}(y_{M+1} | m(x_{N+1}), \sigma^2(x_{N+1})),$$

where

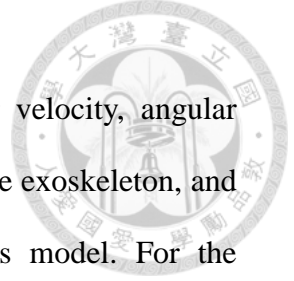
$$m(x_{M+1}) = \mathbf{k}^T \mathbf{C}^{-1} \mathbf{y}, \quad (5.46)$$

$$\sigma^2(x_{M+1}) = c - \mathbf{k}^T \mathbf{C}^{-1} \mathbf{k}, \quad (5.47)$$

$\mathbf{k} := (k(x_{M+1}, x_i))_{i \in \mathbb{N}_M}$, and $c := k(x_{M+1}, x_{M+1}) + \beta^{-1}$.

5.4.3 A Graphical Model for Exoskeleton System

The human-exoskeleton system is modeled as the graphical model according to the causality and the dynamics characteristics. Let e be the measured EMG signal in



the biosignal model; Let q, \dot{q}, \ddot{q} be the angular position, angular velocity, angular acceleration, respectively, τ_E the torque exerted by the actuator of the exoskeleton, and d_{ex} be the exogenous disturbance measurement in the dynamics model. For the universality of the proposed method, we do not limit and therefore do not particularly specify the dimension of the state vectors, e.g. q, e, d_{ex} . Hence, the size of the vectors can vary with different applications.

Apart from the observable random variables defined above, we define the latent random variables: τ_H , the human applying torque, i.e. the human intention, which is the intended applying torque of the operator; τ_D , the transmitted torque of the exogenous disturbance; $\Sigma\tau$ the total torque exerted on the exoskeleton system. These variables are not observable, so they can only be inferred from the observable variables. We remark that we do not assume the specific form of the exogenous disturbance sensor, and that the proposed estimator can automatically optimize the use of information in real time. In the extremity, the disturbance sensor can be just as simple as a footswitch, which is used in our designed exoskeleton. See Section 5.4.5 for more details.

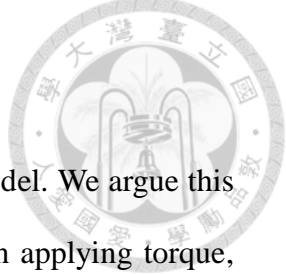
Before proceeding into the details of the graphical model, we summarize the assumptions made in this model.

Assumption 5.7.

1. *The total torque applied on each joint of the exoskeleton and the measured EMG signals e are d -separated by the human applying torque τ_H , i.e.*

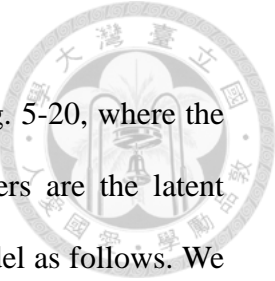
$$p(e, \Sigma\tau | \tau_H) = p(e | \tau_H)p(\Sigma\tau | \tau_H) \quad (5.48)$$

2. *All the random variables defined in the graphical model are independent from time to time. That is, for each sampling time instance, all the random variables are i.i.d.*



samples.

Assumption 5.7.1 is the essential to the proposed graphical model. We argue this is a reasonable assumption, because once we know the true human applying torque, we know the contribution of the operator into the system and therefore the value of the EMG signal become irrelevant. That is, the contribution of the EMG signal e to the total torque $\Sigma \tau$ is blocked when the human applying torque τ_H is observed. On the other hand, Assumption 5.7.2 makes the modeling simpler by neglecting the time dependency of the random variables. Otherwise, hyper-edges can be added into the graphical model to consider the correlation of evolution of different random variables through time, which, in our conjecture, can increase the precision of the prediction and eliminate the noise in the system. One possible way is to consider additionally the contribution of the two previous sampling instances, since the exoskeleton system is essentially a second-order nonlinear system. Canonical state estimation techniques in the system theory can be embedded into this Bayesian formulation easily by defining proper Gaussian distributions, or the extended Kalman filter may be used alternatively. We leave this possibility for the future works, and focus on the model under Assumption 5.7.2.



The graphical model of the exoskeleton system is shown in Fig. 5-20, where the green nodes denote the observable random variables and the others are the latent variables. We now give the detailed description of the graphical model as follows. We assume human is a perfect force controller, so that the EMG signal is determined completely by the human applying torque of the operator, because human is able to adjust the contraction of muscles to track the human applying torque perfectly. In the language of graphical model, the human applying torque node τ_H is the only parent of the EMG signal node e . In the exoskeleton system, there are three torque sources: the human applying torque τ_H , the exogenous torque τ_D , the assistive torque of exoskeleton τ_E . Namely, the identity reads as

$$\Sigma \tau = \tau_H + \tau_D + \tau_E. \quad (5.49)$$

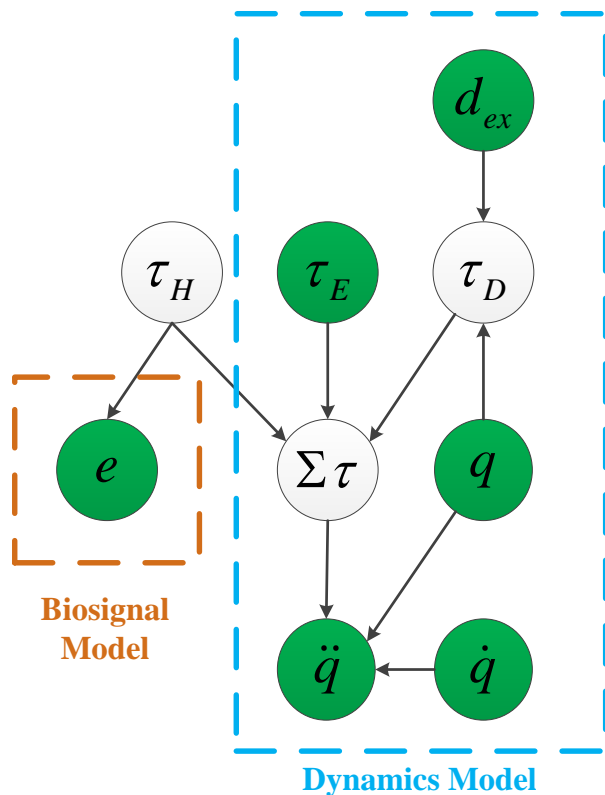


Fig. 5-20. Graphical model of the human-exoskeleton system



On the other hand, the exogenous torque τ_D is related to the exogenous force by the Jacobian matrix of the robot, which is the function of the current configuration q , i.e.

$$\tau_D = J(q)^T d_{ex}. \quad (5.50)$$

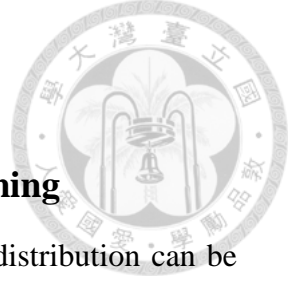
In the end, the last governing equation of the system is the dynamics equation of the human-exoskeleton system, which can be derived from the Euler-Lagrange formulation, that is,

$$M(q)\ddot{q} + B(q, \dot{q})\dot{q} + K(q) = \Sigma\tau, \quad (5.51)$$

where $M(q)$ is the inertia matrix, $B(q, \dot{q})$ is Coriolis/centrifugal matrix, $K(q)$ is the gravity term.

According to Definition 5.6, the path from the sensor information of the dynamics model $d_{ex}, q, \dot{q}, \tau_E$ to the node of the human applying torque τ_H is unblocked when the angular acceleration is observed \ddot{q} . Therefore, the *a posteriori* probability of the human applying torque τ_H can be inferred from the sensory information $d_{ex}, q, \dot{q}, \ddot{q}, \tau_E$ in the dynamics model. In the biosignal model, the observation of the EMG signal e can influence the estimation of the human applying torque τ_H , since it is a descendent of τ_H .

For a time instance, when all the observable random variables are sampled or measured, the *a posteriori* probability of the human applying torque can be inferred by combining the information both of the dynamics model and the biosignal mode. With further inspection, the tree of the human applying torque, the dynamics model, and the biosignal models is actually the Naïve Bayesian assumption. Therefore, the proposed Bayesian human intention estimator is under the framework of *mixture of experts*, in which the two experts are namely the dynamics model and the biosignal



model.

5.4.4 Human Intention Estimation by Bayesian Reasoning

From the graphical model in Fig. 5-20, the joint probability distribution can be factorized into

$$\begin{aligned} & p(e, q, \dot{q}, \ddot{q}, d_{ex}, \tau_E, \tau_D, \tau_H, \Sigma \tau) \\ &= p(e | \tau_H) p(\Sigma \tau | \tau_H, \tau_E, \tau_D) p(\tau_D | d_{ex}, q) \dots \\ & \quad p(\ddot{q} | \Sigma \tau, q, \dot{q}) p(\tau_H) p(\tau_E) p(d_{ex}) p(q) p(\dot{q}) \end{aligned} \quad (5.52)$$

To estimate human intention, it is sufficient to infer the *a posteriori* probability conditioned on all the observable variables,

$$p(\tau_H | e, q, \dot{q}, \ddot{q}, \tau_E, d_{ex}) \sim p(e | \tau_H) p(\tau_H | q, \dot{q}, \ddot{q}, \tau_E, d_{ex}),$$

which is the direct result of Bayes' theorem. By applying Bayes' theorem again, we obtain the factorization

$$p(\tau_H | e, q, \dot{q}, \ddot{q}, \tau_E, d_{ex}) \sim \underbrace{p(\tau_H | e)}_{\text{biosignal model}} \underbrace{p(\tau_H | q, \dot{q}, \ddot{q}, \tau_E, d_{ex})}_{\text{dynamics model}} \quad (5.53)$$

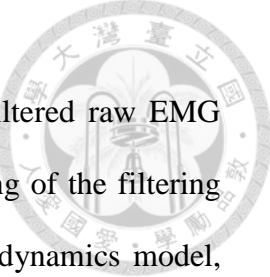
Assume the two conditional probability distribution are two Gaussian distributions with means μ_{Bio} , μ_{Dyn} and covariance matrices Σ_{Bio} , Σ_{Dyn} , i.e.

$$p(\tau_H | e) = \mathcal{N}(\tau_H | \mu_{Bio}, \Sigma_{Bio}), \quad (5.54)$$

$$p(\tau_H | q, \dot{q}, \ddot{q}, \tau_E, d_{ex}) = \mathcal{N}(\tau_H | \mu_{Dyn}, \Sigma_{Dyn}). \quad (5.55)$$

Under the Gaussian assumption and with properly chosen Hilbert space, we can formulate the conditional probability as the Gaussian process model, and the learning problem is then the Gaussian process regression problem, which can be solved easily by solving a linear system.

We now summarize the solution of the Bayesian human intention estimation in the following. The first Gaussian process model is the biosignal model in (5.54). In this model, we assume the human applying torque depends on the EMG signal



linearly. In implementation, the EMG signal is the rectified and filtered raw EMG signal. That is, the Hilbert space (5.42) is the image of the mapping of the filtering from the raw EMG signal to the filtered EMG signal. As for the dynamics model, there are two Gaussian process models: the inverse dynamics model and the exogenous disturbance model.

$$p(\Sigma \tau | q, \dot{q}, \ddot{q}) = \mathcal{N}(\Sigma \tau | \mu_{inv}, \Sigma_{inv}), \quad (5.56)$$

$$p(\tau_D | q, d) = \mathcal{N}(\tau_D | \mu_D, \Sigma_D), \quad (5.57)$$

where μ_{inv} , μ_D and Σ_{inv} , Σ_D are the means and the covariance matrices of the inverse dynamics model and the exogenous disturbance model, respectively. The inverse dynamics is modeled in the feature space by expanding all the unknowns in (5.51), whereas the exogenous disturbance model is in the space of the direct sum of the space of the exogenous disturbance measurement and the space of trigonometric function of q , which is the basis of the Jacobian matrix.

Assume the *a priori* probability distribution of the human applying torque is given as

$$p(\tau_H) = \mathcal{N}(\tau_H | 0, \Sigma_H). \quad (5.58)$$

The dynamics model is the result of combining the two models:

$$\mu_{Dyn} = \Sigma_{Dyn} (\Sigma_{Inv} + \Sigma_D)^{-1} (\mu_{Inv} - \tau_E - \mu_D), \quad (5.59)$$

$$\Sigma_{Dyn} = (\Sigma_H^{-1} + (\Sigma_{Inv} + \Sigma_D)^{-1})^{-1}. \quad (5.60)$$

With the three Gaussian process models (5.54), (5.56), and (5.57), we arrive at the solution of (5.53),

$$p(\tau_H | e, q, \dot{q}, \ddot{q}, \tau_E, d_{ex}) = \mathcal{N}(\tau_H | \hat{\mu}_H, \hat{\Sigma}_H), \quad (5.61)$$

where



$$\hat{\mu}_H = \hat{\Sigma}_H^{-1} (\Sigma_{Bio}^{-1} \mu_{Bio} + \Sigma_{Dyn}^{-1} \mu_{Dyn}), \quad (5.62)$$

$$\hat{\Sigma}_H = (\Sigma_{Bio}^{-1} + \Sigma_{Dyn}^{-1})^{-1}, \quad (5.63)$$

and the estimator is naturally defined as

$$\hat{\tau}_H := \arg \max p(\tau_H | e, q, \dot{q}, \ddot{q}, \tau_E, d_{ex}) = \hat{\mu}_H. \quad (5.64)$$

Proof:

Here we give the proof of the proposed Bayesian human torque estimator from (5.59) to (5.64). We first prove the dynamics model in (5.53). By repetitively applying the Bayes' theorem, we can factorize the dynamics model into

$$\begin{aligned} & p(\tau_H | q, \dot{q}, \ddot{q}, \tau_E, d_{ex}) \\ & \sim p(\tau_H) p(\ddot{q} | q, \dot{q}, \tau_E, \tau_H, d_{ex}) \\ & \sim p(\tau_H) \int p(\ddot{q} | q, \dot{q}, \Sigma\tau) p(\Sigma\tau | q, \tau_E, \tau_H, d_{ex}) d\Sigma\tau \\ & \sim p(\tau_H) \underbrace{\int p(\Sigma\tau | q, \dot{q}, \ddot{q})}_{\text{Inverse Dynamics Model}} p(\Sigma\tau | q, \tau_E, \tau_H, d_{ex}) d\Sigma\tau, \end{aligned} \quad (5.65)$$

since the probability $p(\ddot{q} | q, \dot{q})$ is independent of the integral.

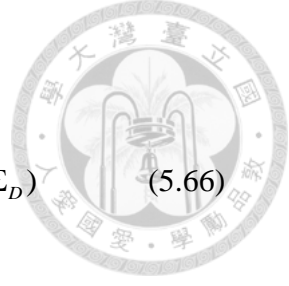
According to the conditional probability of the Gaussian distribution, we have

$$\begin{aligned} & p(\Sigma\tau | q, \tau_E, \tau_H, d_{ex}) \\ & = \int p(\Sigma\tau | \tau_D, \tau_E, \tau_H) \underbrace{p(\tau_D | q, d_{ex})}_{\text{Exogenous Disturbance Model}} d\tau_D \\ & = \mathcal{N}(\Sigma\tau | \tau_E + \tau_H + \mu_D, \Sigma_D) \\ & = \mathcal{N}(\tau_H | \Sigma\tau - \tau_E - \mu_D, \Sigma_D) \end{aligned}$$

and

$$p(\Sigma\tau | q, \dot{q}, \ddot{q}) = \mathcal{N}(\Sigma\tau | \mu_{Inv}, \Sigma_{Inv}).$$

To perform the integral, we recall $p(\Sigma\tau | q, \tau_E, \tau_H, d_{ex})$ is the conditional probability of τ_H given $\Sigma\tau$ and $p(\Sigma\tau | q, \dot{q}, \ddot{q})$ is the prior of $\Sigma\tau$. Therefore, the right hand term



of (5.65) reads as

$$p(\ddot{q} | q, \dot{q}, \tau_E, \tau_H, d_{ex}) \sim \mathcal{N}(\tau_H | \mu_{inv} - \tau_E - \mu_D, \Sigma_{inv} + \Sigma_D) \quad (5.66)$$

Proposition 5.8.

Given two Gaussian distributions $\mathcal{N}(x | \mu_1, \Sigma_1)$ and $\mathcal{N}(x | \mu_2, \Sigma_2)$ of the random variable x , if the probability of x can be factorized into

$$p(x) \sim \mathcal{N}(x | \mu_1, \Sigma_1) \mathcal{N}(x | \mu_2, \Sigma_2)$$

then $p(x)$ is a Gaussian distribution with mean and covariance matrix as

$$\mu = \Sigma(\Sigma_1^{-1}\mu_1 + \Sigma_2^{-1}\mu_2)$$

$$\Sigma = (\Sigma_1^{-1} + \Sigma_2^{-1})^{-1}.$$

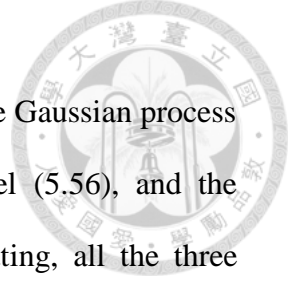
Using Proposition 5.8., the mean and the covariance matrix of the dynamics model can be shown as (5.59) and (5.60), since

$$\begin{aligned} p(\tau_H | q, \dot{q}, \ddot{q}, \tau_E, d_{ex}) \\ \sim \mathcal{N}(\tau_H | 0, \Sigma_H) \mathcal{N}(\tau_H | \mu_{inv} - \tau_E - \mu_D, \Sigma_{inv} + \Sigma_D) \end{aligned}$$

Similarly, we can show the result of the Bayesian human torque estimator as (5.62) and (5.63).

Q.E.D.

From (5.62), the estimator can be viewed as the *time varying* weighted mean of different models by the corresponding precision matrices (the inverse of the covariance matrix). Given the current state, the estimator trusts the estimation of the model with higher precision more, so the resultant estimator can adaptively adjust the estimation. This is the merit of Bayesian model. In contrast, if discriminative models are used in (5.54) and (5.55), the resultant estimator only biases to one of the models and cannot adaptively chose the weighting, unless other sensory information is available.



In summary, the Bayesian human intention estimator uses three Gaussian process models: the biosignal model (5.54), the inverse dynamics model (5.56), and the exogenous disturbance model (5.57). With proper calibration setting, all the three models can be learned by MAP, which will be detailed in the next section. We remark that we cannot learn the conditional probability $p(e | \tau_H)$ directly, but we can approximate the inverse model $p(\tau_H | e)$ instead, and consider the *a priori* probability.

5.4.5 Control and Learning with Graphical Model

In this section, we show how formulation of graphical model can be used in the control of the exoskeleton system and how the Gaussian process models can be learned by MAP.

A. Control with Graphical Model

We adopt the control framework similar to [57] and [45] as in Fig. 5-21. The control scheme consists of two parts: the torque controller and the Bayesian human torque estimator (5.64). The inner torque control loop is aimed to track the torque reference generated by the Bayesian estimator, which is the lowpass filtered version of (5.64), as in Section 5.2. The DC gain of the lowpass filter is set as G_A , which is the assistive gain, and the bandwidth Ω_A is set to be the bandwidth of the human motion. As proved separately in [57] and [45], the additional lowpass filter can guarantee the robust stability of the overall system, and eliminate the discontinuities due to possible switching. In terms of the Bayesian formulation, the lowpass induces changes in the *a priori* probability distribution of the human applying torque in (5.58), such that it is strictly within the prescribed bandwidth Ω_A .

Oracle.

Assume human is a perfect torque controller and inner torque control loop is



perfect. Let G_A be the assistive gain. Given an arbitrary fixed motion, with the assistive control, the human applying torque τ_H becomes

$$\tau_H = \frac{1}{1+G_A} \tau_{H0},$$

where τ_{H0} is the human applying torque of the same motion without the assistive control.

In particular, when the assistive gain G_A is chosen as identity, the exoskeleton will ideally assist half of the human applying torque of the motion.

B. Learning with Graphical Model

(1). The Biosignal Model

To learn the conditional probability $p(\tau_H | e)$, we take the use of the joint force sensor in the exoskeleton in the torque control loop. In the experiments, the operator is asked to wear the exoskeleton with the EMG sensors. As shown in Fig. 5-22 (a), the controller of the exoskeleton is set to position regularization mode with different postures, rejecting any disturbance that deviates the mechanism from the current position. The operator is then asked to perform forward and backward voluntary movements, and the EMG signals e and the exoskeleton torque τ_E are recorded. Assuming that the regulation control is perfect, the Gaussian process model can learn

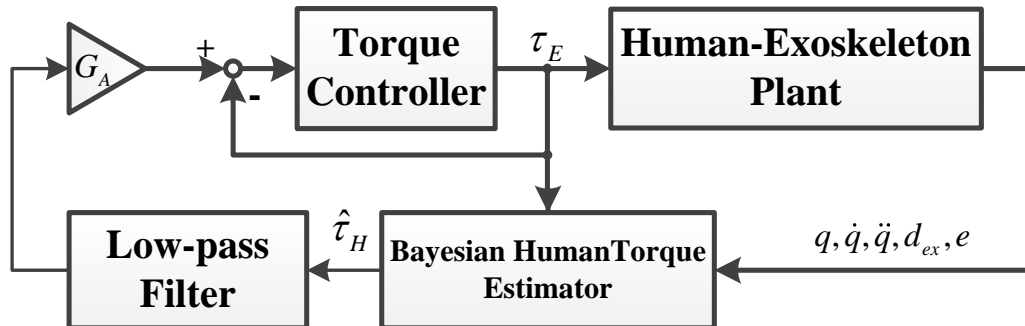


Fig. 5-21. Control block diagram for human assistive exercises



the mapping between the EMG signal and the human applying torque by using the (5.51) and (5.49), i.e.

$$\tau_H = -\tau_E .$$

Linear model in our experience is sufficient to model relationship in most postures. A more complex model considering also the angular position q and the angular velocity \dot{q} is possible or using the nonlinear kernel space, e.g. radial basis kernel. We left it for the future works.

(2). The Inverse Dynamics Model

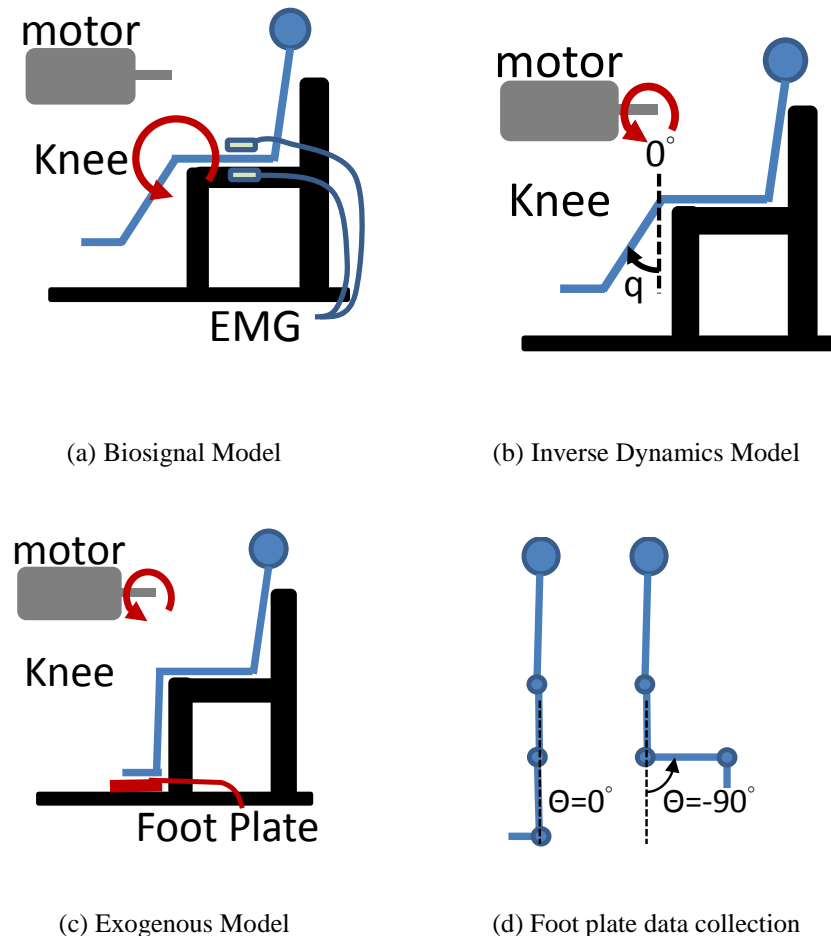
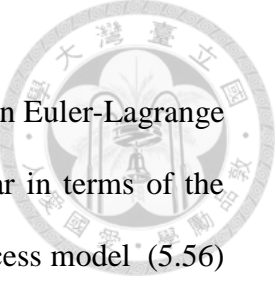


Fig. 5-22. Data collection procedure and the coordinates of joint angle and knee angle

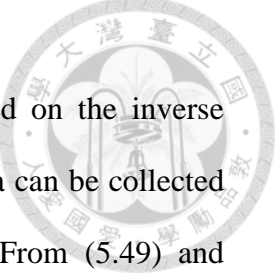


The dynamics of the exoskeleton system can be derived based on Euler-Lagrange equation [92], and it is shown that the total joint torque $\Sigma\tau$ is linear in terms of the unknown parameters. Therefore, we can build a linear Gaussian process model (5.56) as mentioned in the previous section. In the experiments as shown in Fig. 5-22 (b), the operator is asked to wear the exoskeleton and to relax completely. The controller of the exoskeleton is set in position control mode to track some predefined trajectories. If the trajectories are sufficient rich [48], then the underlying model can be identifying by the feedback of the torque sensor information τ_E and the current states of the exoskeleton q, \dot{q}, \ddot{q} .

(3). The Exogenous Disturbance Model

As mentioned in previous section, we do not assume any specific form of the exogenous disturbance sensor. In most of the cases, the exogenous disturbance in the exoskeleton system is the ground reaction force, and the force sensor is footpad. The proposed method, however, are not limited to the sensor above. Other types of the force sensors, even the footswitch in the worst case, can also be adopted to improve the overall accuracy. In the experiments described in the next section, we adopt the footswitch as the force sensor and the results are similar to the switching scheme proposed in [44].

Two possible scenarios of the experiment are both able to learn the conditional probability $p(\tau_D | q, d)$. In the first case, the operator is asked to wear the exoskeleton in relaxation, and the controller of the exoskeleton is set to position regularization with different postures. In each posture, disturbances are injected artificially, and the sensor feedback of the exogenous disturbance senor d_{ex} , the torque sensor τ_E , and the angular position q are recorded.



In the second case, the exogenous disturbance mode is based on the inverse dynamics model learned in the previous experiment, so that the data can be collected more generally without constraining the position of the exoskeleton. From (5.49) and (5.51), we know that the disturbance torque can be estimated if $\tau_H = 0$ and the inverse dynamic model is known. In contrast to the first approach by eliminating the dynamics effect term completely, we can allow the movement of the exoskeleton here by introducing proper prior in (5.42) as long as $\tau_H = 0$.

From the dynamic equation, we know that

$$\tau_D = \Sigma \tau - (\tau_H + \tau_E).$$

Since knowing the human applying torque is generally impossible, we can, however, ask the operator to relax the muscles during the data collection as the trick in the previous experiments. To formulate this into a standard Gaussian process regression problem, we replace the noise model of η in (5.42) to

$$\mathcal{N}(\eta | 0, \Sigma_{inv} + \beta^{-1}I),$$

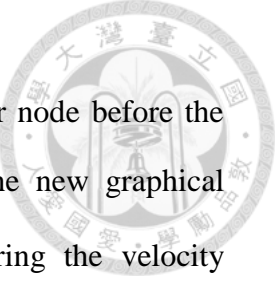
which is a state dependent noise model. Effectively, it is to set \mathbf{C} in (5.45) to

$$\mathbf{C} = \mathbf{K} + \Sigma_{inv} + \beta^{-1}\mathbf{I}_M,$$

where Σ_{inv} is the empirical covariance matrix of the inverse dynamics model in the Gaussian process model computed by (5.47). We note that Σ_{inv} can be chosen to be diagonal by assuming each prediction is independent of time as in Assumption 5.7.2. Since the human applying torque is neglected in this setting, the target of the regression problem, the exogenous transmitted torque, is then

$$\tau_D = \mu_{inv} - \tau_E.$$

We remark that the exogenous disturbance model $p(\tau_D | q, \dot{q}, d)$ can also be



learned in this scenario by modifying the graphical, adding another node before the exogenous disturbance force d_{ex} and another link from \dot{q} to d_{ex} . The new graphical model helps the imprecise disturbance sensor more by considering the velocity information.

In experiment, we collect the data based on the learned inverse dynamics model and the measurements of the torque sensor. As in the case of the inverse dynamics model, the subject is asked to relax totally, and the controller is set to track some predefined position references in which the exogenous force sensor is bound to hit some obstacles. This scenario is designed, because it is sometimes more convenient for the experimenter to collect the data while not constraint the movement of the exoskeleton.

5.4.6 Experiments

In the following experiments, the data acquisition and the controller are implemented on a sbRIO-9642 embedded control and acquisition system (National Instrument Inc.) with sampling rate 250 Hz. To train each Gaussian process model, 6000 training data are sampled uniformly randomly from the recorded data in the previously described experiments. The EMG signals are measured by the active surface EMG electrode with pre-amplifier (B&L Engineering, Inc.) placed on the quadriceps femoris and hamstring muscle, which is later rectified and the DC-component is removed; the exogenous disturbance sensor is the footswitch (B&L Engineering, Inc.); the states of the exoskeleton systems are calculated by numerical difference; the exoskeleton torque τ_E is measured by the backdrivable spring torsion actuator (BTSA) described below. In addition, all the measurements and the control signal are filtered by a second-order Butterworth filter with cutoff frequency 15 Hz.

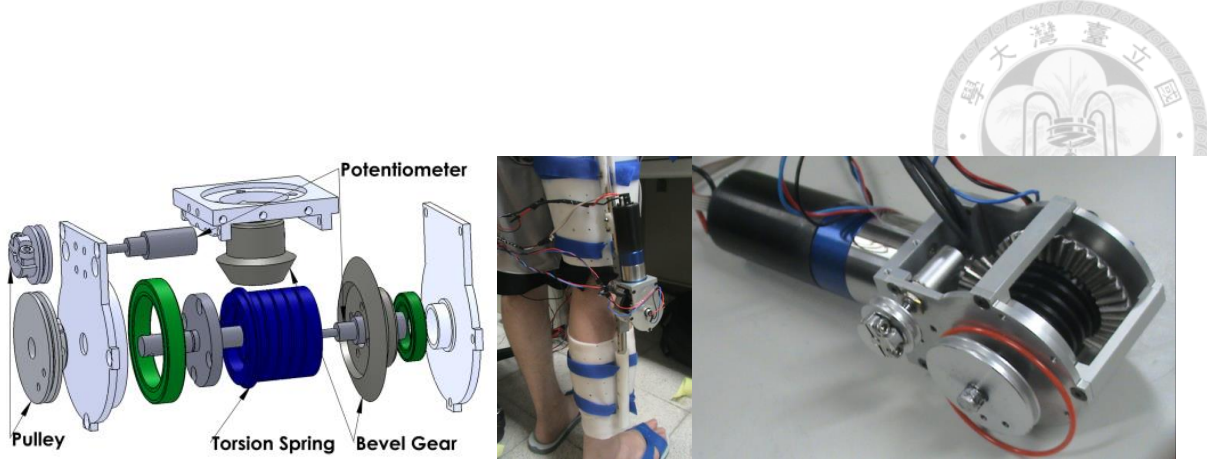


Fig. 5-23. Overview of the proposed backdrivable torsion spring actuator and the knee orthosis exoskeleton

A. Experiment Setting

(1). Backdrivable Spring Torsion Actuator (BTSA)

In order to collect the data and build the biosignal model, the inverse dynamics model, and the exogenous disturbance model for the Bayesian human torque estimator, a simple knee exoskeleton with BTSA [45, 46] is constructed. BTSA is composed of a designed torsion spring, bevel gears, and a DC-actuator. The soft stiffness of the torsion spring provides mechanically intrinsic safety and measures the torque between the human and the actuator. Fig. 5-23 shows the overview of the BTSA. Two potentiometers are used. Inside, one potentiometer is inserted into the spring to measure the deflection of the torsion spring, which can be used to calculate the output torque via Hooke's law. The knee angle θ is measured by the other potentiometer. For the specification of the BTSA, please refer to Section 5.2.2. Finally, we note that with the BTSA the angular position of the output link can be measured directly, so the effect of the spring can be neglected.

(2). Experimental Setting

In this paper, we demonstrate two types of motions with the proposed Bayesian Exoskeleton system: the swing motion and the stair climbing. The swing motion is a

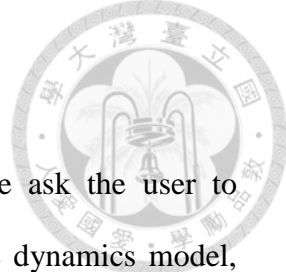


toy example to show how the three Gaussian process models are calibrated with the knee orthosis and to verify the effectiveness of assistive control scheme. The stair climbing, on the other hand, is another example to show how the estimator behaves when the exogenous disturbance comes in.

In the experiments, the subject was a 31-years-old healthy male. The coordinate of the knee angle θ is shown in Fig. 5-22 (d), in which the knee angle θ is 0 degree under knee extension and -90 degrees under knee flexion. We note that the knee angle θ is different from the joint angle q in general, where the joint angle θ is calibrated as in Fig. 5-22 (d), while the joint angle is referred to the world frame as in Fig. 5-22 (b).

Experiments in Swing Motion

In this scenario, the subject is first asked to sit on a chair and drape his leg in relax over the floor, which is the initialization in all the calibrations and in the experiment with assistive control in the swing motion. The calibrations are carried out as detailed in the previous section. In particular, the exogenous disturbance model is based on learned the inverse dynamics model. All the hyper-parameters of the Gaussian process model are chosen by cross-validation in contrast to the expectation maximization approach. In the experiments, we found that the cross-validation gives more satisfactory results, since some of the conditional probabilities are not strictly under the Gaussian assumption. Notably, the exogenous disturbance model fails the assumption when footswitch is used. Also, we model the noise model of the exogenous disturbance model as a function of the exogenous disturbance measurement, where the variance is zero when the force measurement is zero, and a Gaussian random variable with some predefined variance otherwise, due to the nature



of the footswitch.

In the experiment of assistive control in swing motion, we ask the user to perform voluntary movements as in the calibration of the inverse dynamics model, and compare the result with and without the assisting of the exoskeleton. The details are shown in the next section.

Experiments in Climbing Stair up and down

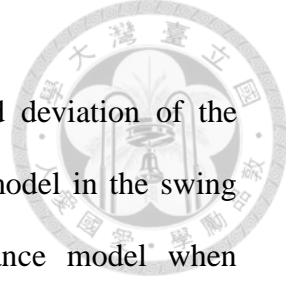
In this experiment, the task is to climb a 20-cm stair up and down repetitively, and the results with and without the assistive control are compared. Assuming the variation of the hip angle is small, the joint angle q and the knee angle θ are similar. Therefore, we assume the joint angle q is the same as the knee angle θ in this task.

B. Experimental Results and Discussions

In section (1), (2), and (3), we show the result of the calibration of the three Gaussian process models: the biosignal model, the inverse dynamics model, and the exogenous disturbance model. Section (4) shows the experimental result of the simple swing motion; Section (5) discusses the results of the stair climbing, which resembles the scenario of the assistive exoskeleton system.

(1). Results of the Biosignal Model

The estimation of the biosignal model and the measured human applying torques are shown in Fig. 5-24, in which the black solid line is the measured human applying torque, the blue solid line is the mode of the prediction, and the blue dash lines indicates the regions within two one standard deviations (corresponding to the 95% confidence region). Despite the inconsistencies in the extreme values, the simple linear EMG signal model and the measurement shares the same tendency, and the prediction errors are acceptable in the sense of 95% confidence. Compared with the



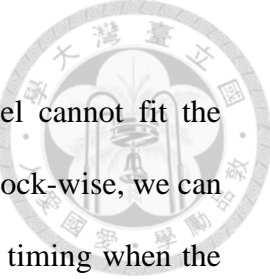
results of the dynamics model in the next section, the standard deviation of the biosignal model is on average higher than that of the dynamics model in the swing motion, and yet smaller than that of the exogenous disturbance model when disturbance comes in. Therefore, it is supposed that the Bayesian human torque estimator should biased to the dynamics model more in the swing phase of the gait cycle.

(2). Results of the Inverse Dynamics Model

The estimated dynamics torque and the measured torque are shown in Fig. 5-25, in which the black solid line is the measured dynamics torque, the blue solid line is the mode of the prediction, and the blue dash lines indicates the regions within two standard deviations (corresponding to the 95 % confidence region). It shows the prediction has the correct tendency and the standard deviation of the prediction varies in different regions. The regions in which the standard deviation is small mean more reliable predictions. We note that the prediction of the estimated dynamics torque has larger prediction variance in the region where the angular acceleration is large, due to the numerical error of the differentiation and the measurement noises. Compared to the other models, the dynamics model has smallest standard deviation, and therefore the Bayesian human estimator will more believe the dynamics model more during the swing phase.

(3). Results of the Exogenous Disturbance Model

The estimated exogenous disturbance torque and the measured torque are shown in Fig. 5-26, in which the black solid line is the measured disturbance torque, the blue solid line is the mode of the prediction, and the blue dash lines indicates the regions within two standard deviations (corresponding to the 95% confidence region). Due the



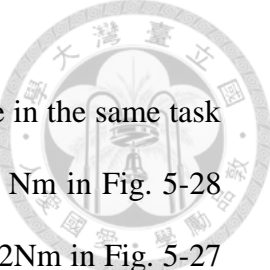
discrete nature of the footswitch, the exogenous disturbance model cannot fit the continuous measurements well. Although the prediction is actually block-wise, we can still infer at least the average exogenous disturbance torque and the timing when the disturbance comes in. The standard deviation of the prediction is the highest among all three models, because the analogue signal of foot switch contains only on (5 Voltage) and off (0 Voltage), which is very inaccurate in estimating exogenous disturbance torque. Therefore, the Bayesian estimator will believe the biosignal model more during the stance phase.

(4). Experimental Results for Swing Motion

The experimental results of the swing motion with and without the assistive control are shown in Fig. 5-27 and Fig. 5-28, respectively. In Fig. 5-27 (a) and Fig. 5-28 (a), the black solid line is the estimation of the Bayesian human torque estimator, the blue dash line is the estimation of dynamics mode, and the yellow dash line is the estimation of the biosignal model. Because the dynamics model has smaller standard deviation than the biosignal model in the swing phase, the human torque of Bayesian estimator is more consistent with the dynamics model. But all of them share the similar tendency. In Fig. 5-27 (b) and Fig. 5-28 (b), the blue solid line denotes the assistive torque of the exoskeleton τ_E and the green dash line denotes the knee angle θ , which is the same as the joint angle q in this experiment. In the swing motion without assistance, the exoskeleton torque τ_E is mainly contributed by the mechanism impedance between the operator and the exoskeleton, whereas in experiment with the assistive control, the exoskeleton torque τ_E is approximately equal to

$$\tau_E \rightarrow G_A \tau_H,$$

where the assistance gain G_A is chosen as identity in this experiment, which means that

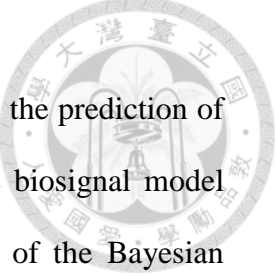


the assistance torque will be about half of the human applying torque in the same task without the assistance. The maximum exoskeleton torque is about 5 Nm in Fig. 5-28 (b) and the maximum human torque of Bayesian estimator is about 12Nm in Fig. 5-27 (a). We can observe that the assistant exoskeleton torque τ_E is nearly half of the human applying torque in the task without assistance, which is consistent with the ideal case in Oracle.

In Fig. 5-27 (c)(d) and Fig. 5-28 (c)(d), the blue lines denote the rectified raw EMG signals and the yellow lines denote the filtered EMG signals, which are used as the input in the biosignal model, of the extensor and the flexor, respectively. During the swing motion, the extensors are the main muscle groups, and therefore the EMG signal of the extensor is larger than that of the flexor. In order to quantify the effectiveness of the assistive control, we compare the magnitude of the filtered EMG signal in Fig. 5-27 (c) and Fig. 5-28 (c). With the assistance of the exoskeleton, the filtered extensor EMG signal in Fig. 5-28 (c) is about half of the magnitude in Fig. 5-27 (c). Finally, the averaged performance is investigated in Fig. 5-27 (e) and Fig. 5-28 (e). The Bayesian exoskeleton decrease the magnitude of the filtered EMG signal, which manifest the human applying torque, decreases about 51% compared to the case without the assistive control. By Oracle, the experiment with swing motion proves the Bayesian human torque estimator.

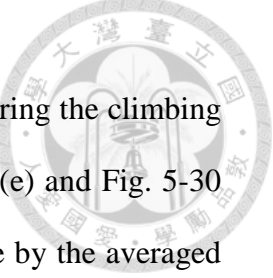
(5). Experimental Results for Climbing Stair Up and Down

The experimental results of the climbing stair up and down with and without the assistive control are shown in Fig. 5-29 and Fig. 5-30, respectively. In Fig. 5-29 (a) and Fig. 5-30 (a), the black solid line denotes estimation of the Bayesian human torque estimator, the blue dash line denotes the estimation of dynamics model, and the



yellow dash line denotes the estimation of biosignal model. Because the prediction of the dynamics model has lower standard deviation than that of the biosignal model without the absence of the exogenous disturbance, the estimation of the Bayesian estimator is more consistent with the dynamics model in the swing phase; In the stance phase, due to the uncertain exogenous disturbance model, the estimation of Bayesian estimator is biased to the biosignal model. Therefore, the discontinuity may occur during phase switching, which can be solved by using a more sophisticated exogenous force sensor than just a simple footswitch. Despite the poor footswitch, this, however, is not a serious problem. As mentioned previously, we can add a lowpass filter after the Bayesian estimator in the control loop to ensure the robust stability and therefore the discontinuity is eliminated [45], because the lowpass filter acts as another important prior information regarding the frequency domain of the human applying torque.

In Fig. 5-29 (b) and Fig. 5-30 (b), the blue solid line denotes the exoskeleton torque τ_E and the green dash line denotes the knee angle θ . As in the swing motion experiment, the small exoskeleton torque in Fig. 5-29 (b) is caused by the mechanical impedance. The maximum exoskeleton torque is about 20 Nm in the Fig. 5-30 (b), which is nearly half of human applying torque, estimated by the Bayesian estimator in Fig. 5-29 (a), in the task without assistance. In Fig. 5-29 (c)(d) and Fig. 5-30 (c)(d), the blue lines denote the rectified raw EMG signals and the yellow lines denote the filtered EMG signals, which are used as the input in the biosignal model, of the extensor and the flexor, respectively. During the climbing stair, the extensors are the main muscle groups and therefore the magnitude of the extensor signal is larger than that of the flexor. The filtered extensor EMG signal in Fig. 5-30(c) is about half of the



signal in Fig. 5-29 (c), because the exoskeleton assists the human during the climbing stair. Finally, the averaged performance is investigated in Fig. 5-29 (e) and Fig. 5-30 (e). As in the swing motion, we quantify the human applying torque by the averaged magnitude of the filtered EMG signal.

In Fig. 5-30 (e), the averaged human applying torque of during 0%~25% climbing cycle increases about 53% percentage compared averaged Fig. 5-29 (e), which means the operator feels a small resistance about 5 Nm during 0%~25% climbing cycle with the assistive control. This is induced by the error of joint angle calibration, since we approximate the joint angle q by the knee angle θ , by assuming the hip angle is small. However, the hip angle is actually large enough to influence the torque estimation from gravity term during 0%~25% climbing cycle, which is the swing phase when climbing up the stair. The problem can be solved by the feedback the hip angle or by adding another gyroscope to determine the joint angle q . However, in our experiments, the assistance performance during the swing phase of climbing up stair is compromised due to the limitation of the hardware. Except 0%~25% climbing cycle, the averaged human applying torque of biosignal model during 25%~50%, 50%~75%, and 75%~100% climbing cycles with assistive control in Fig. 5-30 (e) decrease 36%, 45%, and 11%, respectively, compared to the averaged human applying torque without the assistive control in Fig. 5-29 (e). Because of validity of the hip joint assumption, the performance is a little worse than that of the simple swing experiment. In spite of the imperfection, the Bayesian exoskeleton can still provide assistance to the operator in the climbing task.

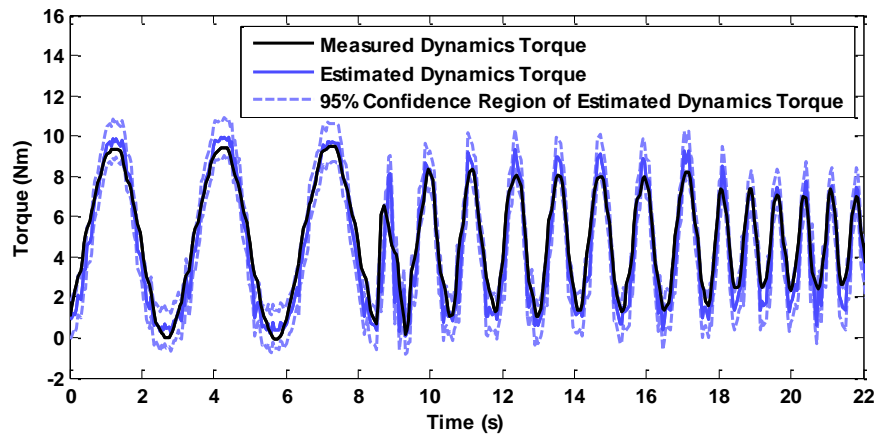
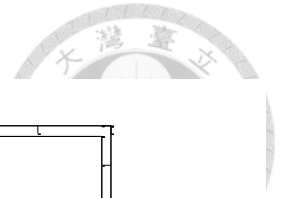


Fig. 5-24. The measured and estimated dynamics torque in dynamics data

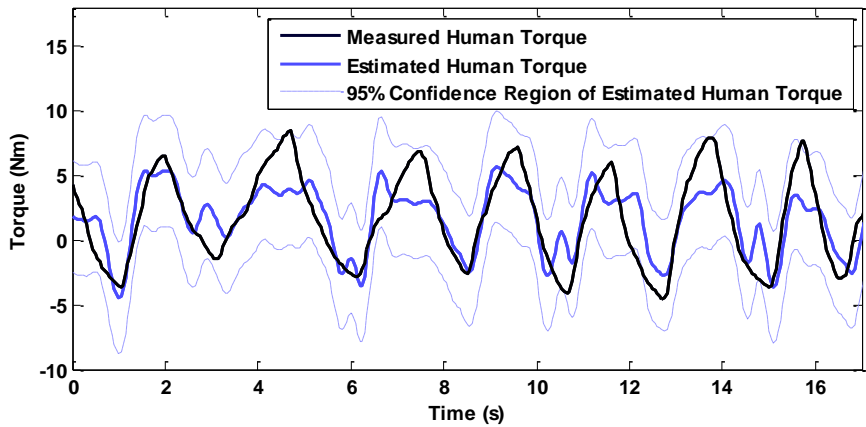


Fig. 5-25. The measured and estimated human torque in EMG model

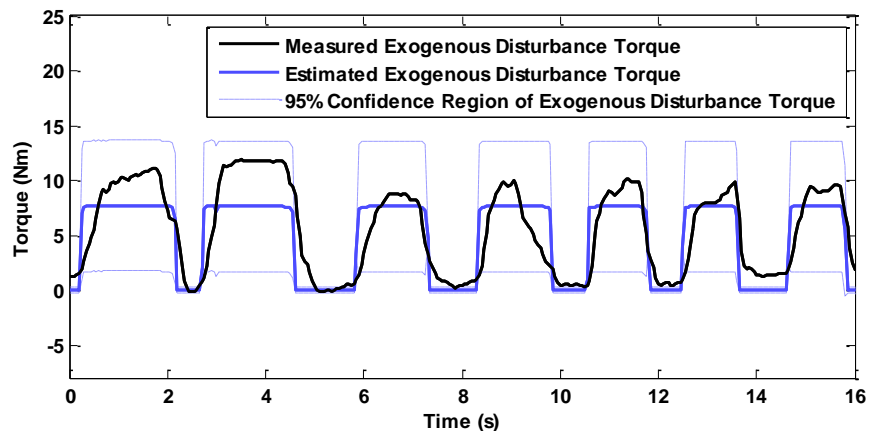
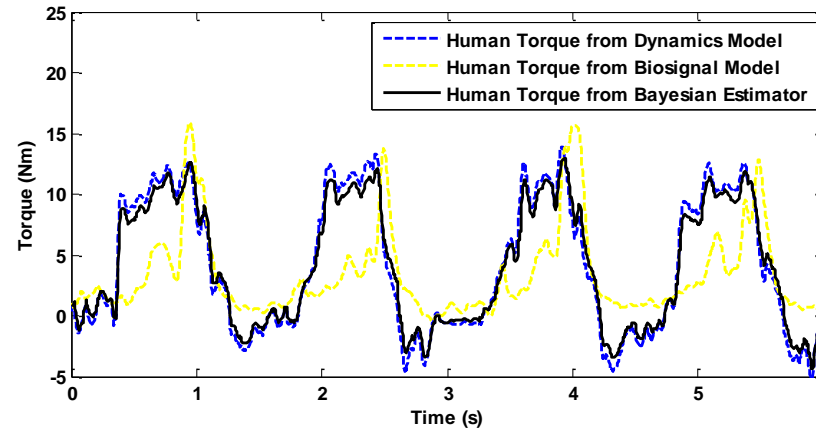
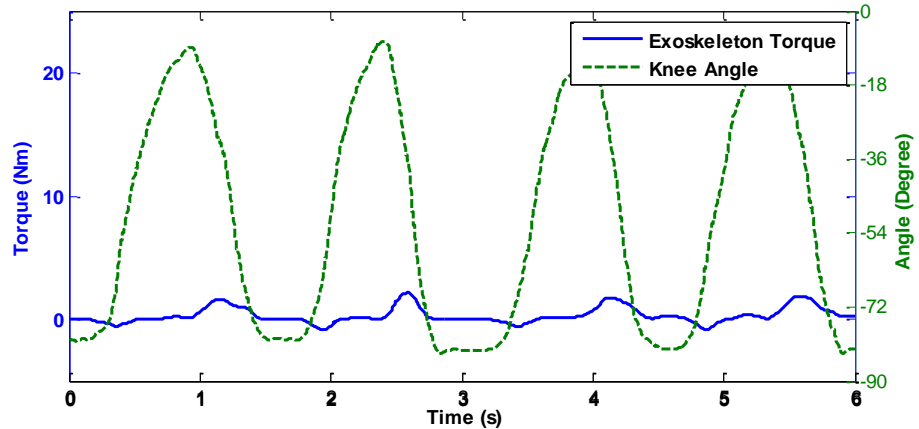


Fig. 5-26. The measured and estimated disturbance torque in the exogenous disturbance mode

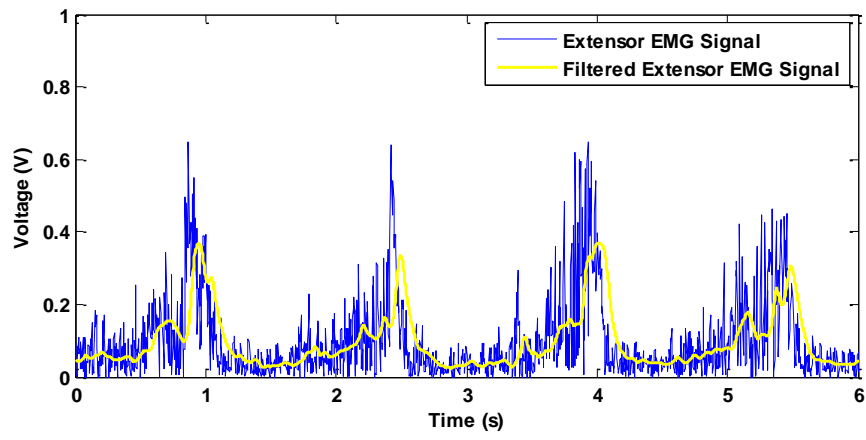


(a)

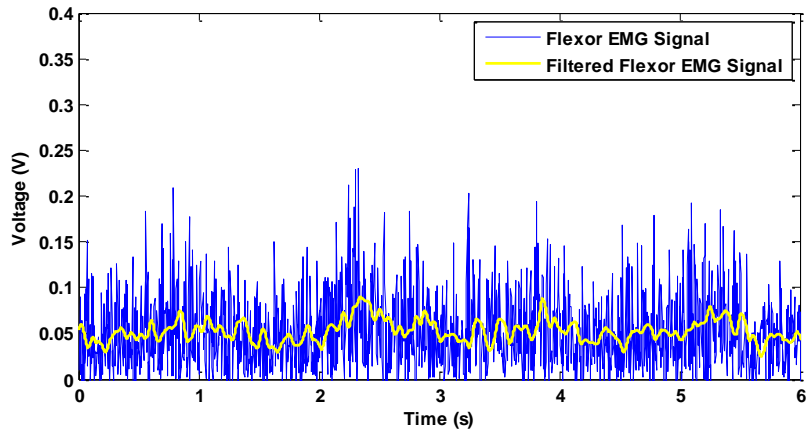


(b)

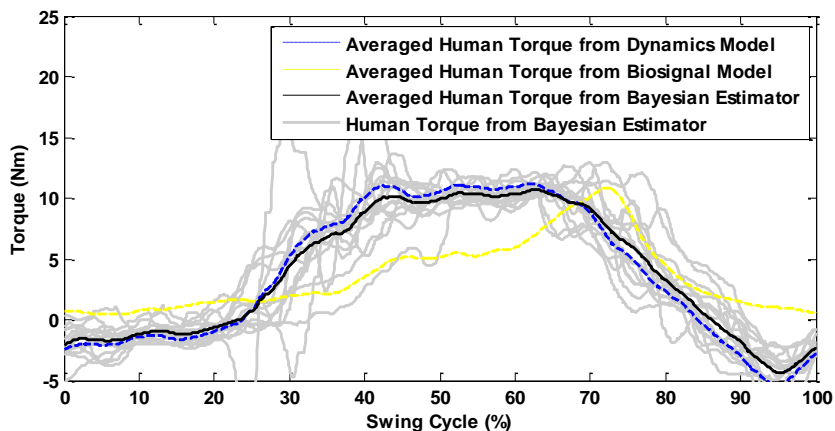
Fig. 5-27. The experimental results of swing motion without the assistive control



(c)

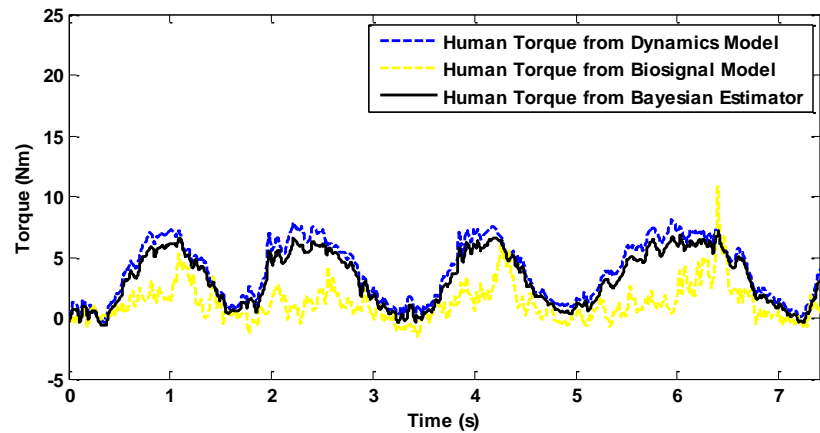


(d)

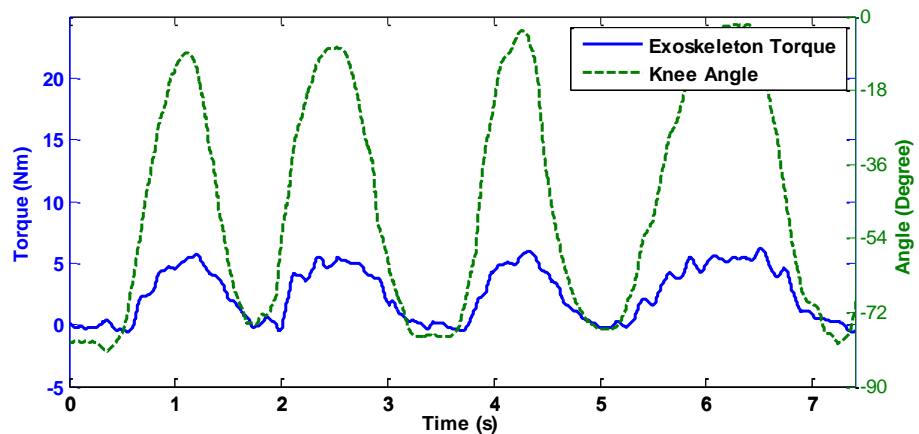


(e)

Fig. 5-27. The experimental results of swing motion without the assistive control

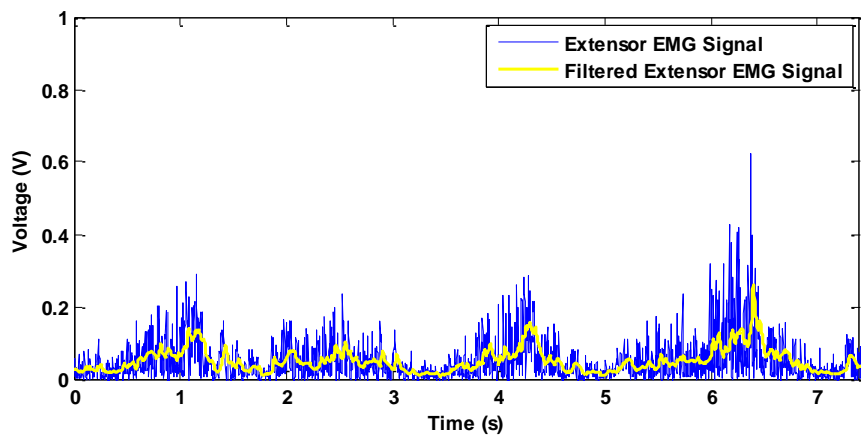


(a)

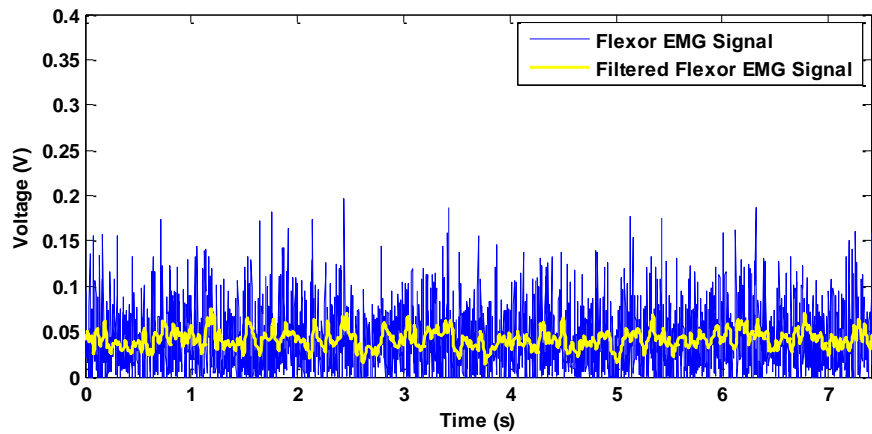


(b)

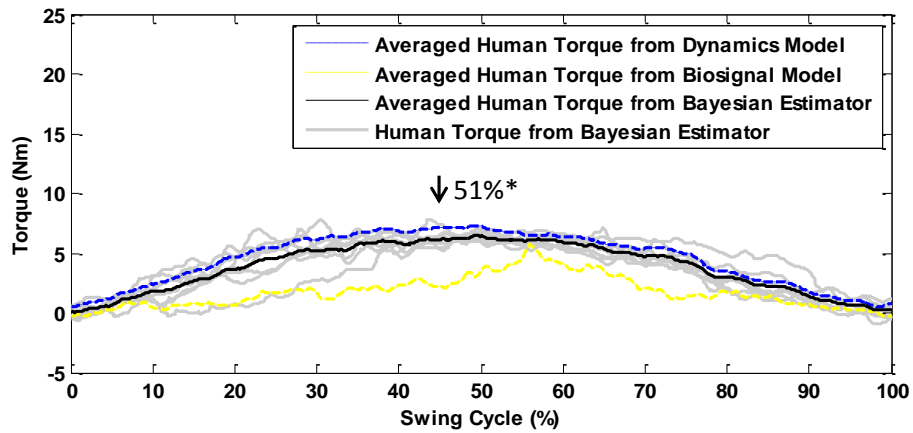
Fig. 5-28. The experimental results of swing motion with the assistive control



(c)

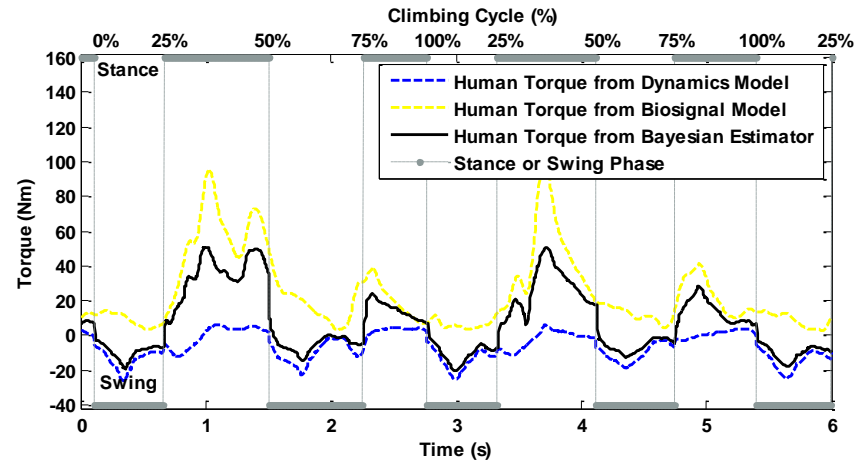


(d)

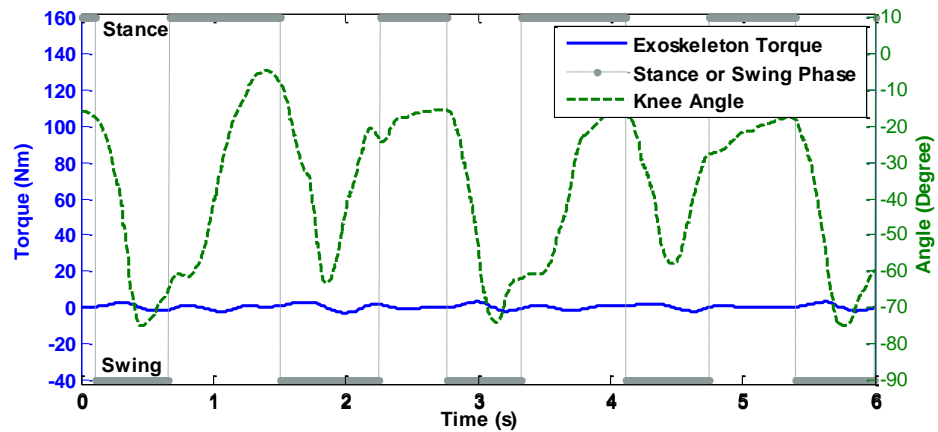


(e)

Fig. 5-28. The experimental results of swing motion with the assistive control

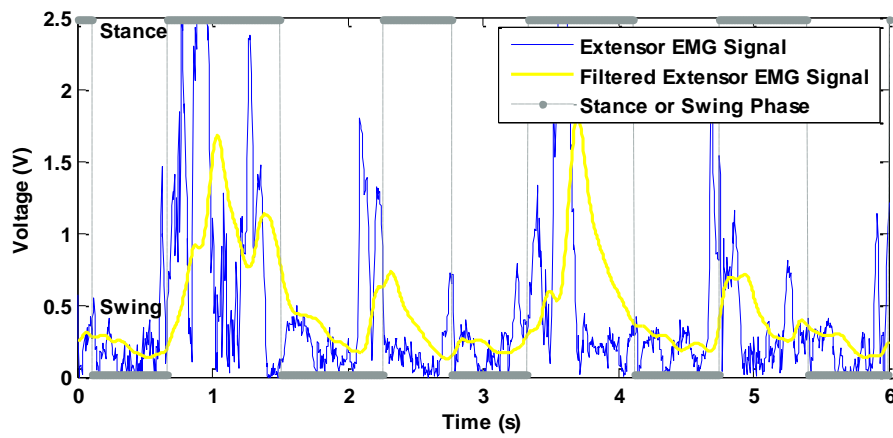


(a)

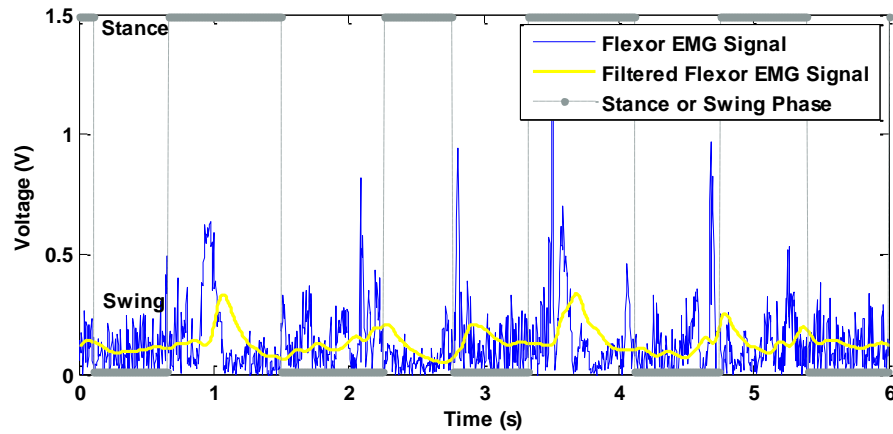


(b)

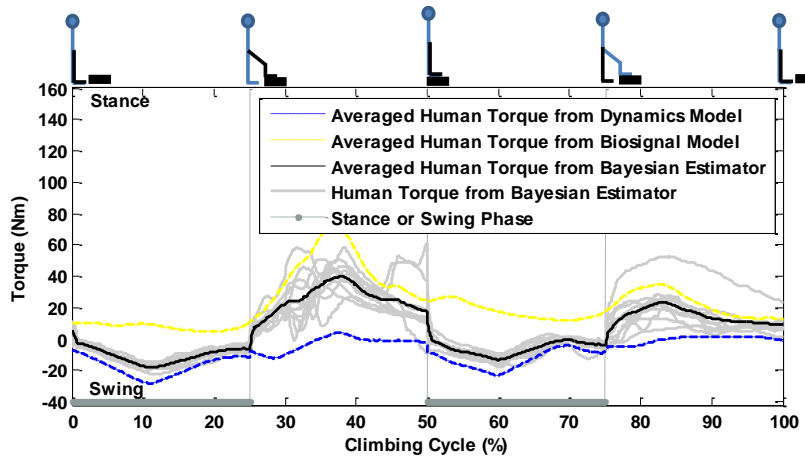
Fig. 5-29. The experimental results of climbing stair up and down without the assistive control



(c)

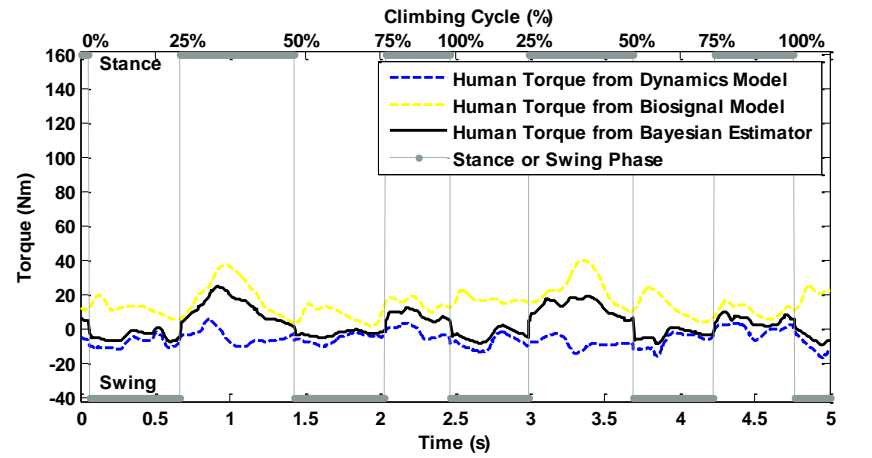


(d)

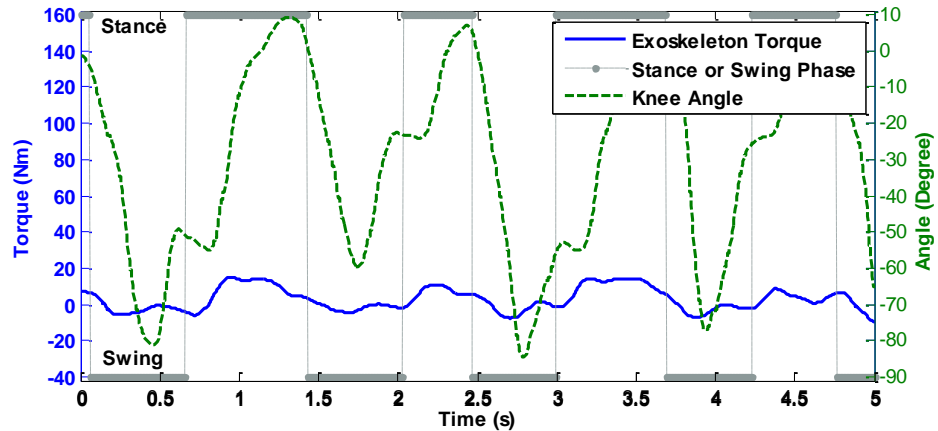


(e)

Fig. 5-29. The experimental results of climbing stair up and down without the assistive control



(a)



(b)

Fig. 5-30. The experimental results of climbing stair with the assistive control

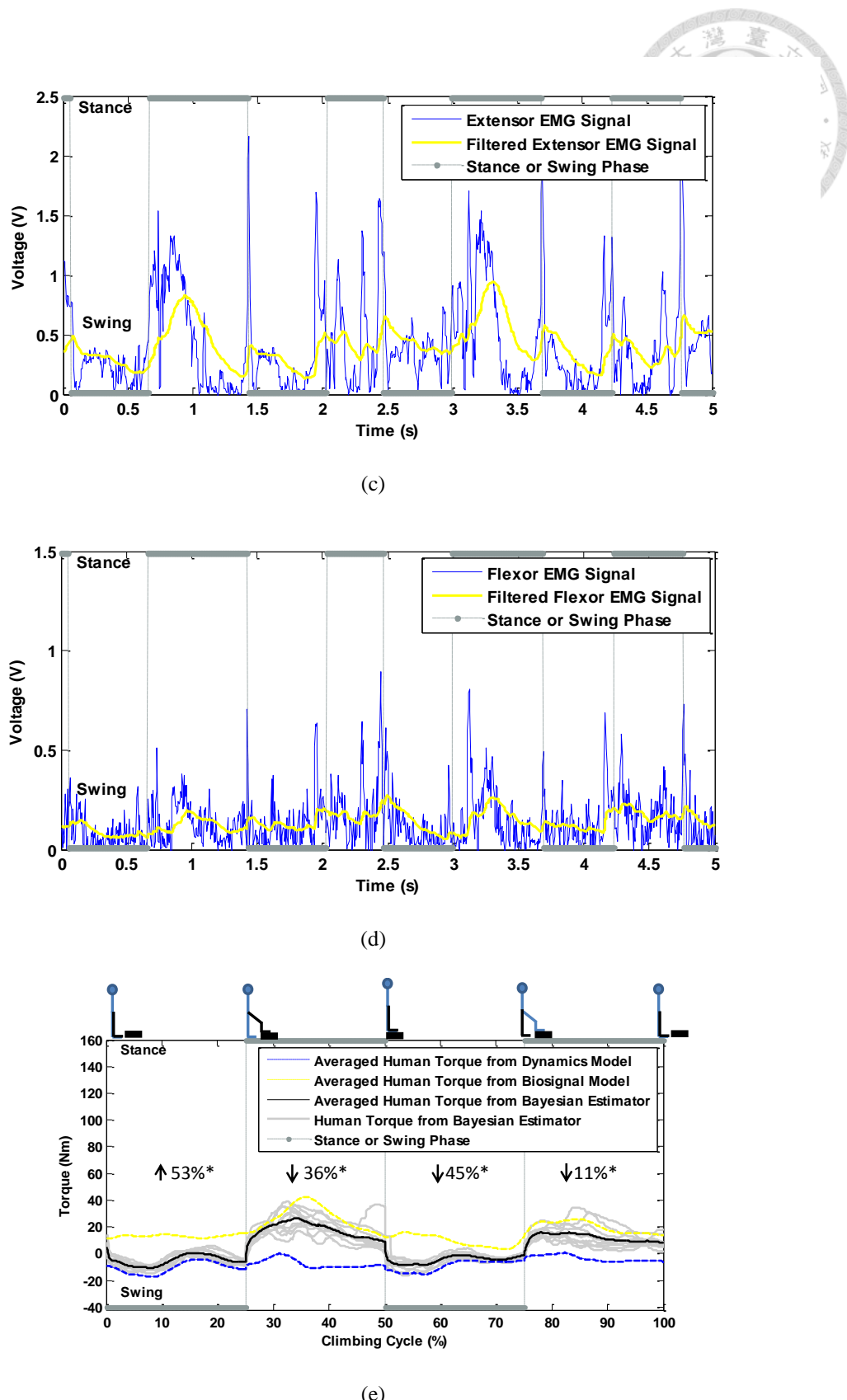


Fig. 5-30. The experimental results of climbing stair with the assistive control

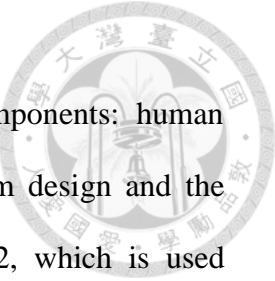


5.4.7 Discussions

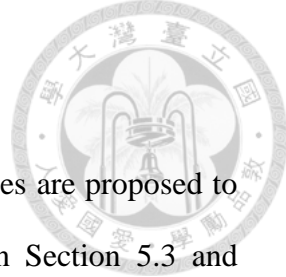
In this section, we propose a general framework of the human-exoskeleton with the probabilistic graphical model. Combined with the robust assistive controller, the Bayesian exoskeleton system can incorporate all the sensory information by means of sensor fusion in a Bayesian manner. The mixture of experts framework can optimally unify the prediction both from the dynamics model and the biosignal model. As a result, the Bayesian exoskeleton system can alleviate the defects of using either one of the model alone by adjusting the weighting between the two models in an adaptive manner. In the experiments, we validate the performance of the proposed system, and the experimental results show prominently that the performance is nearly as good as Oracle guarantees, which proves the accuracy of the Bayesian estimator. In terms of complexity, the training time is short since all the models considered here is the linear model, and the inverse of the covariance matrices can be pre-computed. In the future, we want to adopt the proposed framework into a multi-joint exoskeleton system. The only difference may be complexity of the dynamics model, whereas the biosignal model is not affected. Although the complexity, the expanding terms in the inverse dynamics model, increases, the problem can be solved by introducing proper kernel space. Also, with the multi-joint exoskeleton, the mismatch between the joint angle and the knee angle can be addressed. Finally, whether the performance of the proposed Bayesian estimator in a multi-joint system can be near to Oracle is very interesting.

5.5 Summary

In this chapter, the design and the control of the BTSA knee exoskeleton system



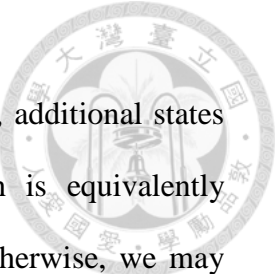
is detailed. The exoskeleton system consists mainly of two components: human intention estimation and the assistive control. First, the mechanism design and the inner robust hybrid assistive control is introduced in Section 5.2, which is used throughout the other sections. The backdrivable BTSA knee exoskeleton provides intrinsically safe human-robot interaction; the robust hybrid scheme can provide the operator support when needed, and therefore the uncomfortable disturbances due to the estimation and modeling errors are efficiently eliminated. To prove the robustness, it is assumed that human is able to compensate any disturbance that is within the bandwidth of the desired movement. Although this holds for healthy subjects, the assumption may hold only partly for the patients with movement impairments. In such condition, a more sophisticated approach should be used. For example, some prior can be introduced to consider the time dependency of the estimation, or the estimator should simultaneously consider the balance of the system. Otherwise, the admissible bandwidth may be too low for normal functionalities. However, it should be mentioned that the strong adaptivity of human seems to be able to learn the dynamics of the augmented system via practicing. Since it is reasonable for the patient to have time to accommodate the new system just as the infant takes time to learn to walk, the property such as *learnability* of an exoskeleton system should be defined. Therefore, instead of designing a *robustly controlled* system with limited functions to bound the effects of the disturbances, a more advanced control scheme should ensure the system is *robustly learnable* or may be adaptive if possible. For example, the system should be biased to perform only simple, limited and robust movements within the canonical robust control, but gradually relax the constraints as the operator learns to control the system. Therefore, a robustly learnable exoskeleton ensures the robustness by



considering the feedback of the operator.

As for the human intention estimation, two different approaches are proposed to combine the dynamics model and the biosignal model shown in Section 5.3 and Section 5.4. The simple self-learning scheme provides adaptivity to learn the non-stationary EMG model, and the sliding mode admittance control ensures the assistive performance robustly. On the other hand, Section 5.4 proposes a general Bayesian framework to model the exoskeleton system regardless of the types of the sensors and the disturbance. Compared to the self-learning scheme, the Bayesian framework adapts to fuse the biosignal model and the dynamics model as the Bayesian committee machine, and therefore the Bayesian human estimator can online optimally combine the two models. The experimental results in Section 5.4 point out an interesting observation that the Bayesian exoskeleton behaves like the self-learning scheme, if the exogenous disturbance sensor is the footswitch. Because the switching nature of the sensor serves as a strong prior, the Bayesian exoskeleton learns to bias to the correct model. If a pressure sensor is used, the evolution of the weighting between the two models may be more continuous. In addition, this result also evidences that the heuristics in the self-learning is a valid approach as the special case of the Bayesian exoskeleton system.

For the future works, we are interested in the control of the multi-joint Bayesian exoskeleton. Since the multi-DOF dynamics model are tedious to be derived, a machine learning approach can be used instead of the traditional analytic approach. In particular, the reproducing kernels proposed in Chapter 3 are good alternatives. However, the current problem is the measurement noise in the EMG measurements and the errors due to numerical differentiation. Since most of the machine learning



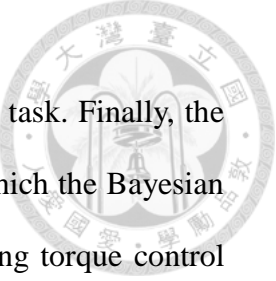
algorithm can only deal with the output noises not the input noises, additional states estimator or a more sophisticated filter should be used, which is equivalently introduced a sets of hidden variables in the Bayesian network. Otherwise, we may derive a similar model based on auto regressive moving average (ARMA) model for sampled system. In addition, the estimation and the assistive control scheme should consider the robust learnability mentioned earlier. We leave this for the future works





Chapter 6 Conclusions

In this thesis, we present three works attempting to use the techniques from various fields for developing the control of the robots in the next generation in terms of the dynamics learning and the human-robot interaction. The kernel methods for learning the system dynamics are improved by the proposed structured kernels proposed in Chapter 3. Derived from the Euler-Lagrange method, these kernels are the natural kernels for learning the dynamics. The first scalar kernel models the function space of the robot dynamics implicitly; the second kernel generalizes the first kernel and considers the correlations between different generalized coordinates by learning the Lagrangian of the system implicitly - the Euler-Lagrangian method is engraved in the structure of the vector-valued RKHS. Due to the structures, the proposed kernels fill the gap between the parametric and the non-parametric learning, and show better generalizations compared to the traditional methods. We remark that this finding is astonishing, showing an interesting links between the machine learning and the traditional system identification of the dynamics system. For the safe human-robot interaction, the virtual impedance control in Chapter 4 is a generalized framework of the robust collision avoidance for the human-robot safety. The proposed scheme unifies all possible collisions in the risk space, in which dynamics is controlled to be a consistent second-order linear system during the collision avoidance. As the consequence, the robot handles the potential collisions smoothly and robustly regardless of the modeling uncertainties. In the experiments, we integrate the proposed method with KinectTM to detect the human and the environment nearby, and the experimental results validate the control scheme. The robot successfully yields to



the command of the human, while trying to accomplish the original task. Finally, the Bayesian exoskeleton is demonstrated as an integrated system, in which the Bayesian estimator inference the human intention optimally and the underlying torque control provides robust assistance. The proposed graphical model gives a transparent view of the dependency of the states and the structure of the human-exoskeleton, and is general for all kinds of exoskeleton systems. Not limited to the mechanisms and the sensors used in this thesis, the Bayesian estimator can inference the human intention adaptively and optimally. Given the estimated human intention, the hybrid control is designed to provide robust assistance. By introducing an insensitive zone, the hybrid scheme not only overcomes the estimation uncertainties but is proved to be robustly stable by the newly proposed human-exoskeleton model. The experimental results show the estimations are accurate and the control law is effective in that the torque from the operator required to perform the tasks is reduced almost as theoretically guaranteed.

In summary, this thesis provides novel algorithms and vast control schema for the development of the human-robot interaction, and each subject is self-contained and worthy of publishing. However, these subjects are essentially linked to each other and can be easily integrated. Although the dynamics learning techniques were developed separately from the controls for the human-robot interaction, it can be directly integrated into the control schema proposed in the previous chapters. In the future works, the theoretical work of structured kernels will be first tested in the experiments in terms of the prediction errors and the tracking errors in the computed torque control. Then this novel modeling techniques can be directly into the Bayesian exoskeleton as the dynamics model, or in the virtual impedance control framework by



replacing the original dynamics as the torque-based impedance control. By fusing these techniques, the overall system can achieve better performances than using either of them alone. More can still be done to improve the theoretical part of the structured kernels. In Chapter 3, the structured kernels are based on the Lagrangian formulation of the dynamics system. However, a similar technique can be used for the Hamiltonian formulation, which covers wider families of dynamics system. Also, the corresponding control schemes can be developed. As for the empirical techniques, a maximum likelihood algorithm can be designed to calibrate the normalization factor of the torque sensors in the vector-valued kernel, since it is assumed that all the measured generalized force should possess the correct unit. Also, the computational time in learning with the vector-valued kernel is another critical issue, which may benefit from the techniques from the compressive sampling, greedy scheme or the reinforcement learning.

As for the control of human-robot interaction, the virtual impedance control and the Bayesian exoskeleton system can still be improved. In the current design of the virtual impedance control, the physical forces from the force sensors or the joint torque sensors do not contribute in the risk space. However, in some circumstances, the physical forces represent the physical collision which may not be detected by the collision avoidance scheme. In this case, the sensed forces should be used in a unified way in the risk space to balance the repulsive force in our current design. That is, the physical forces can be transformed as the forcing term in the second-order linear system in the risk space. In addition, we are interested in the teaching and playing scenario with the virtual impedance control, since the shaping of the robot configuration is more natural by the physical/virtual contact in the Cartesian space



rather than by the joystick. The virtual impedance control may be modified to accustom to this need.

For the Bayesian exoskeleton system, we want to conduct more experiments on different subjects to validate the proposed scheme. Since the biosignal model and the dynamics models are different from subject to subject, how to efficiently calibrating the model with limited data becomes an important topic. Therefore, the proposed structured kernels might cater to this need directly. To provide better estimation, another layer of the graphical model can be designed in the time domain using techniques like Markov chain to eliminate the measurement noises. For example, a transition model of the states like the joint velocity and the joint acceleration, which are used extensively in the dynamics model, can be designed and integrated into the original graphical model. If theses conditional probabilities are too Gaussian distributions, the final estimation can still enjoy a closed form solution. Also, the risk space approach in Chapter 4 can be used as the admittance interface for the torque control of the multiple-joint exoskeleton. As for the implementation, advanced exogenous disturbance sensors and EMG sensors can improve the system's performance at once. Since one of the major defects of the biosignal model is due to the distortions from the slipping of the EMG sensors or the sweats of long-term wearing, a more compact and flexible design or a semi-invasive design can be adopted. On the other hand, using the pressure sensor instead of the footswitch can offer more information. Further, we want to implement the proposed Bayesian exoskeleton system and the robust hybrid control into the full lower-extremity exoskeleton and maybe the upper-extremity exoskeleton as well. When considering the full-body exoskeleton, the balancing control plays an important figure. In walking,



the center of mass or the center of gravity travels along some manifold, so human may proceed. Therefore, the assistive control should honor these constraints as well. We suggest the techniques from the biped-robot can be used.

Finally, we suggest a valuable direction for the future researches. Reviewing all the works in this thesis and some recent literatures, there is a trend of combining the techniques from the control and the machine learning. Since the performance index in the control, e.g. tracking error, is similar to cost function in the machine learning, they share similar characteristics. The only difference is that most of the machine learning algorithms consider only static mappings or stochastic performances rather than the dynamics system as in the control system. However, following the design of the structured kernel or some recent progresses in the machine learning community, e.g. the dynamical systems or the Markov chain in the RKHS, it may be possible to develop a whole new theory that can encode the modern control and sampling techniques in the machine learning algorithms, which should be another milestone of the modern control theory.





References

- [1] A. Albu-Schaffer, O. Eiberger, M. Grebenstein, S. Haddadin, C. Ott, T. Wimbock, *et al.*, "Soft robotics," *IEEE Robotics and Automation Magazine*, Vol. 15, pp. 20-30, 2008.
- [2] R.C. Arkin, "Integrating behavioral, perceptual, and world knowledge in reactive navigation," *Robotics and Autonomous Systems*, Vol. 6, pp. 105-122, 1990.
- [3] N. Aronszajn, "Theory of reproducing kernels," *Transactions of the American Mathematical Society*, Vol. 68, pp. 337-404, 1950.
- [4] B. Bigge and I.R. Harvey, "Programmable springs: Developing actuators with programmable compliance for autonomous robots," *Robotics and Autonomous Systems*, Vol. 55, pp. 728-734, 2007.
- [5] C.M. Bishop, *Pattern recognition and machine learning* Springer, 2007.
- [6] O. Brock, O. Khatib, and S. Viji, "Task-consistent obstacle avoidance and motion behavior for mobile manipulation," in *IEEE International Conference on Robotics and Automation*, Washington, DC, USA., 2002, pp. 388 - 393.
- [7] J. Burbea and P.R. Masani, *Banach and hilbert spaces of vector-valued functions*: Pitman Publishing, 1983.
- [8] A. Caponnetto, C.A. Micchelli, M. Pontil, and Y. Ying, "Universal multi-task kernels," *The Journal of Machine Learning Research*, Vol. 9, pp. 1615-1646 2008.
- [9] A. Caponnetto and E.D. Vito, "Optimal rates for the regularized least-squares algorithm," *Foundations of Computational Mathematics*, Vol. 7, pp. 331-368, 2007.
- [10] C. Carmeli, E. De Vito, and A. Toigo, "Reproducing kernel hilbert spaces and mercer theorem," *Functional Analysis*, 2008.
- [11] C. Carmeli, E. De Vito, and A. Toigo, "Vector valued reproducing kernel hilbert spaces of integrable functions and mercer theorem," *Analysis and Applications*, Vol. 4, pp. 377-408, 2006.
- [12] C. Carmeli, E.D. Vito, A. Toigo, and V. Umanità, "Vector valued reproducing kernel hilbert spaces and universality," *Analysis and Applications*, Vol. 8, pp. 19-61, 2010.

REFERENCES

- [13] C.-A. Cheng, H.-P. Huang, and T.-H. Huang, "On learning the lagrangian for multi-output dynamical system identification with vector-valued reproducing kernel hilbert space," *IEEE Transactions on Robotics*, to be submitted 2013.
- [14] C.-A. Cheng, T.-H. Huang, and H.-P. Huang, "Bayesian exoskeleton system: Intention estimation and assistive control " *IEEE/ASME Transactions on Mechatronics*, p. to be submitted, 2013.
- [15] C.-A. Cheng, T.-H. Huang, and H.-P. Huang, "A structured kernel for learning the robot inverse dynamics," to be submitted 2013.
- [16] C.-A. Cheng, T.-H. Huang, and H.-P. Hunag, "Bayesian human intention estimator for exoskeleton system," in *IEEE/ASME International Conference on Advanced Intelligent Mechatronics*, Wollongong, Australia, 2013, p. submitted.
- [17] C.-A. Cheng, S.-Y. Lo, and H.-P. Huang, "Virtual impedance control for safe human-robot interaction," p. to be submitted, 2013.
- [18] S. Chiaverini, B. Siciliano, and L. Villani, "A survey of robot interaction control schemes with experimental comparison," *IEEE/ASME Transactions on Mechatronics* Vol. 4, pp. 273-285, Sep. 1999.
- [19] R.J.P. de Figueiredo, "A reproducing kernel hilbert space (rkhs) approach to the optimal modeling, identification, and design of nonlinear adaptive systems," in *IEEE Adaptive Systems for Signal Processing, Communications, and Control Symposium*, Lake Louise, Alta., 2000, pp. 42-47.
- [20] A. Dietrich, T. Wimböck, A. Albu-Schäffer, and G. Hirzinger, "Integration of reactive, torque-based self-collision avoidance into a task hierarchy," *IEEE Transactions on Robotics*, Vol. 28 pp. 1278-1293, 2012.
- [21] A. Dietrich, T. Wimböck, H. Taubig, A. Albu-Schäffer, and G. Hirzinger, "Extensions to reactive self-collision avoidance for torque and position controlled humanoids," in *IEEE International Conference on Robotics and Automation*, Shanghai, 2011, pp. 3455-3462.
- [22] A. Dietrich, T. Wimbock, and A. Albu-Schaffer, "Dynamic whole-body mobile manipulation with a torque controlled humanoid robot via impedance control laws," in *IEEE/RSJ International Conference on Intelligent Robots and Systems*, San Francisco, CA, 2011, pp. 3199 - 3206.
- [23] L. Dipietro, M. Ferraro, J.J. Palazzolo, H.I. Krebs, B.T. Volpe, and N. Hogan, "Customized interactive robotic treatment for stroke: Emg-triggered therapy," *IEEE Transactions on Neural Systems and Rehabilitation Engineering*, Vol. 13, pp. 325-334, 2005.



- [24] N.-T. Duy and J. Peters, "Local gaussian process regression for real-time model-based robot control," in *IEEE/RSJ International Conference on Intelligent Robots and Systems*, Nice, France, 2008.
- [25] N.-T. Duy and J. Peters, "Model learning for robot control: A survey," *Cognitive processing*, Vol. 12, pp. 319-340, Nov. 2011.
- [26] N.-T. Duy and J. Peters, "Using model knowledge for learning inverse dynamics," in *IEEE International Conference on Robotics and Automation*, Anchorage, Alaska, USA, 2010, pp. 2677-2682
- [27] N.-T. Duy, B. Schoelkopf, and J. Peters, "Sparse online model learning for robot control with support vector regression," in *IEEE/RSJ International Conference on Intelligent Robots and Systems* St. Louis, MO, USA, 2009, pp. 3121-3126.
- [28] A. Edsinger-Gonzales and J. Weber, "Domo: A force sensing humanoid robot for manipulation research," in *4th IEEE-RAS International Conference on Humanoid Robots*, Santa Monica, CA, United States, 2004, pp. 273-291.
- [29] A.L. Edsinger, "Robot manipulation in human environments," Doctor of Philosophy Doctoral Dissertation, Department of Electrical Engineering and Computer Science, Massachusetts Institute of Technology, Boston, 2007.
- [30] D.J. Estep. (2004, A short course on duality, adjoint operators, green's functions, and a posteriori error analysis.
- [31] T. Evgeniou, C.A. Micchelli, and M. Pontil, "Learning multiple tasks with kernel methods," *Journal of Machine Learning Research*, Vol. 6, pp. 615-637, 2005.
- [32] F. Flacco, T. Kroger, A. de Luca, and O. Khatib, "A depth space approach to human-robot collision avoidance," in *IEEE International Conference on Robotics and Automation* Minnesota, USA, 2012, pp. 338 - 345.
- [33] C. Fleischer and G. Hommel, "A human-exoskeleton interface utilizing electromyography," *IEEE Transactions on Robotics*, Vol. 24, pp. 872-882, August 2008.
- [34] J. Ghan and H. Kazerooni, "System identification for the berkeley lower extremity exoskeleton (bleex)," in *IEEE International Conference on Robotics and Automation*, Orlando, FL, 2006, pp. 3477-3484
- [35] H. Goldstein, C.P.P. Jr., and J.L. Safko, *Classical mechanics*, 3 ed.: Addison-Wesley, 2001.
- [36] A. Gretton, A. Doucet, R. Herbrich, P.J.W. Rayner, and B. Schoelkopf, "Support vector regression for black-box system identification," in *11th IEEE Signal Processing Workshop on Statistical Signal Processing*, 2001, pp. 341-344.

REFERENCES

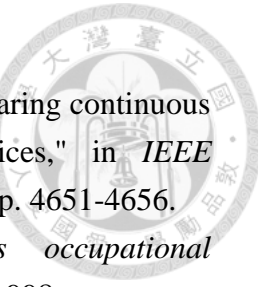
- [37] S. Haddadin, R. Belder, and A. Albu-Schaeffer, "Dynamic motion planning for robots in partially unknown environments," in *Proceedings of the 18th IFAC World Congress*, Milano, Italy, 2011, pp. 6842-6850.
- [38] S. Haddadin, S. Parusel, R. Belder, and J. Vogel, "Holistic design and analysis for the human-friendly robotic co-worker," in *IEEE/RSJ International Conference on Intelligent Robots and Systems*, Taipei, 2010, pp. 4735 - 4742.
- [39] S. Haddadin, H. Urbanek, S. Parusel, D. Burschka, J. Rossmann, A. Albu-Schaffer, *et al.*, "Real-time reactive motion generation based on variable attractor dynamics and shaped velocities," in *IEEE/RSJ International Conference on Intelligent Robots and Systems*, Taipei, 2010, pp. 3109 - 3116.
- [40] T. Hayashi, H. Kawamoto, and Y. Sankai, "Control method of robot suit hal working as operator's muscle using biological and dynamical information," in *IEEE/RSJ International Conference on Intelligent Robots and Systems*, Edmonton, Alberta, Canada, 2005, pp. 3063-3068.
- [41] H.T. Hendricks, J. van Limbeek, A.C. Geurts, and M.J. Zwarts, "Motor recovery after stroke: A systematic review of the literature," *Archives of Physical Medicine and Rehabilitation*, Vol. 83, pp. 1629-1637, Nov 2002.
- [42] A.V. Hill, "The heat of shortening and the dynamic constants of muscle," *Proceedings of the Royal Society of London. Series B, Biological Sciences*, Vol. 126, pp. 136-195, Oct. 10 1938.
- [43] R.A. Horn and C.R. Johnson, *Matrix analysis*: Combridge university Press, 1985.
- [44] T.-H. Huang, C.-A. Cheng, and H.-P. Huang, "Self-learning assistive exoskeleton with sliding mode admittance control," in *IEEE/RSJ International Conference on Intelligent Robots and Systems*, Tokyo, Japan, 2013.
- [45] T.-H. Huang, C.-A. Cheng, H.P. Huang, and Z.-H. Kang, "A robust hybrid control for assistive control with knee orthosis," *IEEE Transactions on Automation Science and Engineering*, 2013.
- [46] T.-H. Huang, H.-P. Huang, C.-A. Cheng, J.-Y. Kuan, P.-T. Lee, and S.-Y. Huang, "Design of a new hybrid control and knee orthosis for human walking and rehabilitation," in *IEEE/RSJ International Conference on Intelligent Robots and Systems* Vilamoura-Algarve, Portugal, 2012, pp. 3653-3658.
- [47] T.-H. Huang, J.-Y. Kuan, and H.-P. Huang, "Design of a new variable stiffness actuator and application for assistive exercise control," in *IEEE/RSJ International Conference on Intelligent Robots and Systems*, San Francisco, California, US, 2011, pp. 372-377.



- [48] P. Ioannou and B. Fidan, *Adaptive control tutorial* SIAM, 2006.
- [49] J. W. Hurst, J. E. Chestnutt, and A.A. Rizzi, "An actuator with mechanically adjustable series compliance," CMU-RI-TR-04-24, April 2004.
- [50] H. Kawamoto, T. Hayashi, T. Sakurai, K. Eguchi, and Y. Sankai, "Development of single leg version of hal for hemiplegia," in *Annual International Conference of the IEEE Engineering in Medicine and Biology Society*, Minneapolis, 2009, pp. 5038-5043
- [51] H. Kawamoto, L. Suwoong, S. Kanbe, and Y. Sankai, "Power assist method for hal-3 using emg-based feedback controller," in *IEEE International Conference on Systems, Man and Cybernetics* Washington D.C., USA, 2003, pp. 1648-1653.
- [52] H. Kazerooni and A. Chu, "Biomechanical design of the berkeley lower extremity exoskeleton (bleex)," *IEEE/ASME Transactions on Mechatronics*, Vol. 11, pp. 128-138, April 2006.
- [53] H.K. Khalil, *Nonlinear systems*, 3rd ed.: Prentice Hall, 2001.
- [54] O. Khatib, "Real-time obstacle avoidance for manipulators and mobile robots," in *IEEE International Conference on Robotics and Automation*, St. Louis, Missouri, 1985, pp. 500-505.
- [55] K. Kiguchi, T. Tanaka, and T. Fukuda, "Neuro-fuzzy control of a robotic exoskeleton with emg signals," *IEEE Transactions on Fuzzy Systems*, Vol. 12, pp. 481-490, August 2004.
- [56] H.A. Kingravi, G. Chowdhary, P.A. Vela, and E.N. Johnson, "Reproducing kernel hilbert space approach for the online update of radial bases in neuro-adaptive control," *IEEE Transactions on Neural Networks and Learning Systems*, Vol. 23, pp. 1130-1141, Jul. 2012.
- [57] K. Kong and M. Tomizuka, "Control of exoskeletons inspired by fictitious gain in human model," *IEEE/ASME Transactions on Mechatronics*, Vol. 14, pp. 689-698, December 2009.
- [58] K. Kong and M. Tomizuka, "A gait monitoring system based on air pressure sensors embedded in a shoe," *IEEE/ASME Transactions on Mechatronics*, Vol. 14, pp. 358-370, June 2009.
- [59] J.-Y. Kuan, T.-H. Huang, and H.-P. Huang, "Human intention estimation method for a new compliant rehabilitation and assistive robot," in *SICE Annual Conference Taiwan*, 2010, pp. 2348-2353.

REFERENCES

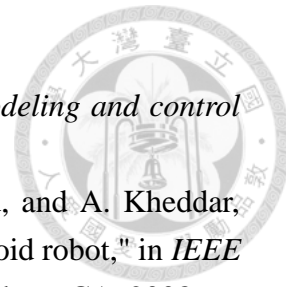
- [60] J.-Y. Kuan, T.-H. Huang, and H.-P. Huang, "Human intention estimation method for a new compliant rehabilitation and assistive robot," in *SICE Annual Conference*, Taiwan, 2010, pp. 2348-2353.
- [61] J.-Y. Kuan, T.-H. Huang, H.-P. Huang, and Y.-T. Chen, "Adaptive coupled elastic actuator developed for physical human-robot interaction," *Advanced Robotics*, Vol. 25, pp. 1473-1491, 2011.
- [62] K. Kyoungchul, B. Joonbum, and M. Tomizuka, "A compact rotary series elastic actuator for human assistive systems," *IEEE/ASME Transactions on Mechatronics*, Vol. 17, pp. 288-297, 2012.
- [63] K. Kyoungchul, B. Joonbum, and M. Tomizuka, "Control of rotary series elastic actuator for ideal force-mode actuation in human & robot interaction applications," *IEEE/ASME Transactions on Mechatronics*, Vol. 14, pp. 105-118, 2009.
- [64] K. Kyoungchul and M. Tomizuka, "Control of exoskeletons inspired by fictitious gain in human model," *IEEE/ASME Transactions on Mechatronics*, Vol. 14, pp. 689-698, 2009.
- [65] G.R.G. Lanckriet, N. Cristianini, P. Bartlett, L.e. Ghaoui, and M.I. Jordan, "Learning the kernel matrix with semidefinite programming," *Journal of Machine Learning Research*, Vol. 5, pp. 27-72, 2004.
- [66] M. Lauria, M.-A. Legault, M.-A. Lavoie, and F. Michaud, "High performance differential elastic actuator for robotic interaction tasks," in *AAAI Spring Symposium*, Stanford, CA, United States, 2007, pp. 39-41.
- [67] Z. Li, Y. Zhang, and Y. Yang, "Support vector machine optimal control for mobile wheeled inverted pendulums with unmodelled dynamics," *Neurocomputing*, Vol. 73, pp. 2773-2782, Aug. 2010.
- [68] S. Mefoued, S. Mohammed, and Y. Amirat, "Knee joint movement assistance through robust control of an actuated orthosis," in *IEEE/RSJ International Conference on Intelligent Robots and Systems* San Francisco, CA, 2011, pp. 1749-1754.
- [69] S.A. Migliore, E.A. Brown, and S.P. DeWeerth, "Novel nonlinear elastic actuators for passively controlling robotic joint compliance," *Journal of Mechanical Design*, Vol. 129, pp. 406-412, 2007.
- [70] B. Mooring, M. Driels, and Z. Roth, *Fundamentals of manipulator calibration*, 1 ed.: Wiley, 1991.



- [71] A. Morbi, M. Ahmadi, A.D.C. Chan, and R. Langlois, "Comparing continuous and intermittent assistance controllers for assistive devices," in *IEEE International Conference on Robotics and Automation* 2011, pp. 4651-4656.
- [72] M.E. Neistadt and E.B. Crepeau, *Willard and spackman's occupational therapy*, 9th ed. Philadelphia: Lippincott Williams & Wilkins 1998.
- [73] C. Ott, *Cartesian impedance control of redundant and flexible-joint robots* Vol. 49: Springer, 2008.
- [74] J.-J. Park, B.-S. Kim, J.-B. Song, and H.-S. Kim, "Safe link mechanism based on nonlinear stiffness for collision safety," *Mechanism and Machine Theory*, Vol. 43, pp. 1332-1348, 2007.
- [75] J.-J. Park, J.-B. Song, and H.-S. Kim, "Safe joint mechanism based on passive compliance for collision safety," in *Recent progress in robotics: Viable robotic service to human*. Vol. 370, ed: Springer, 2008, pp. 49-61.
- [76] G. Pedrick, "Theory of reproducing kernels for hilbert spaces of vector valued functions," University of Kansas Department of Mathematics1957.
- [77] A. Rakotomamonjy, Francis R. Bach, Stéphane Canu, and Y. Grandvalet, "Simplemkl " *Journal of Machine Learning Research*, Vol. 9, pp. 2491-2521, 2008.
- [78] M. Reisert and H. Burkhardt, "Learning equivariant functions with matrix valued kernels," *Journal of Machine Learning Research*, Vol. 8, pp. 385-408, 2007.
- [79] F. Reyes and R. Kelly, "On parameter identification of robot manipulators " in *International Conference on Robotics and Automation*, Albuquerque, New Mexico, 1997, pp. 1910-1915.
- [80] H. Rifai, S. Mohammed, B. Daachi, and Y. Amirat, "Adaptive control of a human-driven knee joint orthosis," in *IEEE International Conference on Robotics and Automation* Saint Paul, MN, 2012, pp. 2486-2491.
- [81] D.W. Robinson, "Design and analysis of series elasticity in closed-loop actuator force control," Doctor of Philosophy in Mechanical Engineering Doctoral Dissertation, Department of Mechanical Engineering, Massachusetts Institute of Technology, Boston, 2000.
- [82] W. Rudin, *Principles of mathematical analysis*, 3rd ed.: McGraw-Hill, 1953.
- [83] M. Sanchez-Fernandez, M. de-Prado-Cumplido, J. Arenas-Garcia, and F. Perez-Cruz, "Svm multiregression for nonlinear channel estimation in multiple-input multiple-output systems," *IEEE Transactions on Signal Processing*, Vol. 52, pp. 2298 - 2307, 2004.

REFERENCES

- [84] A.D. Santis, A. Albu-Schäffer, C. Ott, B. Siciliano, and G. Hirzinger, "The skeleton algorithm for self-collision avoidance of a humanoid manipulator," in *IEEE/ASME international conference on Advanced intelligent mechatronics*, Zurich, 2007, pp. 1-6.
- [85] B. Schoelkopf, R. Herbrich, and A.J. Smolar, "A generalized representer theorem," in *Th Annual Conference on Computational Learning Theory*, 2001, pp. 416-426.
- [86] B. Schoelkopf and A.J. Smola, *Learning with kernels*: The MIT Press, 2001.
- [87] N.A. Scott and C.R. Carignan, "A line-based obstacle avoidance technique for dexterous manipulator operations," in *IEEE International Conference on Robotics and Automation*, Pasadena, CA, 2008, pp. 3353-3358.
- [88] J.W. Sensinger and R.F. Weir, "Design and analysis of a non-backdrivable series elastic actuator," in *IEEE International Conference on Rehabilitation Robotics*, Chicago, IL, United States, 2005, pp. 390-393.
- [89] L. Sentis and O. Khatib, "A whole-body control framework for humanoids operating in human environments " in *IEEE International Conference on Robotics and Automation*, Florida, USA, 2006, pp. 2641-2648.
- [90] F. Seto, K. Kosuge, and Y. Hirata, "Self-collision avoidance motion control for human robot cooperation system using robe," in *IEEE/RSJ International Conference on Intelligent Robots and Systems*, Alberta, Canada, 2005, pp. 3143 - 3148.
- [91] F. Seto, K. Kosuge, and Y. Hirata, "Self-collision avoidance motion control for human robot cooperation system using robe," in *IEEE/RSJ International Conference on Intelligent Robots and Systems* Edmonton, Alberta, Canada, 2005, pp. 3143-3148.
- [92] B. Siciliano and O. Khatib, *Springer handbook of robotics*: Springer, 2008.
- [93] O. Sigaud, C. Salauen, and V. Padois, "On-line regression algorithms for learning mechanical models of robots: A survey," *Robotics and Autonomous Systems*, Vol. 59, pp. 1115-1129, Dec. 2011.
- [94] A.J. Smola and B. Schoelkopf, "A tutorial on support vector regression," *Journal Statistics and Computing*, Vol. 14, pp. 199-222, 2004.
- [95] R. Song, K.-y. Tong, X. Hu, and L. Li, "Assistive control system using continuous myoelectric signal in robot-aided arm training for patients after stroke," *IEEE Transactions on Neural Systems and Rehabilitation Engineering*, Vol. 16, pp. 371-379, 2008.



- [96] M.W. Spong, S. Hutchinson, and M. Vidyasagar, *Robot modeling and control* 1ed.: Wiley, 2005.
- [97] O. Stasse, A. Escande, N. Mansard, S. Miossec, P. Evrard, and A. Kheddar, "Real-time (self)-collision avoidance task on a hrp-2 humanoid robot," in *IEEE International Conference on Robotics and Automation*, Pasadena, CA, 2008, pp. 3200-3205.
- [98] H. Sugiura, M. Gienger, and C. Goerick, "Real-time self collision avoidance for humanoids by means of nullspace criteria and task intervals," in *IEEE-RAS International Conference on Humanoid Robots*, Genova, 2006, pp. 575 - 580.
- [99] K.P. Tee, C. Guan, K.K. Ang, K.S. Phua, C. Wang, and H. Zhang, "Augmenting cognitive processes in robot-assisted motor rehabilitation," in *2nd IEEE RAS & EMBS International Conference on Biomedical Robotics and Biomechatronics*, 2008, pp. 698-703.
- [100] J. Ting, M. Mistry, J. Peters, S. Schaal, and J. Nakanishi, "A bayesian approach to nonlinear parameter identification for rigid body dynamics," in *Robotics: Science and Systems*, Philadelphia, USA, 2006.
- [101] E. Torres-Jara and J. Banks, "A simple and scalable force actuator," in *35th International Symposium on Robotics*, 2004.
- [102] R.Y. Tsai and R.K. Lenz, "A new technique for fully autonomous and efficient 3d robotics hand/eye calibration," *IEEE Transactions on Robotics and Automation*, Vol. 5, pp. 345-358, Jun. 1989.
- [103] D. Tuia, J. Verrelst, L. Alonso, F. Perez-Cruz, and G. Camps-Valls, "Multioutput support vector regression for remote sensing biophysical parameter estimation," *IEEE Geoscience and Remote Sensing Letters*, Vol. 8, pp. 804-808, 2011.
- [104] R. Van Ham, B. Vanderborght, M. Van Damme, B. Verrelst, and D. Lefeber, "Maccepa, the mechanically adjustable compliance and controllable equilibrium position actuator: Design and implementation in a biped robot," *Robotics and Autonomous Systems*, Vol. 55, pp. 761-768, 2007.
- [105] E. Vazquez and E. Walter, "Multi-ouput support vector regression," in *the 13th IFAC Symposium on System Identification*, De Doelen Rotterdam, 2003.
- [106] S. Vijayakumar and S. Schaal, "Locally weighted projection regression: An o(n) algorithm for incremental real time learning in high dimensional space," in *the Seventeenth International Conference on Machine Learning* Stanford, CA, USA, 2000, pp. 1079-1086.

REFERENCES

- 
- [107] G.L. Wang, Y.F. Li, and D.X. Bi, "Support vector machine networks for friction modeling," *IEEE/ASME Transactions on Mechatronics*, Vol. 9, pp. 601-606, Sep. 2004.
 - [108] A. Wege, K. Kondak, and G. Hommel, "Force control strategy for a hand exoskeleton based on sliding mode position control," in *IEEE/RSJ International Conference on Intelligent Robots and Systems*, Beijing, 2006, pp. 4615-4620.
 - [109] E.T. Wolbrecht, V. Chan, D.J. Reinkensmeyer, and J.E. Bobrow, "Optimizing compliant, model-based robotic assistance to promote neurorehabilitation," *IEEE Transactions on Neural Systems and Rehabilitation Engineering*, Vol. 16, pp. 286-297, 2008.
 - [110] S. Wolf and G. Hirzinger, "A new variable stiffness design: Matching requirements of the next robot generation," in *IEEE International Conference on Robotics and Automation*, 2008, pp. 1741-1746.
 - [111] S. Xu, X. An, X. Qiao, L. Zhu, and L. Li, "Multi-output least-squares support vector regression machines," *Pattern Recognition Letters*, Vol. 34, pp. 1078-1084, 2013.
 - [112] W. Yu, J. Rosen, and X. Li, "Pid admittance control for an upper limb exoskeleton," in *American Control Conference*, San Francisco, CA, 2011, pp. 1124-1129.
 - [113] X. Zhu. (2008). *Semi-supervised learning literature survey*. Available: http://pages.cs.wisc.edu/~jerryzhu/pub/ssl_survey.pdf